Fire Resistance of Steel and Composite Columns

Phng Guan Hwee, Eugene

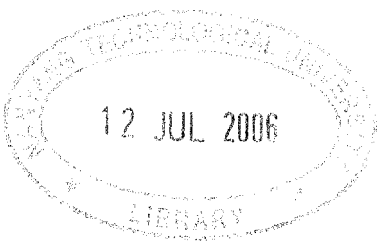

School of Civil and Environmental Engineering

A thesis submitted to the Nanyang Technological University
in fulfilment of the requirement for the degree of
Master of Engineering

2006

ACKNOWLEDGEMENTS

The author would like to express his sincere gratitude to his supervisor, Associate Professor Tan Kang Hai, for providing the opportunity for his postgraduate study. His kind advices, patient understanding and endless encouragement have been most invaluable to the author, in both his work as well as personal life.

Appreciation goes to Associate Professor Ting Seng Kiong, for assessing this thesis. There are special mentors that the author must acknowledge due to their importance in his work. They are Dr. Huang Zhanfei and Dr. Toh Wee Siang. They have been there selflessly helping and guiding the author in his work. The author is indebted to Dr Huang Zhanfei, for he has provided tremendous help and guidance, especially in the FEM analysis part.

The experimental work in this thesis is part of a research program funded by the Building Control Authority (BCA), Singapore, Project no: CRP01/08/14. The author would like to acknowledge BCA for the kind sponsorship in this project.

The technical staffs from Construction Laboratory have been providing the author with conveniences and assistance in many ways during his experimental testing and laboratory session teaching. The author would like to express his gratitude to them.

There are also people, beside the above-mentioned, who have been there giving moral support and creating a motivating atmosphere for the author. These are the members from the Fire Engineering Research Group at Nanyang Technological University (FERGAN) and friends from all areas of life. The author would like to show his appreciation to them.

Last but not least, the author would like to say that he has been greatly indebted to his family members, who are always there to shower him with care and concern, at all times.

ABSTRACT

A programme of experimental testing has been conducted to investigate the behaviour of steel columns and concrete-encased steel section composite columns at elevated temperature. Heating is attained in an electric furnace. Measurements of internal forces, lateral deflections, axial displacements and temperatures are reported.

Twenty steel column specimens were subjected to elevated temperatures. One loading test was carried out at ambient temperature to determine the working load to be applied to the other specimens in the same series for elevated temperature tests. The variable parameters were slenderness ratio and axial restraint ratio. The experimental measurements are presented and compared with predictions from numerical simulations using FEMFAN-3D, a program developed by NTU. It is concluded that buckling temperature decreases as slenderness ratio increases, under a fixed restraint ratio. Applying increased axial restraint to the columns has a negative effect of reducing the buckling temperatures,

Eleven composite column tests were conducted under elevated temperature conditions. The composite columns were categorised into three series with different variable parameters, namely overall cross-sectional size, steel section ratio and axial restraint ratio. Results show that the fire resistance of composite column improves with an increase in overall cross-sectional size. An increase in steel section ratio or axial restraint ratio will lead to a reduction in its fire resistance. Test results are compared with FEMFAN-3D predictions for verifying the accuracy of the program.

Column behaviour under elevated temperatures and predictions and limitations of the numerical program FEMFAN are discussed in the report.

TABLE OF CONTENTS

List of Tables

List of Figures

List of Symbols

A_c = cross-sectional area of concrete

A_f = floor area

A_g = gross sectional area of composite column

A_r = cross-sectional area of steel reinforcement

A_s = cross-sectional area of steel section

A_t = total surface area of the fire enclosure

A_T = overall cross-sectional area of column

A_v = vertical opening area

E = elastic modulus

E_o^{20} = slope of the linear elastic range at ambient temperature

E_o^T = slope of the linear elastic range at elevated temperature

I = second moment of inertia

K_c = column axial stiffness at ambient temperature

K_R = rotational restraint stiffness

K_s = restraining axial stiffness

L = total length of column

L_e = effective length of column

M_p = plastic moment

M_y = first yield moment

N_{cr} = elastic critical load

$N_{pl,Rd}$ = plastic resistance to compression

N_{sd} = design axial load

O = ventilation factor

P = total internal restrained force

P_b = buckling load

P_e = Euler load

P_o = applied working load

$P_{u,20}$ = buckling resistance of column at ambient temperature

S = plastic section modulus

T = steel temperature

T_c = concrete temperature

T_a = ambient temperature, taken as 20°C

T_{cr} = buckling temperature

T_f = flange thickness

T_{fi} = gas atmospheric temperature at time t

V_{cr} = critical shear force

V_{ult} = ultimate shear capacity

Z = elastic section modulus

Z = slope of the secondary creep-strain relationship

a = constant

a = plate girder panel span length

a/d = aspect ratio

b = breadth

b = constant

c = constant / concrete cover

d/t = slenderness ratio of a plate girder

d = web depth

e = load eccentricities

f_c' = concrete characteristic strength

f_{pp}^{T} = proportional limit at elevated temperature

f_y = structural steel characteristic strength

f_{yr} = steel reinforcement characteristic strength

f_y^{T} = effective yield strength at elevated temperature

h = height

h_v = vertical opening height

i_1, i_2, i_3 = initial crookedness along column length

k_b = conversion factor to account for the influence of fire enclosure linings

k_c = factor accounting for different types of construction

$k_{c,T}$ = retention factor for the reduced compressive strength

$k_{E,T}$ = retention factor for the reduced elastic modulus

$k_{p,T}$ = retention factor for the reduced proportional limit

$k_{y,T}$ = retention factor for the reduced yield strength

$q_{f,d}$ = design fire load density per floor area

r = radius of gyration

t = web thickness

t = standard fire exposure time

t^* = variable

t^*_{max} = variable

t_{eqv} = equivalent time

t_w = web thickness

w_f = ventilation factor

x = variable

α_k = axial restraint ratio

δ = steel section contribution ratio to total axial capacity

δ_{mid} = mid-height displacement

ε_σ = stress related strain

$\varepsilon_{1,2}$ = principal strain

ε_{cr} = creep strain

ε_{cr0} = intercept at the creep strain axis by the secondary creep strain slope line

ε_d = 45˚-diagonal strains in the x-y plane

$\varepsilon_{pp}^{\ T}$ = strain at the proportional limit at elevated temperature

ε_{th} = thermal expansion strain of steel

ε_x = horizontal strains in the x-y plane

ε_y = vertical strains in the x-y plane

$\varepsilon_y^{\ T}$ = strain at elevated temperature

γ_r = partial safety factor

γ_s = partial safety factor

γ_{xy} = shear strain

γ_y = partial safety factor

$\Delta H/R$ = constant

λ = slenderness ratio of column

λ_c = thermal conductivity of concrete

θ = temperature compensated time

θ_p = principal angle

Θ_g = gas temperature in the fire compartment

σ_{cr} = critical stress

σ_t = tensile membrane stress

σ_y = yield strength

ρ = area of steel section to overall column cross-section ratio

ρ_s = area of steel reinforcement bars to overall column cross-section ratio

τ_{cr} = critical shear stress

φ = variable

χ = reduction coefficient

CHAPTER ONE

INTRODUCTION

1.1 Background

Steel has become increasingly popular as a construction material to architects and structural engineers in buildings, especially for multi-storey buildings. The advantages of using steel in construction are cost effectiveness, speed of erection, high strength/weight ratio, reliability and durability. A typical steel building can be constructed in at least 30% less time than it takes to construct a conventional reinforced concrete building. Steel modules and components may be fabricated in the factory and assembled on site. The design of some buildings, especially commercial and institutional buildings, requires large-span column-free space. Steel-concrete composite flooring system, with a high strength-to-weight ratio, is conventionally used for steel structures.

However, the fact that both the yield strength and the stiffness deteriorate in elevated temperature shows that bare steel is not fire resistant; it is vulnerable at elevated temperature. A collapse happens when its stiffness and material properties have degraded to such an extent that the applied load cannot be supported by the steel structures anymore. Therefore, adequate fire safety has to be factored into the structures to reduce the risk of injury, death and loss of property. Fire protection is used to extend the fire resistance of steel members by preventing the steel temperature from rising and hence retarding the degradation of the steel properties. Fire protection can be categorised into two types – passive and active. Active protection systems, such as sprinklers, suppress the growth of fire. They are activated in the event of a fire occurrence. Passive protection prevents fire from affecting the structure and comes in the form of sprays, boarding and other insulation methods. However, this kind of fire protection through insulation of steel elements is costly and can be up to 30% of the entire construction cost (Robinson & Latham, 1986). Also, construction will be delayed if application of fire protection

falls on the critical path of a building erection process. Furthermore, additional costs are needed to regularly maintain the fire protection materials.

Until very recently, measures to tackle fires in a building have followed prescriptive procedures that have evolved over the years. These practices are adopted by different regulations and codes. Design performance criteria that dictate the quantity of fire protection have previously been based on preventing the steel rising to a critical temperature of 550°C. However, more recent design codes such as BS5950 Part 8 and EC3 Part 1.2 have a more holistic approach to fire resistant design. Data used to support structural performance assessment are collected from extensive standard fire resistance testing of isolated members. On the other hand, it is evident that heated structural elements behave in a more complex manner when interacting with other non-heated adjacent members.

Large amount of recent research conducted into the behaviour of steel structures in fire conditions has led to more comprehensive fire engineering approaches. Rational analysis of structural behaviour in fire can reduce the need for fire protection considerably, resulting in a large reduction in construction cost. Detailed fire engineering design can only be carried out successfully if structural behaviour in fire is well understood. Specific attention is paid to columns as they are the primary load-bearing members. Column stability under fire conditions is particularly crucial to structural robustness.

Current fire design codes, such as BS5950 Part 8 and Eurocode 3 Part 1.2, provide guidelines for designing columns under elevated temperature. The Broadgate development fire (SCIF, 1991) and the experimental Cardington fire tests (Wang, 1998b) have shown that traditional fire resistance tests for columns designed as an isolated member subjected to ISO834 standard fire curve are over-conservative and do not take into account the true building behaviour. Therefore, there is a need to study the effect of structural continuity on the behaviour of steel columns in fire. Thermal expansion during the heating phase of steel columns in any framed structure is likely to be restrained by adjacent unheated structures.

It is important to conduct more experimental tests under axial restrained conditions to understand the actual behaviour of steel columns under fire conditions. The generation of additional axial forces in columns due to thermal restraint was highlighted as a possible cause of column failure within a frame (SCIF, 1991). To investigate this behaviour, relevant experiments were carried out in this study to determine the fire resistance of unprotected steel columns with various axial restraint ratios.

As a means of fire protection for structural steel in buildings, steel-concrete composite columns were developed. Early in the last century, the method of encasing steel stanchions in concrete became widespread. There is a wide variety of columns with various types of cross-section, but the most commonly used and studied are the *encased I-section* and the *concrete-filled steel tube*. Initially, steel I-section elements were encased with concrete for the purpose of fire protection, and no one quantified the increase in strength afforded by the concrete until the 1950's (Faber, 1956). Since then, research and application of composite columns has advanced. Concrete encasement was found to increase the carrying capacity of the bare steel column significantly. Therefore, it substantially reduces the amount of encased steel required to support a given load, while the dimensions of the column are smaller than those of a reinforced concrete column of the same strength.

There is little research on the behaviour of concrete-encased steel section composite columns under elevated temperature. It is essential to conduct more experimental tests to study the behaviour of concrete-encased steel composite columns at elevated temperature. Similar to the study on bare steel columns, composite columns subjected to axial restrained conditions are tested under elevated temperatures, to shed light on the actual behaviour of composite columns.

1.2 Objectives and Scopes

The main objectives of this research are to study the behaviour of steel columns and concrete-encased steel section composite columns at elevated temperature.

Transient-state tests are carried out on the column specimens. Certain predetermined working loads are applied to the specimen and held constant. Specimens are exposed to increasing temperature in an electric furnace until they fail.

Parametric studies on these structural elements are carried out. Effects of different slenderness ratios and axial restraint ratios are included in the steel column tests. And effects of different cross-sectional sizes, steel section ratios and axial restraint ratios are investigated in the composite column tests. Experimental results are compared with those from Finite Element Analysis (FEA) from the program FEMFAN-3D, an NTU self-developed numerical program. These tests also aim to validate the accuracy of FEMFAN-3D predictions.

1.3 Organisation of Report

Chapter one provides the basic background on fire resistance of steel structures and the motivations for this study. Objectives and scopes of work performed are listed out.

Chapter two presents a thorough literature review on the effects of fire on steel and concrete properties. It also reports on research works conducted on steel columns and concrete-steel composite columns separately, and the motivations for conducting (a) bare steel column tests and (b) concrete-encased composite column tests.

Chapters three, four and five report and discuss the results of a series of experimental testing on unprotected steel columns subjected to elevated temperature conditions. The tests were carried out in the Construction Annex, Nanyang Technological University. The experimental results of the steel column tests are compared with FEA predictions.

Chapters six and seven report and discuss the results of the second series of tests on concrete-encased steel section composite columns subjected to elevated temperature. The test results are also compared to FEA predictions.

Finally, chapter eight summarises the author's research work, with recommendations for future research.

CHAPTER TWO

REVIEW OF THEORY AND PREVIOUS WORK

2.1 Fire Resistance

Fire safety objectives are usually met with a combination of active and passive fire protection systems. Active systems control the fire or fire effects by some action taken by a person or an automatic device. The best form of active fire protection strategy is an automatic sprinkler system that will spray water over a local area under the activated sprinkler head.

Passive systems control the fire or fire effects by systems that are built into the structure or fabric of the building, not requiring specific operation at the time of a fire. For pre-flashover fires, passive control includes selection of suitable materials for building contents and interior linings that do not support rapid flame spread in the growth period. In post-flashover fires, passive control is provided by structures and assemblies that have sufficient fire resistance to prevent both the spread of fire and structural collapse. The most important component of passive fire protection is fire resistance. To prevent structural collapse, structural elements must be provided with sufficient fire resistance to maintain stability for the design fire scenarios. Prevention of collapse is essential for load-bearing structural members.

2.2 Behaviour of an Enclosure Fire

Fire development in an enclosure undergoes a number of stages. Briefly, in the early stage, combustion is restricted to local area near the ignition source and the combustion gas temperature is low, rarely threatening the safety of a structure. Structural fire engineers usually focus their attention on the later fire stage when the fire involves all combustible materials and the combustion gases attain very high

temperature. The stability of the structure may be threatened, resulting in rapid fire spread and loss of human lives and properties.

The development of an enclosure fire may be divided into three stages; fire growth stage, steady burning stage and decaying stage (Figure 2.1). Fire growth starts from ignition of burning item inside the enclosure. With effective active fire protection systems, the fire may be successfully suppressed. In structural fire engineering, it is assumed that fire spread will occur within a fire compartment. During the fire growth stage, hot gases will be released from burning combustible materials. Due to buoyancy, these hot gases will rise towards the ceiling. Fresh air is entrained and more hot smoke is released. At this stage, the enclosure fire environment is divided into two zones, namely, an upper zone of hot smoke and a lower zone of cold air.

The smoke temperature increases as the volume of smoke is stabilized with more hot combustion gases being continuously supplied into the smoke layer. A large quantity of partially burnt fuel will accumulate in the smoke layer due to a lack of oxygen. When the burning flame grows and penetrates into the smoke layer, the partially burnt fuel aids in the horizontal flame spread. At the instant when the incident radiation on unburned combustible materials in the enclosure becomes so high, they become ignited at almost the same time. This stage is referred to as "flashover". After flashover, fire temperature increases rapidly and enters a steady burning stage. The fire is now ventilation-controlled, that is, the burning rate depends on the amount of fresh air that can be supplied. Burning rate of the fire reaches the maximum during post-flashover. This fire stage is of main concern to structural fire engineers.

After a period of sustained burning, most combustible materials will be consumed and the burning rate of the fire starts to decrease. This is known as the decaying stage. In the end, fire will eventually die out when all combustible materials in the enclosure have been consumed.

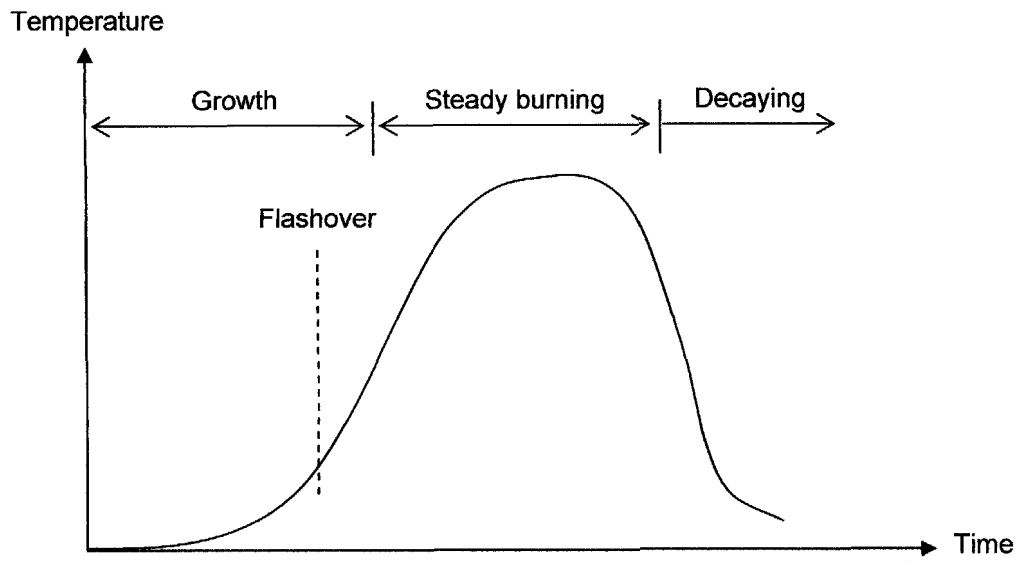

Figure 2.1 Temperature-time relationship of an enclosure fire

2.3 Standard Fires

Nominal temperature-time curves

Current designs for structural fire safety are based on achieving a standard fire rating. For common fires based on fuel such as wood or cellulosic materials, the standard fire resistance design from Eurocode1 Part1.2 (2000a) calculates the fire temperature as

$$\Theta_g = 20 + 345 \log_{10}(8t+1) \qquad (2.1)$$

where

Θ_g is the gas temperature (°C) in the fire compartment at time t;

t is the standard fire exposure time (min);

the ambient temperature is taken as 20°C.

For fire resistant design of offshore structures, the standard hydrocarbon fire curve should be used. This type of fire has a much more rapid rate of initial temperature rise. The temperature-time relationship for a standard hydrocarbon fire is

$$\Theta_g = 1080\,(1 - 0.325e^{-0.167t} - 0.675e^{-2.5t}) + 20 \qquad (2.2)$$

where

Θ_g is the gas temperature (°C) in the fire compartment at time t;

t is the standard fire exposure time (min);

the ambient temperature is taken as 20°C.

The two standard fire curves described above are plotted in Figure 2.2.

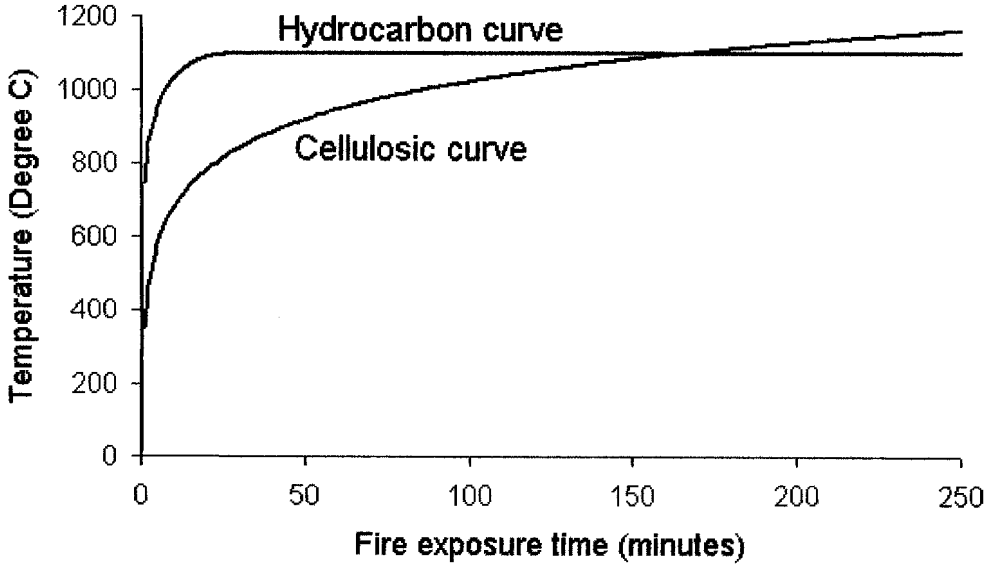

Figure 2.2 Standard cellulosic and hydrocarbon fire temperature-time relationships

Using standard fire exposure has some advantages over using realistic fire exposure. The concept of standard fire exposure has been around in fire safety design for a very long time, almost a century. It has proven to be safe by the fact that building structures rarely fail in fires due to inadequate specification of the standard fire

resistance time. Since temperature-time relationship is standardized, it provides a convenient means for design calculations and for comparison purpose.

Parametric temperature-time curves

Eurocode1 Part1.2 (2000a) also introduces parametric temperature-time curves for fire compartments up to 500m^2 of floor area, without openings in the roof and for a maximum compartment height of 4m. It is assumed that the fire load of the compartment is completely burnt out. A set of parametric equations are given for both the heating and cooling cycles, taking into account the fire load, ventilation characteristics (vertical and horizontal), geometry of the compartment and thermal properties of the floor, walls and ceiling.

The temperature-time curves in the heating phase are given by:

$$\Theta_g = 20 + 1325\,(1 - 0.324e^{-0.2t^*} - 0.204e^{-1.7t^*} - 0.472e^{-19t^*}) \qquad (2.3)$$

where

Θ_g is the gas temperature (°C) in the fire compartment at time t;

t is the standard fire exposure time (hr);

the ambient temperature is taken as 20°C;

t^* accounts for compartment characteristics and openings (EC1 Part 1.2, 2000a).

The temperature-time curves in the cooling phase are given by:

$$\Theta_g = \Theta_{max} - 625\,(t^* - t^*_{max} \cdot x) \quad \text{for} \quad t^*_{max} \le 0.5 \qquad (2.4)$$

$$\Theta_g = \Theta_{max} - 250\,(3 - t^*_{max})\,(t^* - t^*_{max} \cdot x) \quad \text{for } 0.5 < t^*_{max} < 2 \qquad (2.5)$$

$$\Theta_g = \Theta_{max} - 250\,(t^* - t^*_{max} \cdot x) \quad \text{for} \quad t^*_{max} \ge 2 \qquad (2.6)$$

where

t^*_{max} accounts for fire load, compartment characteristics and openings and x is a variable (EC1 Part 1.2, 2000a).

2.4 Properties of Steel in Fire

Steel progressively weakens with increasing temperature and eventually failure occurs in a member as a result of its inability to sustain the applied load, such as buckling in a column or excessive deflection in a flexural member. The effects of a fire on the behaviour of a steel structure are caused by changes in the mechanical properties of steel, temperature-induced strains, and thermal restraints. To understand the complex behaviour of a steel structure under fire conditions, it is necessary to gain basic information of steel material properties at elevated temperature.

2.4.1 Temperature Induced Strains

Temperature-induced strains of steel include thermal expansion and creep strain. Thermal expansion strain (ε_{th}) of steel is given by (EC3 Part 1.2, 2000b):

$$\varepsilon_{th} = -2.416 \times 10^{-4} + 1.2 \times 10^{-5} T + 0.4 \times 10^{-8} T^2 \quad \text{for } T \leq 750°C; \tag{2.7}$$

$$\varepsilon_{th} = 0.011 \quad \text{for } 750 < T \leq 860°C; \tag{2.8}$$

$$\varepsilon_{th} = -0.0062 + 2 \times 10^{-5} T \quad \text{for } T > 860°C. \tag{2.9}$$

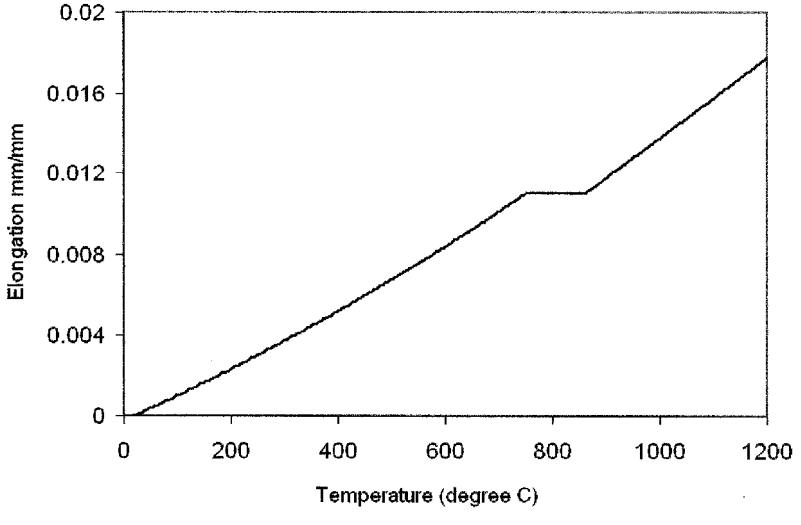

Figure 2.3 Thermal elongation of steel as a function of temperature

Figure 2.3 illustrates a graphical representation of this relationship. The step change for temperature between 750 to 860°C is due to a phase change in steel material, from Ferrite to Austenite (Jacot, Rappaz and Reed 1997). The coefficient of thermal expansion of steel may be assumed to be a constant for simple calculations, and the thermal expansion strain is given by

$$\varepsilon_{th} = 14 \times 10^{-5} \Delta T \qquad (2.10)$$

High temperature creep strain of steel contributes to an increase in steel strain when steel is simultaneously subjected to high temperature and high stress over time. Past creep tests show that steel creep strain experiences three phases, namely, primary, secondary and tertiary creep (Figure 2.4).

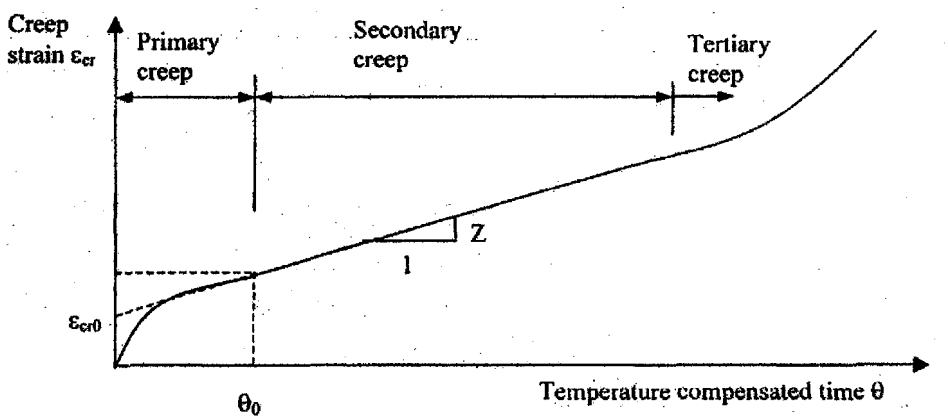

Figure 2.4 Creep strain model for steel at high temperature

As exposure to fire attack is within a short duration, tertiary creep is not considered. Plen (1975) presented a simplified creep strain model, which describes the primary creep strain as a parabola and the secondary creep strain as a straight line. The expressions are shown below:

$$\varepsilon_{cr} = 2\varepsilon_{cr0} \sqrt{(Z \times \theta / \varepsilon_{cr0})} \qquad \text{for } \theta \leq \theta_0 \qquad (2.11)$$

$$\varepsilon_{cr} = \varepsilon_{cr0} + Z \times \theta \qquad \text{for } \theta > \theta_0 \qquad (2.12)$$

where

θ is the temperature compensated time;

Z is the slope of the secondary creep-strain relationship;

ε_{cr0} is the intercept at the creep strain axis by the secondary creep strain slope line.

The temperature compensated time is evaluated as

$$\theta = \int_0^t e^{\frac{-\Delta H}{RT}} dt \tag{2.13}$$

where

t is time in second;

T is the temperature in K;

$\Delta H/R$ is a constant.

The temperature-compensated time, θ_0 that divides the primary creep and the secondary creep can be obtained as:

$$\theta_0 = \frac{\varepsilon_{cr0}}{Z} \tag{2.14}$$

It is very tedious to calculate the steel creep strain at high temperature. Practically, the time period for a steel structure exposed to high temperature is short. Therefore creep strain may be neglected. To compensate for this simplification, the effect of creep strain is implicitly included in the stress-strain relationships of steel at high temperatures. This can be achieved by obtaining the stress-strain relationships under two types of testing procedure, known as isothermal (steady state) and anisothermal (transient state) creep tests, as discussed in the next section.

2.4.2 Stress-strain Relationships of Steel at Elevated Temperature

Stress-strain relationships of steel at elevated temperature can be obtained from isothermal and anisothermal creep tests. Several researchers, such as Witteveen, Twilt & Bijlarrd (1977), Skinner (1972), Jorgenson & Sorenson (1980), have reported their findings.

2.4.2.1 Isothermal Creep Tests

An isothermal creep test is carried out under constant temperature and constant load. Normally tests are conducted over the temperature range of 350 to 650°C, as creep has insignificant influence on the stress-strain curve below 350°C (Skinner, 1972). Strain is measured and plotted against load at a constant temperature and constant load. Further increase in strain is recorded continuously over time. A wide range of loads is used during the tests to give a wide range of strain covering from low to high rates of deformation.

Witteveen, Twilt & Bijlarrd (1977) carried out isothermal tests on steel using both high and low rates of deformation, 200mm/min and 0.5mm/min, respectively. It was found that at temperature below 400°C, creep has no significant effect on stress-strain curves. The results show that at higher temperature the strain rate due to creep effect increases, as illustrated in Figure 2.5.

2.4.2.2 Anisothermal Creep Tests

In an anisothermal creep test, the specimen is subjected to constant load under increasing temperature. Witteveen, Twilt & Bijlarrd (1977) carried out warm-creep tests with heating rates between 5°C /min and 50°C /min. It was reported that the effect of heating rate is insignificant. The measured stress-strain relationships were obtained from transforming the temperature-strain curves at constant loading to stress-strain curves at constant temperature. The material properties of steel determined from this kind of test is more conservative as the influence of creep is

implicitly included in these stress-strain curves. Figure 2.6 shows the stress-strain curves obtained from a warm-creep test.

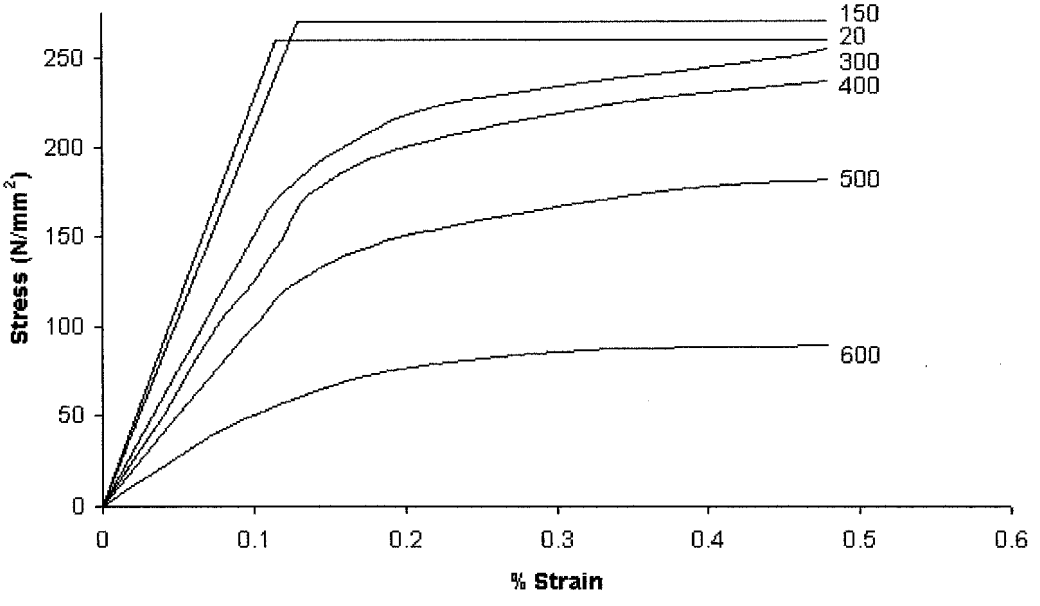

Figure 2.5 Isothermal creep test results

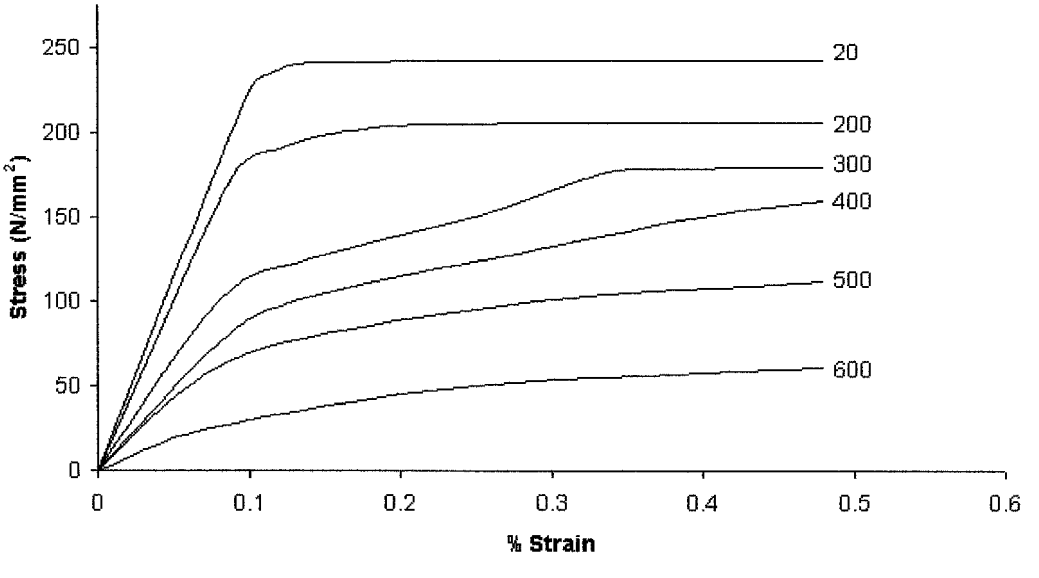

Figure 2.6 Anisothermal creep test results

The stress-strain relationship for steel at elevated temperatures presented in Eurocode 3 Part 1.2 (CEN 2000b) implicitly considers creep effect and has been well accepted. It describes the stress-strain curve as a straight line in the initial portion, followed by an elliptical relationship and then a plateau (Figure 2.7).

At ambient temperature, Eurocode 3 assumes that the stress-strain relationship is bilinear and the proportional limit f_p at the end point of the linear-elastic portion of the stress-strain curve is equal to the yield strength f_y. It also assumes no strain hardening. The first yield moment M_y can be obtained from:

$$M_y = f_y Z \tag{2.15}$$

where Z is the elastic section modulus.

At elevated temperature, the stress-strain relationship becomes linear elliptical. The initial elastic portion is linear up to the proportional limit and then becomes non-linear in the trend of an ellipse up to the yield strength, f_y^T. Thereafter it becomes a plateau. The plastic moment M_p can be obtained from:

$$M_p = f_y^T S \tag{2.16}$$

where S is the plastic section modulus.

Table 2.1 shows the mathematical model of the stress-strain relationship of steel at elevated temperature. Figure 2.7 provides a graphical illustration of this model. To use this model at elevated temperature, the reduced strength and stiffness of steel are required as input data. These values, known as retention factors, are shown in Table 2.2, expressed as a ratio of the value at elevated temperature to that at ambient temperature. Figure 2.8 gives a graphical representation of these retention factors.

Table 2.1 EC3 Stress-strain relationship for steel at elevated temperature (CEC, 1995a)

Stain Range	Stress σ	Tangent modulus
$\varepsilon \le \varepsilon_{pp}^{T}$	$\varepsilon \cdot E_0^T$	E_0^T
$\varepsilon_{pp}^{T} < \varepsilon < \varepsilon_{y}^{T}$	$f_{pp}^{T} - c + (b/a)\sqrt{a^2 - (\varepsilon_y^T - \varepsilon)^2}$	$\frac{b \cdot (\varepsilon_y^T - \varepsilon)}{a \cdot \sqrt{a^2 - (\varepsilon_y^T - \varepsilon)^2}}$
$\varepsilon_{y}^{T} < \varepsilon < \varepsilon_{t}^{T}$	f_y^T	0
$\varepsilon_{t}^{T} < \varepsilon < \varepsilon_{u}^{T}$	$f_y^T \left[1 - (\varepsilon - \varepsilon_t^T)/(\varepsilon_u^T - \varepsilon_t^T)\right]$	-
$\varepsilon = \varepsilon_u^T$	0	-

In which:

$$a^2 = (\varepsilon_y^T - \varepsilon_{pp}^T) \cdot (\varepsilon_y^T - \varepsilon_{pp}^T + c / E^T)$$

$$b^2 = c \cdot E_0^T \cdot (\varepsilon_y^T - \varepsilon_{pp}^T) \cdot c + c^2$$

$$c^2 = \frac{(f_y^T - f_{pp}^T)}{(\varepsilon_y^T - \varepsilon_{pp}^T) E_0^T - 2(f_y^T - f_{pp}^T)}$$

where

f_y^T is the effective yield strength at elevated temperature (MPa);

f_{pp}^T is the proportional limit at elevated temperature (MPa);

E_0^T is the slope of the linear elastic range at elevated temperature (MPa);

E_0^{20} is the slope of the linear elastic range at ambient temperature (MPa);

$\varepsilon_{pp}^T = \frac{f_{pp}^T}{E^T}$ is the strain at the proportional limit at elevated temperature;

$\varepsilon_y^T = 2\%$ is the yield strain at elevated temperature;

$\varepsilon_t^T = 15\%$ is the limiting strain for yield strength at elevated temperature;

$\varepsilon_u^T = 20\%$ is the ultimate strain at elevated temperature;

T is the steel temperature (°C).

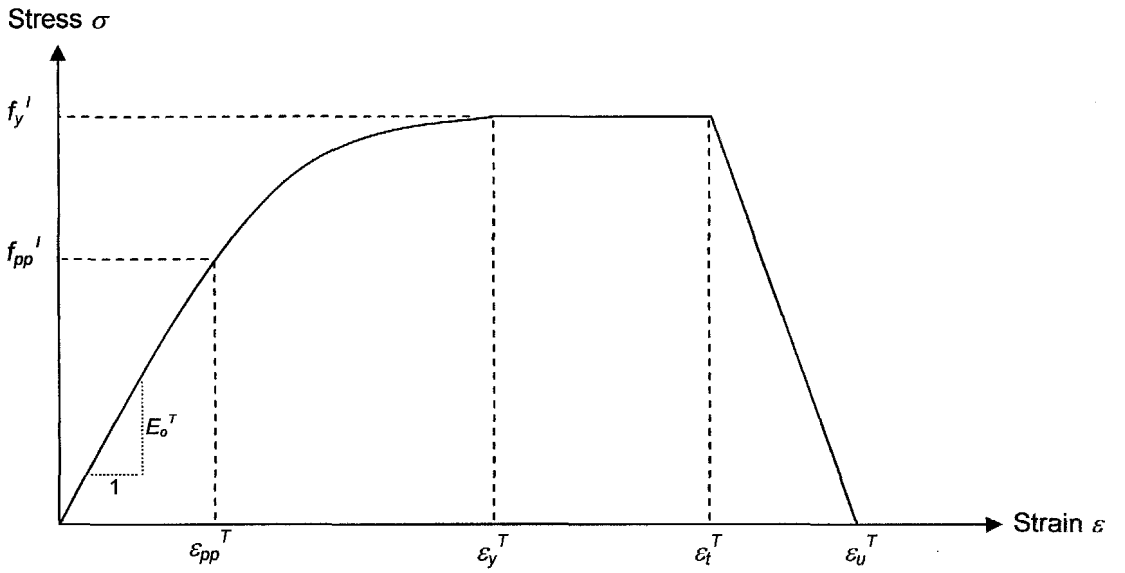

Figure 2.7 Stress-strain relationship of steel at elevated temperature

Table 2.2 Retention factors of steel at elevated temperatures

Steel temperature T (°C)	Effective yield strength (relative to f_y at 20°C) $k_{y,T} = f_y^T / f_y$	Proportional limit (relative to f_y at 20°C) $k_{p,T} = f_{pp}^T / f_y$	Slope of the linear elastic range (relative to E_o^{20} at 20°C) $k_{E,T} = E_T / E_o^{20}$
20	1.000	1.000	1.000
100	1.000	1.000	1.000
200	1.000	0.807	0.900
300	1.000	0.613	0.800
400	1.000	0.420	0.700
500	0.780	0.360	0.600
600	0.470	0.180	0.310
700	0.230	0.075	0.130
800	0.110	0.050	0.090
900	0.060	0.0375	0.0675
1000	0.040	0.0250	0.0450
1100	0.020	0.0125	0.0225
1200	0.000	0.0000	0.0000

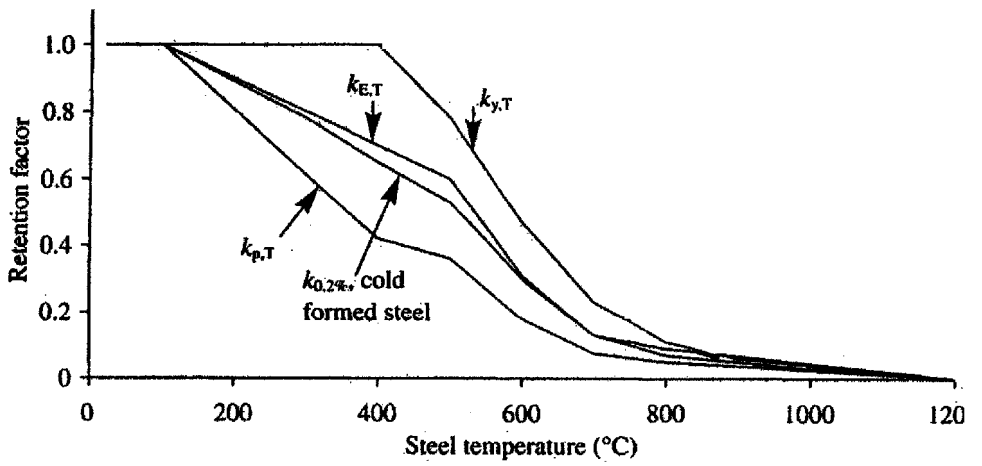

Figure 2.8 Retention factors of steel at elevated temperatures

Retention factors for the reduced yield strength, elastic modulus, and proportional limit are to be used to determine the steel mechanical properties at elevated temperature. These are applied to all conventional hot-rolled structural steel members. It should be noted that for cold-formed thin-walled steel, the material may be stressed beyond its yield strength into the strain-hardening region. Therefore, cold-formed steel may have a higher effective yield strength than hot-rolled steel. However, this increase in steel yield strength by cold-forming is gradually reduced at elevated temperature. Therefore, the retention factors of cold-formed steel are lower than those of hot-rolled steel. In the definition of yield strength, Eurocodes take the effective yield strength for hot-rolled steels at 2% strain. However, for cold-formed thin-walled steel, where local buckling has great influence on design, the effective yield strength is defined as that at 0.2% plastic strain (or 0.2% proof stress).

2.5 Properties of Concrete in Fire

When concrete is exposed to high temperatures, sudden changes in its properties occur. As its temperature increases the concrete will expand, and the absorbed energy will progressively evaporate the moisture within the concrete matrix, reducing the rate of temperature increase. Loss of moisture will also cause shrinkage of the concrete, offsetting its rate of thermal expansion. Concrete has a low thermal conductivity, and thus a rise in the temperature of its surface will be transferred slowly throughout the section. To calculate temperatures within structural assemblies it is necessary to know the thermal properties of the materials.

2.5.1 Thermal Properties of Concrete

Concrete density depends on the aggregate and the mix design. Typical concrete has a density of about 2300kg/m^3. There are many lightweight concretes that use porous aggregates or air entrainment to reduce the density to half or two-thirds of this value. When heated to 100°C the density of most concretes will be reduced by up to 100kg/m^3 due to the evaporation of free water, which has a minor effect on thermal response. Other than moisture changes, the density of concrete does not change much at elevated temperature, except for limestone (calcareous) aggregate concrete that decomposes above 800°C with a corresponding decrease in density.

Thermal conductivity λ_c of concrete is temperature-dependent, and varies in a broad range, depending on the type of aggregate. Figure 2.9 shows the values of thermal conductivity from Eurocode 2 (1993). An approximate value of 1.6W/m°C is commonly used for siliceous concrete at 20°C, and this value at elevated temperature takes on the following equation:

$$\lambda_c = 2.0 - 0.24\,(T_c / 120) + 0.012\,(T_c /120)^2 \qquad \text{for } 20^\circ\text{C} \le T_c < 800^\circ\text{C} \qquad (2.17)$$

where

λ_c is the thermal conductivity of concrete (W/mK) at temperature T_c;

T_c is the temperature of concrete.

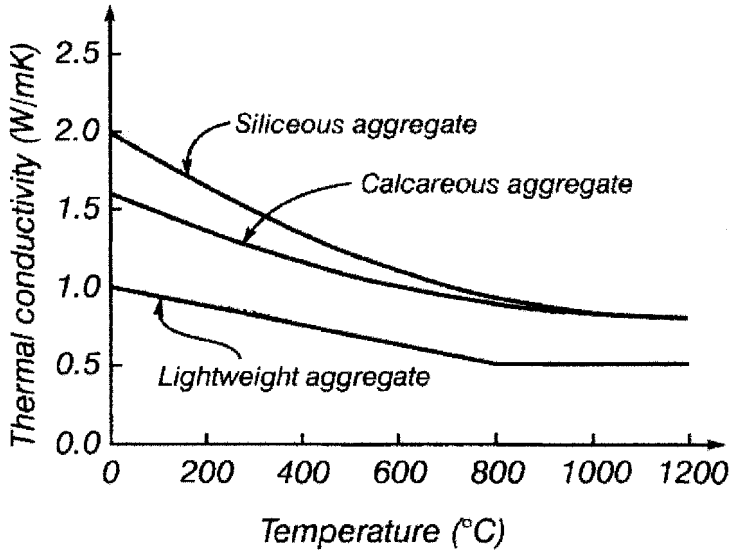

Figure 2.9 Thermal conductivity of concrete at elevated temperature

Specific heat of concrete also varies in a broad range, depending on the moisture content, with design values from Eurocode 2 (1993) shown in Figure 2.10. The peak value between 100 and 200°C allows for water being driven off during the heating process. An approximate value of 1000J/kgK is commonly used for siliceous and calcareous aggregate concrete.

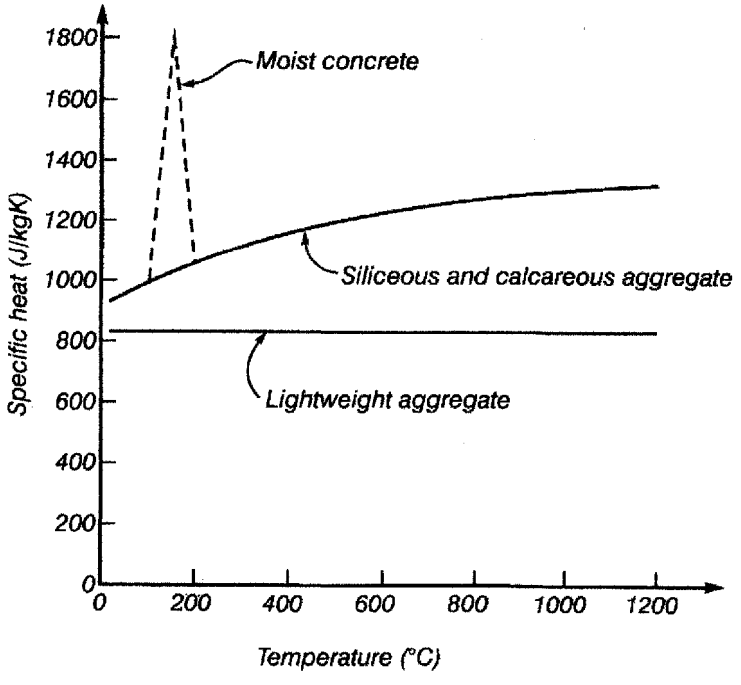

Figure 2.10 Specific heat of concrete

Equation of specific heat of normal-weight concrete is

$$c_c = 900 + 80\,(T_c / 120) - 4\,(T_c/120)^2 \qquad (2.18)$$

where

c_c is specific heat of concrete (J/kgK) at temperature T_c;

T_c is the temperature of concrete.

Thermal elongation of normal-weight concrete is given by (EC2, 1993):

$$\Delta l/l = -1.8 \times 10^{-4} + 9 \times 10^{-6}\, T_c + 2.3 \times 10^{-11}\, T_c^{\,3} \qquad \text{for } 20^{\circ}\text{C} \le T_c < 700^{\circ}\text{C} \qquad (2.19)$$

$$\Delta l/l = 14 \times 10^{-3} \qquad \text{for } 20^{\circ}\text{C} \le T_c < 700^{\circ}\text{C} \qquad (2.20)$$

where

$\Delta l/l$ is the thermal elongation of concrete at temperature T_c;

T_c is the temperature of concrete;

l is the concrete length at 20°C.

2.5.2 Mechanical Properties of Concrete at Elevated Temperature

Deformation of concrete at elevated temperature is slightly more complicated than that of steel, because of an additional component of strain called transient strain. Deformation of concrete is usually described by assuming that the total strain ε consists of four components (Buchanan, 2001):

$$\varepsilon = \varepsilon_{th}(T) + \varepsilon_{\sigma}(\sigma, T) + \varepsilon_{cr}(\sigma, T, t) + \varepsilon_{tr}(\sigma, T) \qquad (2.21)$$

where

$\varepsilon_{th}(T)$ is the thermal strain being a function only of temperature T;

$\varepsilon_\sigma (\sigma, T)$ is the stress related strain, being a function of both the applied stress σ and the temperature;

$\varepsilon_{cr} (\sigma, T, t)$ is the creep strain, being a function of applied stress, temperature and time t;

$\varepsilon_{tr} (\sigma, T)$ is the transient strain, being a function of both the applied stress and the temperature.

2.5.2.1 Thermal Strain

Thermal elongation $\Delta l/l$ of concrete is shown in the section 2.5.1.

2.5.2.2 Creep Strain and Transient Strain

Creep strain and transient strain are closely related. Khoury *et al.* (1985) have measured creep strains during testing under constant temperature and stress. The results are shown in Figure 2.11. Transient strain occurs during the first time heating of concrete under load up to 600°C, but not on subsequent heating.

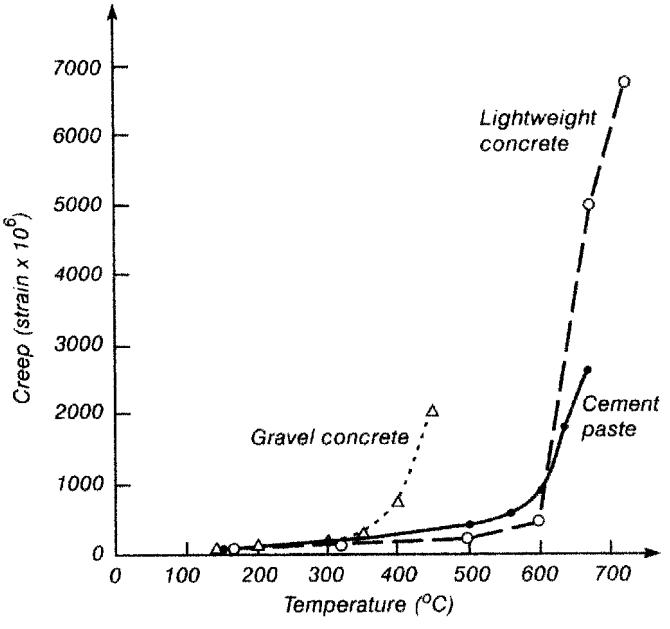

Figure 2.11 Creep in concrete one day after loading at 10% of initial strength

2.5.2.3 Stress related Strain

Stress-related strain includes the elastic and plastic components of strain resulting from applied stresses. Typical stress-strain relationships for normal concrete at elevated temperatures (EC2, 1993) are shown in Figure 2.12. It can be seen that the ultimate compressive strength drops, and the strain at peak stress increases with increasing temperature.

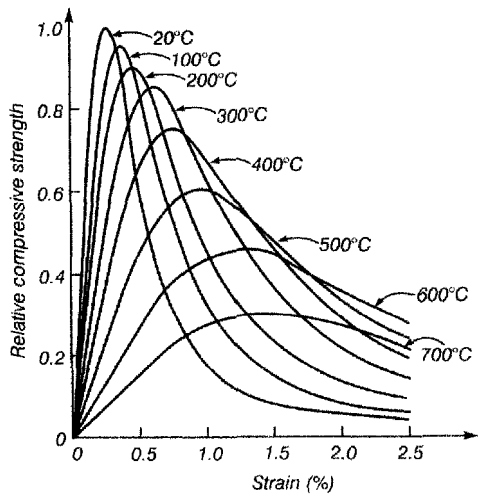

Figure 2.12 Stress-strain relationships of concrete at elevated temperatures

The reduction in ultimate compressive strength with temperature for typical structural concrete is shown in Figure 2.13 (Schneider, 1988).

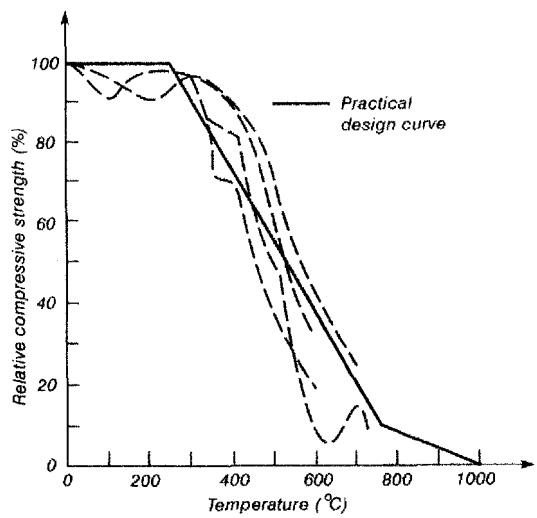

Figure 2.13 Reduction in compressive strength with temperature

Table 2.3 shows the mathematical model of the stress-strain relationship of concrete at elevated temperature (EC2, 1993). Two parameters are defined here, namely the compressive strength $f_{c,\theta}$ and the strain $\varepsilon_{cu,\theta}$ corresponding to $f_{c,\theta}$. Table 2.3 gives the reduction factor $k_{c,\theta}$ to be applied to $f_{c,20°C}$ in order to determine $f_{c,\theta}$ and the strain $\varepsilon_{cu,\theta}$ at elevated concrete temperatures θ_c.

Table 2.3 Reduction factors and strain of normal weight concrete (NC) and light weight concrete (LC) at elevated temperatures

Concrete Temperature θ_c (°C)	$k_{c,\theta}=f_{c,\theta}/f_{c,20°C}$		$\varepsilon_{cu,\theta}$ x 10^3
	NC	LC	NC
20	1.00	1.00	2.5
100	0.95	1.00	3.5
200	0.90	1.00	4.5
300	0.85	1.00	6.0
400	0.75	0.88	7.5
500	0.60	0.76	9.5
600	0.45	0.64	12.5
700	0.30	0.52	14.0
800	0.15	0.40	14.5
900	0.08	0.28	15.0
1000	0.04	0.16	15.0
1100	0.01	0.04	15.0
1200	0.00	0.00	15.0

2.6 History and Development

2.6.1 Steel Columns in Fire

The first experimental study performed on columns subjected to fire was carried out by Bauschinger in 1885. He reported the results of a series of tests where horizontally placed columns were loaded, heated and sprinkled with water. At that time, temperatures were measured using various metals with different melting points. In the tests, cast iron was found to be a more fire resistant material compared to wrought iron and mild steel. A large number of column tests have been conducted in Europe, Japan and America during the last hundred years.

Knublauch *et al.* (1974) reported on the results of 23 column tests. The columns were of box-shaped insulation made of vermiculite plates. As the temperature increased, the axial loading was kept constant, and thermal expansion was allowed. Different types of steel cross sections with similar lengths were tested. The main conclusion of the tests was that 95% of all the columns had a critical temperature of 500°C. Critical temperature of a load bearing steel element or structural assembly was defined as the temperature corresponding to the limit state of failure.

Stanke, J. (1977) tested 14 steel columns with varying degrees of axial restraint on thermal expansion at BAM, Berlin. The main observation was that, during the initial heating the load increased rapidly due to the restrained axial elongation. Then the columns buckled and lost their load-bearing capacity.

Kertsma *et al.* (1979) re-examined some of the test results obtained by Knublauch. Instead of assuming a hinge at the column base, he introduced an elastic linear restraint in the model. His calculations showed a considerable increase in the critical temperature with the inclusion of non-uniform temperature distribution and a small elastic restraint, when compared to Knublauch's test results.

Vandamme & Janss (1981) and Janss & Minne (1982) reported a total of 29 column tests carried out at the University of Ghent. Both ends of the columns were clamped inside the furnace. Twenty-seven specimens were tested, covered with different types of insulation. Two uninsulated columns were also tested. The load was kept constant and no restraint was imposed on the longitudinal expansion. A model based on the European buckling curve *c*, with a correction factor *f* included in the calculations, accurately predicted the critical temperatures.

Olesen, F.B. (1980) reported the test results of 24 hinged end specimens with different lengths tested in a more versatile furnace, at the University of Aalborg. The tests were performed in a horizontal position with the weak axis vertical so that buckling occurred in the horizontal plane. Eighteen columns were loaded at a constant rate at specific temperature levels, until failure was attained. The remaining 6 tests were carried out under a constant axial load during heating. The column bearings were located outside the furnace without any axial restraint. The test results showed acceptable agreement with the Ghent design method.

Creep effect on column strength was studied at the University of Rennes (Aribert & Randriantsara 1980 & 1983, and Randriantsara 1984). Thirty-three pinned and uninsulated columns with the same steel cross section and length were placed in a vertical position in an electric furnace. Tests were carried out either under loading at specific temperature with and without moment at the top end, or under heating at constant axial load with and without axial restraint. Column deflections were measured at mid-height and at quarter points. Results showed that creep started to influence the column strength at 450°C, and at a temperature of 600°C the reduction of column strength became significant.

At the Technical University of Brunswick, steel columns exposed to ISO standard fire were tested. Hoffend (1977, 1980 and 1983) reported on the 75 column test results. The tests comprised the following parameters: column slenderness, load level, axis of buckling, load eccentricity, hinged or clamped column ends, thermal gradients along column due to partial insulation, various types of steel sections,

heating rate and full axial restraint. The tests concluded that: (i) slender columns had higher critical temperature than stockier ones; (ii) load level became more important for columns with smaller slenderness ratios due to the tendency of inelastic buckling; (iii) critical temperature for weak axis buckling was lower than that for strong axis buckling, due to the presence of residual stresses; (iv) load eccentricity had a more detrimental effect on critical temperature for columns with high slenderness. The author disagrees with Hoffend's first conclusion that slender columns had higher critical temperature than the more stocky ones. This behaviour will be studied experimentally by testing columns with different slenderness ratios at elevated temperature. The author, however, agreed fully with points (iii) and (iv) brought up by Hoffend.

Lie *et al.* (1980) described a new Canadian test furnace for measuring column mid-height deflections. A new type of test rig based on conductive electric heating has also been developed at the Technical University of Brunswick (Ruge & Linnemann 1983).

Randall, M. J. (1998) carried out a series of experiments on 44 heated columns to investigate the behaviour of axially restrained steel columns in fire. The columns were 1.8m long. Three different slenderness ratios were used by the choice of three different section sizes, namely UC152 x 152 x 23, UB178 x 102 x 19 and UB127 x 76 x 23. Three axial restraint ratios were chosen, namely, 0.1, 0.2 and 0.3. Four different load levels were used in the tests, viz. 0, 0.2, 0.4 and 0.6. General trends of column failure temperature variation with slenderness, axial restraint ratio and applied load were reported. He concluded that column failure at elevated temperatures could be accurately predicted if inelastic buckling theory and an accurate material model at elevated temperature were used. He had commented that the axial restraint ratios that he adopted were within the high end of practical range. He suggested that continued investigation to be carried out with lower restraint levels that are more representative of rectangular unbraced frames.

Correia *et al.* (2000) carried out experiments on 168 hinged bars to study the critical temperature of compressed steel elements with restrained thermal elongation. Four slenderness ratios, 2 eccentricities of the compression load and 6 levels of axial restraint were investigated. Results of their tests and computer simulation showed that neglecting the effect of thermal axial restraint may result in overestimation of the fire resistance of columns.

Faris *et al.* (2001) conducted a parametric experimental investigation on the performance of rotationally restrained steel column in fire, at the University of Ulster. One axial restraint of 0.29 and two values of rotational restraint 0.18 and 0.93 were used in the fire tests. Axial load levels at 0, 0.2, 0.4, 0.6 and 0.8 were used. Their study concluded that increasing the load level caused a significant reduction in the generated restraint forces, and therefore resulted in a drop in the failure temperature. An additional rotational restraint had a relatively minor effect on the values of generated restraint forces but failure temperatures were greatly increased.

Correia *et al.* (2000) came up with a proposal, based on the results of tests and calculations, to correct the values of the critical temperature of steel columns free to elongate, taking into account the restraint effect of the structure. They also showed that the reduction in critical temperature became less pronounced as the load eccentricity increased.

In his research, the author conducted further tests on restrained steel columns, with the intention to increase the understanding of restrained column behaviour under elevated temperature. Restraint ratios within the practical range were chosen. The elevated temperature test results primarily served to validate the accuracy of NTU self-developed numerical program FEMFAN. Further details are discussed in Chapters 3, 4 and 5.

2.6.2 Composite Columns in Fire

Schleich *et al.* (1986) presented a computer program CEFICOSS for the analysis of steel and composite structures under fire conditions. The numerical results were compared with full-scale tests on steel and composite structural elements and frames. The comparison yielded good agreement. Although the program CEFICOSS was able to simulate in a correct way the structural behaviour in a fire resistance test and that it provided good estimation of the fire resistance time, it was not able to substitute real fire tests, because the real fire test was the only way to detect local problems such as spalling of concrete, lack of adherence to reinforcing bars, bad behaviour of welded joints or local buckling of exposed steel reinforcement due to spalling of concrete.

Kordina, K. (1988) reported on results of fire resistance tests of composite columns with concrete filled hollow steel sections, of composite columns with steel sections completely embedded in concrete and of columns concreted between the flanges. Kordina showed ways of incorporating those results in a fire design guide, in terms of dimensioning of composite columns with respect to their fire resistance.

Roik, K. and Bergmann, R. (1990) carried out 12 tests on composite columns with unsymmetrical cross-sections to verify their proposed design method, for the case of axial compression and combined compression and bending. The proposed design method was based on the simplified method for composite columns with symmetrical cross sections given in Eurocode 4.

Shakir-Khalil, H. (1991) conducted tests on 12 hollow circular columns of composite shell walls to investigate their behaviour when subjected to eccentric end compressive forces. The cross-section of the columns consisted of two concentric thin steel shells, and the ring-shaped space in-between was filled with either grout or microconcrete. The test results confirmed the viability of such novel columns as a practical solution to unusual situations.

Kato, B. (1996) investigated the buckling strength of centrally loaded composite columns, based on a collection of 100 test results of concrete-filled circular and square steel tubes and concrete-encased steel H-section members. It was found that the design formula given by ISO standard for steel structures could be applied to the composite columns with appropriate modifications for each type of column.

Wang, Y. C. (1997) reported on the fire resistant design of centrally loaded unprotected concrete-filled steel tubular columns using Eurocode 4 Part 1.2. He compared the predicted column fire resistance using Eurocode 4 Part 1.2 calculation method with the test results on 36 concrete-filled circular hollow section columns and 7 square hollow section columns conducted at the National Fire Laboratory of Canada. For the standard fire resistance design, a simple method to implement the general calculation method in Eurocode 4 Part 1.2 was proposed. The author also suggested introducing a multiplication factor in the equivalent time equation in Eurocode 1 Part 2.2, to cater for different types of construction element.

Wang, Y. C. (1999) carried out 2 series of load tests on slender composite columns; eight tests on concrete filled rectangular hollow steel section and seven tests on concrete encased rolled steel joist columns, both with end eccentricities producing moments other than single curvature bending. Based on the steel column approach in BS 5950, a design method was proposed for composite columns, which was simple and time effective.

Wang, Y. C. (1999b) presented a series of theoretical studies on the effects of structural continuity on the fire resistance of composite columns of concrete filled steel tubes. The results of his studies validated the recommendation in Eurocode 4 Part 1.2 that the boundary conditions for continuous columns may be assumed to be built-in. He also suggested that at the fire limit state, additional axial loads in columns due to restrained thermal expansions were very small and that column bending moments became much lower than those at ambient temperature. For calculating fire resistance, a column may be assumed to be under pure axial load

equal to its ambient temperature value, the result of which may only slightly overestimate the exact column fire resistance.

Han, L. H. (1999) applied finite element method for the calculations of temperature fields of concrete filled steel tubes under fire. A theoretical model used to calculate deformations and strength of beam-column in fire and fire resistance was described and compared with test results. Effects of the changing strength of the materials, dimension of the section, steel ratio, load eccentricity and slenderness ratio on the fire resistance were discussed.

Shanmugam *et al.* (2001) reviewed all research works carried out on composite columns with emphasis on experimental and analytical work. Collected experimental data were compiled with the parameters listed. The review included research work that had been carried out accounting for the effects of local buckling, bonding strength, seismic loading, confinement of concrete and secondary stresses on the behaviour of steel-concrete composite columns.

Han *et al.* (2003) developed a mathematical model to study the influence of important parameters that determine the fire resistance of concrete-filled hollow steel columns, such as sectional dimension, load eccentricity ratio and fire protection thickness. The team also investigated the behaviour of concrete-filled hollow structural steel columns with or without fire protection and subjected to axial or eccentric loads. They concluded that the column section size and thickness of fire protection material had significant influence on fire resistance, but not load eccentricity as long as the column load ratio was maintained.

Axial restraint factor that affects the behaviour of a steel column which forms part of a complete structure is equally applicable to a composite column. However, up till the time of writing this review, there was no reported elevated temperature test on restrained composite columns. The series of composite column tests also served to validate the accuracy of NTU self-developed numerical program FEMFAN, which has incorporated concrete material properties at elevated temperature

according to EC2: 1.2. Thus, this forms the second part of the author's experimental programme, details of which are discussed in Chapters 6 and 7.

CHAPTER THREE

Experimental Testing on Steel Columns - Series 1

3.1 Elevated Temperature Test Programme on Steel Columns

In the experimental study on the behaviour of steel columns at elevated temperature, two parameters were investigated, namely, slenderness ratio and axial restraint ratio. The applied working axial load was chosen to be 50% of the section's ultimate capacity, to represent the maximum possible design value. Steel columns of varying slenderness ratios were tested at elevated temperature subjected to various axial restraint ratios, which are defined as:

$$\alpha_k = \frac{K_s}{K_c} \tag{3.1}$$

where

K_s = restraint axial stiffness;

K_c = column axial stiffness at ambient temperature = EA/L_e

E = elastic modulus of steel

A = cross sectional area of steel section

L_e = effective length of steel column

Restraint ratio governs the rate and magnitude of restraint force generated and ultimately, the collapse temperature of the column when it is subjected to elevated temperature. Simms (1997) investigated the values of axial stiffness of the Cardington Frame, as well as the Broadgate Phase 8 structure which experienced a real fire during its construction. The column stiffness and the axial restraint parameter of several columns in both structures give α_k in the range between 0.02 and 0.90. Three levels of axial restraint, α_k, were chosen in this programme; namely 0.08, 0.11 and 0.14. These values were within the realistic parameter range. It is known that when stiff bracing is introduced into conventional rectangular sway

frames, as often in the case of high rise buildings, restraint ratios can be raised significantly, as high as 0.9 (SCIF, 1991).

Collapse of columns under elevated temperature and about the minor axis was investigated in this project. In reality, columns tend to bend and fail about the minor axis, therefore this research emphasizes on more practical issue. Different slenderness ratios about this axis were required to make the study as comprehensive as possible. The effect of different restraint ratios was investigated for each slenderness ratio. Column slenderness ratio about the minor axis λ takes on 45, 55, 81 and 97. Two of the ratios, 81 and 97, lie in the high slenderness range, while the other two, 45 and 55, in the low slenderness range.

At ambient temperature, axial load capacity tests were carried out for each set of steel columns with a certain slenderness ratio, to obtain their respective buckling loads. Initially, 20 tests were planned. However, for column with λ of 45, difficulties were encountered in producing the required restraint ratio of 0.14 and so this particular test was discarded. Therefore, there are a total of 19 tests with a range of axial restraint and slenderness ratios. The tests are summarised in Table 3.1, with RS01 to RS20 as column labels. Each set of columns with the same slenderness ratio includes one unrestrained ambient loading test, one unrestrained elevated temperature test and three restrained elevated temperature tests at α_k = 0.08, 0.11 and 0.14, respectively.

Table 3.1 Test parameters and specimen markings (Series 1)

Slenderness Ratio, λ	Ambient Test	Elevated Temperature Test			
		Axial restraint ratio, α_K			
		0.00	0.08	0.11	0.14
45	RS01	RS02	RS03	RS04	-
55	RS06	RS07	RS08	RS09	RS10
81	RS11	RS12	RS13	RS14	RS15
97	RS16	RS17	RS18	RS19	RS20

3.2 Test Apparatus

3.2.1 Test Rig

A horizontal self-reaction test rig of very high stiffness was used for the entire test set-up, as shown in Figure 3.1. The test rig had a testing capacity of 5000 kN. It has the overall dimensions of 9.2m x 3m x 3m (height), with a movable bulkhead that could be adjusted to allow testing of columns of up to 4.2m. Loading was applied horizontally. Knuckle bearings were used at both ends of a specimen to provide pinned end conditions. Columns were orientated such that they bent about the weak axis, instead of stronger axis. A 5-tonne overhead gantry crane provided means for all lifting work such as installation of specimen into the test rig.

3.2.2 Furnace

Steel specimens were uniformly heated by electrical furnaces. Six units of L-shaped electrical furnaces (Figure 3.2) were fabricated and configured to provide various heating scenarios, such as three-face or four-face heating for different specimen lengths. Each furnace had four units of heating modules made of metallic spiral heating elements embedded in foamed ceramic fibre insulation. The four heating modules formed two heating surfaces with respective area of 575×1200mm and 800×1200mm. Two individual programmable temperature controllers separately monitored the two areas. The furnace rating was 22kW/400V/2 phase, with a maximum operating temperature of 1050°C and a maximum heating rate of 12°C/min. For the column tests in this study, two L-shaped electric furnaces were used to provide a uniform heating condition all round the cross-section (Figure 3.1). A constant heating rate of 7°C/min was chosen for all elevated temperature tests to ensure sufficient time for more-or-less uniform temperature distribution across the specimen cross-section and along the member length. Obviously, this furnace cannot simulate the standard fire curve like ISO 834, in which the temperature rises very rapidly in the initial period, with a rate of about 30 to 60°C per minute. Furnace

temperatures were monitored by thermocouples located at the centre of each heating surface.

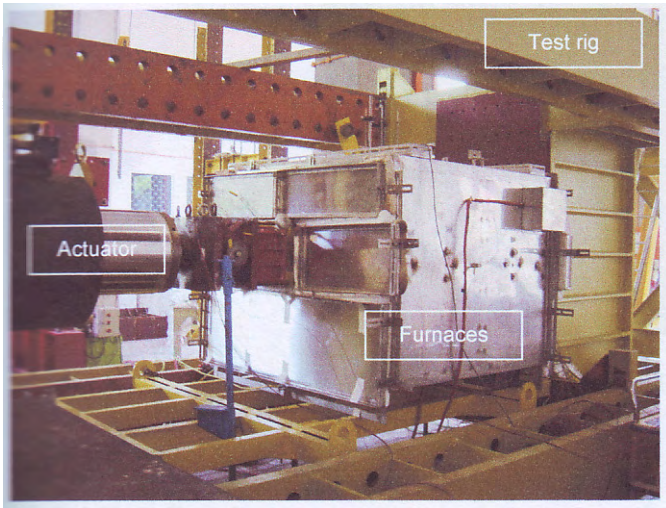

Figure 3.1 Test apparatus

Figure 3.2 L-shaped electric furnace

3.2.3 Axial Restraint System

Thermal expansion of the steel column was restrained by a transverse steel beam, simply supported onto a set of reaction A-frames, as shown in Figure 3.3. Using beams with different cross-sections allowed different axial restraint stiffnesses K_s to be applied. The actual value of K_s was calibrated from testing, and is shown in the later section of this report. Mid-span deflection of the restraint beam and applied force on both beam ends were measured. The total stiffness value was calculated from the ratio of the total restrained force to the total measured deflection at the beam mid span.

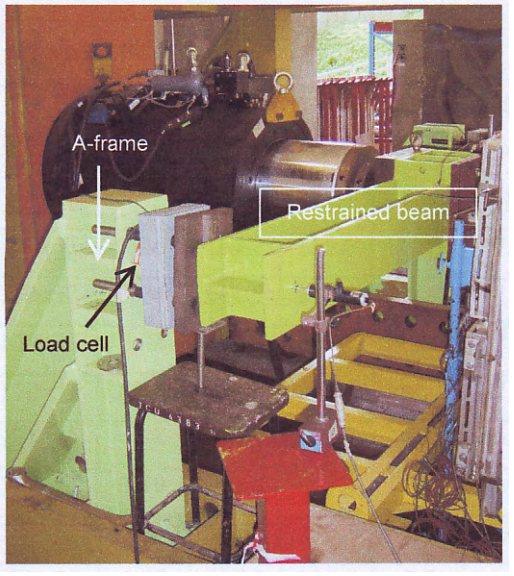

Figure 3.3 Axial restraint system

3.2.4 Test Specimens

The series of pinned-pinned steel columns were subjected to different axial loads. The 1.5m long column had an effective length of 1.74m when attached to the knuckle bearings at both ends. To achieve the required four different slenderness ratios, four different hot-rolled sections were chosen, namely, UC152×152×37, UB203×133×25, UB152×89×16 and UB127×76×13, corresponding to minor axis slenderness ratios λ of 45, 55, 81 and 97 respectively. A summary of the end plate eccentricities e, section dimensions (width b, height H, flange thickness T_f and web thickness t_w) and initial crookedness along the column length measured prior to testing for all columns (i_1, i_2 and i_3 denote imperfections at $L/4$, $L/2$ and $3L/4$, respectively) are shown in Table 3.2. A small amount of eccentricity (e =5mm) was applied to ensure that the specimen bend towards a desired direction during testing. However, due to poor fabrication, this could not be achieved in practice. Again, Column RS05 (λ = 45, α_k=0.14) was not tested because it was not feasible to achieve the required restraint level on the existing system. Moreover, Column RS13 was tested twice to evaluate the repeatability of the tests.

Table 3.2 Specimen data (Series 1)

λ (1)	No. (2)	Section (3)	e (mm) (4)	H (mm) (5)	B (mm) (6)	T_f (mm) (7)	t_w (mm) (8)	i_1 (mm) (9)	i_2 (mm) (10)	i_3 (mm) (11)
45	RS01	UC152x152x37	3.26	162.0	155.6	11.0	7.6	0.4	-0.1	-0.2
	RS02	UC152x152x37	1.74	161.5	155.8	10.9	7.6	-0.7	-0.8	-1.0
	RS03	UC152x152x37	2.94	161.5	155.7	11.0	7.6	-0.8	-0.4	0.1
	RS04	UC152x152x37	6.49	162.0	155.7	11.0	7.6	-0.1	-0.5	-0.4
55	RS06	UB203x133x25	4.88	202.4	135.4	7.6	5.4	-1.0	-0.3	-0.5
	RS07	UB203x133x25	3.19	203.3	135.4	7.7	5.41	0.8	1.0	0.9
	RS08	UB203x133x25	3.43	203.1	135.5	7.6	5.41	-0.1	-0.3	-0.7
	RS09	UB203x133x25	5.05	203.2	135.5	7.7	5.41	-0.7	-0.5	-1.1
	RS10	UB203x133x25	3.67	203.3	135.4	7.7	5.41	0.3	0.0	-0.3
81	RS11	UB152x89x16	0.78	152.5	88.9	8.1	4.78	0.4	0.4	0.6
	RS12	UB152x89x16	2.38	152.4	88.9	8.1	4.78	0.1	-0.4	-0.8
	RS13a	UB152x89x16	2.61	154.4	90.7	7.9	4.54	-1.6	-1.4	-0.7
	RS13b	UB152x89x16	1.78	154.5	90.5	7.9	4.54	-1.3	-1.5	-1.3
	RS14	UB152x89x16	1.99	154.7	90.5	7.9	4.54	-0.5	-0.6	-0.8
	RS15	UB152x89x16	2.94	152.7	88.8	8.1	4.78	-1.5	-1.5	-0.6
97	RS16	UB127x76x13	0.74	129.8	76.6	7.73	4.54	0.1	0.1	0.0
	RS17	UB127x76x13	4.08	127.9	76.2	7.09	4.54	-0.4	-0.6	-0.1
	RS18	UB127x76x13	1.90	127.8	76.1	7.07	4.54	-1.3	-1.3	-0.6
	RS19	UB127x76x13	1.54	127.8	76.0	7.10	4.54	-0.2	-0.2	-0.8
	RS20	UB127x76x13	1.65	129.9	76.4	7.94	4.54	-0.2	-1.0	-0.8

3.3 Instrumentation

3.3.1 Loadings

Applied loads were controlled and recorded by the 5000kN servo-hydraulic actuator. Two load cells placed at the supports of the restrained beam, in the restrained column test, measured the restrained force (see Figure 3.3). Total column internal axial force was the summation of the applied constant load from the actuator and the increasing restrained forces due to elevated temperature.

3.3.2 Displacements

Linear Variable Displacement Transducers (LVDTs) were used to measure the displacements directly for all points except the lateral displacements at the column mid-height. This is because the column was inside the furnace and LVDT could not withstand the high temperature if placed internally. Specially fabricated measurement probes were used to transfer readings from Alsint rod of the specimen inside the furnace to an external LVDT (see Figure 3.4).

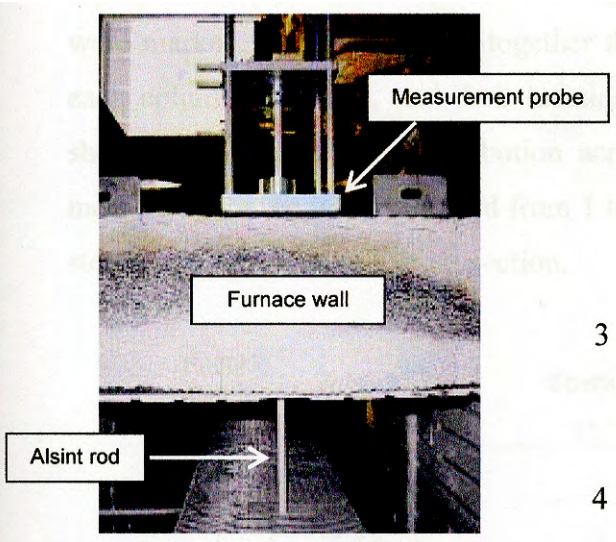

Figure 3.4 Displacement measurement probe

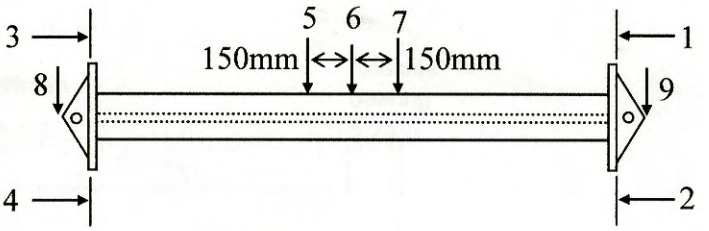

Figure 3.5 Location of LVDTs on column specimen

The displacement measurement probe was made up of an aluminium alloy support and a highly refractory Alsint 99.7 rod. The Alsint 99.7 rod has good thermal expansion shock resistance, high flexible strength of 300 MPa, and low coefficient of thermal expansion with a value of 7.8×10^{-6} K^{-1}. Although minimal, the thermal expansion of the rod was still calibrated during elevated temperature tests, and subtracted from the recorded lateral displacement of the column. Locations of LVDTs in the test set-up are shown in Figure 3.5.

3.3.3 Temperatures

Temperatures of the inner atmosphere of furnace as well as the specimen were closely monitored using thermocouples. As mentioned earlier in section 3.2.2, gas temperature was monitored by internal thermocouples. Temperature distribution across the column section was measured at three locations, namely, at 150mm from both ends and at mid-height (Figure 3.6 (a)). Across each cross-section, five thermocouples were installed on the flanges and web, marked as T1 to T5 (Figure 3.6 (b)). There were also four thermocouples installed along the web, so as to monitor the temperature distribution along the column length. These thermocouples were marked as W1 to W4. Altogether there were 19 thermocouples installed on each column specimen, and their locations are shown in Figure 3.6. Test results showed that temperature distribution across the section was quite uniform. The mean temperature was calculated from 1 to 5 (Figure 3.6 (b)) to represent the mean steel temperature at each cross section.

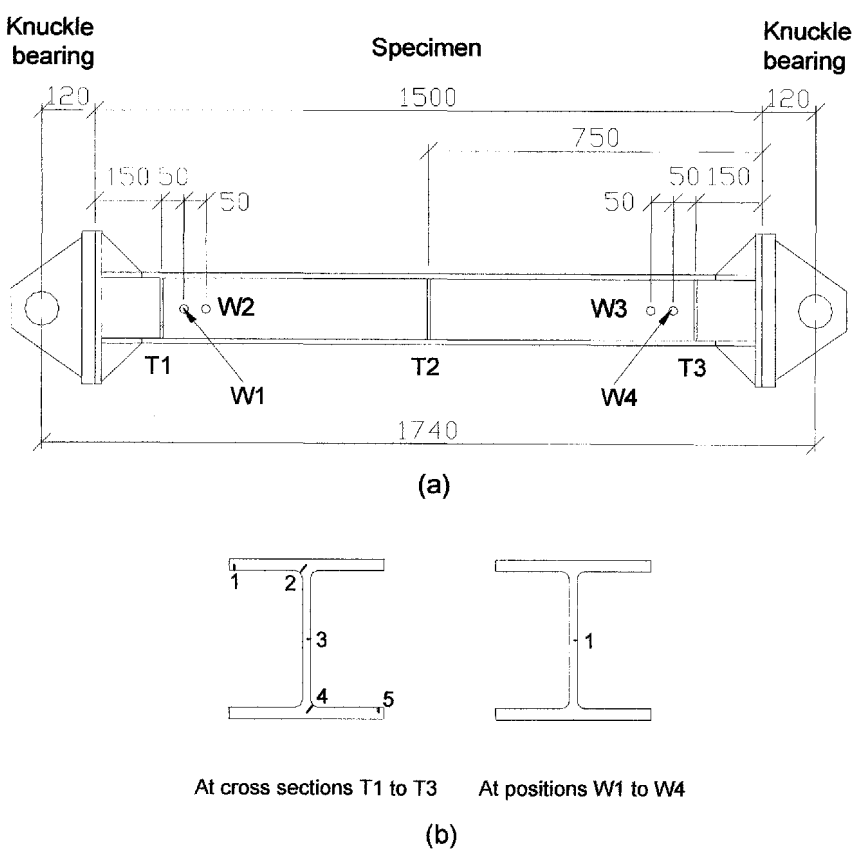

Figure 3.6 Location of thermocouples on column specimen

3.4 Test Procedure

All elevated temperature tests were performed under transient state heating. A predefined working load P_o was first applied to the specimen and held constant. The temperature was then raised in steps until failure occurred. The working load was taken as 50% of the buckling resistance of the column at ambient temperature, $P_{u,20}$. The value of $P_{u,20}$ was determined experimentally from ambient tests carried out for every group of columns with different slenderness ratios (see Table 3.4).

The procedure for setting up and carrying out of an elevated temperature test on each column specimen is as follows:

1. Installing thermocouples onto the column specimen (T1 to T5 and W1 to W4);
2. Using a 5-tonne gantry crane to lift the specimen and to set it up in the test rig, with the top of the furnace left open;
3. Placing a cover over the furnace top and sealing all gaps with insulation wool and cloth;
4. Setting up LVDTs;
5. Connecting LVDT wires to data logger terminals;
6. Connecting thermocouple wires to computer system;
7. Connecting electrical furnace cables to control panel;
8. Checking various instrumentations for proper functioning;
9. Preloading and unloading the specimen at least twice to eliminate undesirable slack in the system due to closing of gaps;
10. Initialising all instrumentations;
11. Applying working load to the specimen at a constant rate and then holding it constant;
12. Applying axial restraint by connecting supports of restraint beam to reaction frames until load cells give small readings;
13. Start heating up the furnace until the applied working load cannot be sustained.

Figure 3.7 shows the complete set-up of the test with some dimensions indicated in Figure 3.8.

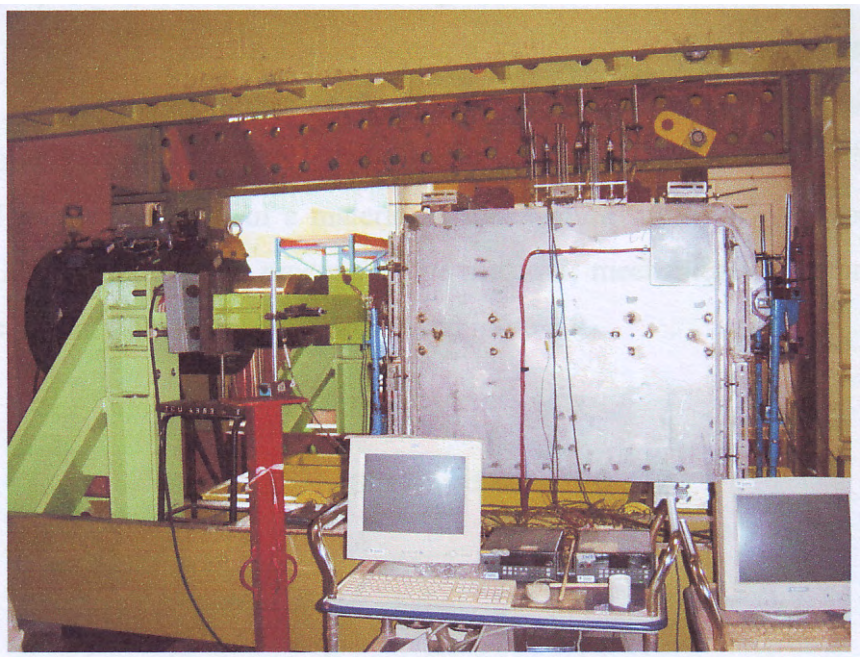

Figure 3.7 Test set-up

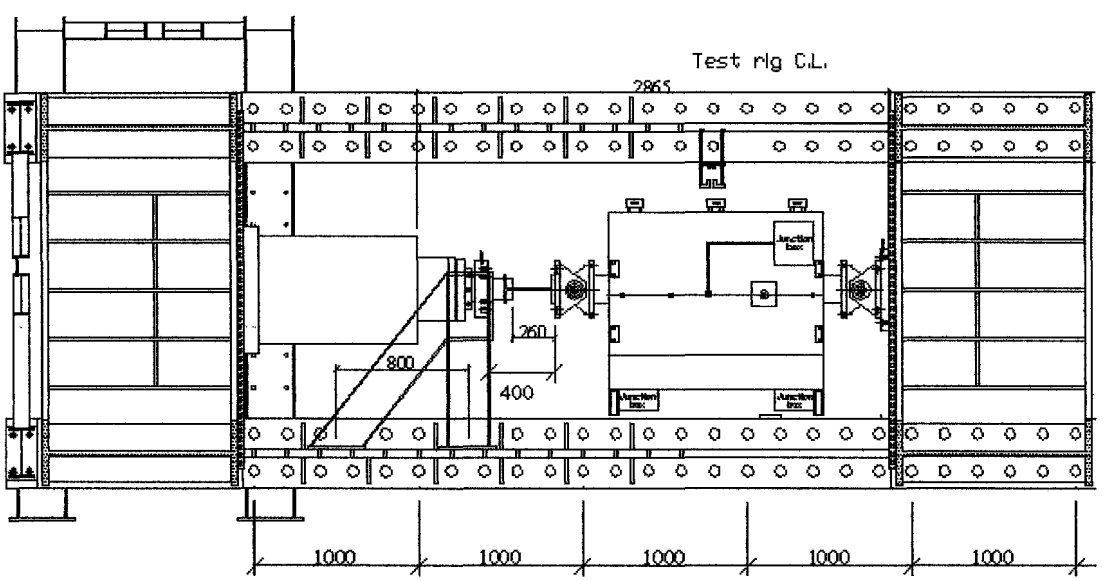

Figure 3.8 Elevation view of test set-up

3.5 Material Properties

Accurate prediction of column failure temperature in analysis depends on the material properties of the steel used. For grade S275 steel, nominal values of the Young's modulus E, and the yield strength σ_y, given in codes of practice are generally taken as 210kN/mm^2 and 275N/mm^2, respectively. Young's Modulus is dependent on the chemical composition of the material and is not affected by strain history. The yield strength of a material is much more susceptible to mechanical changes. During the rolling process of the material, mechanical strain hardening may increase the yield strength, as shown in Figure 3.9.

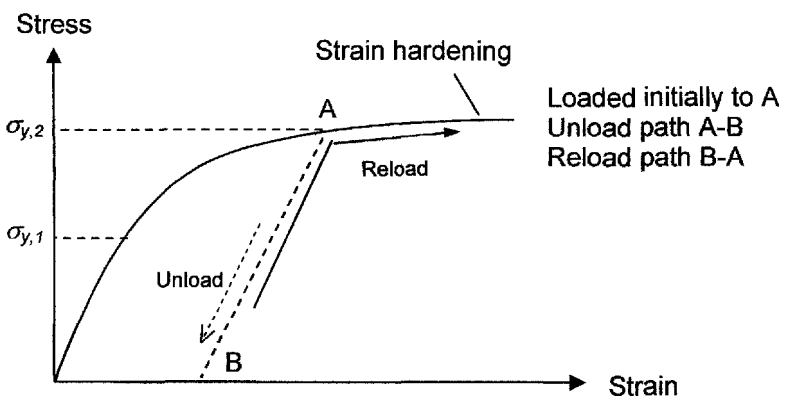

Figure 3.9 Strain hardening

Steel used in construction usually has higher yield strength than the value proposed by design codes, such as EC3 Part 1.2, in order to be on the conservative side of any specified strength. Therefore, it is desirable to obtain an accurate value of the yield strength through experiment. The results can then be adopted in the detailed numerical analysis.

Values for steel elastic modulus, yield strength and ultimate strength of test specimens were obtained from tensile coupon tests. At least 3 coupons from each sample were tested to determine the material properties. The tests were performed on a 1000kN Universal Testing Machine. Displacement and strain readings were measured using LVDTs and strain gauges, respectively. Figure 3.10 shows a coupon

tensile test being carried out at ambient temperature and Figure 3.11 shows a fractured coupon. Figure 3.12 shows the stress-strain relationship of steel at ambient temperature. Unfortunately, there was no facility for conducting tensile coupon test at elevated temperature during the time of testing. This facility has just been commissioned in the Heavy Structure Lab in January 2005.

Table 3.3 summarises the material properties of test specimens. Three coupon tests were conducted for each flange and web of the steel section. It is noteworthy that columns with section UB 152×89×16 came from two groups, namely, UB 152×89×16a and UB 152×89×16b, since they came from two batches. All values of elastic modulus fall into the range of 200 to 210 GPa. Ultimate stresses were calculated by dividing the respective ultimate loads by the cross sectional area of the coupon at the breaking points. Values of the ultimate strengths were shown on the Universal Testing Machine. Equivalent values of the strengths from flanges and webs were obtained from averaging the test results in proportional to their cross-sectional areas. These equivalent values were used in the finite element analysis. However, material properties for steel at elevated temperature were not determined as there was no such facility at that time. Therefore, EC3 material model was adopted in numerical simulations. This implies that strain hardening phenomenon beyond yield point is not accounted for. This tends to somewhat overestimate the structural deformation of heated specimen and resulting in an underestimation of the column critical temperature.

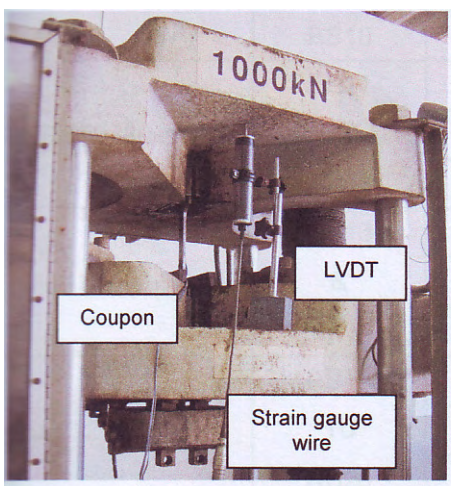

Figure 3.10 Tensile coupon test

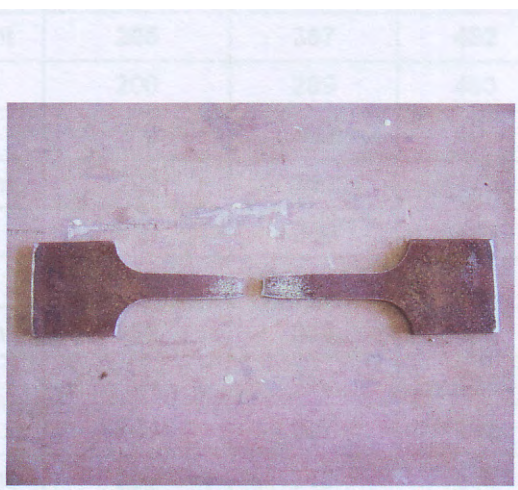

Figure 3.11 Coupon after tensile test

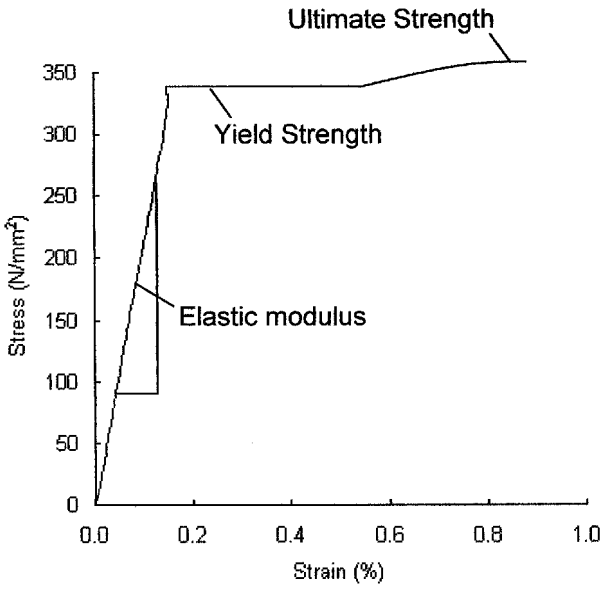

Figure 3.12 Stress-strain relationship of steel from tensile coupon test

Table 3.3 Material properties of column specimens at room temperature (Series 1)

Section	Column Marking		Elastic Modulus (kN/mm^2)	Yield Strength (N/mm^2)	Ultimate Strength (N/mm^2)
UC 152×152×37	RS01 To RS05	Flanges	200	320	470
		Web	205	352	486
		Equivalent	**201**	**326**	**473**
UB 203×133×25	RS06 To RS10	Flanges	205	326	467
		Web	205	416	511
		Equivalent	**205**	**357**	**482**
UB 152×89×16a	RS11 RS12 & RS15	Flanges	200	289	463
		Web	200	362	496
		Equivalent	**200**	**312**	**473**
UB 152×89×16b	RS13 & RS14	Flanges	210	330	476
		Web	205	336	481
		Equivalent	**208**	**332**	**478**
UB 127×76×13	RS16 To RS20	Flanges	200	312	491
		Web	200	327	481
		Equivalent	**200**	**316**	**488**

3.6 Experimental Axial Restraint

Values of experimental restraint stiffness obtained from tests are shown in Table 3.4. LVDTs were used to record the axial deformation of the column specimen and the restraint beam in the test. Together with the restraint beam, the servo-hydraulic actuator provided the total internal axial force to the columns. Deflection at the mid-span of the restraint beam included slight movement of supporting A-frames as well. Load cells at the supports of the restrained beam provided measurement for the restraint force imposed at different time steps. Figure 3.3 shows the test set-up for the axial restraint force system. Actual axial restraint stiffness, $K_{s,test}$, was calculated as the ratio of the imposed restrained force to the measured total deflection indicated by the LVDTs at locations 1 to 4 in Figure 3.5. The imposed restraint force was plotted against the mid-span deflection of the restrained beam for each restrained elevated temperature test (Figure 3.13). The actual axial restraint stiffnesses were calculated from the gradients of the linear graphs. Missing points in Figure 3.13 (c) was due to an accidental break in recording by the computer system during the testing of Column RS08.

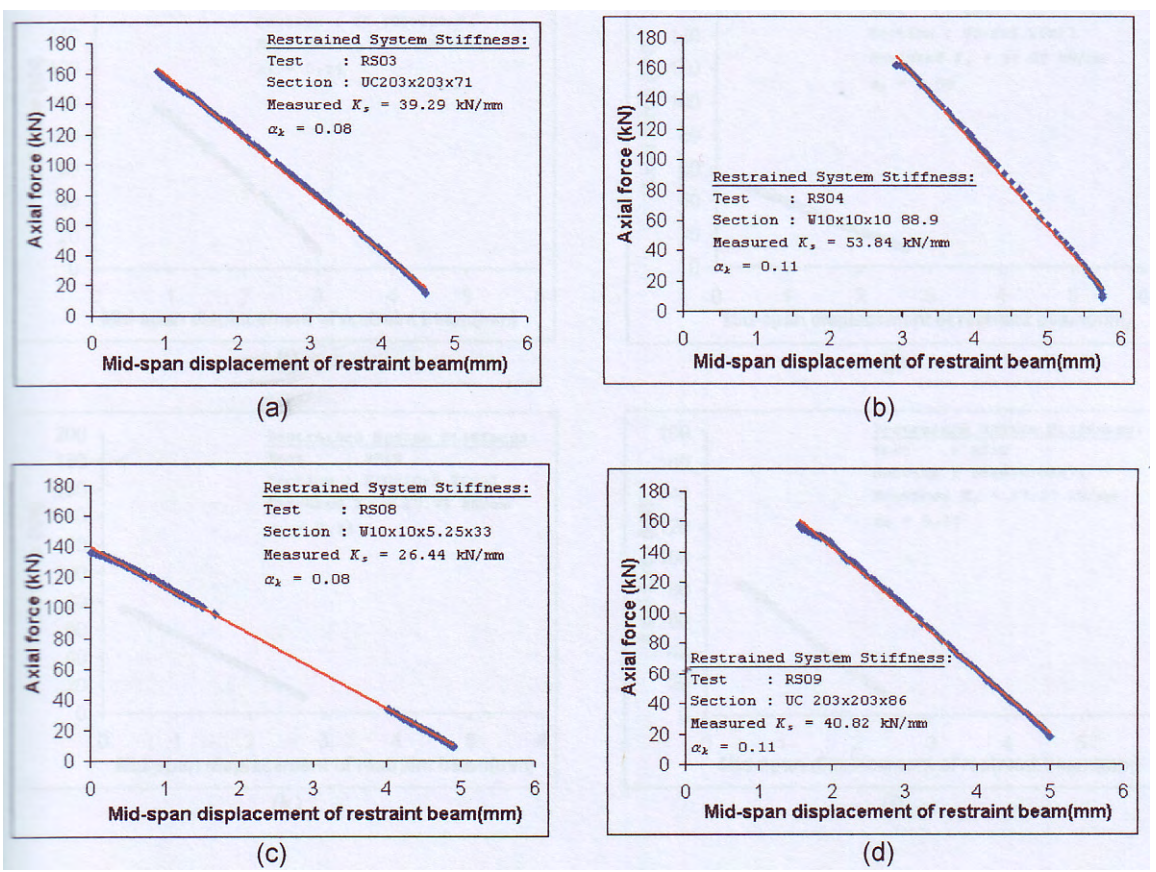

Figure 3.13 Force-displacement relationships of restraint beams (Series 1)

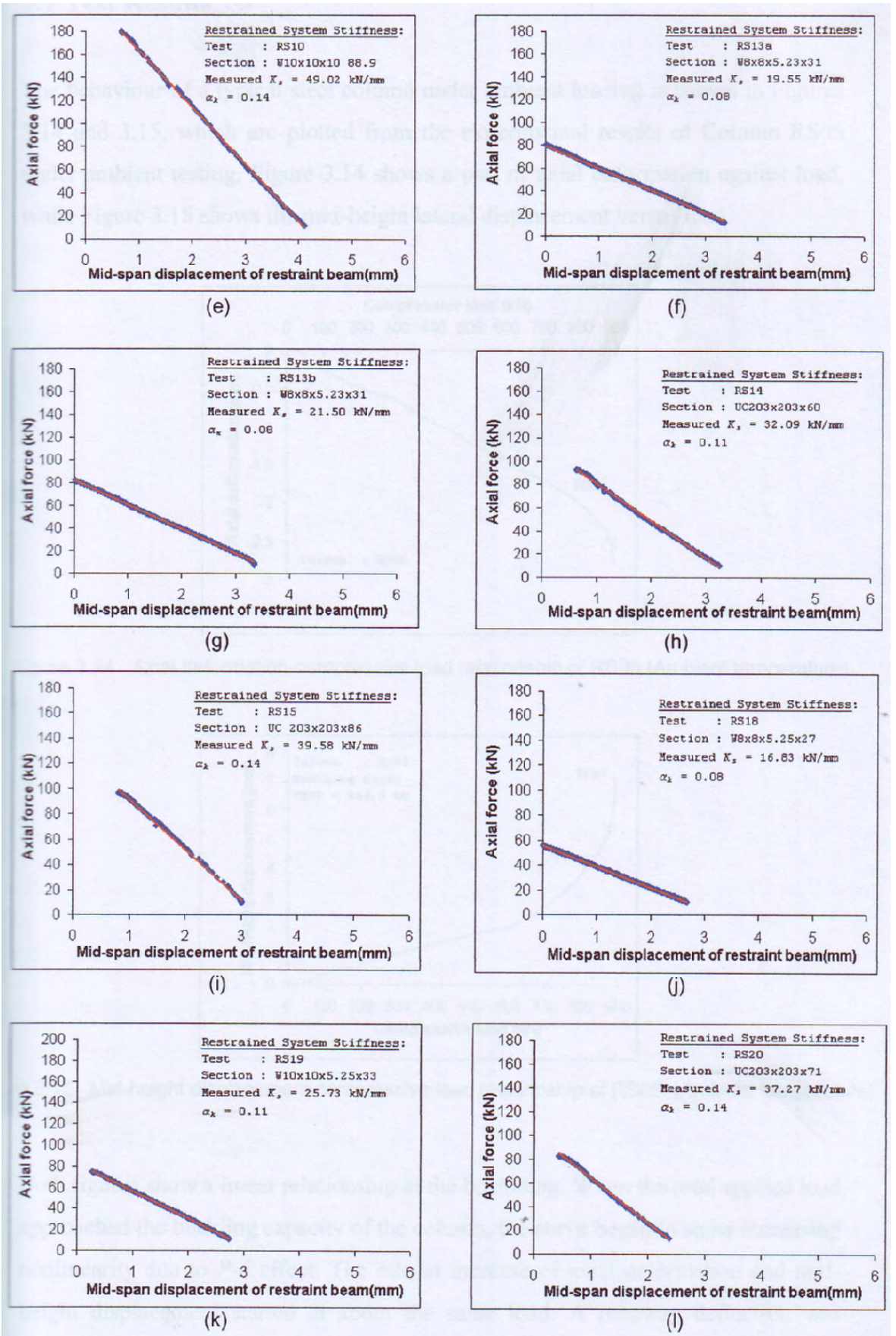

Figure 3.13 Force-displacement relationships of restraint beams (Series 1) (continued)

3.7 Test Results

The behaviour of a typical steel column under ambient loading is shown in Figures 3.14 and 3.15, which are plotted from the experimental results of Column RS06 under ambient testing. Figure 3.14 shows a plot of axial deformation against load, while Figure 3.15 shows the mid-height lateral displacement versus load.

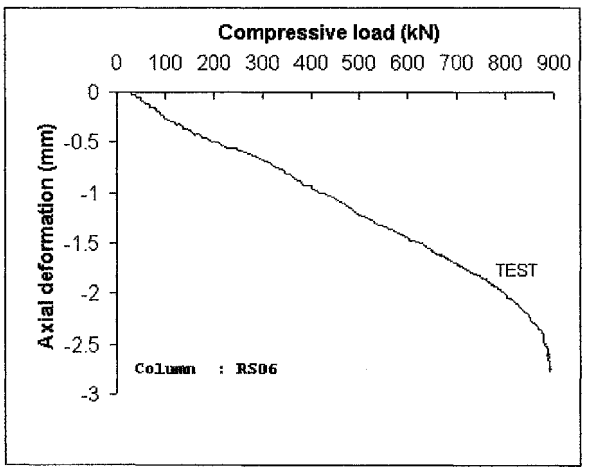

Figure 3.14 Axial deformation-compressive load relationship of RS06 (Ambient temperature)

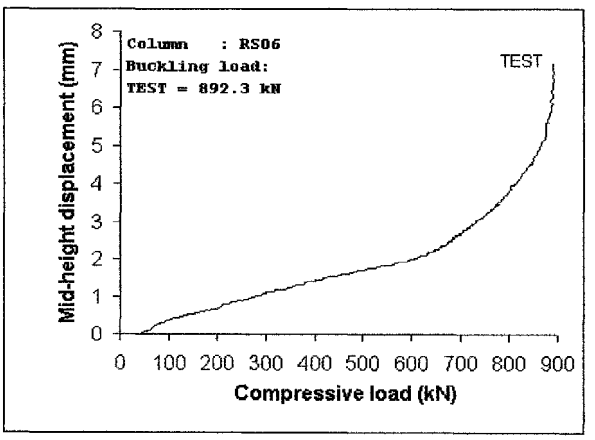

Figure 3.15 Mid-height displacement-compressive load relationship of RS06 (Ambient temperature)

Both figures show a linear relationship at the beginning. When the total applied load approached the buckling capacity of the column, the curve began to show increasing nonlinearity due to P-δ effect. The rate of increase of axial deformation and mid-height displacement started at about the same load. A runaway deflection was

observed in each curve when the buckling load was reached. Column RS06 had a buckling load of 892.3kN. Therefore the working load P_o to be applied to heated Columns RS07 to RS10 would be 50% of 892.3kN, which is 446.15kN.

The behaviour of a restrained column under elevated temperature is shown in Figures 3.16 to 3.19. Plots from restrained column RS08 for elevated temperature test are shown in these figures. A working load, P_o of 446.6kN was applied to RS08 and held constant, after which, the temperature in the furnace was increased at a constant heating rate of 7°C/min. This rate was chosen so that the steel temperature could follow the furnace temperature closely.

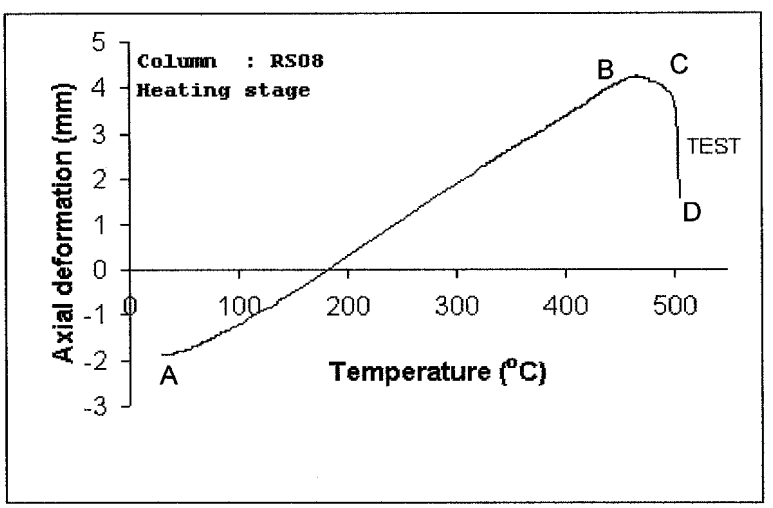

Figure 3.16 Axial deformation-temperature relationship of RS08

Figure 3.16 shows a plot of axial deformation against rising temperature. The initial negative axial deformation was due to the application of axial force before heating commenced. The axial deformation-temperature may be divided into three stages: the first stage (A-B) was due to thermal expansion of the steel column under a restrained system. At high temperature (B-C), the rate of increase in the axial deformation was reduced and the mechanical shortening became more important. Finally stage (C-D) showed that the mechanical shortening overtook free thermal expansion of the column. The shortening of column was due to significant development of lateral displacement. In the end, the column could not sustain the

initial applied load which was held constant by the actuator throughout the rise of temperature, and it buckled at 504.7°C.

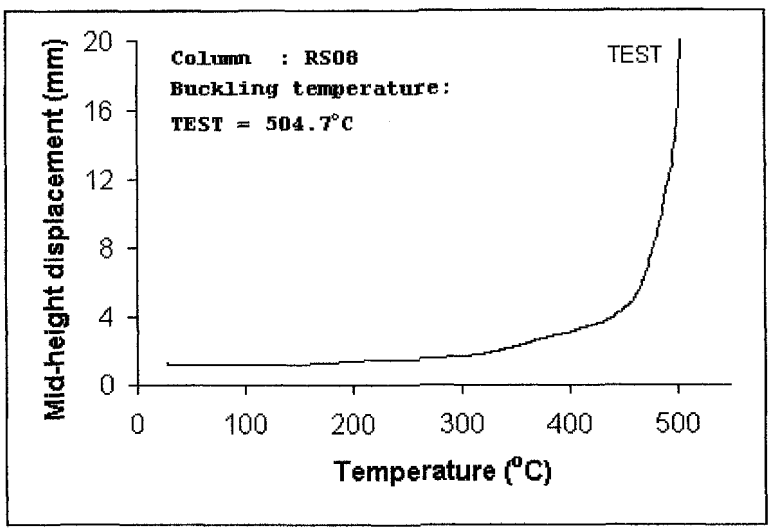

Figure 3.17 Mid-height displacement-temperature relationship of RS08

Figure 3.17 shows a plot of mid-height displacement against temperature for Column RS08. The initial mid-height displacement of 1.22mm was caused by the application of axial force before heating began, where the column experienced some initial bending deformation. This initial displacement depended on the value of inevitable load eccentricities and initial crookedness. The larger the initial imperfection, the larger the initial lateral displacement would be. From Figure 3.17, the change in the mid-height lateral displacement was not so significant before 300°C. The runaway phenomenon took place when the temperature approached the buckling temperature. Here, it was defined as the temperature at which the column internal resistance reduced to the original load P_o, or the temperature at which the column suddenly buckled, whichever came earlier.

Figure 3.18 plots the ratio of the restrained force to the working load P/P_o against temperature for Column RS08. The non-dimensional ratio P/P_o is unity at the beginning of heating. After heating has commenced, P/P_o is observed to remain stagnant until temperature is above 60°C. This thermal slack is expected since there are gaps between contact surfaces (such as between the column and the end

supports). Besides, it takes a finite time to heat up the members to close the gaps. This phenomenon is observed in all other restrained column elevated temperature tests as well, as shown in section 4.3.2. This is due to the axial restraint system, which inevitably had some slack, and could not be instantaneously activated in the initial period of heating, known as *thermal slack effect*. Nevertheless, from experimental results, the restraint system did provide the desired restraint stiffness for each test after 60°C, as had been discussed in section 3.6.

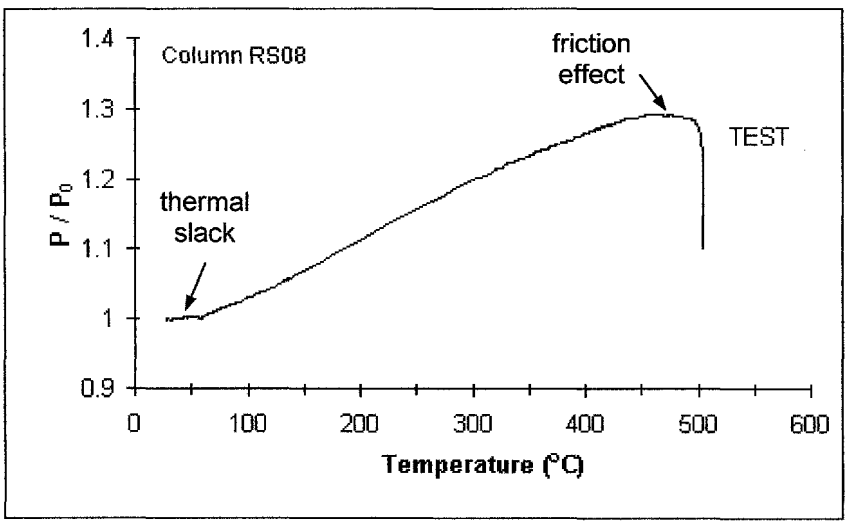

Figure 3.18 P/P_o - temperature relationship of RS08

After the stabilising stage, the restrained force P increased linearly until it reached the peak value (Figure 3.18). This illustrated that the column remained elastic during the pre-buckling stage. When P/P_o had reached the peak value, the load P stagnated at the maximum value for an additional period of heating, before P either immediately or gradually reduced until it reached the initial working load P_o. Figure 3.18 illustrated that Column RS08 experienced an immediate global buckling. As the system was under load control, the drop in buckling load was quite sudden. For the current set-up, it was not possible to monitor the column behaviour beyond the buckling temperature, as the restraint system only worked in compression and not tension.

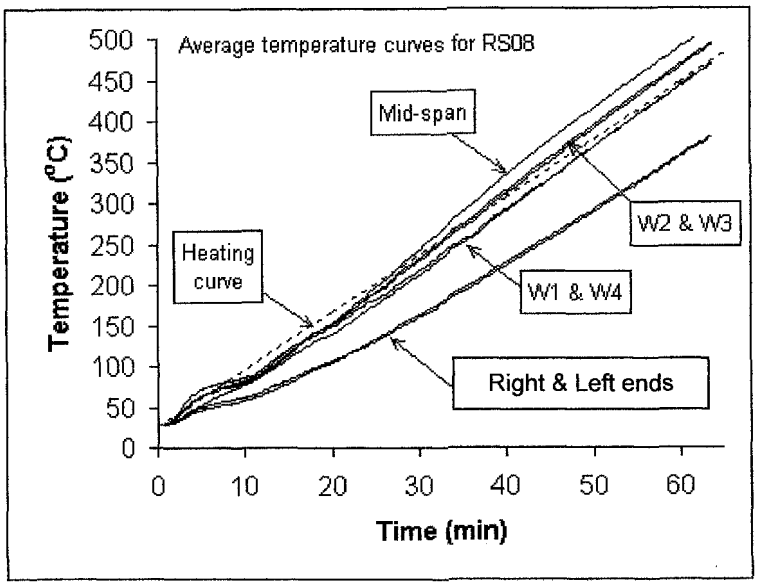

Figure 3.19 Temperature-time relationship of RS08

Figure 3.19 presents the temperature histories of Column RS08. It illustrates typical temperature variations of a steel column during an elevated temperature test. The temperature histories measured at various cross sections along the column length were also plotted in the same figure. The temperatures at the middle section of the column were consistently higher than those at both ends for the whole period of heating. This was because both ends of the steel column were wrapped with insulation material before bolting onto the end knuckle-bearings, to prevent heat from being lost by conduction.

In finite element analysis (FEA), the columns were divided into three sections; the middle 1m span length was subjected to a higher rate of increase in temperature profile compared to the two ends of 0.25m, which had a lower rate of increase in temperature. The knuckle bearings were not placed in the furnace and this was also reflected in FEA. Figure 3.20 shows a plot of temperature profile along the column length at various temperatures. It indicates that the temperature distribution along the middle stretch of 1m was quite uniform. Therefore, the cross-sectional mean temperature at column mid-height was used to represent the column steel temperature in finite element analysis (FEA).

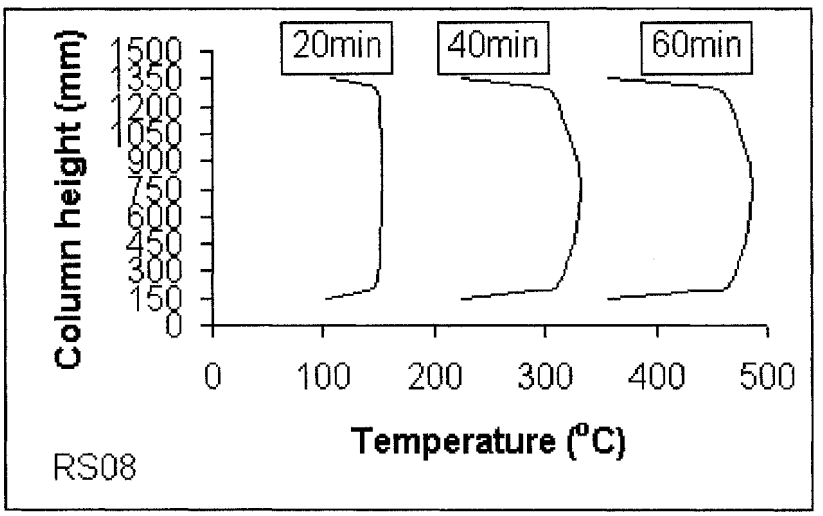

Figure 3.20 Temperature profile along column length for RS08

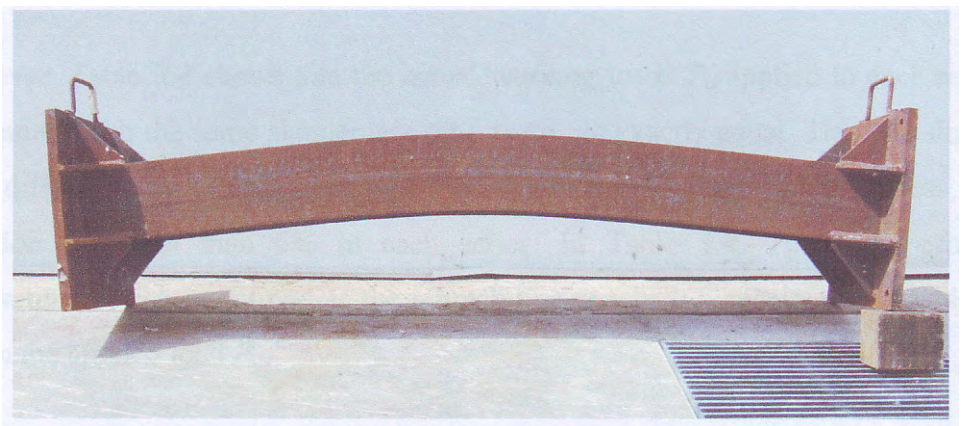

Figure 3.21 Global buckling of steel column RS08

Figure 3.21 shows the buckled steel column RS08. It illustrates a typical global buckling behaviour. Table 3.4 summarises the results for all steel column tests. It shows the overall performance of the steel columns under elevated temperature and gives the main details of the experimental objectives: namely, the buckling temperature and the axial restraint ratio.

RS01, RS06, RS11 and RS16 were specimens in unrestrained ambient loading tests carried out to obtain the respective column buckling resistance, which were then used to compute the working loads P_o to be imposed on the column tests at elevated temperature. RS02, RS07, RS12 and RS17 were specimens subjected to

unrestrained elevated temperature tests, while the rest of the columns were subjected to restrained elevated temperature tests.

The actual values for restraint stiffness, $K_{s,test}$, measured during the testing for individual restrained test are also presented in Table 3.4, together with the column stiffness K_c, and the actual restraint ratio, $\alpha_{k,test}$. Column stiffness K_c is simply found by taking the ratio of EA/L_e, where E is the elastic modulus, A is the cross sectional area and L_e is the effective length, taken as 1.74m. The mean value of the ratio $\alpha_{k,test}$ to $\alpha_{k,design}$ (design restraint ratio) is 1.07, with a standard deviation, SD = 0.14 and a coefficient of variation, COV = 0.13. These values indicate that the restraint system was effective in providing the necessary amount of axial restraint in the experimental programme.

Moreover, Table 3.4 shows that the actual working loads P_o applied to each series of columns with the same slenderness ratio were not exactly equal. This was due to some difficulty in the control of INSTRON hydraulic actuator. Nevertheless, the deviation was less than 5% in each series. In Table 3.4, T_{cr} is the critical temperature, which is defined as the temperature at which a specimen is unable to sustain the applied load P_o.

Table 3.4 Column test results summary (Series 1)

λ	Column Marking	Section	K_c (kN/mm)	$K_{s,test}$ (kN/mm)	$\alpha_{k,test}$	$\alpha_{k,design}$	$\frac{\alpha_{k,test}}{\alpha_{k,design}}$	P_0 (kN)	T_{cr} (°C)
45	RS01	UC152x152x37	520.5	0.00	0.00	0.00	-	1378.1#	-
	RS02	UC152x152x37	520.5	0.00	0.00	0.00	-	708.5	595.0
	RS03	UC152x152x37	520.5	39.29	0.08	0.08	1.00	723.1	554.6
	RS04	UC152x152x37	520.5	53.84	0.10	0.11	0.91	711.5	452.8
55	RS06	UB203x133x25	369.8	0.00	0.00	0.00	-	892.3#	-
	RS07	UB203x133x25	369.8	0.00	0.00	0.00	-	444.3	545.8
	RS08	UB203x133x25	369.8	26.44	0.07	0.08	0.88	446.6	504.7
	RS09	UB203x133x25	369.8	40.82	0.11	0.11	1.00	451.3	455.0
	RS10	UB203x133x25	369.8	49.02	0.13	0.14	0.93	452.8	483.3
81	RS11	UB152x89x16	246.5	0.00	0.00	0.00	-	518.9#	-
	RS12	UB152x89x16	246.5	0.00	0.00	0.00	-	260.6	488.2
	RS13a	UB152x89x16	246.5	19.55	0.08	0.08	1.00	260.4	525.2
	RS13b	UB152x89x16	246.5	21.50	0.09	0.08	1.13	266.0	544.4
	RS14	UB152x89x16	246.5	32.09	0.13	0.11	1.18	265.0	379.1
	RS15	UB152x89x16	246.5	39.58	0.16	0.14	1.14	270.5	315.7
97	RS16	UB127x76x13	194.6	0.00	0.00	0.00	-	388.4#	-
	RS17	UB127x76x13	194.6	0.00	0.00	0.00	-	193.8	317.3
	RS18	UB127x76x13	194.6	16.83	0.09	0.08	1.13	197.5	453.1
	RS19	UB127x76x13	194.6	25.73	0.13	0.11	1.18	197.7	304.7
	RS20	UB127x76x13	194.6	37.27	0.19	0.14	1.36	199.2	313.9

Buckling resistance at ambient temperature

Mean:	1.07
Standard Deviation (SD):	0.14
Coefficient of Variation (COV):	0.13

3.8 Overall Observations of Column Behaviour

Axial expansion against the restraint system generated additional compressive forces in the steel columns. The restraint system produced a linear increase in force with axial displacement from about 60°C onwards, as the axial expansion was proportional to the temperature increase for a straight elastic column. Before this temperature, any increase in axial force was not possible due to the presence of *thermal slack*. The slack in the restraint force before the expected linear behaviour was due to existence of small gaps between the specimen and the support bearings of the test rig. This gap was being closed up by axial expansion before the column began to interact with the restraint system.

With increasing temperature, the restraint force curve would either come to a peak or plateau off after some time, as shown in Figure 3.22. When the peak restraint force was reached and began to decrease, shortening of column started. This was due to material properties degradation, where column shortening and bending under an increased load counteracted the thermal expansion. Behaviour after this point depended very much on the column slenderness. Stocky columns would experience gradual shortening prior to buckling, whereas slender columns would buckle relatively quickly. The most slender section (λ = 97) in each series of restraint ratio, as indicated in Figures 3.22 (a) to (c), namely, RS18, RS19 and RS20, respectively, generated additional restraint force up to a peak value and then buckled immediately, with a sharp decline in the restraint force. P-δ effect in column contributed greatly towards buckling as well. This occurred when the bending deflection shifted the column centroid at mid-height away from the line of action of the compression force, resulting in additional bending moment, of a magnitude equal to the product of compression force and the deflection. Therefore, slender columns were very sensitive to this effect, compared to stocky ones.

With a reduction in slenderness ratio, as in the case of the more stocky columns in each restraint ratio category (λ = 45 and 55), marked as RS03, RS04 and RS10 in Figures 3.22 (a) to (c) respectively, it was observed that the restraint force levelled

off gradually before buckling occurred. This behaviour was caused by the gradual loss of column stiffness before buckling, associated with inelastic buckling. Besides the increased lateral displacement, the shortening was also due to the acute degradation of material properties. At elevated temperature the stress-strain behaviour of steel changes, which changes the buckling behaviour. Inelastic buckling may become dominant for columns with intermediate slenderness and may begin to govern the strut behaviour as temperature rises. Rather than having a distinct proportional limit, which coincides with the yield point, as at ambient temperature, steel stress-strain diagrams at elevated temperature become significantly curvi-linear and therefore the yield point and proportional limit become quite separate values. If the buckling load remains below the proportional limit, as for high slenderness, then elastic buckling occurs, and when the buckling load exceeds the yield strength (for columns with low slenderness), collapse through material yielding takes place.

Figures 3.23 (a) to (c) show consistent trends in all tests for the effects of *slenderness on the maximum generated restraint force. As column slenderness* increased, the maximum internal force reduced proportionally because the collapse load was reduced. Maximum restraint force generated varied with slenderness in a proportional manner similar to the buckling temperatures. In Chapter 4, the trends of P/P_o will be illustrated and discussed.

Further issues on the results are discussed in the following sections and also in Chapter 4, where finite element analysis results will be compared with those from testing.

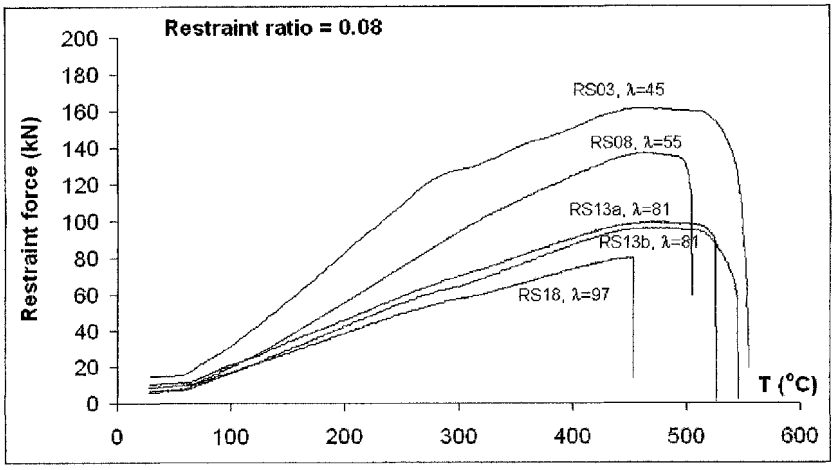

(a) Restraint ratio = 0.08

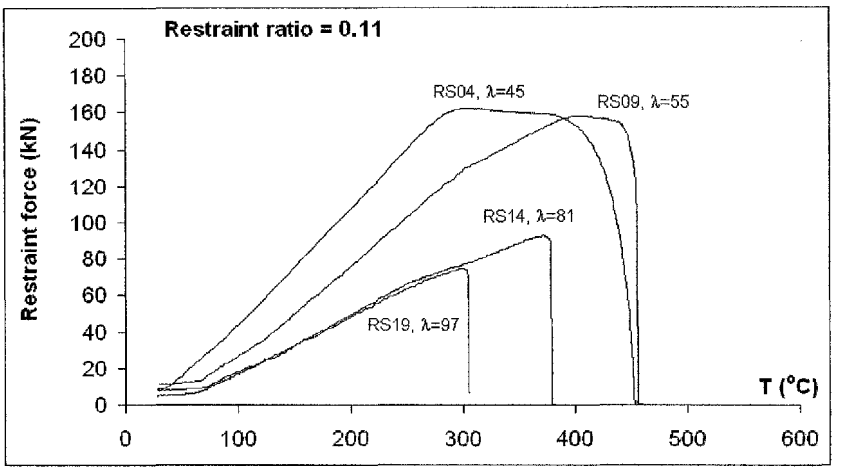

(b) Restraint ratio = 0.11

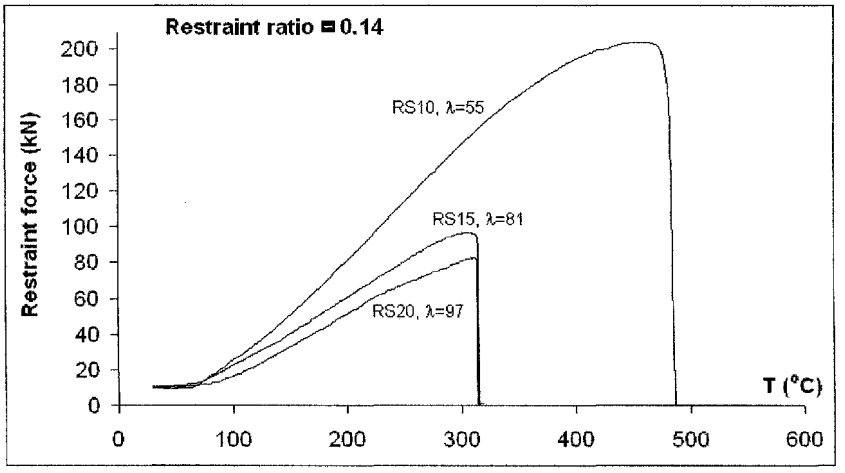

(c) Restraint ratio = 0.14

Figure 3.22 Graphs of restraint force against temperature (Series 1)

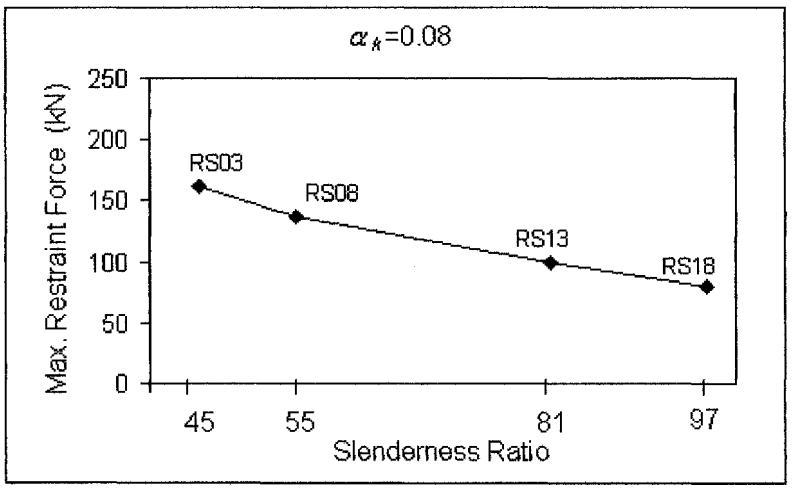

(a) Restraint ratio = 0.08

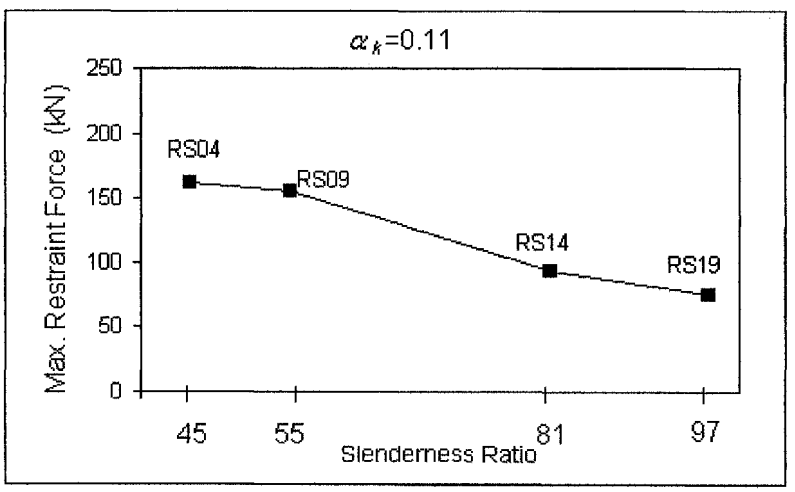

(b) Restraint ratio = 0.11

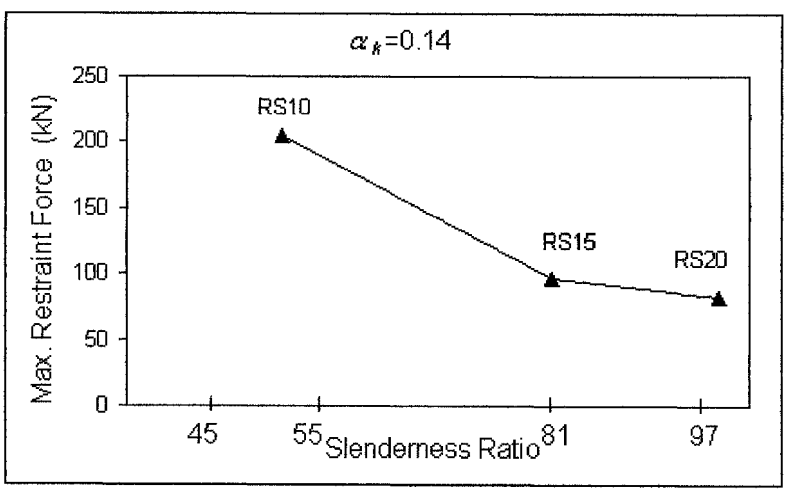

(c) Restraint ratio = 0.14

Figure 3.23 Graphs of maximum generated restraint force against slenderness (Series 1)

3.9 Failure Temperature

There were two different definitions of failure temperature when considering axially restrained columns. First, *buckling temperature* was defined as the point at which runaway lateral displacement of columns occurred. However, in the case of stocky columns, the restraint force rose to a peak value before levelling off gradually, due to degradation of material properties up to a point where the total applied force exceeded the collapse load of the column at that specified temperature (Column RS04 in Figure 3.22 (b)). The temperature at which the restraint force started to decrease was defined as the *collapse temperature*. In the case of slenderer columns, the two defined temperatures were almost the same. This was because buckling of these columns occurred when the collapse temperature was reached (Column RS19 in Figure 3.22 (b)).

Buckling temperature T_{cr} was taken as the failure temperature during the column test, as it was considered to be the more significant of the two failure temperatures defined above. It was the point at which the column could no longer sustain the applied load. Two main concerns on the buckling temperature are discussed in this section, namely, the effects of slenderness ratio λ and axial restraint ratio α_k on the buckling temperature T_{cr}.

3.9.1 Effects of Slenderness Ratio on Buckling Temperature

Figures 3.24 (a) to (d) show the trends of buckling temperature T_{cr} with slenderness λ, under axial restraint ratios α_k = 0.0, 0.08, 0.11 and 0.14, respectively.

An overview shows that in general, T_{cr} decreases as λ increases, except for the point for λ = 81 and α_k = 0.08 in Figure 3.24 (b). This column has a higher buckling temperature than expected. This particular point takes the mean T_{cr} associated with specimens RS13a and RS13b, which are of the same λ and α_k (Table 3.4). The reason for this non-conformity may be due to the effect of friction. In normal range

of load eccentricity e from 0 to 20mm, the presence of e will decrease the buckling temperature T_{cr}. Figure 3.22 (a) shows that it was friction that delayed the buckling temperature T_{cr} of Columns RS13a and RS13b. For these two columns, RS13a had a load eccentricity of 2.61mm and that of RS13b was 1.78mm. With a higher load eccentricity, Column RS13a failed earlier at 525.2°C, compared to Column RS13b, which failed at 544.4°C. Cabrita Neves (1995) commented on the effects of eccentricity on collapse temperature. Cabrita stated that load eccentricity would affect the restraint ratio trends of failure temperature quite severely, producing erratic test results in both restraint and slenderness trends.

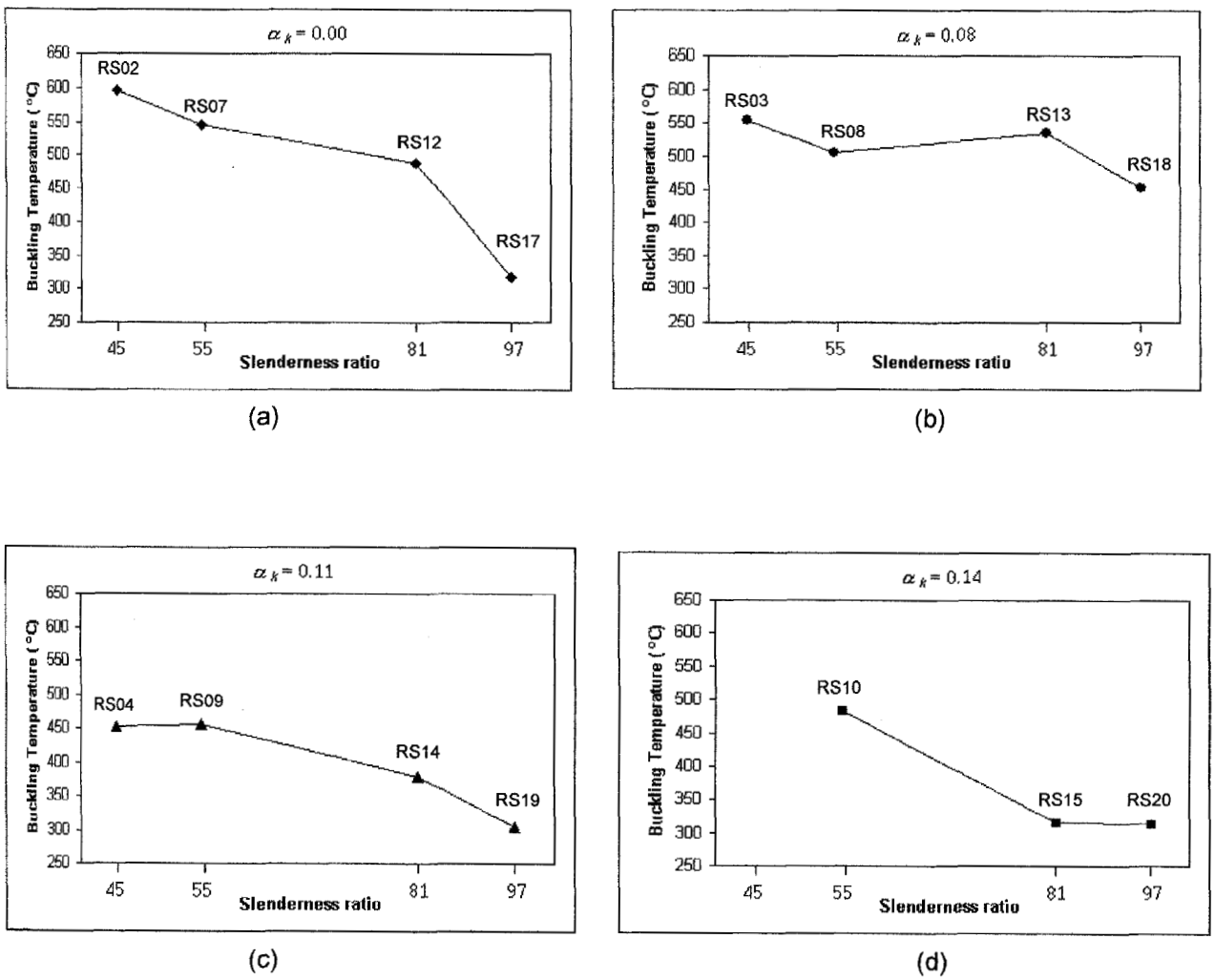

Figure 3.24 Trends of buckling temperatures with slenderness ratios (Series 1)

3.9.2 Effects of Axial Restraint Ratio on Buckling Temperature

Trends of buckling temperature with axial restraint ratio, for slenderness ratios of 45, 55, 81 and 97, are illustrated in Figures 3.25 (a) to (d), respectively. Imposition of increased axial restraint to the columns generally had the effect of reducing the buckling temperatures, for columns with the same slenderness ratio subjected to the same applied working load. This was due to the fact that an increase in the level of axial restraint increased the rate at which restraint force was generated. Therefore, higher loads were on the columns at lower temperatures, and ultimately the columns buckled at lower temperatures.

At low slenderness ratio, as in the stocky columns, an increase in the axial restraint ratio caused only very small reductions in the buckling temperature of the columns. This highlighted the greater post buckling capacity of stocky columns. Although imposition of a greater restraint caused collapse to occur earlier, the columns were able to maintain stability after the maximum load has been reached. This was shown by the presence of "plateau" in the restraint force against temperature plots. For stocky columns, failure was dependent on yield strength and so significantly higher loads were required before buckling would occur, due to slower degradation of yield stress compared to elastic modulus at the same elevated temperature. This generally means that stocky columns have greater fire resistance than slender ones, when subjected to similar restraint ratio at the same temperature.

For the more slender columns with λ of 81 and 97, there was significant variation in the buckling temperatures. Unlike stocky columns, slender columns were unable to maintain their stability under imposition of restraint. A further increase in slenderness caused the effects of low levels of restraint to be more severe. The decay of elastic modulus was the primary cause for the reduction in column stiffness.

Experimental errors were noticed on the column specimens RS13a, RS13b and RS18. RS13a and RS13b are indicated in Figure 3.25 (c) at an axial restraint ratio,

α_k of 0.08, whereas RS18 was located in Figure 3.25 (d) at α_k = 0.08. These test results were unexpected for buckling temperature against axial restraint ratio. Presence of unexpected rotational restraint at the supports due to friction may also result in a higher buckling temperature than expected. The effect of friction was more significant in stocky columns, than in the slender ones.

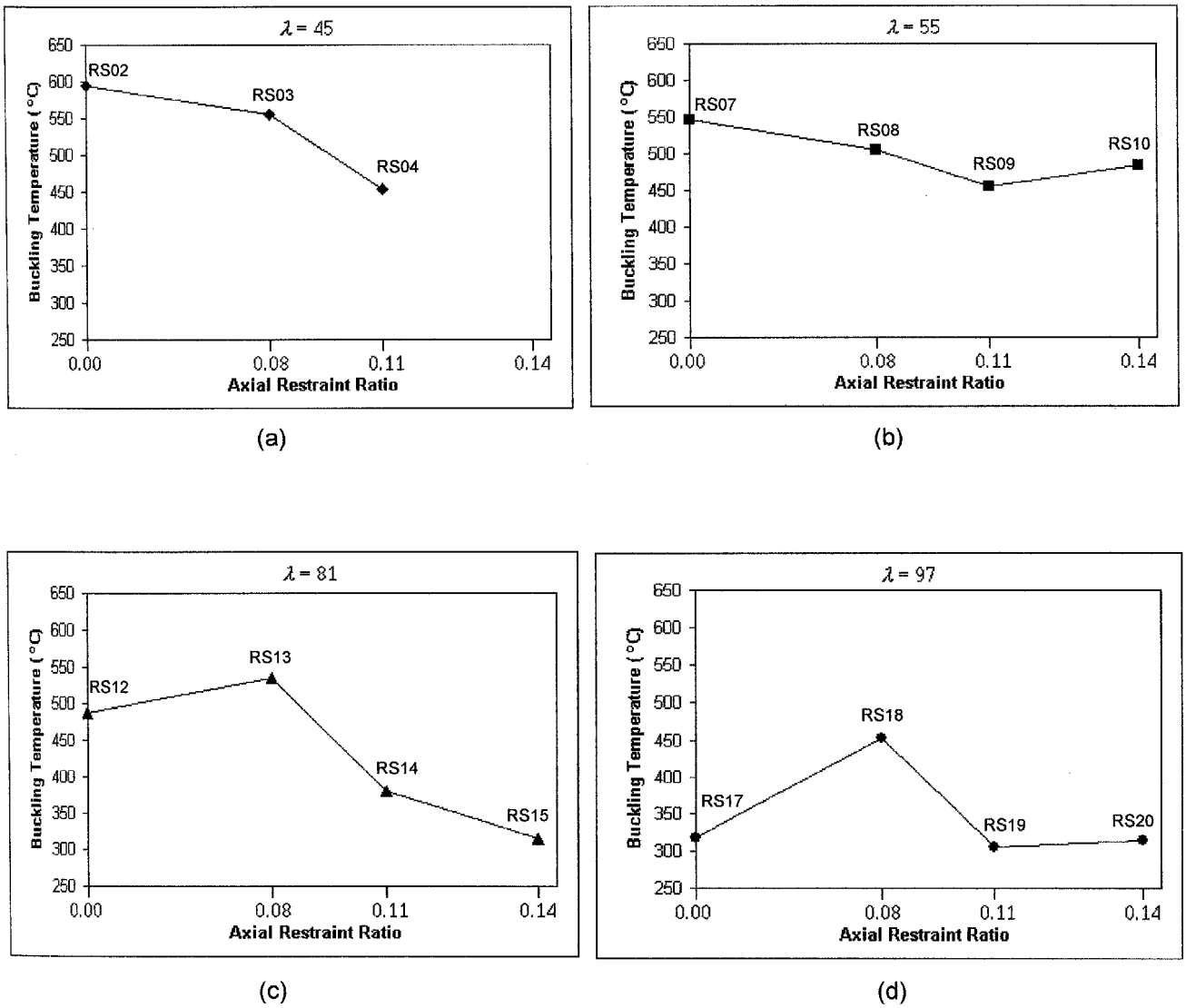

Figure 3.25 Trends of buckling temperatures with axial restraint ratios (Series 1)

CHAPTER FOUR

Finite Element Analysis on Steel Column Tests - Series 1

4.1 Introduction

In engineering, many practical problems are either extremely difficult or impossible to solve by conventional analytical methods. Such methods involve finding mathematical equations where required variables are defined. Finite Element Method (FEM) is a versatile numerical method that provides a solution to this problem.

FEM originated in the field of structural analysis and was widely developed and exploited in the aerospace industries during the 1950s and 1960s. FEM involves dividing a physical system, such as a structure, into small sub-regions or elements. Each element is an essentially simple unit where its behaviour can be readily analysed. A large number of elements may be used to accommodate the complexities of an overall system. One attraction of FEM is the ease with which they can be applied to geometrically complicated systems. It can be applied to one-, two- as well as three-dimensional problems, such as plate, shell and solid bodies. In FEM, an actual continuum is replaced by an equivalent idealised structure composed of discretised elements connected together at a finite number of nodes. By incorporating a known constitutive law and an iterative procedure, the non-homogeneous and non-linear nature of the composite construction can be accounted for. FEM can easily simulate both material and geometrical nonlinearity, such as fracture and damage of structures.

4.2 FEMFAN

FEMFAN is a non-linear finite element program, developed in Nanyang Technological University, Singapore, by Dr. Toh Wee Siang in 2000 (Toh, W. S., 2000), and further modified by Dr. Huang Zhanfei in 2002 (Huang, Z. F., 2002), who extended the original FEMFAN 2-D into FEMFAN 3-D. FEMFAN is able to predict the structural response of a 2-D steel frame at ambient and elevated temperatures. In the ambient temperature analysis, a structure is subjected to monotonically increasing external load until failure takes place. In the elevated temperature analysis, a structure is subjected to increasing temperature but constant external load. FEMFAN is an elasto-plastic creep program, with solution based on tangent stiffness approach. It is capable of performing small-strain, large-displacement analysis. Stress-strain models that are incorporated belong to three categories; bi-linear, tri-linear and bi-linear with elliptical models. In the numerical analysis for this research on restrained steel columns, the EC3 (CEN, 2000b) material model is used in FEMFAN.

4.3 Comparison of FEMFAN Results with Experimental Results

This section presents the comparisons of experimental data with the predictions of FEMFAN. Both ambient and elevated temperature tests are considered. In the 2D FEM modelling, 8 elements made up the 1.5m long specimen and the extreme 2 ends were the knuckle bearings. An axial spring was used at one end to simulate the axial restraint condition. The temperature profile along the column was modelled into three sections; the middle section of 1m length and 2 end sections of 0.25m each. Temperature of the steel at these three sections followed the test closely, as discussed in Section 3.7. The geometric imperfection of the real column was represented in the model. The measured values of ambient temperature material properties, f_y and E_o^{20}, were also used. However, unavoidable friction at both ends of the column is not considered in FEA. The EC3 (CEN, 2000b) material model was

used in FEMFAN for elevated temperature analysis. Appendix D shows a sample FEMFAN results for a steel column test at elevated temperature.

4.3.1 Column Ambient Loading Test

Four columns subjected to buckling load capacity test at ambient temperature are examined here. These columns are marked as RS01, RS06, RS11 and RS16. Figures 4.1 and 4.2 show the test results as well as FEMFAN predictions. A graph of mid-height displacement against applied compressive load is plotted in Figure 4.1. Figure 4.2 shows the axial deformation-compressive load relationship. Table 4.1 lists the respective experimental and numerical buckling loads, and they are compared graphically in Figure 4.3.

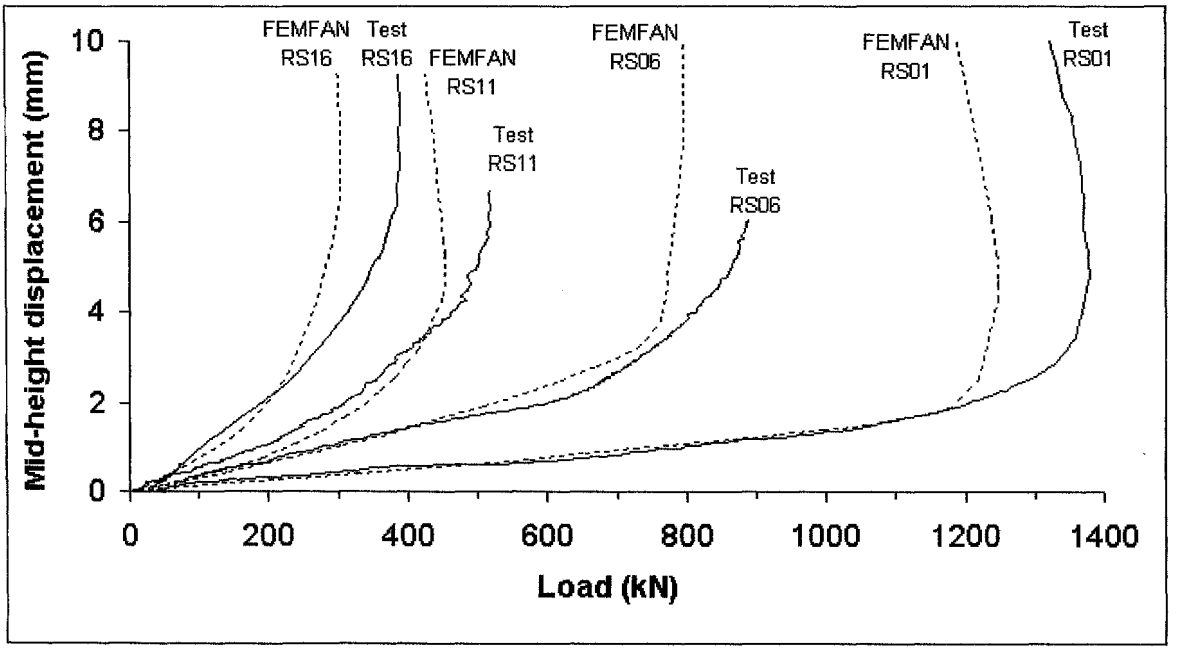

Figure 4.1 Experimental and FEMFAN results for mid-height displacement-compressive load relationship (ambient tests) (Series 1)

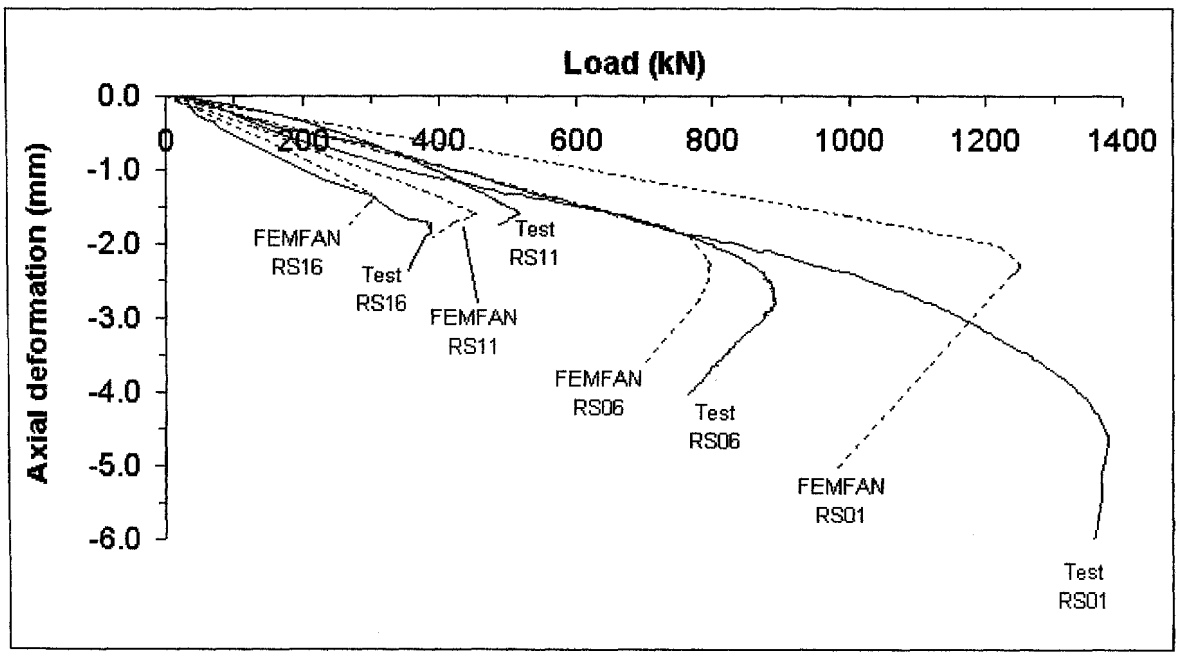

Figure 4.2 Experimental and FEMFAN results for axial deformation -compressive load relationship (ambient tests) (Series 1)

Table 4.1 Experimental and FEM buckling loads at ambient tests (Series 1)

Column Marking	Slenderness ratio, λ	Test Buckling Load, $P_{b,test}$ (kN)	FEMFAN Buckling Load, $P_{b,FEMFAN}$ (kN)	$\frac{P_{b,FEMFAN}}{P_{b,test}}$
RS01	45	1378.1	1248.0	0.91
RS06	55	892.3	795.9	0.89
RS11	81	518.9	453.5	0.87
RS16	97	388.4	303.8	0.78
			Mean:	0.86
			Standard Deviation (SD):	0.06
			Coefficient of Variation (COV):	0.07

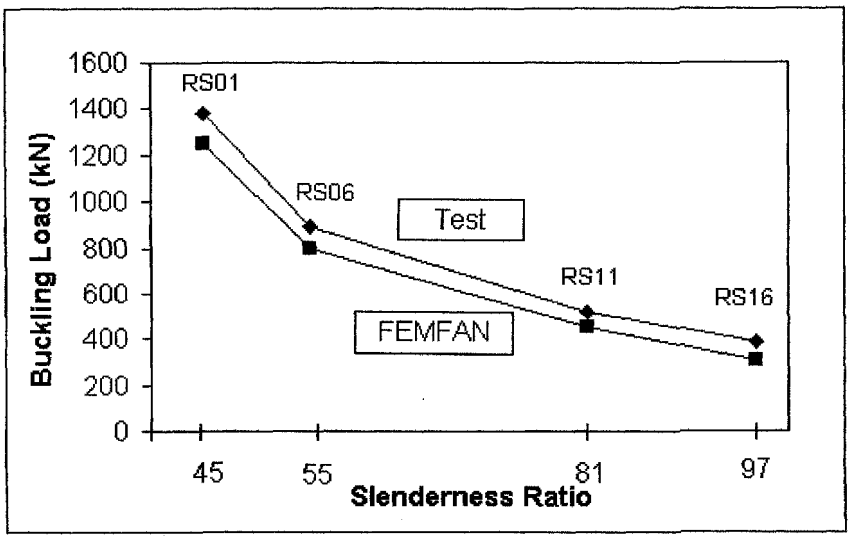

Figure 4.3 Experimental and FEM buckling loads at ambient tests (Series 1)

In Figure 4.1, FEMFAN had shown close prediction of the mid-height displacement for pre-buckling stage of all four columns in the ambient loading tests. In Figure 4.2, there is consistency in FEMFAN predictions of axial deformation when compared to the test results. For Columns RS06, FEMFAN predicted a very close axial deformation-compressive load relationship in the pre-buckling stage. For Columns RS01 and RS16, FEMFAN underestimated the axial deformation in the pre-buckling stage. And for Column RS11, FEMFAN had overestimated it.

Numerical predicted values for buckling loads are consistently lower than the experimental results (Table 4.1 and Figure 4.3). Table 4.1 computes the closeness of the buckling loads predicted by FEMFAN to those obtained in experiment. It results in a mean value of 0.86 for $P_{b,FEMFAN}/P_{b,test}$, with a standard deviation SD = 0.06 and a coefficient of variation COV = 0.07. This suggests that FEMFAN is conservative and reliable in predicting the buckling load for ambient temperature test, which is clearly demonstrated in Figure 4.3. FEMFAN's predictions are conservative; this is mainly due to two reasons. (1) The use of EC3 material model in the numerical analysis, which does not consider strain hardening behaviour of steel after yielding. This gives an underestimation of $P_{b,FEMFAN}$, especially for stocky

columns. (2) Negligence of friction at both ends of column tends to underestimate $P_{b,FEMFAN}$, especially for slender ones.

4.3.2 Column Elevated Temperature Test

Figures 4.4(a) to (d) show the mid-height displacement δ_{mid} versus temperature relationships for elevated temperature tests, from experiment and FEMFAN.

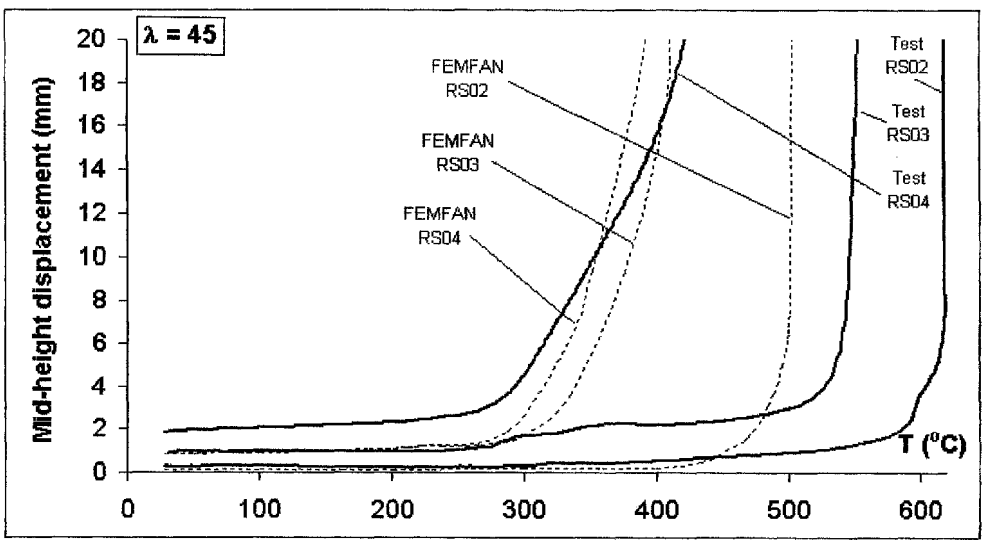

(a) Results for λ = 45

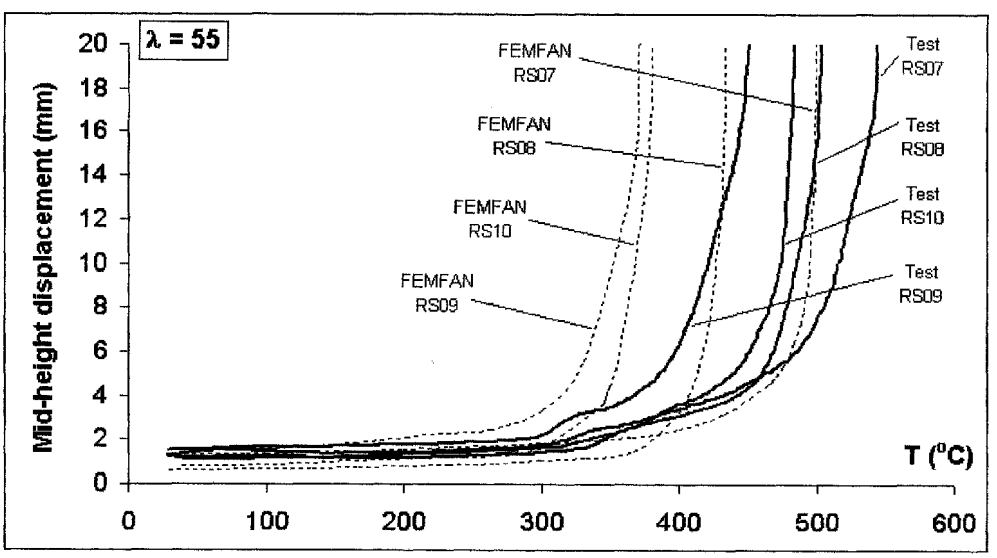

(b) Results for λ = 55

Figure 4.4 Experimental and FEMFAN results for mid-height displacement-temperature relationship (Series 1)

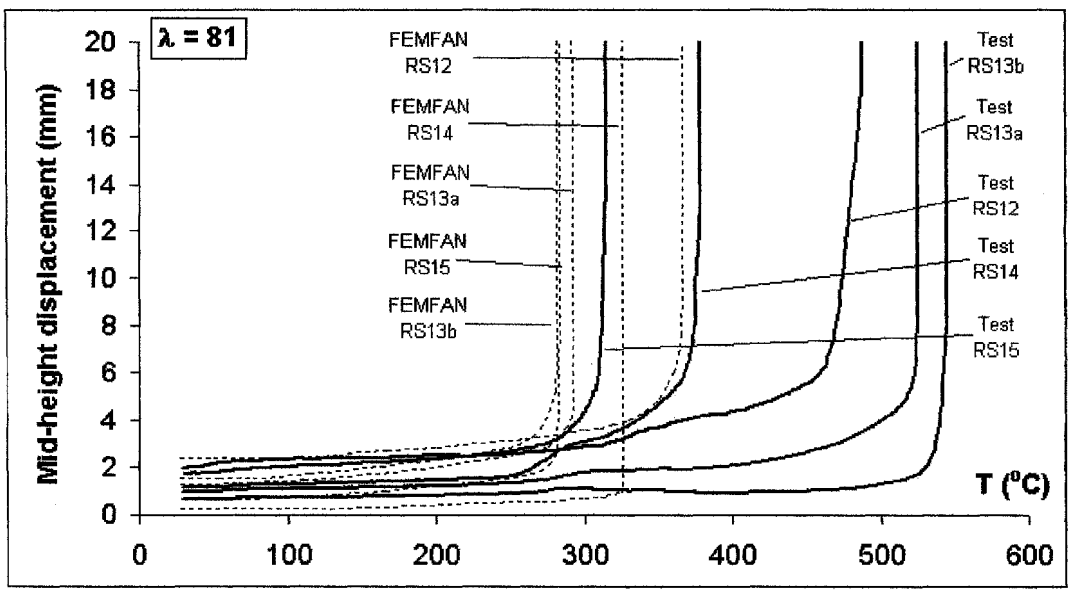

(c) Results for λ = 81

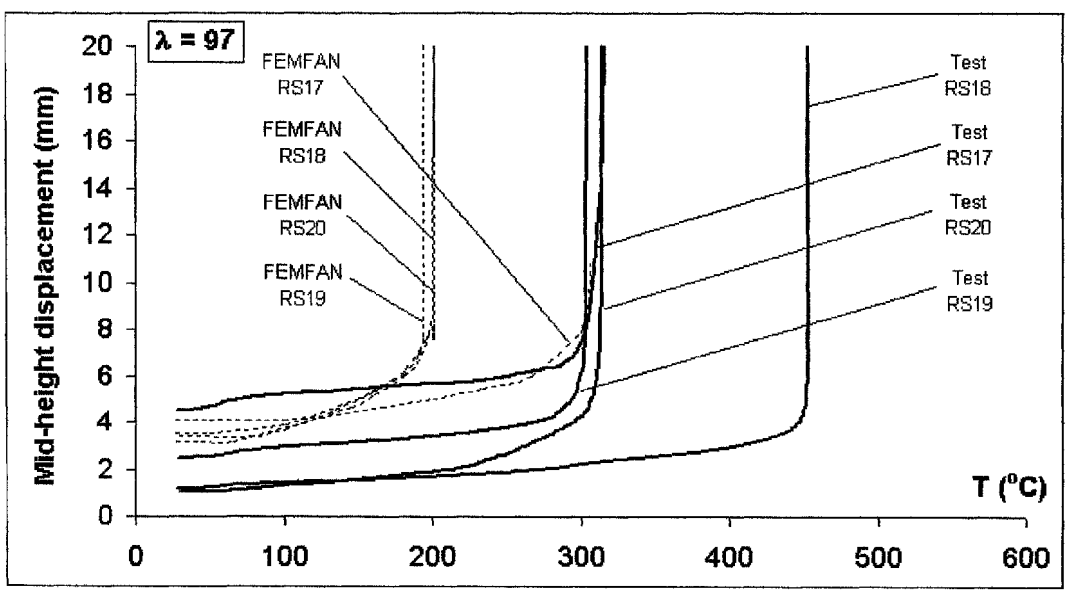

(d) Results for λ = 97

Figure 4.4 Experimental and FEMFAN results for mid-height displacement-temperature relationship (Series 1) (continued)

Initial displacements depend on the values of inevitable load eccentricities from fabrication and initial crookedness. The greater the initial imperfections, the greater are the initial lateral displacements. A general trend can be seen from the curves plotted. For the same slenderness, an increase in axial restraint ratio reduces the buckling temperature. This phenomenon is shown both experimentally and numerically. The results also show that for stockier columns, with λ = 45 and 55 (Figures 4.4 (a) and (b) respectively), column lateral deflection develops more gently than slender columns, with λ = 81 and 97 (Figures 4.4 (c) and (d) respectively). For the latter, a runaway lateral deflection is noted when the buckling temperature is reached. Obviously, this is owing to the more significant P-δ effect experienced by slender columns. FEMFAN predictions agreed well in this aspect.

There are a few unexpected test results. Columns RS10, RS13a, RS13b and RS18 are outside the norm of expectations. It is interesting to note that FEMFAN had predicted a similar trend for Column RS10, possibly due to the high initial curvature and load eccentricity. For the other three columns, i.e. RS13a, RS13b and RS18, FEMFAN did not show similar out-of-trend behaviour. From Table 3.2, the load eccentricity for Column RS18 was small, measured only 1.90mm, and its imperfection measurements along the length showed that the column was close to centrally loaded, therefore resulting in a higher buckling temperature. Columns RS13a and RS13b experienced some rotational restraint induced by friction at both end bearings during the tests (Figure 3.22 (a)). As such, column effective lengths were reduced and the developments of δ_{mid} were noticeably retarded, especially towards the end of heating. From Figures 4.4, these columns failed at a higher temperature than expected. Does it mean that a certain degree of rotational restraint is beneficial and it actually delays column buckling? More test information is required to quantify this statement. To reduce friction over the surface of bearings, the closely fit surfaces were filed and smoothened. A new series of steel columns were fabricated and tested under elevated temperature with axial restraint. The results will be discussed in the next chapter.

Development of P/P_o (ratio of total internal axial force to working load) is also examined. Figures 4.5(a) to (d) show the relationships between P/P_o and

temperature under the elevated temperature tests. Results from both experiment and numerical analyses are plotted for comparison. In these figures, P_o denotes the initial working load applied to individual columns.

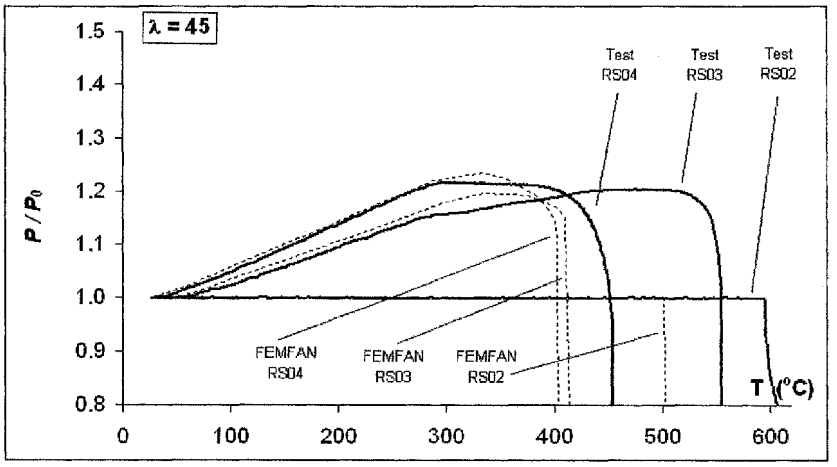

(a) Results for λ = 45

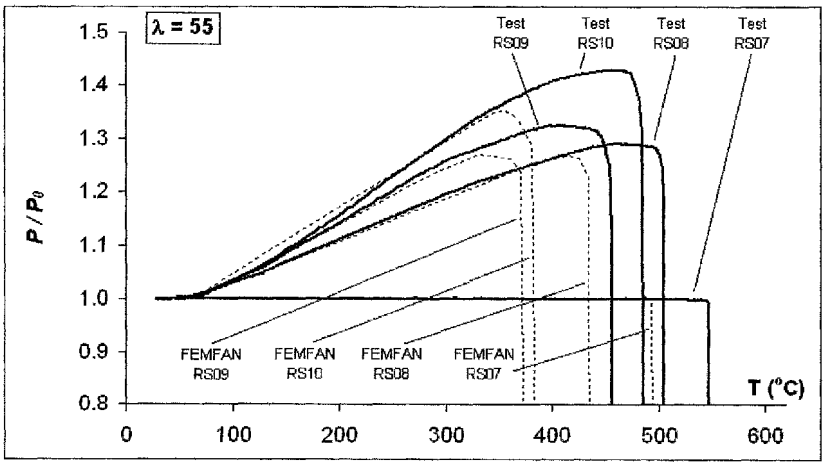

(b) Results for λ = 55

Figure 4.5 Experimental and FEMFAN results for P/P_o - temperature relationship (Series 1)

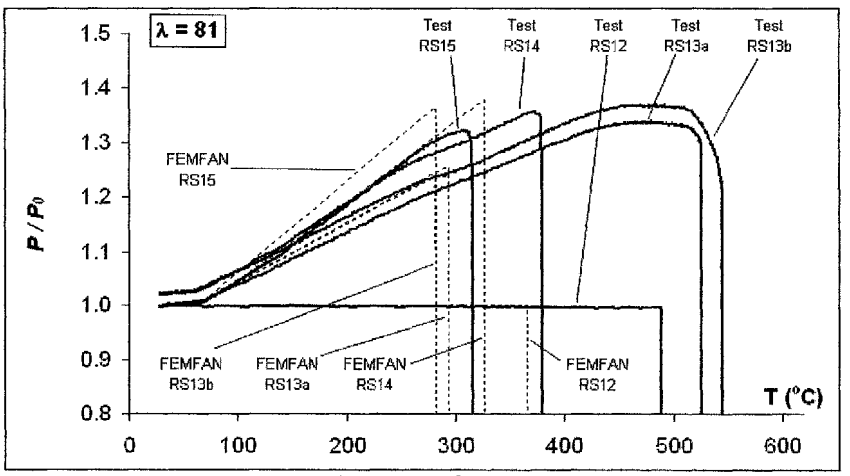

(c) Results for λ = 81

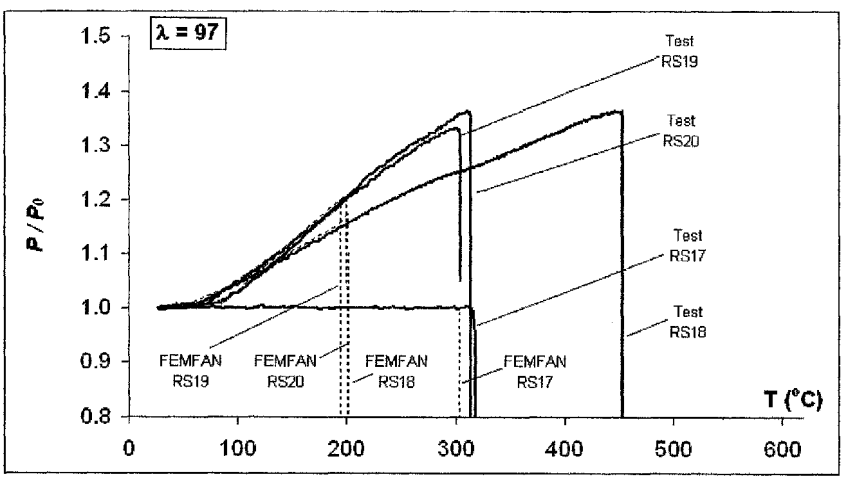

(d) Results for λ = 97

Figure 4.5 Experimental and FEMFAN results for P/P_o - temperature relationship (Series 1) (continued)

Restrained axial compressive force was built up in the steel columns due to axial expansion against the restraint system as temperature increased. At the beginning of every elevated temperature test, P/P_o started from unity. As temperature increased, axial restraint force developed and P/P_o increased. With the restraint force approaching a peak value after some time, P/P_o also reached a maximum value. This was then followed by an abrupt drop of P/P_o, implying that the column had buckled.

Figures 4.5 (a) to (d) show that for columns with similar slenderness ratios, one with a greater axial restraint ratio would experience a higher rate of increase in P/P_o under a rising temperature. This can be observed from the increasing gradient of the P/P_o graphs in the pre-buckling stage. The graphs also show that stocky columns would experience gradual shortening prior to buckling, whereas slender columns would buckle rapidly, almost instantaneously. For instance, Figure 4.5(a) shows that the stockiest columns at λ = 45 experienced a gentle peak before collapse or buckling occurred. On the other hand, the slender columns at λ = 97 in Figure 4.5(d) buckled immediately after reaching their maximum load ratio P/P_o. FEMFAN results show this behaviour as well. During the pre-buckling stage, the rate of increase in P/P_o with temperature predicted by FEMFAN for each column test is very close to experimental results, as illustrated in the figures by the closeness of the gradients for each test. This shows that FEMFAN is capable of modelling the increasing restraint force accurately.

Axial deformation plots in most cases show good agreement between FEMFAN and test results, in terms of the rate of axial expansion (Figures 4.6 (a) to (d)). This can be observed from the gradients of the graphs during the pre-buckling stage. This illustrates that the coefficient of thermal expansion used in FEMFAN modelling is reasonably accurate. Despite a few poor test results, a trend can be deduced from the plots. Axial deformation is greater for stocky columns loaded without axial restraint. With an increase in slenderness and/or axial restraint, the maximum axial deformation before buckling decreases. This indicates an inverse relationship between maximum axial deformation and slenderness or axial restraint. This is because a stocky column has high stiffness and bending is not as prominent as slender column. And with an increase in axial restraint, the build up of internal restrained force is faster, therefore decreasing the maximum axial deformation.

As discussed earlier, Columns RS10, RS13a, RS13b and RS18 are outside the norm. In Figures 4.4, 4.5 and 4.6, these 4 columns are observed to be outside the expected trend too, in terms of buckling temperatures.

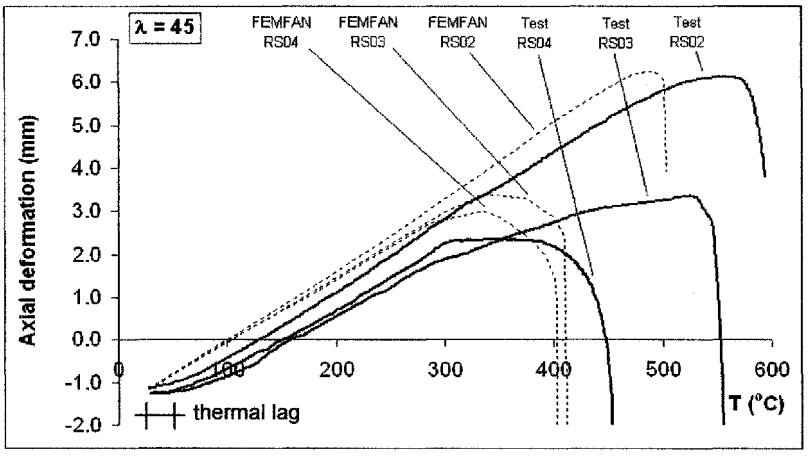

(a) Results for λ = 45

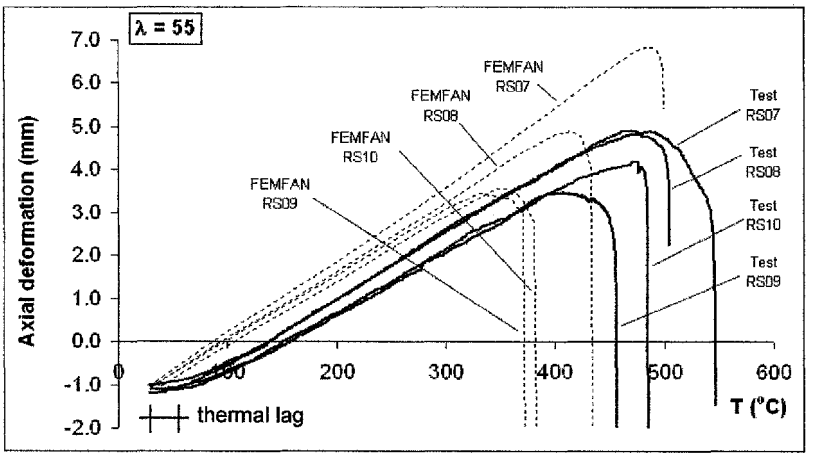

(b) Results for λ = 55

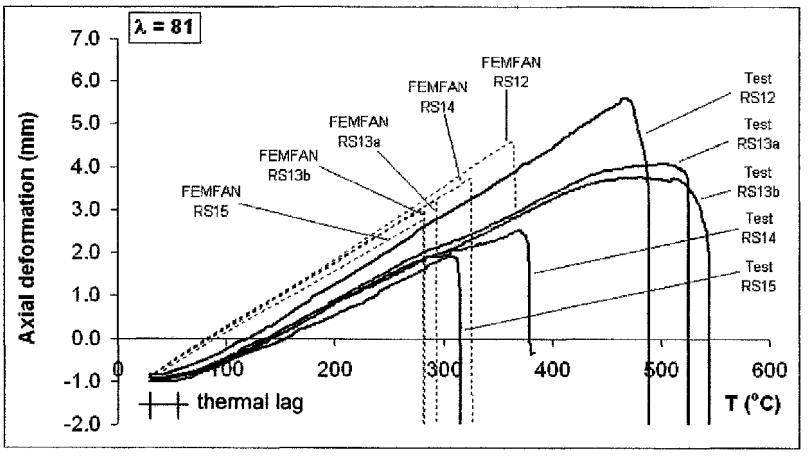

(c) Results for λ = 81

Figure 4.6 Experimental and FEMFAN results for axial deformation - temperature relationship (Series 1)

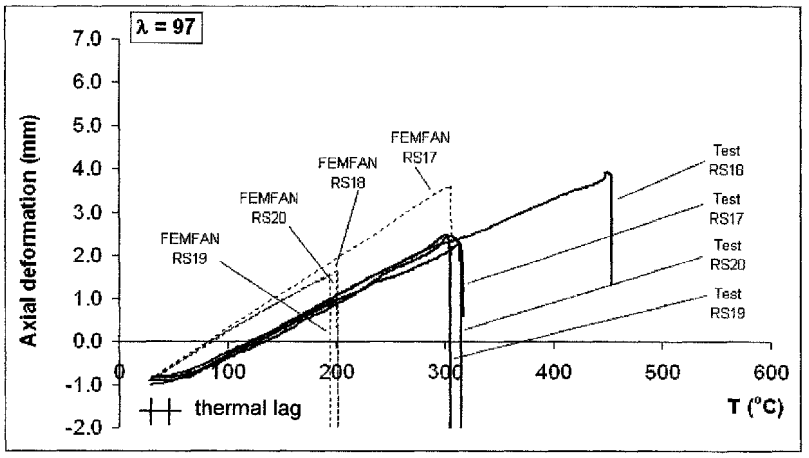

(d) Results for λ = 97

Figure 4.6 Experimental and FEMFAN results for axial deformation - temperature relationship (Series 1) (continued)

Table 4.2 summarises the buckling temperatures T_{cr} of the elevated temperature tests. FEMFAN has predicted lower values for T_{cr} than those obtained in experiments. This may be due to the choice of EC3 material model in FEMFAN analyses, the absence of friction and a slight overestimation of the stiffness of linear spring. In EC3, strain hardening is not considered, therefore giving conservative results. A mean value of 0.76 is found for $T_{cr,FEMFAN}$ / $T_{cr,test}$, with a standard deviation SD = 0.15 and a coefficient of variation COV = 0.20. There are some large discrepancies amongst the results (RS10, RS13a, RS13b and RS18), but in most cases the accuracy of FEMFAN is reasonably good. If these 4 columns are not included for comparison, out of the sixteen specimens, the results would yield a mean of 0.82 for $T_{cr,FEMFAN}/T_{cr,test}$, with a standard deviation SD = 0.10 and a coefficient of variation COV = 0.13. This increases the reliability of FEMFAN prediction.

Table 4.2 Experimental and FEM buckling temperatures (Series 1)

Column Marking	Slenderness Ratio, λ	Restraint Ratio, α_k	$T_{cr,test}$ (°C)	$T_{cr,FEMFAN}$ (°C)	$\frac{T_{cr,FEMFAN}}{T_{cr,Test}}$
RS02	45	0.00	595.0	503.3	0.85
RS03	45	0.08	554.6	415.7	0.75
RS04	45	0.11	452.8	402.3	0.89
RS07	55	0.00	545.8	494.7	0.91
RS08	55	0.08	504.7	437.6	0.87
RS09	55	0.11	455.0	370.4	0.81
RS10	55	0.14	483.3	380.4	0.79
RS12	81	0.00	488.2	365.3	0.75
RS13a	81	0.08	525.2	293.1	0.56
RS13b	81	0.08	544.4	281.2	0.52
RS14	81	0.11	379.1	326.1	0.86
RS15	81	0.14	315.7	281.6	0.89
RS17	97	0.00	317.3	306.0	0.96
RS18	97	0.08	453.1	201.1	0.44
RS19	97	0.11	304.7	194.0	0.64
RS20	97	0.14	313.9	199.7	0.64
				Mean:	0.76
				Standard Deviation (SD):	0.15
				Coefficient of Variation (COV):	0.20

4.4 Southwell Plot

In this series of steel column tests, all the columns failed through loss of stability due to flexural buckling. When flexural instability governs, column capacity is given by the well-known Euler buckling load (Trahair *et al*, 2001):

$$P_e = \frac{\pi^2 EI}{L_e^2} \tag{4.1}$$

where

P_e is the Euler load (kN);

EI is the flexural rigidity of the compression member (kNmm^2);

L_e is the effective length (mm).

The main deficiency of the Euler Theory is that it assumes that the strut is perfectly straight and concentrically loaded, which in reality is virtually impossible to achieve. Real structural members have small initial curvatures. The buckling behaviour of the hypothetical straight members must therefore be interpreted as the limiting behaviour of real members with infinitesimally small initial curvatures. The initial curvature of the real member causes it to bend from the commencement of application of the axial load, and this increases the maximum stress in the member.

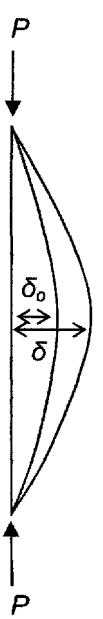

Figure 4.7 Column displacement

Perry Robertson came out with an analysis to predict the behaviour of a column with an initial curvature (Figure 4.7). He assumed that a column had the initial shape of a sine wave with amplitude δ_o. Under the action of an axial load P, it was found that the increase in magnitude of deflection was dependent on the relationship between the axial load P and Euler load P_e, as follows:

$$\frac{\delta}{\delta_o} = \frac{P/P_e}{1-P/P_e} \tag{4.2}$$

The simple load-deflection relationship of Equation 4.2 is the basis of the Southwell plot technique for extrapolating the elastic buckling load from test measurements. Equation 4.2 can be rearranged as:

$$\frac{\delta}{P} = \frac{1}{P_e}\delta + \frac{\delta_o}{P_e} \tag{4.3}$$

The linear relation between δ/P and δ can be obtained by plotting experimental measurements. A best-fit straight line is drawn. The reciprocal of the slope of this line gives an experimental estimate of the Euler load P_e. An estimate of the magnitude δ_o of the initial crookedness can also be determined from the intercept on the horizontal axis. This is the Southwell plot.

Southwell plots were conducted for the steel column tests at ambient temperature, i.e. Columns RS01, RS06, RS11 and RS16. In its present form (Equation (4.2)), it cannot be applied to columns tested at elevated temperatures, since it describes a relationship between δ and P. Test data from the experiments were used to plot the best-fit straight lines. Figures 4.8 (a) to (d) show the respective plots.

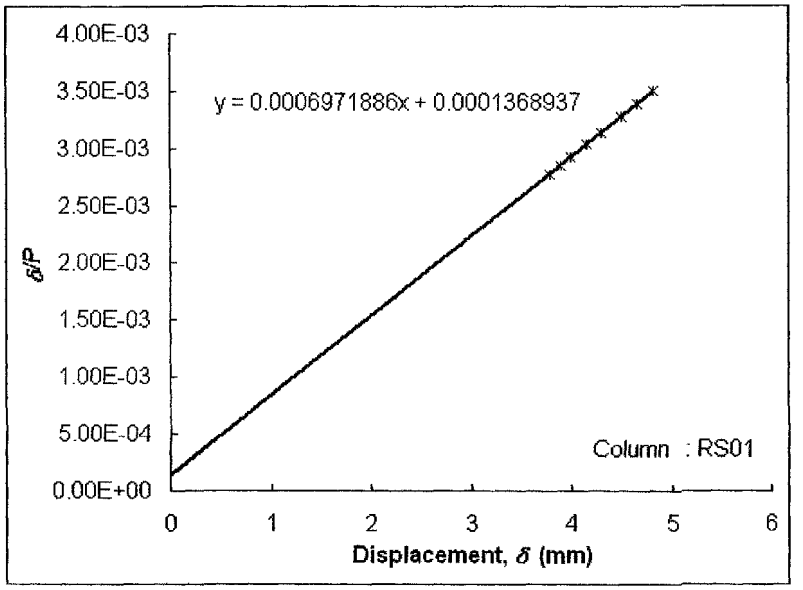

(a) Steel Column RS01

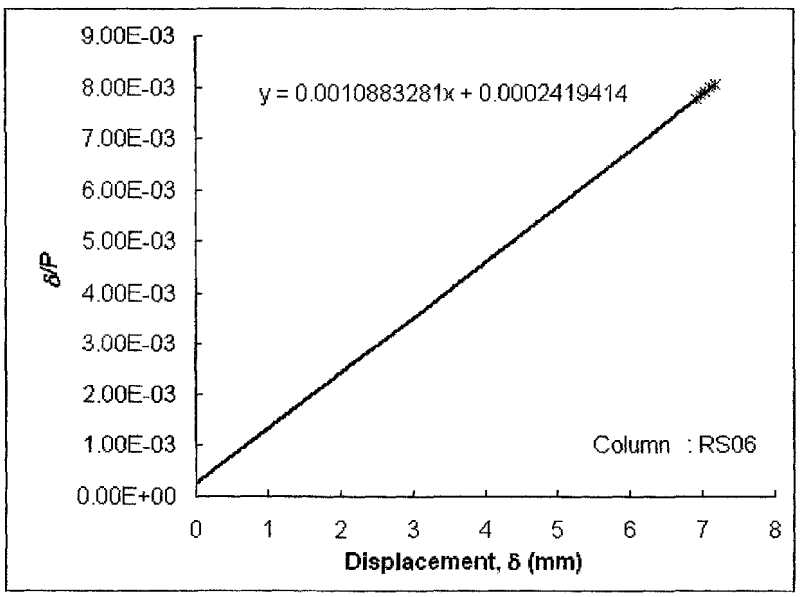

(b) Steel Column RS06

Figure 4.8 Southwell plots for steel column ambient tests (Series 1)

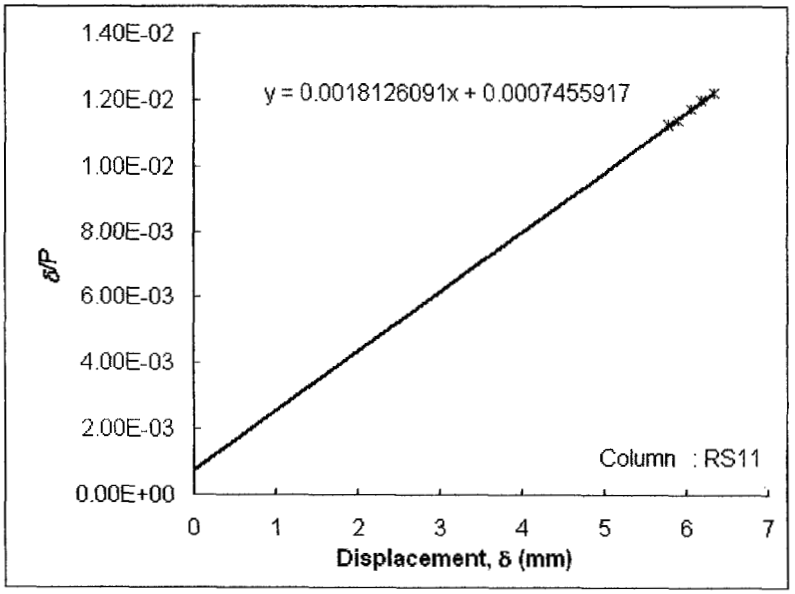

(c) Steel Column RS11

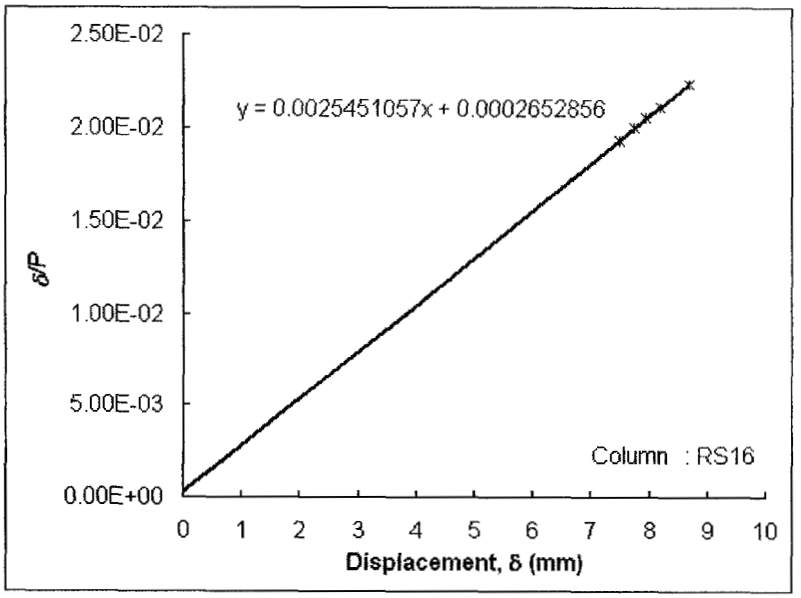

(d) Steel Column RS16

Figure 4.8 Southwell plots for steel column ambient tests (Series 1) (continued)

Table 4.3 Critical loads and values of initial crookedness from tests and Southwell plots (Series 1)

Column Marking	$P_{cr,test}$ (kN)	$P_{e,Southwell}$ (kN)	$\frac{P_{e,Southwell}}{P_{cr,test}}$	$\delta_{o,test}$ (mm)	$\delta_{o,Southwell}$ (mm)	$\frac{\delta_{o,Southwell}}{\delta_{o,test}}$
RS01	1378.1	1434.3	1.04	3.16	0.20	0.06
RS06	892.3	918.8	1.03	4.58	0.22	0.05
RS11	518.9	551.7	1.06	1.18	0.41	0.35
RS16	388.4	392.9	1.01	0.84	0.10	0.12

Euler load P_e and initial crookedness δ_o obtained from the plots are presented in Table 4.3. The test measurement of the initial crookedness, $\delta_{o,test}$, could be obtained from Table 3.2 from the summation of initial load eccentricity e and mid-height curvature i_2. Buckling loads from tests are also shown in Table 4.3. It is observed that the values of Euler loads produced by Southwell plots are very close to the test buckling loads, with ratios of $P_{e,Southwell}$ / $P_{cr,test}$ ranging from 1.01 to 1.06. This shows that Southwell plot was an accurate tool for predicting buckling loads. However, the values of initial crookedness were quite different from those measured. Does it indicate that the measured initial crookedness was inaccurate, and the value from Southwell plot was actually the true one?

To verify the reliability of the initial crookedness obtained from Southwell plot, one case study was carried out on Column RS06. The value of initial crookedness from Southwell plot for RS06 was used in FEMFAN. One assumption was that the initial curvature of the column followed the shape of a sine wave. Results are shown in Figures 4.9 and 4.10. Figure 4.9 shows the comparison of FEMFAN and test results for mid-height displacement. There is little agreement from FEMFAN results with the test in the development of the mid-height displacement. Figure 4.10 shows the comparison of FEMFAN and test results for axial deformation-compressive load relationship. In this case, FEMFAN predicted reasonably well for the axial deformation development. From both graphs, a runaway deflection of the curve was

observed at the instant when the compressive load was 1090kN. This is the buckling load predicted by FEM. Compared to the test buckling load of 892.3kN, FEMFAN had overestimated the buckling load by 22%. The author contends that the value of initial crookedness obtained from Southwell plot was much lower due to the presence of rotational restraint arising from friction at column ends. This was not implemented in the FEA in this case study. This effect of friction will be investigated in the next section.

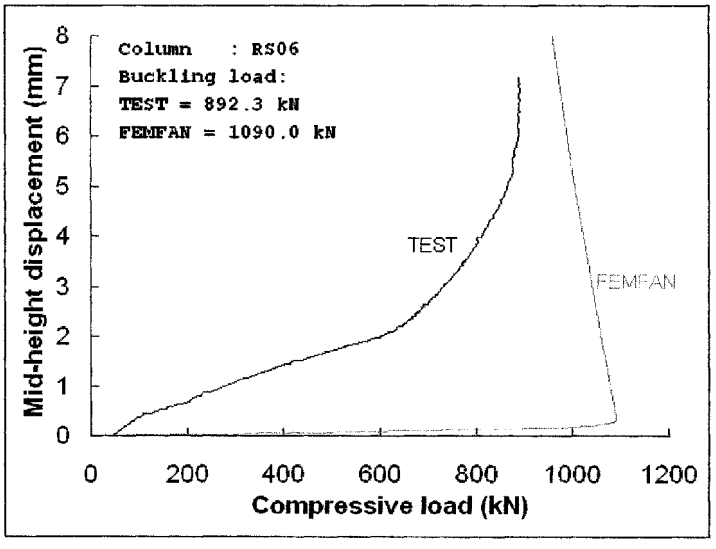

Figure 4.9 Case study on Column RS06 mid-height displacement-compressive load relationship

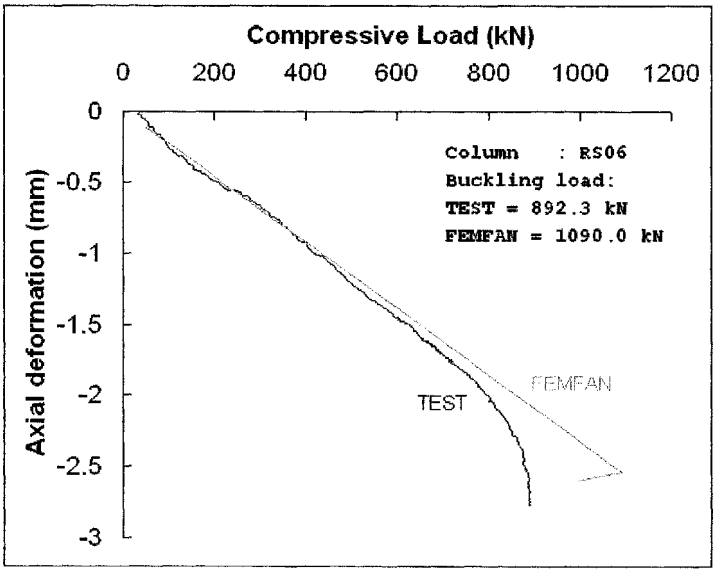

Figure 4.10 Case study on Column RS06 axial deformation-compressive load relationship

4.5 Investigation on the Effect of Friction

In Section 4.3.2, it was postulated that the presence of undesirable friction on the knuckle bearing surfaces had caused an increase in the buckling temperature, T_{cr}, especially in the case of stocky columns. This friction mobilised a certain degree of rotational restraint caused by thermal expansion of the column. A case study was carried out to verify this hypothesis. Column RS04 was chosen. From Figures 4.5 (a) and 4.6 (a), Column RS04 experienced a plateau in its curves for P/P_o against temperature and axial deformation against temperature, showing that there was rotational friction in the test. In the case study, a small amount of rotational restraint was applied to both end bearings in RS04 input file for FEMFAN. This rotational restraint stiffness, K_R was taken as:

$$K_R = \frac{0.2rP}{\theta} \tag{4.4}$$

where

the coefficient of friction between steel contact surfaces is taken as 0.2

K_R = rotational restraint stiffness (kNm/rad)

r = radius of cylinder block (m)

P = total internal force (kN)

θ = angle of rotation (rad)

Appendix A illustrates a drawing showing the parameters used to find K_R. Test values for P, r and θ were used to obtain K_R. The results are shown in Figures 4.11 to 4.13. Figures 4.11 (a), 4.12 (a) and 4.13 (a) show the graphs for test and FEMFAN without incorporation of rotational restraint. Figures 4.11 (b), 4.12 (b) and 4.13 (b) show the graphs for test and FEMFAN with rotational restraint applied.

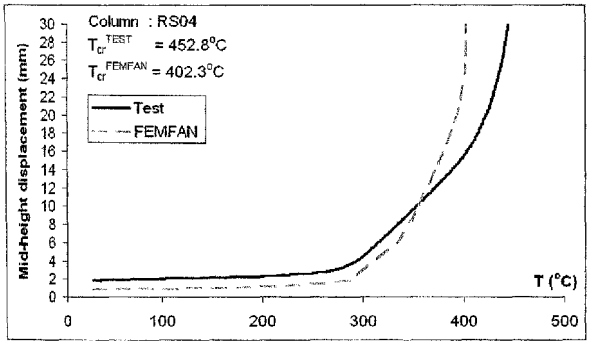

(a) Without rotational restraint

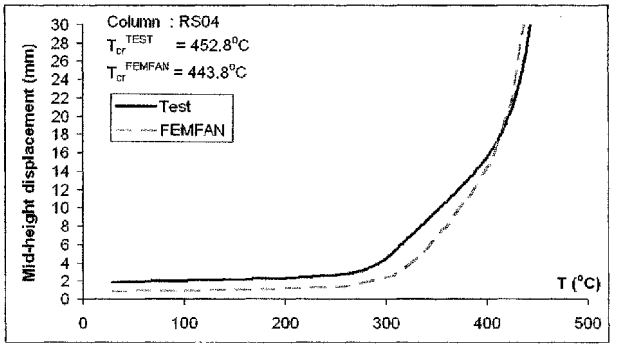

(b) With rotational restraint

Figure 4.11 Case study on effect of rotational restraint on mid-height displacement-temperature relationship

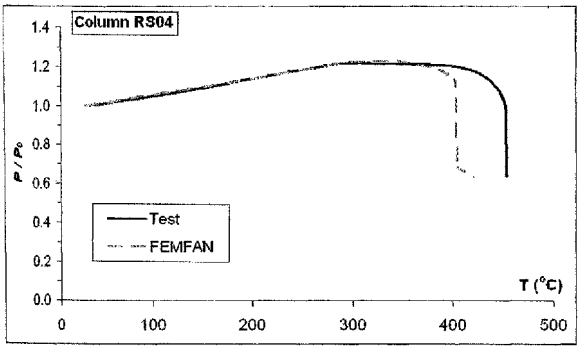

(a) Without rotational restraint

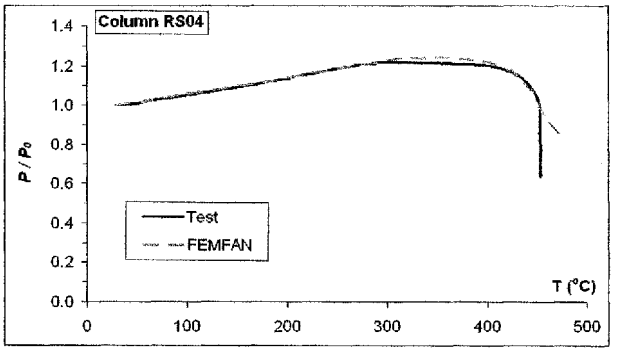

(b) With rotational restraint

Figure 4.12 Case study on effect of rotational restraint on P/P_o – temperature relationship

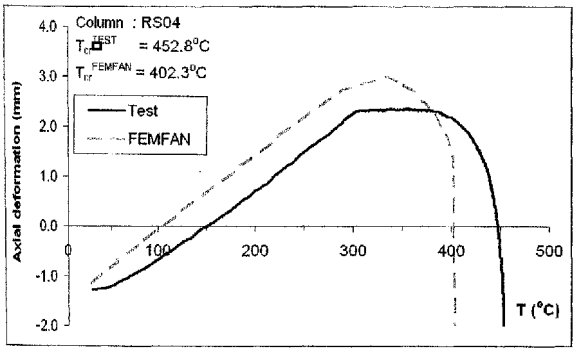

(a) Without rotational restraint

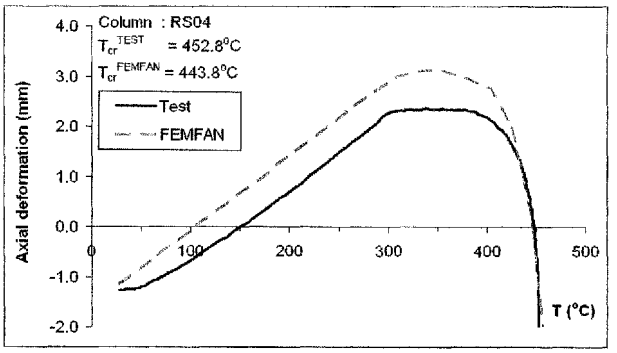

(b) With rotational restraint

Figure 4.13 Case study on effect of rotational restraint on axial deformation-temperature relationship

Rotational restraint extended the buckling temperature in the FEMFAN prediction, as shown in Figures 4.11 to 4.13, from a previous value of 402.3°C to a higher value of 443.8°C, which was very close to the test results of 452.8°C. Furthermore, the shapes of the graphs predicted in FEMFAN for all the three relationships; mid-height displacement, P/P_o and axial deformation (Figures 4.11 (b), 4.12 (b) and 4.13 (b)), followed closely to the test behaviour, when compared to those without rotational restraint (Figures 4.11 (a), 4.12 (a) and 4.13 (a)). In Figure 4.11 (b), rotational restraint caused the deflection of the graph to run at a gentler slope. And in Figures 4.12 (b) and 4.13 (b), FEMFAN also illustrated a plateau on each graph due to the effect of rotational restraint. This case study shows that a small amount of rotational restraint is beneficial, as it will delay buckling when the column has reached its stability limit. It also shows that there was some rotational restraint present in the steel column test, due to thermal expansion of column.

4.6 Investigation on the Effect of Initial Crookedness

In Section 4.3.2, Figures 4.4 (a) to (d), it was observed that the initial mid-height displacements for some columns in the FEA predictions did not start off with the same values as test results, although the initial crookedness input into FEA were those measured from tests. This brought up a question; was initial crookedness an important factor contributing towards the fire resistance of steel column?

A case study was carried out to answer this question. Column RS20 was chosen for this purpose. From Figures 4.4 (d), this column showed an initial mid-height displacement of 1.06mm in the test, and the initial FEM analysis mid-height displacement was 3.39mm, when using test measurements as the input data. FEA was carried out again with a smaller initial mid-height displacement of 1.06mm, and the initial crookedness of the column was assumed to follow the shape of a half-sine curve.

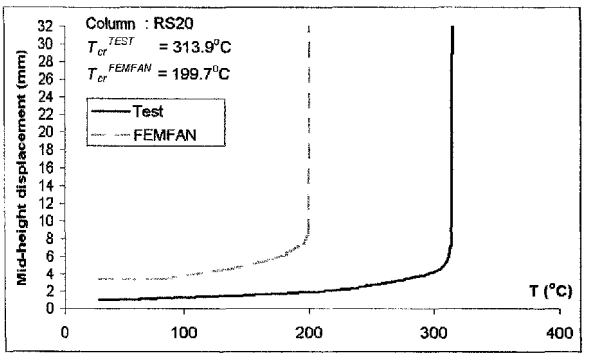

(a) Without reducing initial crookedness

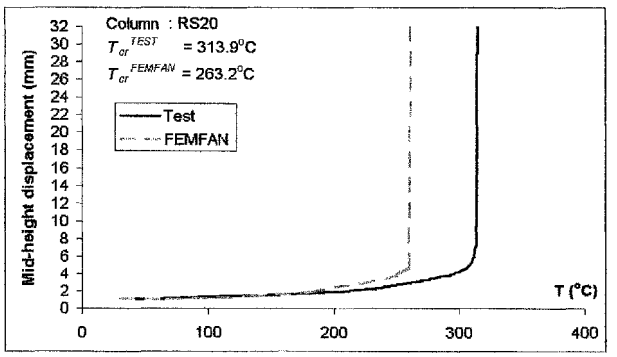

(b) With initial crookedness reduced in FFA

Figure 4.14 Case study on effect of initial crookedness on mid-height displacement-temperature relationship

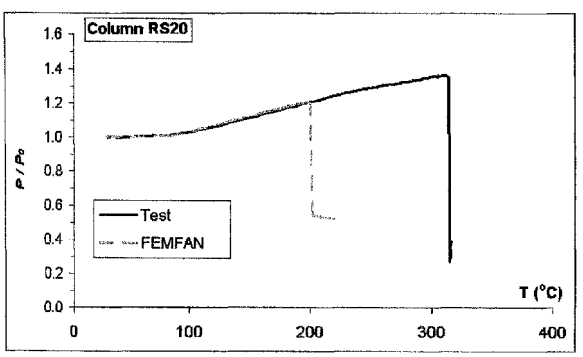

(a) Without reducing initial crookedness

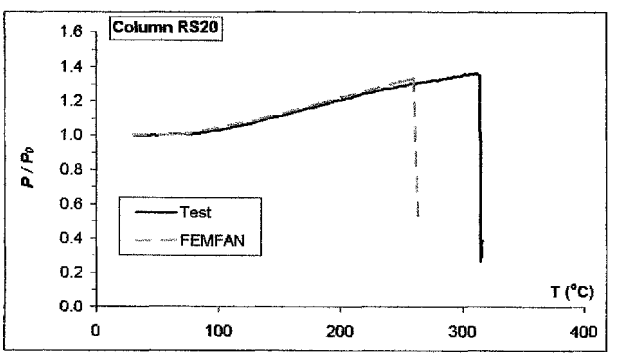

(b) With initial crookedness reduced in FFA

Figure 4.15 Case study on effect of initial crookedness on P/P_o – temperature relationship

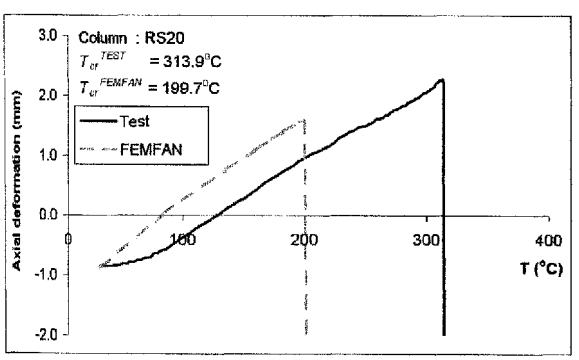

(a) Without reducing initial crookedness

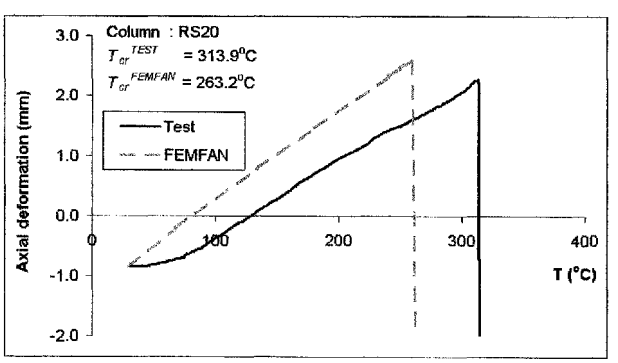

(b) With initial crookedness reduced in FFA

Figure 4.16 Case study on effect of initial crookedness on axial deformation-temperature relationship

Figures 4.14, 4.15 and 4.16 show the effect of initial crookedness on fire resistance of steel column. From the graphs, FEA showed that with a decrease in initial mid-height displacement δ_o, the buckling temperature T_{cr} was increased from a previous prediction of 199.7°C to 263.2°C, which was closer to the test results of 313.9°C by 20% (from a previous $T_{cr,FEMFAN} / T_{cr,Test} = 0.64$ to $T_{cr,FEMFAN} / T_{cr,Test} = 0.84$). With the adjustment of δ_o, there was better agreement in FEMFAN curve for mid-height displacement-temperature relationship with test (Figures 4.14 (a) and (b)). The rise of P/P_o-temperature curve for FEMFAN prediction fitted perfectly well before and after adjustment of initial crookedness in FEA (Figures 4.15 (a) and (b)). This shows that a change in initial crookedness does not affect the increase of total internal axial force due to axial restraint. This is also shown in Figures 4.16 (a) and (b), where the gradient of axial deformation-temperature curve was unaffected by the change in initial crookedness.

4.7 Test and FEMFAN Observations

From the test results as well as finite element analyses, certain observations can be drawn:

Application of axial restraint governed the amount of additional axial forces generated in heated columns, and also the buckling temperature. Coefficient of thermal expansion was one of the most significant parameters. This value dictated the amount of thermal expansion that occurred in the column, and governed the amount of axial force generated throughout the test.

It was crucial to ensure that the material properties of steel were modelled as accurately as possible. Results from tensile coupon tests at ambient temperature were used in FEMFAN analyses. These values controlled the point of initial collapse of the columns. If nominal values were used, the model would underestimate column failure temperature.

The effects of geometric imperfections were essentially important in modelling the tests in FEMFAN. Experimental measurement of load eccentricities, column curvatures and dimensions were used in numerical analysis. It should be noted that the load eccentricities were measured from the centres of the knuckle bearings to the web of the column on ground, and not from the horizontal loaded position. Therefore, there were inaccuracies in the measurement of initial load eccentricities, resulting in inconsistency of mid-height displacement at the beginning of heating between test and FEA results (Figures 4.4 (a) to (d)). This indicates that initial load eccentricities as well as crookedness play an important part in finite element analysis.

In FEMFAN, due to thermal expansion to fill up the gap between contact parts of the test rig and specimen ends, a time lag is included for analysis. This time lag, ranging between 0 and 10minutes, was found from the test results, defined as the time required for axial restraint to be mobilised. By putting in a time lag in the FE model, the linear generation of restraint force did not begin until an appropriate temperature was reached. This method gave better predictions to test results in terms of P/P_o versus temperature relationship.

Results showed that slender columns buckled immediately after reaching the peak force and collapsed rapidly through loss of stability. Stocky columns collapsed gradually upon hitting a peak and might plateau off for a moment.

Unrestrained columns showed a decrease in buckling temperature as slenderness increased. Restrained columns also showed a decrease in buckling temperature as slenderness increased. This was the exact opposite of that commented by Hoffend (1977, 1980 and 1983), in which he stated that slender columns had higher critical temperature than the more stocky ones. This remark was incorrect, as it is shown in ECCS (1983) that at any particular temperature, the critical stress, σ_{cr}, of steel decreases as slenderness ratio increases. ECCS also shows that the critical stress of steel decreases as temperature increases. This simply implies that unrestrained steel columns will have a lower buckling temperature as slenderness increases.

Overall the variation of the two parameters considered in this study produced considerable changes in the column buckling temperatures; they were axial restraint ratio and slenderness ratio. It must be highlighted that the interaction of these two parameters produces considerable variation in column response.

In this series of tests under transient state heating conditions, the friction at the end bearings caused some errors. This friction induced undesirable rotational restraint in the test and reduced the column effective length. It was observed that rotational restraint delayed column buckling. The bearings were machined to reduce friction over their contact surfaces, and a new series of steel columns were fabricated and tested under the same conditions. Their results are discussed in the next chapter.

CHAPTER FIVE

Experimental Testing on Steel Columns - Series 2

5.1 Series 2 Steel Column Test Programme

As discussed in Chapter 4, unexpected results arose from some column tests. Some columns were suspected to have experienced a certain amount of rotational restraint induced by friction at both end bearings during test. This would reduce the column effective length and slow down the development of δ_{mid}, especially towards the end of heating. Did rotational friction result in an artificially high failure temperature for the column? Did it delay column buckling? To answer some of these questions, the end bearings were machined at the joints to reduce frictional forces. With this repaired bearing, a new series of steel columns were tested under the same set-up. Similar parameters were studied; slenderness ratio and axial restraint ratio.

Table 5.1 shows the column labels used for this series of test, with a variation of axial restraint ratio α_K and slenderness ratio λ. Three steel sections were investigated here, with slenderness ratios λ = 55, 81 and 97. For each of these sections, there was an axial load capacity test conducted at ambient temperature, to obtain the respective ultimate load capacity. In addition, there were two transient tests conducted at elevated temperature with axial restraint ratio α_K = 0.08 and 0.14.

Table 5.1 Test parameters (Series 2)

Slenderness Ratio, λ	Ambient Test	Elevated Temperature Test	
		Axial restraint ratio, α_K	
		0.08	0.14
55	NRS06	NRS08	NRS10
81	NRS11	NRS13	NRS15
97	NRS16	NRS18	NRS20

The applied axial load ratio used in the transient state testing was as before, fixed at 50% of the section's ultimate capacity. This load capacity was achieved in the ambient load capacity test. Test apparatus, instrumentations, set-up and procedure remained unchanged and were similar to the first series of steel column test programme, as discussed in Chapter 3.

5.2 Test Specimens

Table 5.2 shows a summary of Series 2 steel column, with details such as actual load eccentricities e, section dimensions (width b, height H, flange thickness T_f and web thickness t_w) and the initial crookedness along column lengths (i_1, i_2 and i_3 denote imperfections at $L/4$, $L/2$ and $3L/4$, respectively) measured prior to testing.

Table 5.2 Specimen data (Series 2)

No. (1)	Section (2)	λ (-) (3)	e (mm) (4)	H (mm) (5)	B (mm) (6)	T_f (mm) (7)	t_w (mm) (8)	i_1 (mm) (9)	i_2 (mm) (10)	i_3 (mm) (11)
NRS06	UB203x133x25	55	1.43	204.2	133.9	7.3	5.40	0.0	0.1	0.1
NRS08	UB203x133x25	55	3.51	204.0	133.7	7.4	5.40	-0.4	0.2	0.3
NRS10	UB203x133x25	55	3.24	204.4	133.8	7.5	5.40	-0.2	0.4	0.2
NRS11	UB152x89x16	81	2.19	154.2	89.6	7.1	5.16	-0.4	-0.1	0.0
NRS13	UB152x89x16	81	0.65	154.0	90.1	7.0	5.16	-0.3	0.2	0.2
NRS15	UB152x89x16	81	6.29	154.1	89.9	7.1	5.16	-0.9	0.2	0.1
NRS16	UB127x76x13	97	4.37	128.4	77.1	7.2	4.36	-0.2	-0.5	0.1
NRS18	UB127x76x13	97	4.16	128.3	76.8	7.2	4.36	-0.3	0.0	0.0
NRS20	UB127x76x13	97	2.57	128.3	76.9	7.3	4.36	-0.7	0.3	0.3

5.3 Material Properties

Table 5.3 summarises the material properties of Series 2 test specimens. Values of elastic modulus ranged from 205 to 220 GPa. It was noticed that the ultimate strength of this series was much lower (in the range of 300 N/mm^2) than those in Series 1, which was at least 473 N/mm^2 (Table 3.3).

Table 5.3 Material properties of column specimens (Series 2)

Section	Column Marking		Elastic Modulus (kN/mm^2)	Yield Strength (N/mm^2)	Ultimate Strength (N/mm^2)
UB 203×133×25	NRS06, NRS08, & NRS10	Flanges	225	300	344
		Web	215	330	359
		Equivalent	**220**	**310**	**349**
UB 152×89×16	NRS11, NRS13, & NRS15	Flanges	215	295	356
		Web	215	320	368
		Equivalent	**215**	**305**	**360**
UB 127×76×13	NRS16, NRS18, & NRS20	Flanges	200	320	367
		Web	210	340	375
		Equivalent	**205**	**325**	**369**

5.4 Experimental Axial Restraint

Values of experimental restraint stiffness obtained from Series 2 steel column testing are shown in Table 5.4. Figures 5.1(a) to (f) plots the imposed restraint force against the mid-span deflection of the restrained beam for each restrained elevated temperature test. The actual axial restraint stiffnesses were calculated from the gradients of the linear graphs. The restraint ratios achieved in Series 2 experimentally were very close to those in Series 1 for each of the corresponding tests.

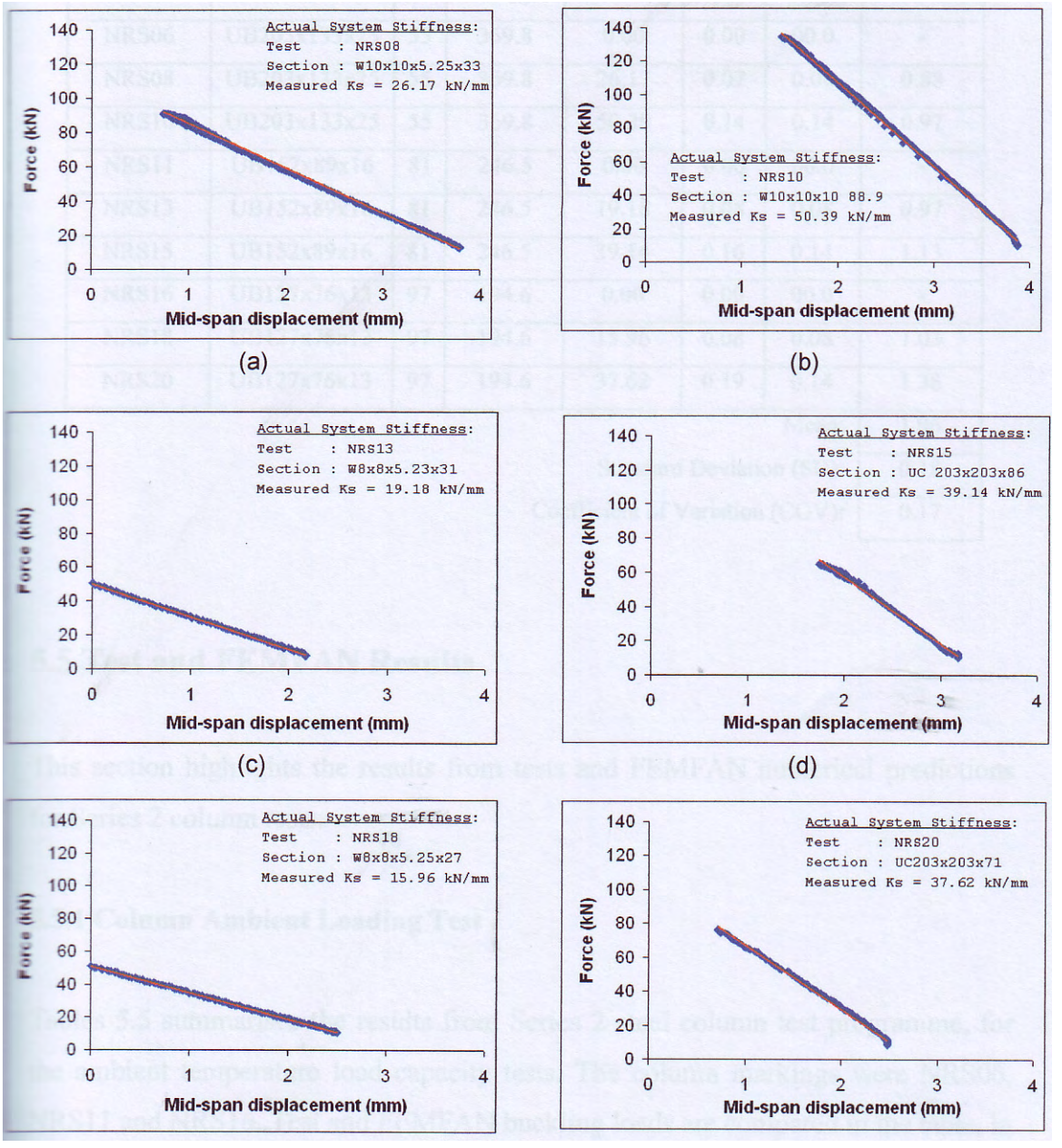

Figure 5.1 Force-displacement relationships of restraint beams (Series 2)

Table 5.4 Restraint ratio summary (Series 2)

Column Marking	Section	λ	K_c (kN/mm)	$K_{s,test}$ (kN/mm)	$\alpha_{k,test}$	$\alpha_{k,design}$	$\frac{\alpha_{k,test}}{\alpha_{k,design}}$
NRS06	UB203x133x25	55	369.8	0.00	0.00	00.0	-
NRS08	UB203x133x25	55	369.8	26.17	0.07	0.08	0.88
NRS10	UB203x133x25	55	369.8	50.39	0.14	0.14	0.97
NRS11	UB152x89x16	81	246.5	0.00	0.00	00.0	-
NRS13	UB152x89x16	81	246.5	19.18	0.08	0.08	0.97
NRS15	UB152x89x16	81	246.5	39.14	0.16	0.14	1.13
NRS16	UB127x76x13	97	194.6	0.00	0.00	00.0	-
NRS18	UB127x76x13	97	194.6	15.96	0.08	0.08	1.03
NRS20	UB127x76x13	97	194.6	37.62	0.19	0.14	1.38
						Mean:	1.06
						Standard Deviation (SD):	0.18
						Coefficient of Variation (COV):	0.17

5.5 Test and FEMFAN Results

This section highlights the results from tests and FEMFAN numerical predictions for Series 2 column tests.

5.5.1 Column Ambient Loading Test

Tables 5.5 summarises the results from Series 2 steel column test programme, for the ambient temperature load capacity tests. The column markings were NRS06, NRS11 and NRS16. Test and FEMFAN buckling loads are compared in the table, in terms of the ratio $P_{b,FEMFAN}/P_{b,test}$. Series 2 columns had lower buckling load capacities than corresponding columns in Series 1. Two factors might have caused this. First, it might be due to the minimisation of rotational friction at the knuckle bearings used in experiment. Second, lower yield and ultimate strengths of Series 2 columns might have induced earlier failure. FEMFAN predictions were very close to test for Columns NRS11 and NRS16, but on the high side for Column NRS06.

This is shown graphically in Figure 5.2. The results have a mean value of 1.05 for $P_{b,FEMFAN}/P_{b,test}$, with a standard deviation SD = 0.16 and a coefficient of variation COV = 0.15.

Table 5.5 Experimental and FEM buckling loads (Series 2)

Column Marking	Slenderness ratio, λ	Test Buckling Load, $P_{b,test}$ (kN)	FEMFAN Buckling Load, $P_{b,FEMFAN}$ (kN)	$\frac{P_{b,FEMFAN}}{P_{b,test}}$
NRS06	55	765.1	935.3	1.22
NRS11	81	398.1	399.6	1.00
NRS16	97	271.6	249.2	0.92
			Mean:	1.05
			Standard Deviation (SD):	0.16
			Coefficient of Variation (COV):	0.15

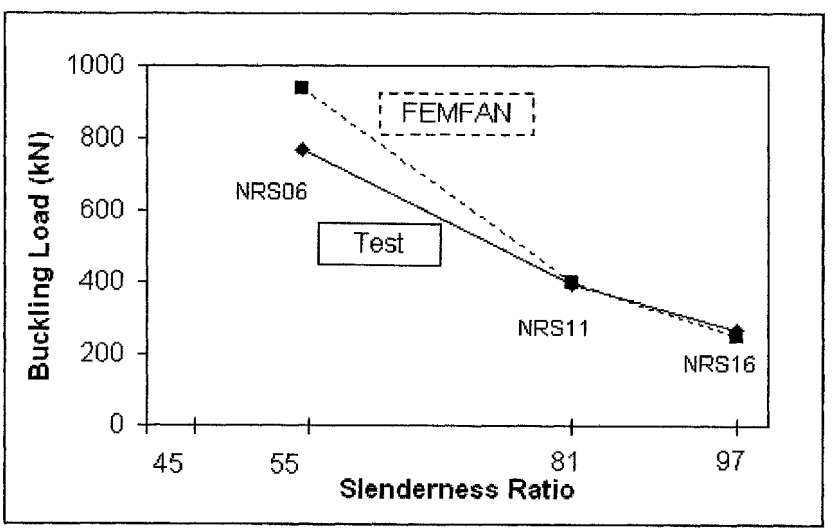

Figure 5.2 Experimental and FEM buckling loads (Series 2)

Figure 5.3 shows a plot of mid-height displacements against applied compressive loads for the 3 ambient load capacity tests, and Figure 5.4 plots the axial deformation versus compressive load relationship. Figure 5.5 shows that FEMFAN had underestimated the mid-height displacements in the pre-buckling stage for all

three Series 2 ambient load capacity tests. In Figure 5.4, FEMFAN had predicted well for the axial deformation development for Columns NRS11 and NRS16. However it had under-predicted that for Column NRS06.

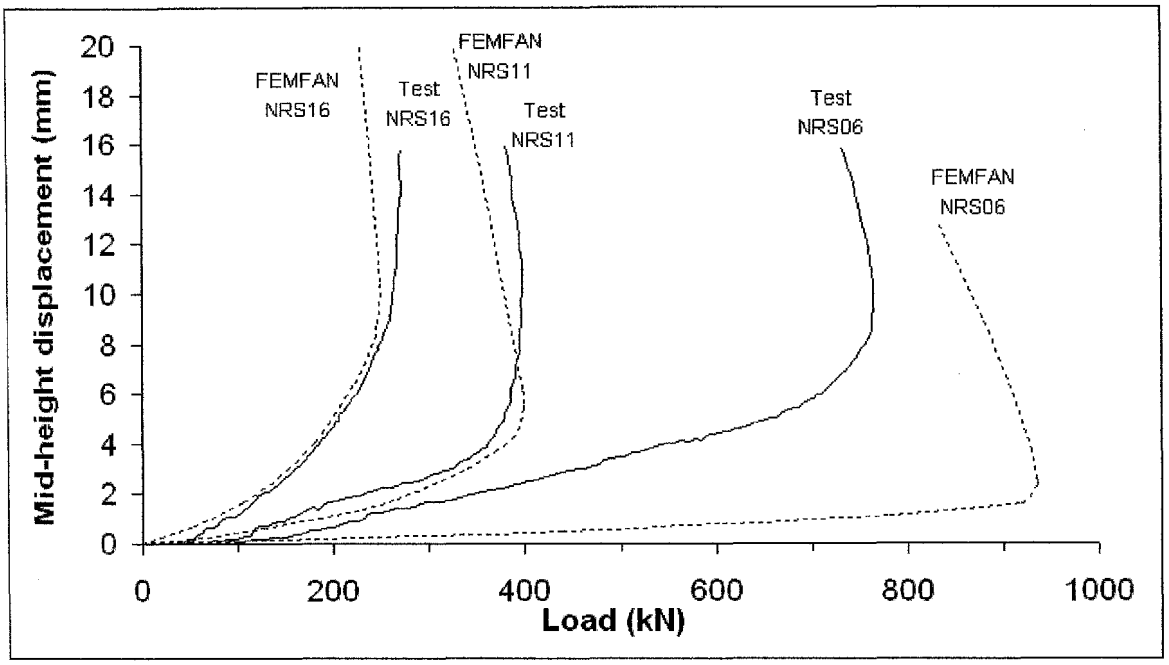

Figure 5.3 Experimental and FEMFAN results for mid-height displacement-compressive load relationship (Series 2)

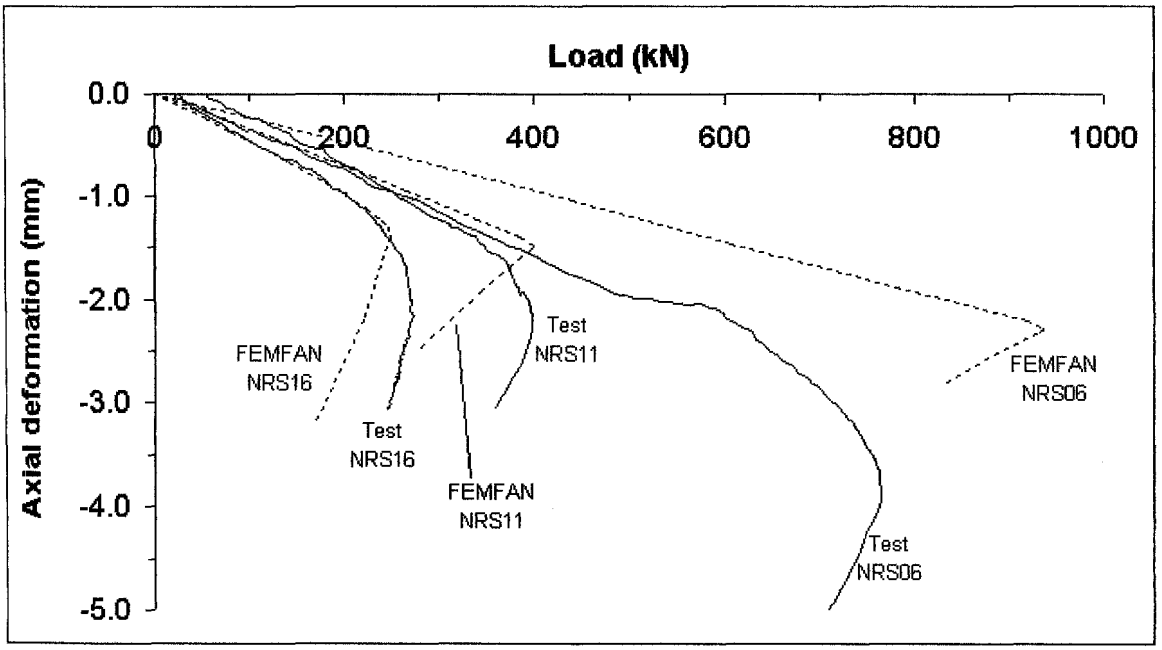

Figure 5.4 Experimental and FEMFAN results for axial deformation -compressive load relationship (Series 2)

5.5.2 Column Elevated Temperature Test

Table 5.6 summarises the results for Series 2 steel column elevated temperature tests, and FEMFAN analyses. It shows the column buckling temperatures for different axial restraint ratios.

Table 5.6 Experimental and FEM buckling temperatures (Series 2)

Column Marking	Slenderness Ratio, λ	Restraint Ratio, α_k	P_o (kN)	$T_{cr,test}$ (°C)	$T_{cr,FEMFAN}$ (°C)	$\frac{T_{cr,FEMFAN}}{T_{cr,Test}}$
NRS08	55	0.08	381.5	395.3	436.8	1.10
NRS10	55	0.14	378.5	380.8	401.5	1.05
NRS13	81	0.08	198.1	296.0	290.1	0.98
NRS15	81	0.14	194.8	243.4	239.2	0.98
NRS18	97	0.08	134.7	379.7	284.5	0.75
NRS20	97	0.14	140.1	316.2	269.0	0.85
					Mean:	0.95
					Standard Deviation (SD):	0.13
					Coefficient of Variation (COV):	0.14

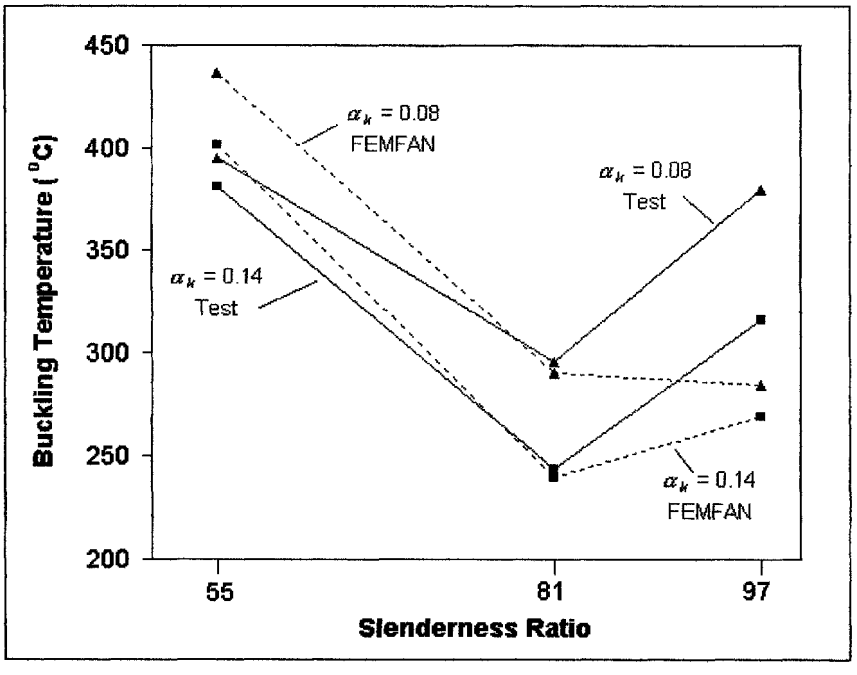

Figure 5.5 Trends of buckling temperatures with slenderness ratios (Series 2)

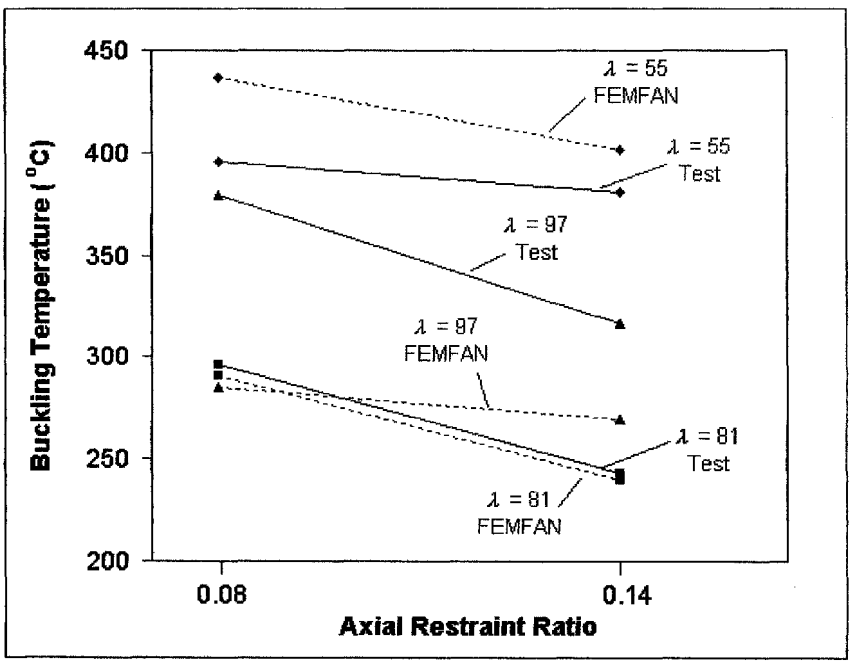

Figure 5.6 Trends of buckling temperatures with restraint ratios (Series 2)

In Table 5.6, Columns NRS18 ($\lambda = 97$, $\alpha_K = 0.08$) and NRS20 ($\lambda = 97$, $\alpha_K = 0.14$) failed at much higher buckling temperatures compared to Columns NRS13 ($\lambda = 81$, $\alpha_K = 0.08$) and NRS15 ($\lambda = 81$, $\alpha_K = 0.14$), even though they were more slender and were subjected to similar axial restraint ratio, respectively. This unexpected trend is shown graphically in Figures 5.5 and 5.6. From Series 2 column steel material properties (Table 5.3), it shows that the section with slenderness $\lambda = 97$ (for Columns NRS16, NRS18 and NRS20) had the highest yield and ultimate strengths. Its yield strength was higher than that of section with $\lambda = 81$ by 20N/mm^2. An interesting point is that FEMFAN agreed well with test results for Column NRS20 ($\lambda = 97$, $\alpha_K = 0.14$), giving out-of-trend predictions too (Figures 5.5 and 5.6). Another possibility that had caused Column NRS15 ($\lambda = 81$, $\alpha_K = .14$) to yield such low buckling temperature might be its large initial load eccentricity (Table 5.2), which was difficult to control in test situation. The large eccentricity might have caused premature buckling.

FEMFAN predictions for column tests at elevated temperature give a mean value of 0.95 for $T_{cr,FEMFAN}/T_{cr,test}$, with a standard deviation SD = 0.13 and a coefficient of variation COV = 0.14. These satisfying statistical values confirmed the reliability of FEMFAN numerical analysis.

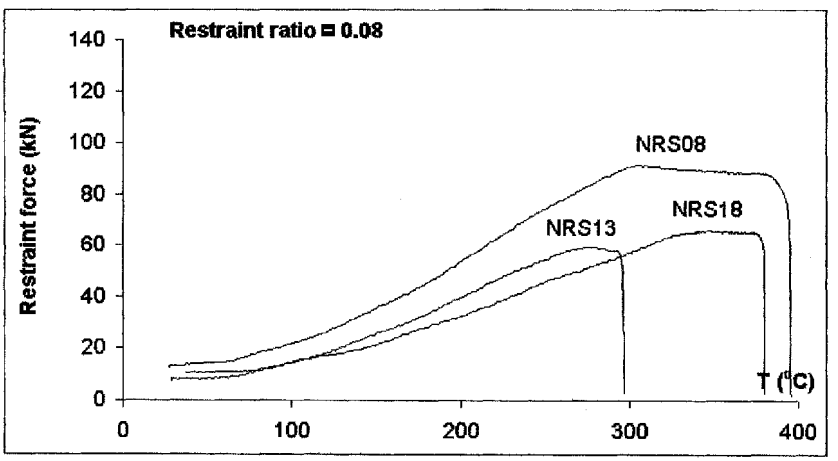

(a) Restraint ratio = 0.08

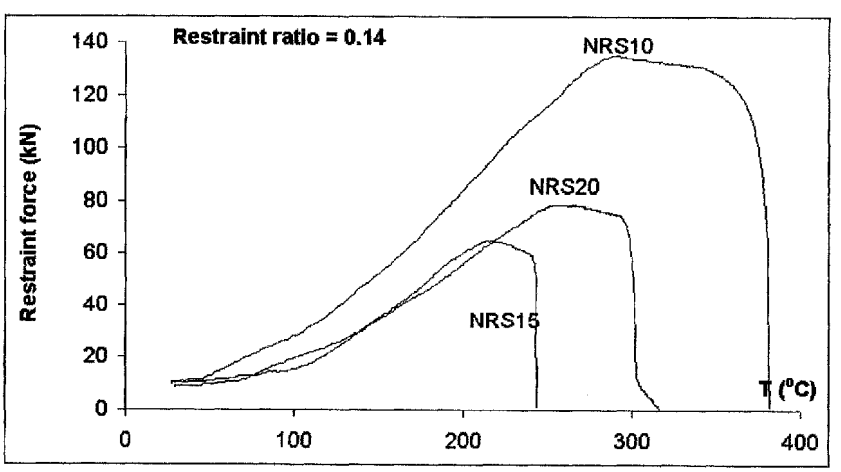

(b) Restraint ratio = 0.14

Figure 5.7 Graphs of restraint force against temperature (Series 2)

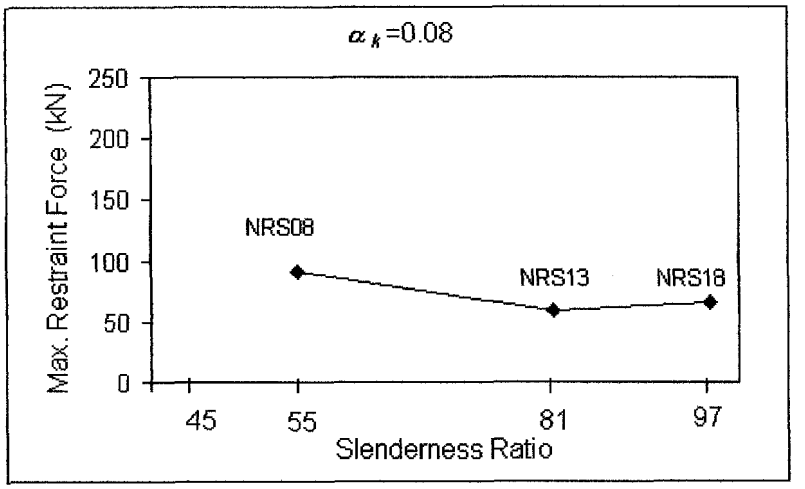

(a) Restraint ratio = 0.08

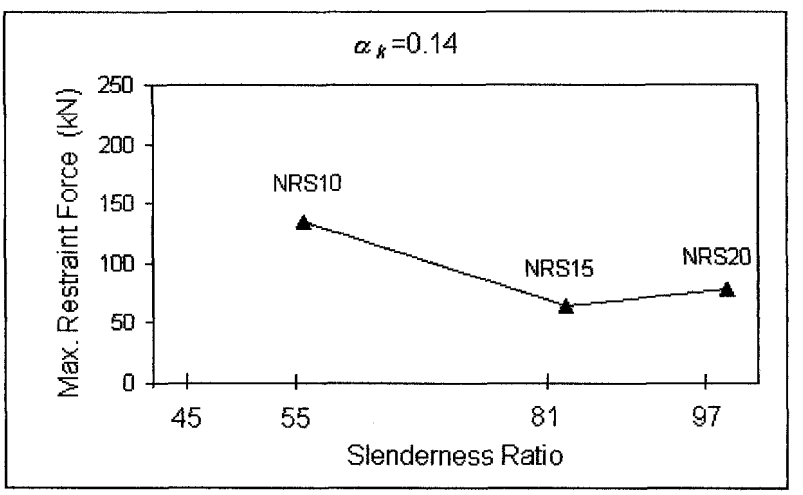

(b) Restraint ratio = 0.14

Figure 5.8 Graphs of maximum generated restraint force against slenderness (Series 2)

During thermal expansion, axial expansion against the restraint system generated additional compressive forces in the steel columns. Figures 5.7 (a) and (b) plots the restraint force development in the elevated temperature tests. A proportional increase in restraint force was noted for all restrained columns. Similar to Series 1 tests, the stocky columns in Series 2 experienced a peak and plateau off after some time, with increasing temperature. As discussed in Chapter 3, this was possibly due to frictional effects.

Figures 5.8 (a) and (b) shows the maximum generated restraint force for Series 2 elevated temperature tests. Columns NRS18 and NRS20 had unexpected higher values for maximum restraint forces compared to the less slender columns NRS13 and NRS15, since the former had stronger material properties.

Mid-height displacement δ_{mid} versus temperature relationships for elevated temperature tests, from experiment and FEMFAN, are plotted in Figures 5.9 (a) to (c). FEMFAN predictions were close in the rate of increase of mid-height displacement δ_{mid} during the pre-buckling stage, as observed in the parallel gradients of the test and FEMFAN graphs. An interesting behaviour was noted in Columns NRS08 and NRS10 in the development of mid-height displacement (Figure 5.9 (a)). After the first runaway in lateral deflection, the columns seemed to have regained some stability. The rate of increase of lateral displacement decreased as temperature increased steadily. Subsequently, these two columns failed by bending about 80°C later. Checking against the development of P/P_o with temperature (Figure 5.10 (a)), it was discovered that for Columns NRS08 and NRS10, at the point of their first runaway lateral displacement, P/P_o had reached a peak and plateau off for the same period of 80°C. There was neither an increase nor decrease in the additional restraint forces to the columns; therefore the columns were able to sustain the compressive force for a longer period before buckling.

Figures 5.10 (a) to (c) show that FEMFAN had predicted a close rate of increase of P/P_o to the tests. Gradients of the P/P_o against temperature graphs in the pre-buckling stage were quite similar. It also showed that for columns with similar slenderness ratio, a higher rate of increase in P/P_o under rising temperature occurred when a greater restraint ratio was applied.

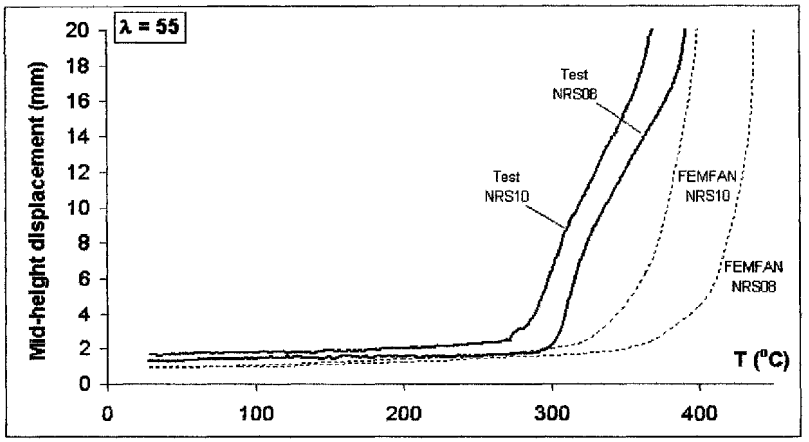

(a) Results for λ = 55

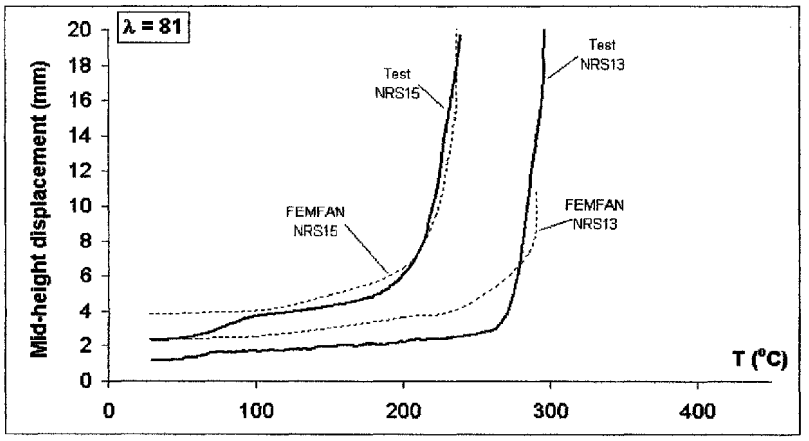

(b) Results for λ = 81

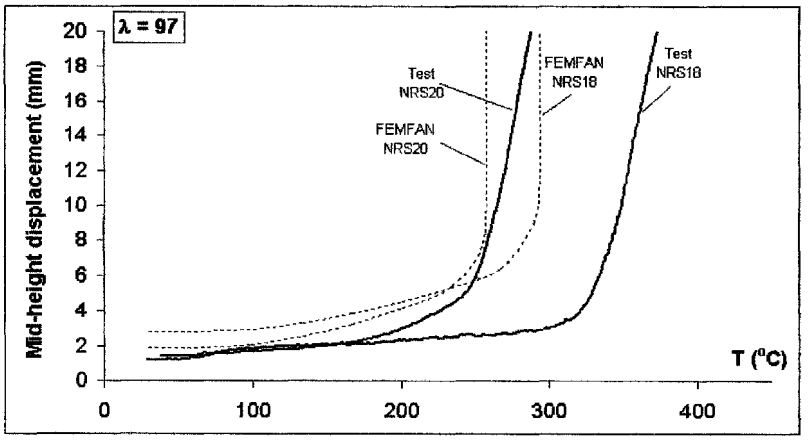

(c) Results for λ = 97

Figure 5.9 Experimental and FEMFAN results for mid-height displacement-temperature relationship (Series 2)

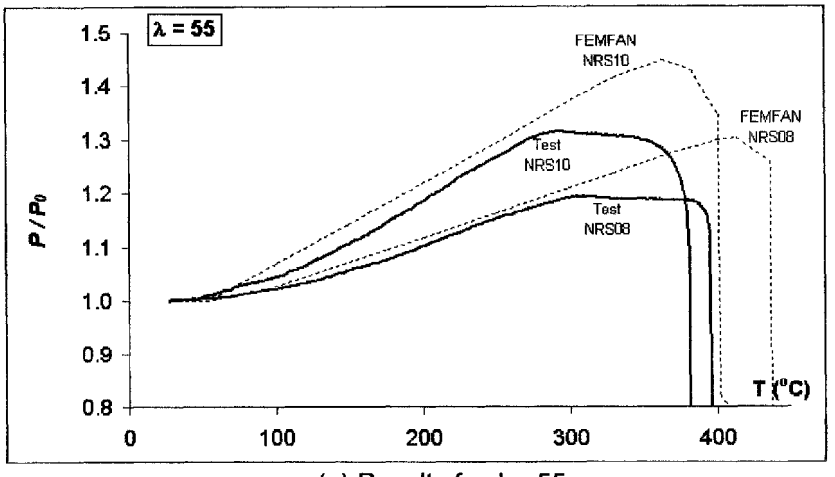

(a) Results for λ = 55

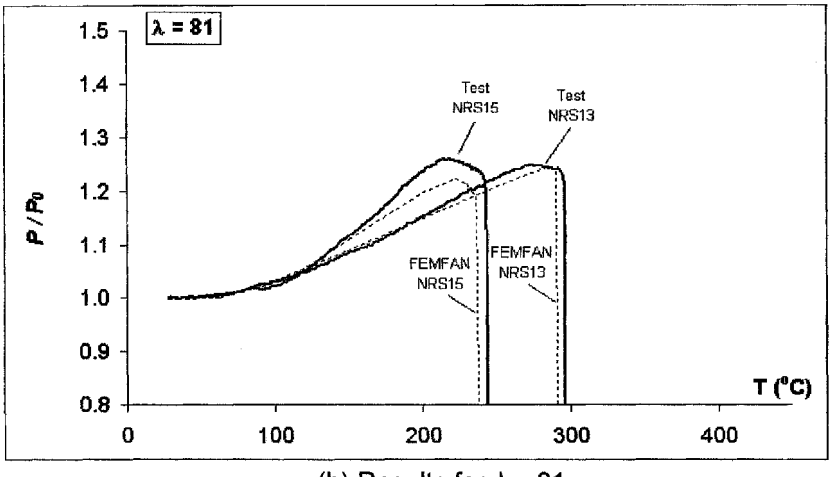

(b) Results for λ = 81

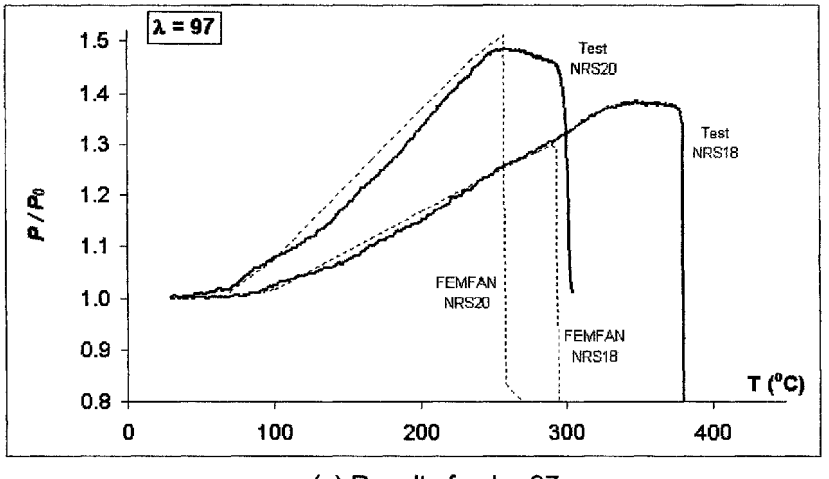

(c) Results for λ = 97

Figure 5.10 Experimental and FEMFAN results for P/P_o - temperature relationship (Series 2)

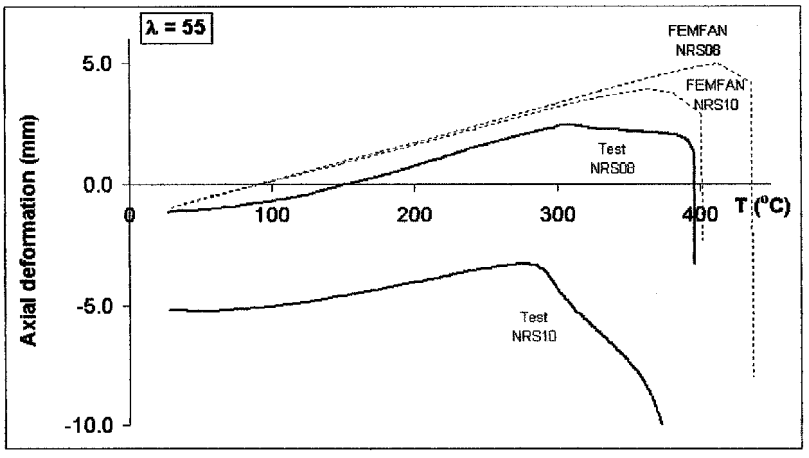

(a) Results for λ = 55

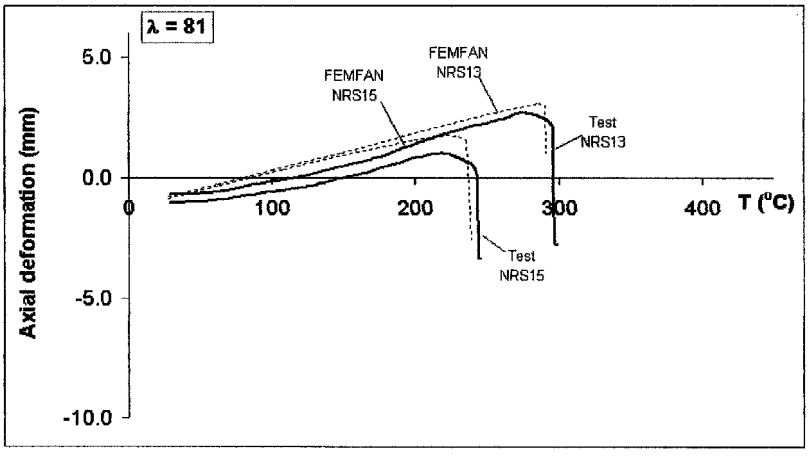

(b) Results for λ = 81

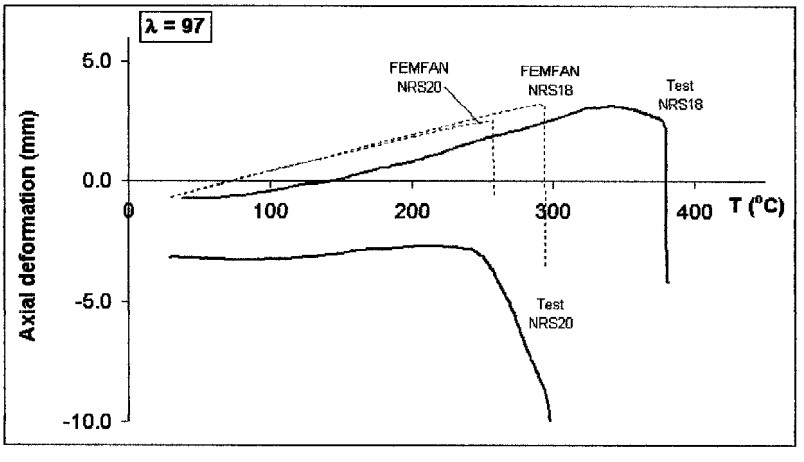

(c) Results for λ = 97

Figure 5.11 Experimental and FEMFAN results for axial deformation - temperature relationship (Series 2)

Axial deformation against temperature relationships are plotted in Figures 5.11 (a) to (c). The rate of axial expansion is shown by the gradient of each graph. FEMFAN can predict the rate of increment in axial expansion well. In the test results of Columns NRS10 and NRS20, it shows that there were larger gaps in these two test set-up, as indicated by the large values of initial axial deformations.

5.6 Conclusions from Series 2 Test Programme

As discussed, Series 2 test programme was carried out to investigate the influence and possible benefit of rotational restraint due to friction. It was suspected that there was some rotational restraint present at the end bearings of the test set-up in Series 1 tests. The bearings were machined and friction was eliminated. From Series 2 tests, it was noticed that the ultimate load capacities for columns were much lesser than those in Series 1. Buckling temperatures for elevated temperature tests were also found to be lower in Series 2 than in Series 1, for each respective column except Column NRS20 (Series 2) whose buckling temperature was 2.3 ^{o}C higher than that of RS20 (Series 1).

It seemed to show that rotational restraint due to friction had a beneficial effect; it increased column strength at ambient temperature and delayed buckling at elevated temperature. It also suggested that rotational friction was still present (as shown in Figure 5.10 (a)), in spite of machining the contact surfaces. Perhaps a new set of bearings had to be designed.

CHAPTER SIX

Experimental Testing on Composite Steel-Concrete Columns

6.1 Elevated Temperature Test Programme on Composite Steel – Concrete Columns

There is little research on the behaviour of concrete-encased steel section composite columns under elevated temperature. This research aimed to understand the mechanical behaviour of concrete-encased steel section composite members under elevated temperature. An encased composite member is a general case that in it includes appropriate behaviour parameters to model both reinforced concrete and bare steel members. The findings in this research may be useful for implementation of an analysis model incorporating thermal effects due to fire, for application onto concrete-encased steel section composite members with steel reinforcement.

In the experimental study on the behaviour of concrete-encased steel composite columns at elevated temperature, the columns were categorised into three series to investigate their behaviour due to the effects of three parameters, namely, overall cross-sectional size, steel section ratio and axial restraint ratio.

Eleven specimens with uniform lengths of 3.3m were prepared for the tests in the three series. The columns had a total effective length of 3.54m when attached to the knuckle bearings at both ends, giving a pinned-pinned and a pinned-on-roller simply supported boundary conditions. Column CC01 was tested to failure at ambient temperature, by the application of an increasing axial compressive load until the column buckled. This first test was meant as a trial run as it was used to check for any set-up and instrumentation error. In each of the other 10 elevated temperature tests, an axial compressive load was applied, with 70% of the respective column's design load capacity at ambient temperature. Under the applied load, the column

was subjected to transient heating state, similar to the steel column tests described in Chapter 3. Design load capacities were calculated based on Eurocode 4 Part 1.1 (1995). Load ratio was maintained at 70% of the column's design load capacity, according to EC4 (1995), which was at the high end of the practical range. This value was chosen so that for the elevated temperature tests, each column would fail within a reasonable time span. The dimensions of the composite columns that were tested were different. It would be tedious to perform an ambient loading test for every single specimen size. This is the reason why the working load of the composite column was calculated from the design method in Eurocode 4 Part 1.1 (1995), unlike the steel column test discussed in Chapters 3 to 5. Finite element analyses from the program FEMFAN were also carried out to compare with the EC4 design method, which is discussed in Section 6.4.

6.2 Test Series

In this test programme, an experimental investigation of composite columns under elevated temperature was conducted, to examine the effects of overall cross-sectional size, steel section ratio and axial restraint ratio on its mechanical behaviour. The findings will be beneficial towards the improvement of design recommendations in standard codes for fire resistance design for encased composite columns. The columns were marked as CC01 to CC11. All column tests were conducted in Construction Annex, Nanyang Technological University, Singapore. Columns CC01 to CC05 were tested to failure by a previous research fellow, Dr. Toh Wee Siang. The remaining tests were performed by the author when he started his M.Eng research programme. Table 6.1 shows the column labels for each series of tests investigating a different parameter.

Table 6.1 Test parameters

Series	Parameter	Specimens
1	Cross-sectional Size	CC02, CC03, CC04, CC05
2	Steel Section Ratio	CC03, CC06, CC07, CC08
3	Axial Restraint Ratio	CC08, CC09, CC10, CC11

6.2.1 Series 1: Overall Cross-sectional Size of Column

Table 6.2 General characteristics of series 1 columns

Column Notation	Overall Column Size		Steel Section		Steel Section Ratio, $\rho = A_s / A_T \times 100\%$
	Cross-section (mm x mm)	Area, A_T (mm^2)	Size	Area, A_s (mm^2)	
CC02	250x250	62500	UC152x152x37	4590	7.34
CC03	300x300	90000	UC203x203x52	6668	7.41
CC04	350x350	122500	UC254x254x73	9357	7.64
CC05	400x400	160000	UC305x305x97	11999	7.50

In the study of the effect of cross-section (Series 1), four different square section columns (Columns CC02 to CC05), with dimension 250, 300, 350 and 400mm were designed (Table 6.2), such that the cross-sectional area of steel A_s to the overall cross-sectional area had a constant ratio of around 7.5% for all four columns. From EC4 (1995), the steel section contribution ratio δ to total axial capacity lies in between 0.2 and 0.9. Section 6.4 will show more details on this. During the planning stage, it was after consideration of many different combinations of steel and concrete cross sectional sizes before achieving this constant steel section ratio for all the columns in this series. The only variable parameter was the overall cross-sectional size of the column. This parameter was investigated to check whether the strength of the composite column is linearly proportional to the increase in its dimension, and whether there is any added advantage in using a bigger dimension composite column.

6.2.2 Series 2: Steel Section Ratio

Table 6.3 General characteristics of series 2 columns

Column Notation	Overall Column Size		Steel Section		Steel Section Ratio, $\rho = A_s / A_T \times 100\%$
	Cross-section (mm x mm)	Area, A_T (mm^2)	Size	Area, A_s (mm^2)	
CC06	300x300	90000	UC152x152x23	2925	3.25
CC07	300x300	90000	Joist114x114x27	3450	3.83
CC08	300x300	90000	UC152x152x37	4711	5.23
CC03	300x300	90000	UC203x203x52	6668	7.41

In the study of the effect of steel section ratio (Series 2), four values of steel ratio; 3.25%, 3.83%, 5.23% and 7.41%, were investigated (Columns CC06, CC07, CC08, and CC03, respectively). Composite Column CC03 in Series 2 was the same column tested in Series 1. Its dimensions and specifications made it suitable to be used in both series. All these four columns had the same overall cross-sectional area of 300 × 300mm (Table 6.3). The steel section ratio was taken as the percentage of steel section over the whole cross sectional area of the column. In Table 6.3, the column notations were arranged so that the steel section ratio was in an incremental order. This test series checked for the influence of different steel section ratios on ultimate strength.

6.2.3 Series 3: Axial Restraint Ratio

Table 6.4 General characteristics of series 3 columns

Column Notation	Overall Column Size		Steel Section		Steel Section Ratio, $\rho = A_s / A_T \times 100\%$
	Cross-section (mm x mm)	Area, A_T (mm^2)	Size	Area, A_s (mm^2)	
CC08 to CC11	300x300	90000	UC152x152x37	4711	5.23

Table 6.5 Axial restraint ratios of series 3 columns

Column Notation	Column Stiffness, K_c (kN/mm)	Restraint Beam	Restraint System Stiffness, K_s (kN/mm)	Restraint Ratio $\alpha_k = K_s / K_c$
CC08	304.17	-	0.00	0.00
CC09	304.17	W8x8x5.25x27	30.61	0.10
CC10	304.17	UC203x203x60	27.95	0.09
CC11	304.17	W10x10x10xx88.9	52.45	0.17

Series 3 composite steel-concrete columns were tested at elevated temperature subjected to various axial restraint ratios, which are defined as:

$$\alpha_k = \frac{K_s}{K_c} \tag{6.1}$$

where

K_s = actual restraint axial stiffness measured in test;

K_c = column axial stiffness at ambient temperature

$= [(EA)_{rebars} + (EA)_{steel\ section} + (EA)_{concrete}] / L_e$

E = elastic modulus at room temperature

A = cross sectional area

L_e = column effective length

The restraint ratio is defined as the ratio of the stiffness of restraint system relative to the stiffness of composite column. In the study of the effects of axial restraint ratio (Series 3), four different restraint levels, namely 0%, 9%, 10% and 17%, were achieved in the tests for four identical columns (CC08 to CC11) (Tables 6.4 and 6.5), by means of using restrained beams of different stiffnesses. Column CC08 in Series 3 was the same column tested in Series 2. The three restrained beams used were: W8 x 8 x 5.25 x 27, UC203 x 203 x 60 and W10 x 10 x 10 x 88.9. More details are shown in Section 7.4. The column notations in Tables 6.4 and 6.5 were arranged in order of increasing axial restraint ratios.

6.3 Test Specimens and Material Properties

Table 6.6 Overall dimensions of composite columns

Column No.	Overall Size					
	b mm	h mm	A_g mm^2	I_g $x10^8 mm^4$	L_e mm	Mass kg
CC01	250	250	62500	3.3	3540	631
CC02	250	250	62500	3.3	3540	630
CC03	300	300	90000	6.8	3540	904
CC04	350	350	122500	1.3	3540	1232
CC05	400	400	160000	2.1	3540	1601
CC06	300	300	90000	6.8	3540	831
CC07	300	300	90000	6.8	3540	841
CC08	300	300	90000	6.8	3540	866
CC09	300	300	90000	6.8	3540	866
CC10	300	300	90000	6.8	3540	866
CC11	300	300	90000	6.8	3540	866

Table 6.7 Steel sections material properties at ambient temperature

Column No.	Steel Section					
	Section Size	A_s mm^2	I_s x10^{6}mm^4	f_y MPa	ρ %	E MPa
CC01	UC152x152x37	4629	6.98	332	7.41	205000
CC02	UC152x152x37	4590	6.97	338	7.34	205000
CC03	UC203x203x52	6668	18.2	317	7.41	205000
CC04	UC254x254x73	9357	40.2	320	7.64	205000
CC05	UC305x305x97	11999	70.6	400	7.50	205000
CC06	UC152x152x23	2925	0.4	320	3.25	205000
CC07	Joist 114x114x27	3450	2.24	320	3.83	205000
CC08	UC152x152x37	4711	7.06	320	5.23	205000
CC09	UC152x152x37	4711	7.06	320	5.23	205000
CC10	UC152x152x37	4711	7.06	320	5.23	205000
CC11	UC152x152x37	4711	7.06	320	5.23	205000

Table 6.8 Reinforcement bars material properties at ambient temperature

Column No.	Reinforcement					
	Size	No.	A_s mm^2	I_r x10^{6}mm^4	f_{sk} MPa	ρ_s %
CC01	T13	4	531	4.2	460	0.85%
CC02	T13	4	531	4.2	460	0.85%
CC03	T13	4	531	6.8	460	0.59%
CC04	T13	4	531	1.0	460	0.43%
CC05	T13	4	531	1.4	460	0.33%
CC06	T13	4	531	6.8	460	0.59%
CC07	T13	4	531	6.8	460	0.59%
CC08	T13	4	531	6.8	460	0.59%
CC09	T13	4	531	6.8	460	0.59%
CC10	T13	4	531	6.8	460	0.59%
CC11	T13	4	531	6.8	460	0.59%

Table 6.9 Concrete material properties at ambient temperature

Column No.	Concrete			
	A_c mm^2	I_c x10^{8}mm^4	f_c' MPa	E_c MPa
CC01	57340	3.14	40	25
CC02	57379	3.14	42	26
CC03	82801	6.50	43	26
CC04	112612	12.0	44	26
CC05	147471	20.5	44	26
CC06	86544	6.68	45	26
CC07	86019	6.66	43	26
CC08	84758	6.61	43	26
CC09	84758	6.61	43	26
CC10	84758	6.61	43	26
CC11	84758	6.61	43	26

The 3.3m long composite steel-concrete columns had an effective length of 3.54m when measured from the centroid of the knuckle bearings at both ends. A summary of the dimensions and material properties of the steel sections, concrete and reinforcement are shown in Tables 6.6 to 6.9. Design drawings of the columns are shown in Appendix B.

Table 6.6 shows the overall dimensions of composite columns, where:

b = breadth of column cross section

h = height of column cross section

A_g = gross cross-sectional area of composite column

I_g = second moment of area of composite column

L_e = effective length of column

Table 6.7 shows the material properties of steel sections, where:

A_s = cross-sectional area of steel section

I_s = second moment of area of steel section

f_y = structural steel characteristic strength

ρ = steel section to overall column cross-section ratio

Table 6.8 shows the material properties of reinforcement bars. In each composite column, a total of four T13 reinforcement bars were used, where:

A_r = cross-sectional area of steel reinforcement

I_r = second moment of area of reinforcement bars

f_{yr} = reinforcement bars characteristic strength

ρ_s = area of steel reinforcement bars to overall column cross-section ratio

Table 6.9 shows the material properties of concrete, where:

A_c = cross-sectional area of concrete

I_c = second moment of area of concrete

f_c' = concrete characteristic strength

E_c = elastic modulus of concrete

6.4 Determination of Working Load

The working load used in the composite test was calculated based on the simplified design method from Eurocode 4 Part 1.1 (1995). The load ratio used in the test was 70% of the column's design load capacity. FEM analyses were conducted for all the ambient tests for comparison of with the ultimate load capacities found from EC4 design method.

6.4.1 Simplified Design Method for Composite Column

Eurocode 4 Part 1.1 (1995) provided a simplified design method for composite columns of double symmetry and uniform cross section over the column length. There are a few limitations for applying this design method:

- The steel section contribution ratio δ to total axial capacity should lie in between 0.2 and 0.9
- The non-dimensional slenderness ratio λ should not exceed 2.0
- The concrete cover c to steel section:
  - In the z-direction (to section flange), 40mm $\leq c \leq 0.4b$ (b = section width)
  - In the y-direction (orthogonal to z-direction), 40mm $\leq c \leq 0.3h$ (h = section height)
- The area of longitudinal reinforcement should lie in between 0.3% and 4% of the area of concrete
- The concrete cylinder strength f_{ck} should not exceed 50 MPa
- The yield strength of structural steel should not exceed 355 MPa

The following describes the design calculations for a composite column under pure compression. At ambient temperature, the member has sufficient resistance if the design axial load N_{Sd} is less than the design strength when considering bending about x-axis (strong axis) or y-axis (weak axis) separately:

$$N_{Sd} = \chi N_{pl,Rd} \tag{6.2}$$

where $N_{pl,Rd}$ is the plastic resistance to compression; and χ is the reduction coefficient for the relevant buckling mode.

The plastic resistance to compression $N_{pl,Rd}$ of a composite cross-section should be determined by adding the plastic resistance of its components, as follows:

$$N_{pl,Rd} = A_s f_y / \gamma_s + A_c (0.85 f_c' / \gamma_c) + A_r f_{yr} / \gamma_r \tag{6.3}$$

where

A_c, A_r and A_s are the cross-sectional areas of concrete, reinforcement and structural steel, respectively;
f_c', f_{yr} and f_y are the characteristic strength of concrete, reinforcement and structural steel, respectively; and
γ_c = 1.5, γ_r = 1.15 and γ_s = 1.10, are the partial safety factors at the ultimate limit state.

For members of constant cross-section subjected to axial compression, the reduction coefficient χ is a function of slenderness $\bar{\lambda}$, as follows:

$$\chi = \frac{1}{\varphi + \sqrt{\varphi^2 - \bar{\lambda}^2}} \quad \text{but } \chi \leq 1 \tag{6.4}$$

$$\text{where } \varphi = \frac{1}{2}\left[1 + \alpha(\bar{\lambda} - 0.2) + \bar{\lambda}^2\right] \tag{6.5}$$

where

α is the imperfection factor; α = 0.34 for fully concrete-encased I-sections with bending about the strong axis of steel section; α = 0.49 for bending about the weak axis.

The non-dimensional slenderness $\bar{\lambda}$ for out-of-plane bending is given by

$$\bar{\lambda} = \sqrt{N_{pl,R} / N_{cr}} \tag{6.6}$$

where

$N_{pl,R}$ = the value of $N_{pl,Rd}$ when the partial safety factors γ_c, γ_r and γ_s are taken as 1.0.

The elastic critical load is given by:

$$N_{cr} = \pi^2 (EI)_e / l^2 \tag{6.7}$$

The effective elastic modulus is determined from:

$$(EI)_e = E_s I_s + 0.8 E_{cd} I_c + E_r I_r \tag{6.8}$$

I_s, I_c, I_r = second moment of area for structural steel, concrete and reinforcement, respectively;

E_s, E_r = elastic modulus for structural steel and reinforcement, respectively;

E_{cd} = $9.5(f_c'+8)^{0.33} / 1.35$ (6.9)

l = buckling length

6.4.2 Design Calculations for Composite Column

As an illustration, the design calculations for the column resistance to axial compression for composite column CC08 are included here.

Steel Section:

UC152x152x37

$A_a = 4711 \text{mm}^2$

$I_a = 7.06 \times 10^6 \text{mm}^4$

$f_y = 320 \text{N/mm}^2$

$E_a = 205 \text{kN/mm}^2$

$\gamma = 1.0$

$f_y / \gamma = 320 \text{N/mm}^2$

Concrete:

$f_c' = 43 N/mm^2$

$E_c = 26 kN/mm^2$

For material strength $\gamma_m = 1.0$

$0.85 f_c' / \gamma_m = 36.55 kN/mm^2$

The concrete cover is within the range given in *Clause* 4.8.3.1(3) (d).

The area of concrete A_c is given by:

$A_c = 300 \times 300 - 4711 - 531 = 84758 \text{ mm}^2$

The area of longitudinal reinforcement ($531 mm^2$) exceeds 0.3% of A_c and therefore may be included in the calculation for column resistance.

The design resistance of cross-section to axial load $N_{pl,Rd}$ is calculated using *Clause* 4.8.3.3(1).

$N_{pl,Rd} = [4711 \times 320/1 + 84758 \times 0.85 \times 43/1 + 531 \times 460/1] / 1000 = 4849.65 kN$

The column is constrained to bend about the minor axis of the steel section by the knuckle bearings used in the test. The second moment of area of concrete section about this axis is given by:

$I_c = 300^4/12 - 7.06 \times 10^6 = 6.61 \times 10^8 \text{ mm}^4$

Using *Clause* 4.8.3.5(1), the effective flexural stiffness is:

$(EI)_e = 205 \times 10^3 \times 7.06 \times 10^6 + 0.8 \times 26 \times 6.61 \times 10^8 + 205 \times 10^3 \times 6.8 \times 10^6$

$= 2.86 \times 10^{12} Nmm^2$

The elastic critical load N_{cr} and the relative slenderness λ are (*Clause* 4.8.3.7):

$N_{cr} = \pi^2 \times 2.86 \times 10^{12} / 1000 / 3540^2 = 2256.17 kN$

λ $= (4849.65 / 2256.17)^{0.5} = 1.47$

φ $= 0.5x\ [1+0.49(1.47-0.2) +1.47^2] = 1.88$

Reduction coefficient, $\chi = 1/\ [1.88 + (1.88^2 - 1.47^2)^{0.5}] = 0.326$

Therefore, total design load $N_{sd} = 0.326$ x 4849.65 = 1579.86kN

Applied axial compression force P_o is taken as 70% of the total design load N_{sd}.

$P_o = 0.7$ x 1579.86 = **1105.9kN**

Table 6.10 shows a summary of the design calculations for all 11 composite columns. Appendix C shows a table illustrating the design data for the 11 columns.

Table 6.10 Design Axial Load Capacities for CC01 to CC11 at Ambient Temperature

Column Notation	$N_{pl,Rd}$ (kN)	$(EI)_e$ ($x10^{12}Nmm^2$)	N_{cr} (kN)	λ	φ	χ	N_{sd} (kN)	$P_o=0.7N_{sd}$ (kN)
CC01	3730.67	2.29	1804.45	1.44	1.84	0.336	1251.76	876.24
CC02	3844.21	2.29	1803.37	1.46	1.87	0.328	1260.30	882.21
CC03	5384.25	5.15	4055.54	1.15	1.40	0.457	2461.68	1723.17
CC04	7450.18	1.04	8152.14	0.96	1.14	0.566	4215.88	2951.11
CC05	10559.05	1.74	13728.87	0.88	1.05	0.614	6483.60	4538.52
CC06	4490.54	1.50	1180.72	1.95	2.83	0.205	919.86	643.90
CC07	4492.22	1.88	1477.64	1.74	2.40	0.247	1110.59	777.41
CC08	4849.65	2.86	2256.17	1.47	1.88	0.326	1579.86	1105.90
CC09	4849.65	2.86	2256.17	1.47	1.88	0.326	1579.86	1105.90
CC10	4849.65	2.86	2256.17	1.47	1.88	0.326	1579.86	1105.90
CC11	4849.65	2.86	2256.17	1.47	1.88	0.326	1579.86	1105.90

6.4.3 FEM Results for Ultimate Capacity at Ambient Temperature

FEM analyses were carried out to determine the ultimate capacity of each individual composite column at ambient temperature, for the purpose of comparison with the EC4 design calculations. Chapter 7 gives more details on the FEM program FEMFAN-3D.

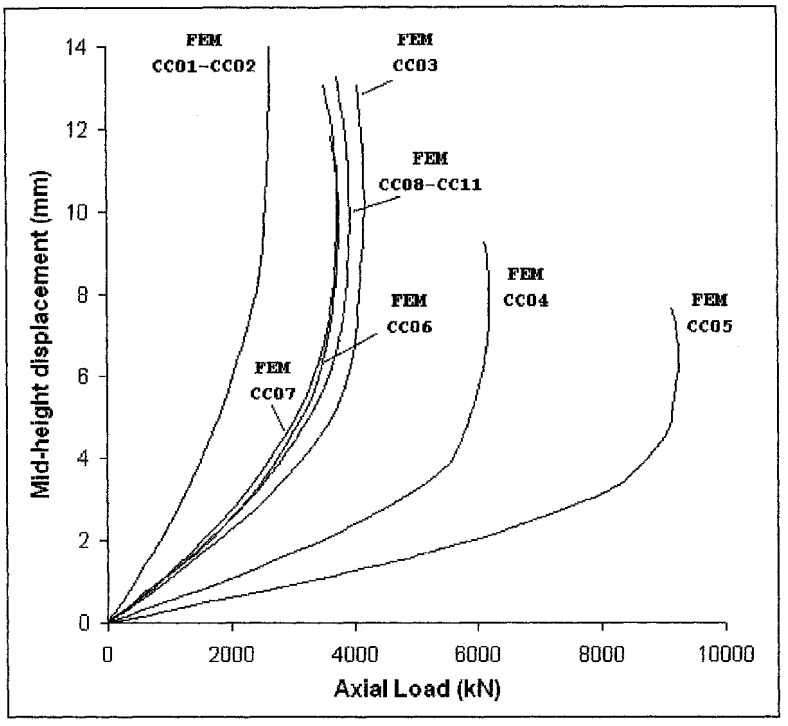

Figure 6.1 FEM predictions for column ultimate loads at ambient temperature

Table 6.11 Column ultimate load capacity and load ratio

Column Marking	Working load used in test (kN)	Ultimate load capacity from EC4 (kN)	Load ratio to EC4	Ultimate load capacity from FEM (kN)	Load ratio to FEM
CC01-CC02	882.21	1260.30	0.7	2644.80	0.33
CC03	1723.17	2461.68	0.7	4164.30	0.41
CC04	2951.11	4215.88	0.7	6176.30	0.48
CC05	4538.52	6483.60	0.7	9237.90	0.49
CC06	643.90	919.86	0.7	3643.00	0.18
CC07	777.41	1110.59	0.7	3698.00	0.21
CC08-CC11	1105.90	1579.86	0.7	3927.50	0.28

Figure 6.1 shows the FEM predictions for the relationship between mid-height displacement and axial load for columns CC01 to CC11, at ambient temperature. A summary of the predicted ultimate load capacities is shown in Table 6.11, together with the EC4 design load calculations and the load ratios used in the test with respect to EC4 calculations and numerical analyses. As mentioned in Section 6.1, the load ratio in the test was taken as 70% of the EC4 design load capacity. Load ratio is normally based on either the experimental value, numerical analysis or design value. It would be very tedious to perform an ambient loading test for every single specimen size; therefore the first option was not chosen. As for numerical analysis, FEMFAN-3D, the numerical program used in this research, was still under development at the time of testing, so it was not possible to base the load ratio on numerical predictions. Therefore, EC4 design method was chosen in the end.

From Table 6.11, it shows some difference between the load ratios from EC4 design calculations and from FEM predictions. Generally, the load ratio applied in the test varied.

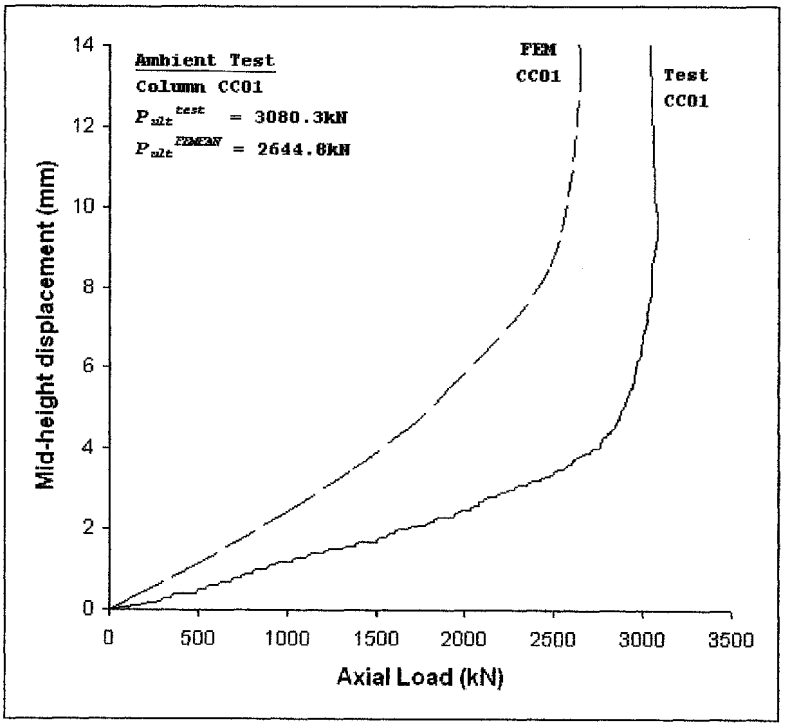

Figure 6.2 Experimental and FEMFAN results for mid-height displacement-axial load relationship for CC01

Figure 6.2 shows the test results and FEMFAN predictions for the mid-height displacement against axial load relationship at ambient temperature. In terms of the ultimate load capacity, FEMFAN-3D predicted a value of 2644.8kN compared to the actual failure load of 3080.3kN, giving a ratio of 0.86. However, no other ambient test results are available for comparison with FEM predictions.

6.5 Test Set-up

The composite column tests were carried out using the same test rig, furnace and axial restraint system as in the steel column tests discussed in Chapter 3. Two sets of furnace were used, to provide a 3m span length of heating condition to the composite column. The effective length of the column is 3.54m. The test set-up is shown in Figures 6.3 and 6.4. Notice that a protruded length of 270mm at each end of the column remained unheated during the test. The openings around this region were heavily insulated by rockwool and insulation board, to minimise heating differential along the member length.

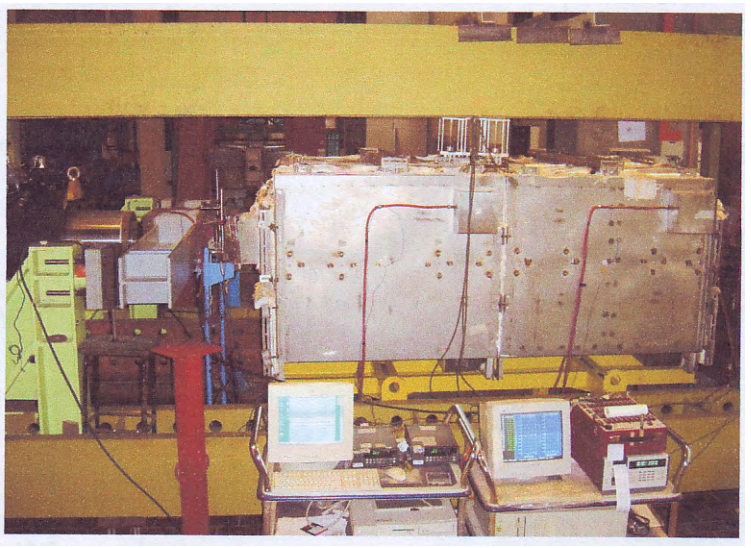

Figure 6.3 Composite test set-up

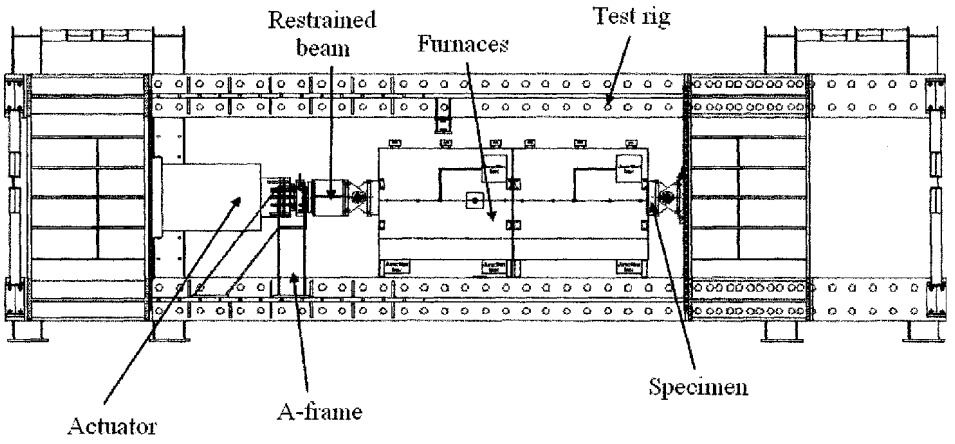

Figure 6.4 Elevation view of composite test set-up

Linear Variable Displacement Transducers (LVDTs) were used to measure the displacements of the specimens. Locations of LVDTs in the test set-up are similar to the steel column test, as shown in Figure 3.5.

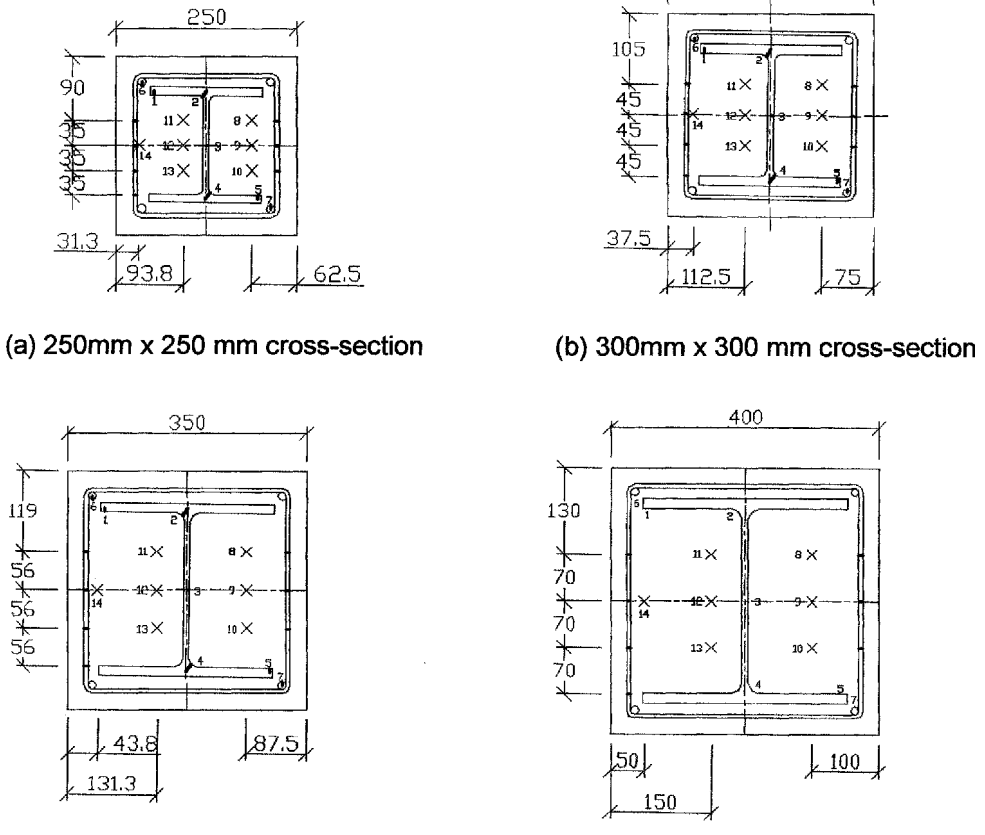

(a) 250mm x 250 mm cross-section

(b) 300mm x 300 mm cross-section

(c) 350mm x 350 mm cross-section

(d) 400mm x 400 mm cross-section

Figure 6.5 Location of thermocouples in composite columns

Temperature readings were obtained from 28 thermocouples embedded in the specimens at various points. A total of fourteen thermocouples were positioned at the mid-span and another fourteen at quarter-span of each composite column. These thermocouples measured the temperatures of the concrete, flanges and web of the steel section. Figures 6.5 (a) to (d) show locations of thermocouples in the specimens with dimensions 250mm x 250mm, 300mm x 300mm, 350mm x 350mm and 400mm x 400mm.

6.6 Test Procedure

The composite column tests were carried out under transient heating state condition, similar to the steel column tests. A predefined load P_o was first applied to the specimen and held constant. The temperature was then raised in steps according to a modified heating curve (Figure 6.6).

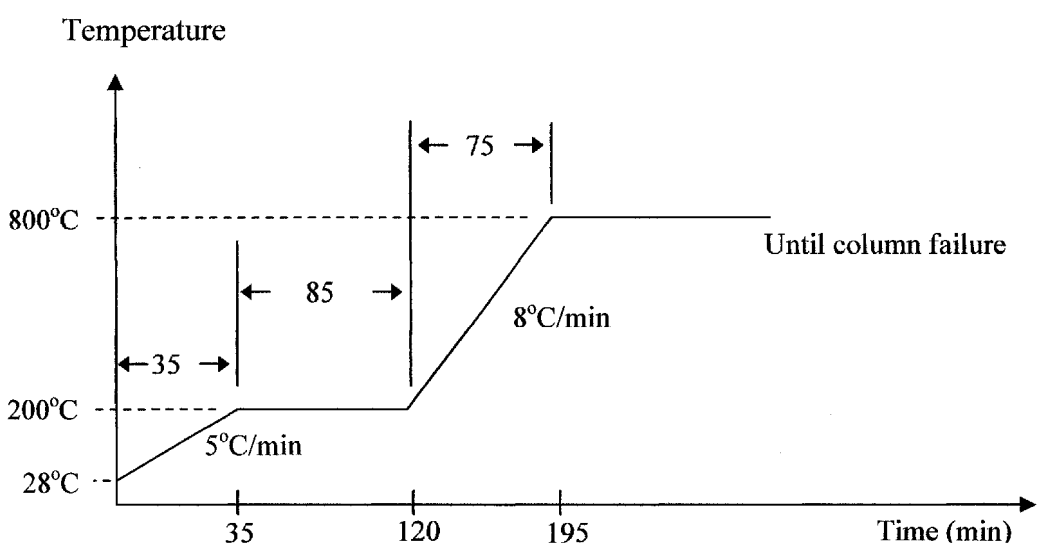

Figure 6.6 Modified heating curve for composite column tests

This heating curve was so chosen for two reasons. Firstly, the use of electrical furnace was unable to achieve similar heating rate as the ISO fire curve, and secondly, spalling of concrete was to be minimised by holding the temperature

constant at 200°C for a period of 85 minutes, so that free water content was mostly purged out of the column.

The working load was taken as 70% of the column's design load capacity at ambient temperature, N_{sd}. This working load was on the high end of the practical range, so that the test column would fail within a reasonable time. The value of N_{sd} was determined from calculations based on Eurocode 4 Part 1.1 (1995), as shown in Table 6.10.

The procedure for setting up and performing an elevated temperature test on each composite column specimen was as follows:

1. Encasing the composite column using steel mesh to prevent physical damage to the heating elements of the furnaces due to spalling or crushing of concrete;
2. Using a 5-tonne gantry crane to lift the specimen and to set it up in the test rig, with the top of furnace open;
3. Placing a cover over the furnace top and sealing all gaps with insulation wool and cloth;
4. Setting up LVDTs;
5. Connecting LVDT wires to the terminals of a data logger;
6. Connecting thermocouple wires to a computer system;
7. Connecting electrical furnace cables to the control heating panel;
8. Checking various instrumentations for proper functioning;
9. Preloading and unloading the specimen at least twice to eliminate undesirable slack in the test rig;
10. Initialising all instrumentations;
11. Applying working load to a test specimen at a constant rate and then holding it constant;
12. Connecting supports of restraint beam to reaction frames and applying small loads through the actuator until the load cell at each end gives small readings, indicating proper contact;

13. Applying heat according to the heating curve (Figure 6.6) until the applied working load cannot be sustained by the test specimen.

6.7 Test Results

6.7.1 Unrestrained composite column test

The behaviour of a typical unrestrained composite steel-concrete column under elevated temperature is shown in Figures 6.7 to 6.14. Plots for unrestrained composite column CC03 are shown. A working load P_o of 1723kN was applied to CC03; this value was 70% of the calculated column's design axial load capacity at ambient temperature, based on Eurocode 4 Part 1.1 (1995). Figure 6.7 shows a plot of axial deformation against applied compressive load, during the loading stage.

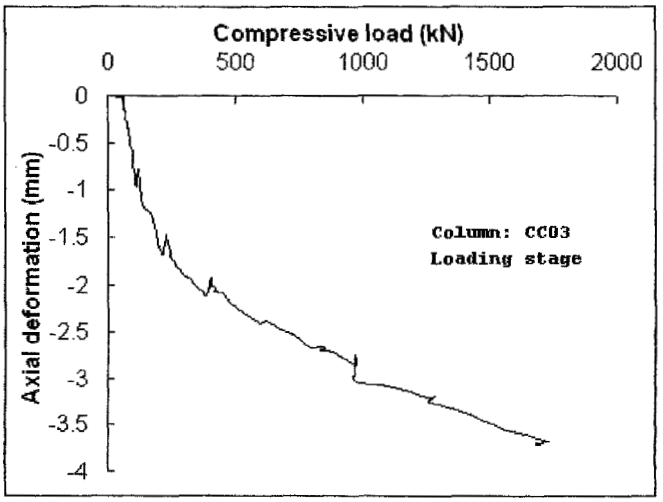

Figure 6.7 Axial deformation-compressive load curve during loading stage for CC03

In Figure 6.7, it should be noted that the axial deformation-compressive load curve was not linear in the beginning. This was due to the presence of inevitable mechanical slack in the 3.54m long test set-up. It took some time for the actuator to close up the thermal gap before full contact was achieved. The loading was done in

increment of 200kN; at every increment of 200kN, the actuator was allowed to stabilise by holding it constant for 5 minutes before increasing the load again. This was the reason for the kinks along the curve in Figure 6.7. When the required axial compressive working load was reached, it was held constant for 20 minutes before heating commenced.

The heating curve used was shown in Figure 6.6. Figure 6.8 shows the temperature readings recorded by the thermocouples attached to the interior walls of a furnace. These thermocouples measured the "gas" temperature in the furnace. The graphs showed that the "gas" temperature in the furnace was uniform and followed the heating curve reasonably closely.

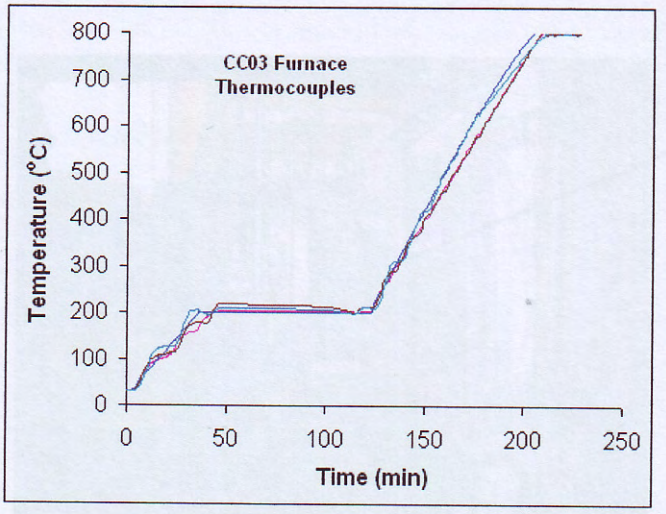

Figure 6.8 Furnace atmospheric temperatures for CC03 test

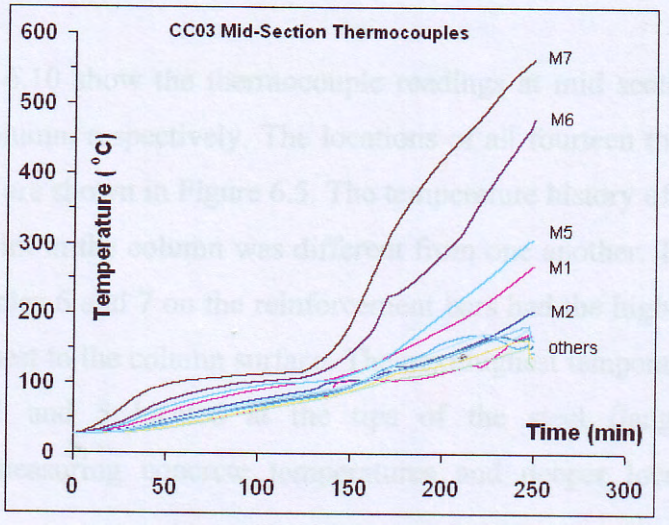

Figure 6.9 Column mid-section temperature profiles for CC03 test

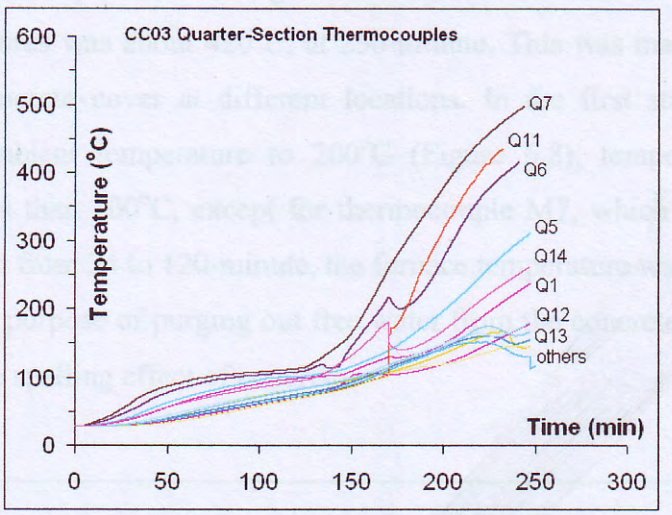

Figure 6.10 Column quarter-section temperature profiles for CC03 test

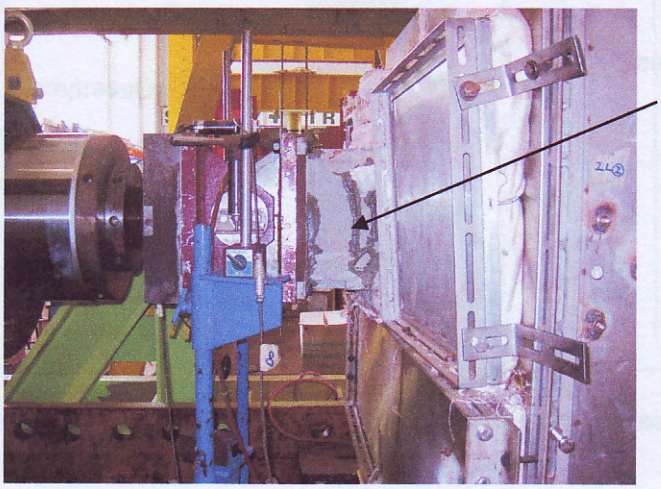

Figure 6.11 Water purging out from end of column

Figures 6.9 and 6.10 show the thermocouple readings at mid section and quarter section of the column, respectively. The locations of all fourteen thermocouples in the cross section are shown in Figure 6.5. The temperature history of each particular thermocouple point in the column was different from one another. Typically at any time, thermocouples 6 and 7 on the reinforcement bars had the highest temperature as they were closest to the column surface. The next highest temperature came from thermocouples 1 and 5 located at the tips of the steel flanges. The other thermocouples measuring concrete temperatures and deeper locations of steel

yielded the lowest temperatures. The greatest difference between the lowest and the highest temperatures was about 420°C, at 250-minute. This was mainly due to the difference in concrete cover at different locations. In the first stage of furnace heating from ambient temperature to 200°C (Figure 6.8), temperatures in the column were less than 100°C, except for thermocouple M7, which was at 100°C. During the period from 34 to 120-minute, the furnace temperature was held constant at 200°C, for the purpose of purging out free water from the concrete (Figure 6.11), so as to minimise spalling effect of concrete.

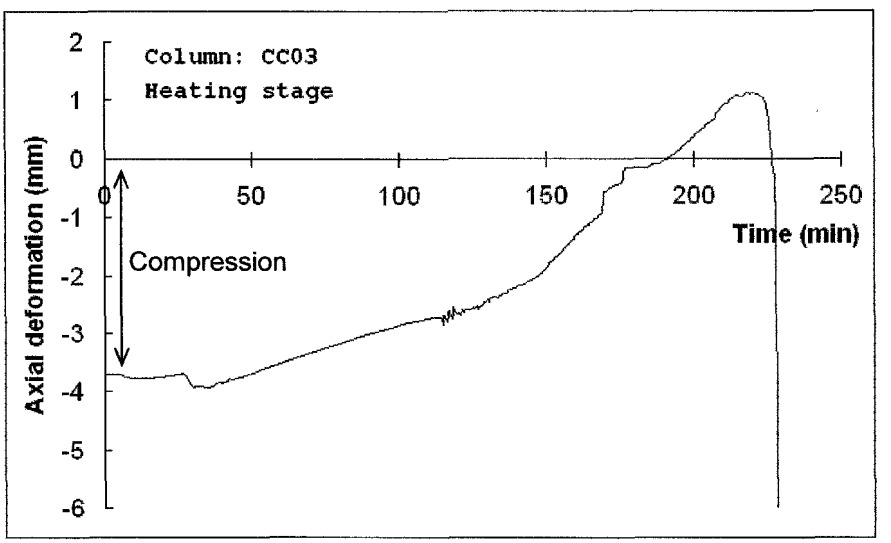

Figure 6.12 Axial deformation-time relationship of CC03 during heating stage

Figure 6.12 shows a plot of axial deformation against time during the heating stage, for composite column CC03. The initial negative axial deformation was due to the application of axial force before heating commenced, as well as the closing of some mechanical slack. In the first stage of heating from ambient temperature to 200°C, the axial deformation curve was rather linear, from time 30 to 110-minute. A sudden slight axial movement was noticed at 30-minute. This was probably due to concrete spalling. During the period from 34 to 120-minute when temperature was held constant, noticeable cracking or spalling of concrete could be heard, signifying that cracks might have occurred. After 120 minutes, the furnace temperature was raised at constant rate of 8°C/min, until the gas temperature was 800°C. Under

constant rising temperature, the applied heat penetrated into the column. An increase in the rate of column expansion was noted in the axial deformation curve in Figure 6.12 after 120 minutes. At 210-minute, the rate of increase in the axial deformation was reduced and mechanical shortening became more important again. At 228-minute, significant axial compression developed, as the composite column was unable to sustain the applied working load. This was indicated as the failure time of composite column CC03.

It was difficult to measure the lateral deformation due to the occurrence of concrete spalling. The LVDT reading at column mid-height showed a sudden change in measurement at 170-minute (Figure 6.13). This was not the actual failure time, which was 228-minute. This phenomenon was probably due to detachment of pieces of concrete at the measuring point, which jolted the measuring ceramic rod. As shown in Figure 6.13, the reading of a lateral displacement of 30mm was not meaningful. Therefore, the mid-height lateral displacement will not be discussed in this composite column test.

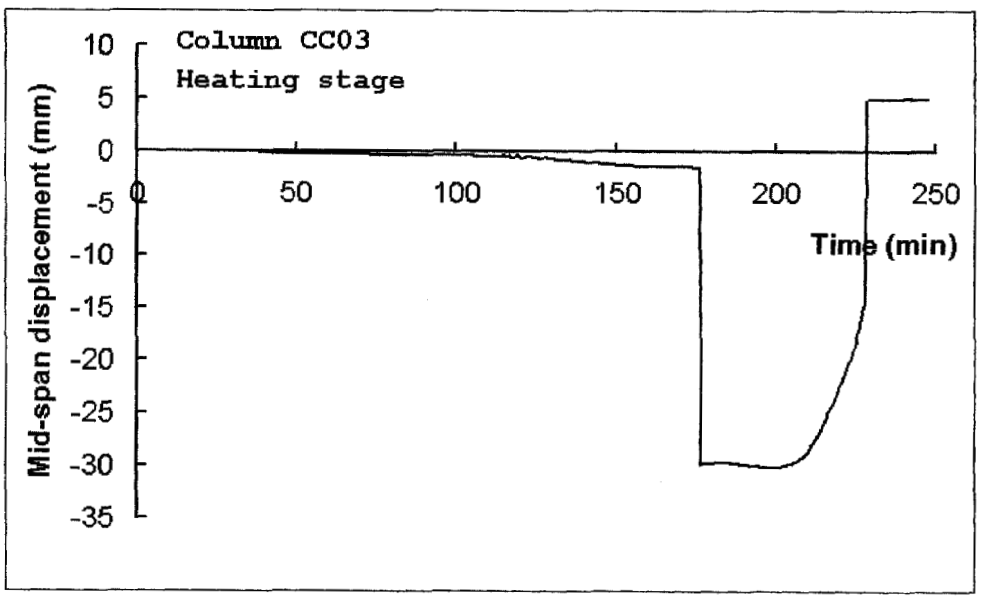

Figure 6.13 Mid-height displacement-time relationship of CC03 during the heating stage

Figure 6.14 shows the failure mode of composite column CC03. Crushing of concrete at the column mid-height was observed. Reinforcement was exposed. Deep cracks in concrete showed that heat could penetrate through the cracks into the steel section, causing thermal elongation and an increase in internal stress. Lateral deflection of column occurred due to a reduction in bending stiffness. A global flexural bending failure was shown.

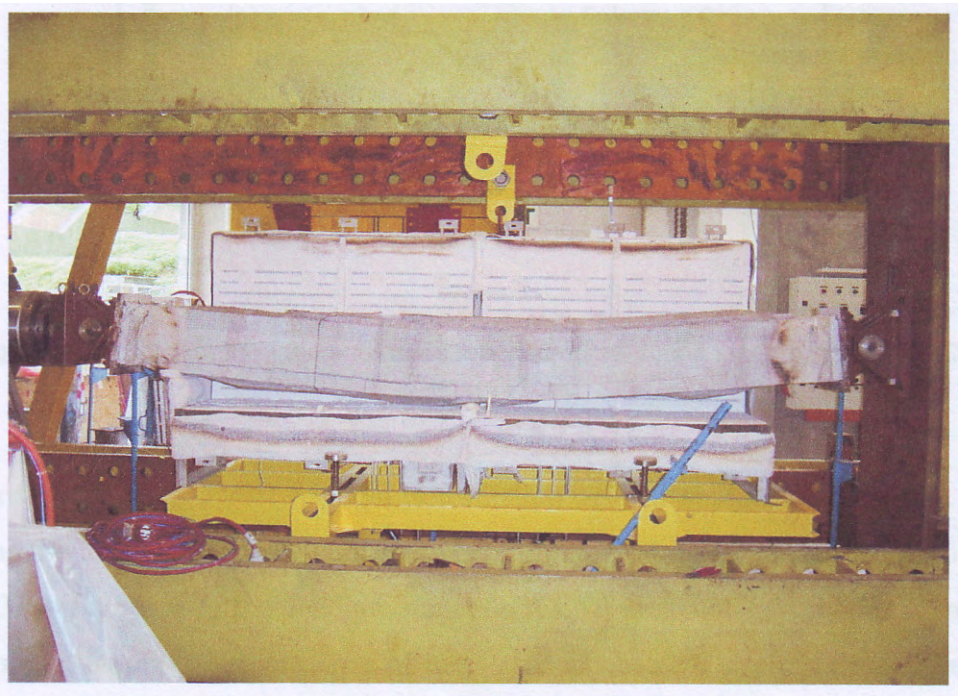

Figure 6.14 Failure mode of composite column CC03

6.7.2 Restrained composite column test

The behaviour of a typical restrained composite steel-concrete column test under elevated temperature is shown in Figures 6.15 to 6.20. Plots for the restrained composite column CC10 are included. A working load P_o of 1105kN was applied to CC10, equivalent to 70% of the design axial load capacity at ambient temperature, calculated in line with Eurocode 4 Part 1.1 (1995). The composite column was restrained by means of a restraint system consisting of a crossbeam and reaction A-frames, similar to the set-up for the steel column test. The cross beam used for

restraining composite column CC10 was UC203x203x60, and the restraint ratio α_k achieved experimentally was 0.09 (Table 6.5).

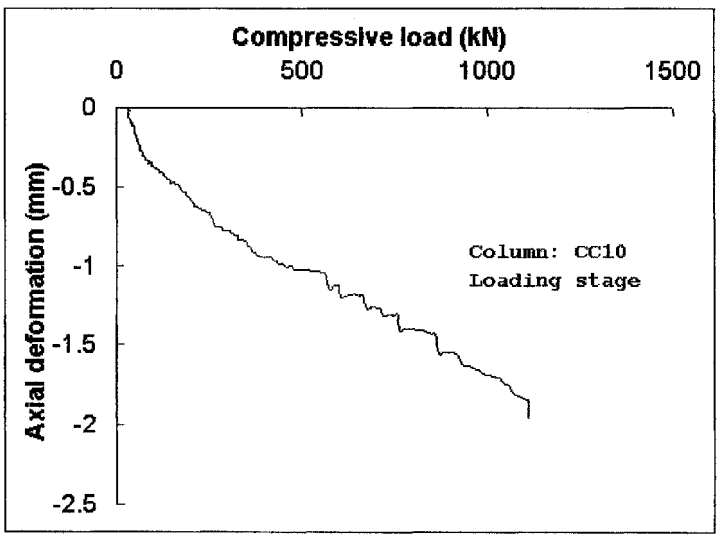

Figure 6.15 Axial deformation-compressive load curve during loading stage for CC10

Figure 6.15 shows a plot of axial deformation against applied compressive load, during the loading stage, for composite column CC10. Similar to composite column CC03 in Figure 6.7, the loading stage for CC10 was not exactly linear in the beginning, owing to the presence of inevitable mechanical slack in the test set-up, and "noises" were noted along the loading curve.

Figure 6.16 shows the gas temperature readings in the furnace, and Figure 6.17 the thermocouple readings at the mid section along the column. Similar to all other composite column tests, the concrete and steel temperatures in CC10 were always lagging behind the gas temperature, due to insulation by concrete cover. Thermocouple temperature readings at M6 and M7 rose rapidly as they were nearest to the column surface, where concrete cover was the least. Besides they measured the temperatures of steel reinforcement. Temperature difference between any other thermocouples was less than 100°C. During the test, some thermocouples were damaged. Those temperature readings were not plotted. In CC10 test, thermocouples M13, Q1, Q6, Q10 and Q13 were damaged.

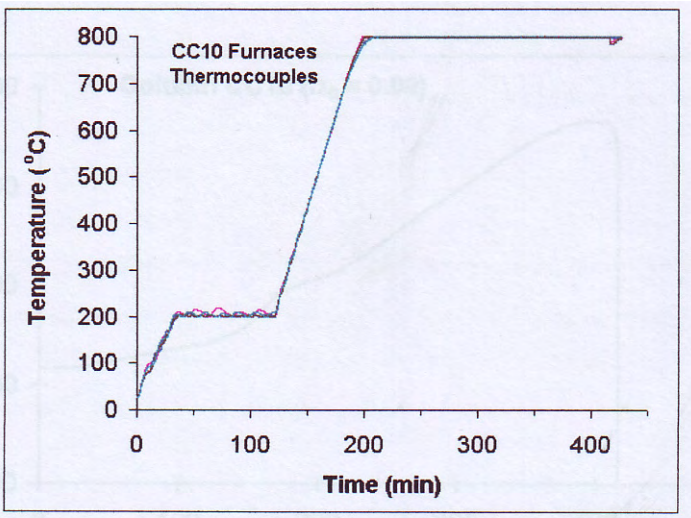

Figure 6.16 Furnace atmospheric temperatures for CC10 test

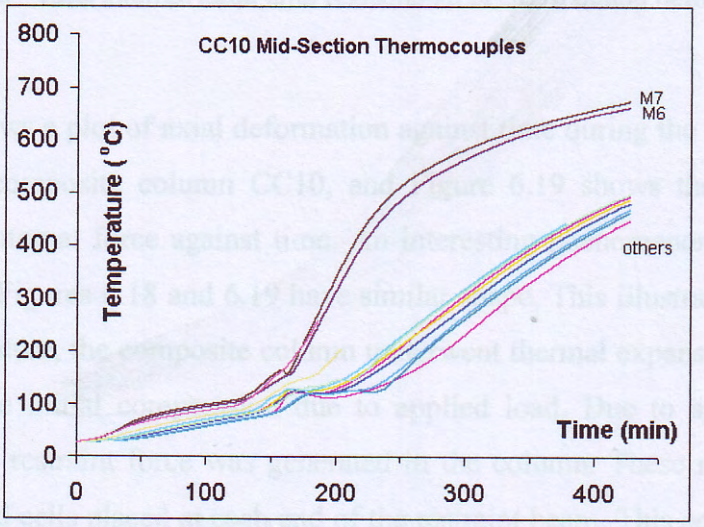

Figure 6.17 Column cross-sectional temperature profiles for CC10 test

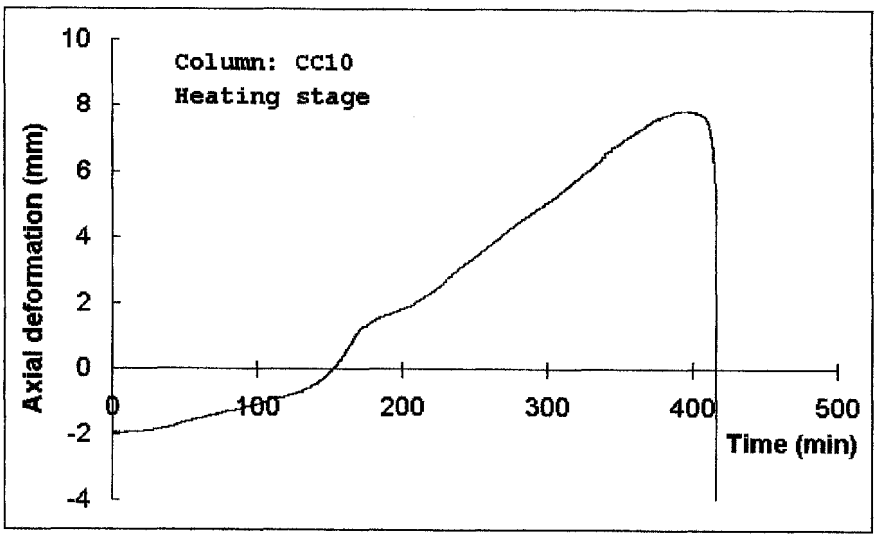

Figure 6.18 Axial deformation-time relationship of CC10 during heating stage

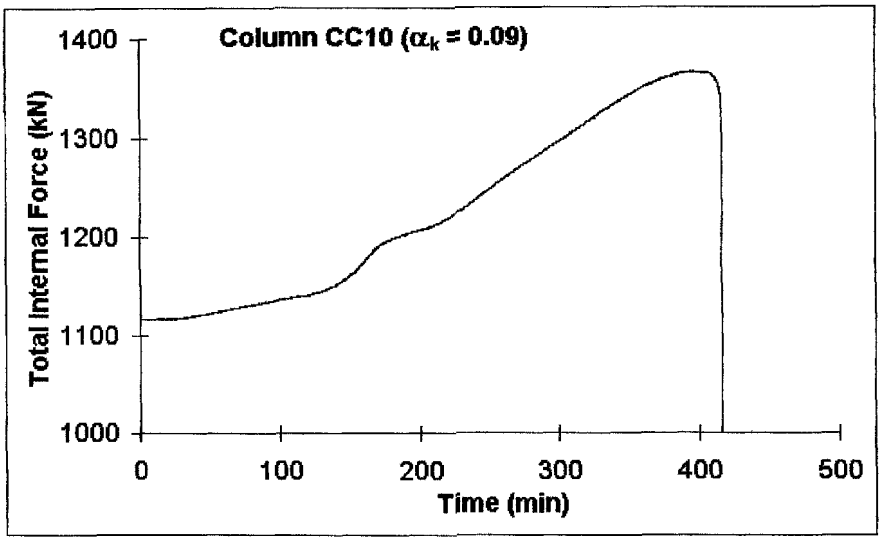

Figure 6.19 Total internal force-time relationship of CC10 during heating stage

Figure 6.18 shows a plot of axial deformation against time during the heating stage, for restrained composite column CC10, and Figure 6.19 shows the relationship between total internal force against time. An interesting phenomenon is observed. Both curves in Figures 6.18 and 6.19 have similar shape. This illustrates that under a rising temperature, the composite column underwent thermal expansion first. This counteracted the initial compression due to applied load. Due to axial restraint, additional axial restraint force was generated in the column. These readings were recorded by load cells placed at each end of the restraint beam. This additional axial restraint force was directly proportionally to the axial expansion/deformation of the column. A maximum total internal force reached in CC10 was 1366kN. This was an additional 261kN on top of the initial working load of 1105kN, which was maintained constant. The thermal induced force was equivalent to 24% of the working load. Composite column CC10 buckled at 416-minute.

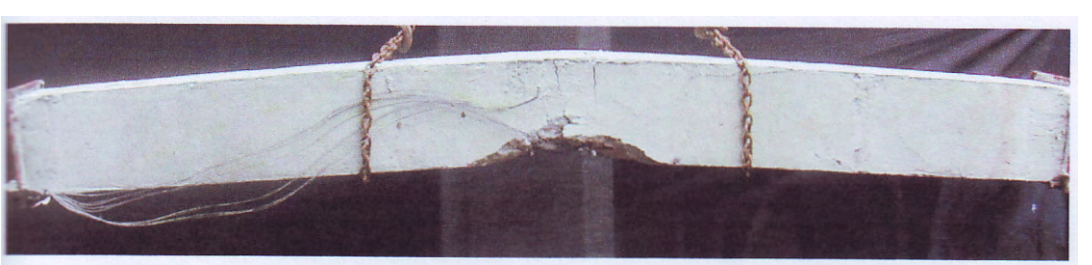

Figure 6.20 Failure mode of restrained composite column CC10

Figure 6.20 shows the failure mode of composite column CC10. Crushing of concrete was observed at mid-section. The column failed by global flexural bending.

In the next chapter, results of all three series of composite column tests are compared and discussed with predictions from finite element analysis.

CHAPTER SEVEN

Experimental Results and Finite Element Analysis of Composite Steel-Concrete Column Tests

7.1 Introduction

This chapter summarises the test results for the composite steel-concrete column series and predictions from finite element analysis. The program FEMFAN was also used here predicting the results of the composite column tests. As FEMFAN-3D was still under development at the time of writing, it was unable to perform heat transfer analysis for composite columns. The program SAFIR was used to perform the heat transfer analysis instead. In SAFIR modelling of thermal response, the entire column cross section was discretised into 182 rectangular elements and 210 nodes. The discretisation was in line with that used in the program FEMFAN-3D. In the cross section, each steel reinforcement of diameter 13mm and area 133mm^2 was assigned as a rectangular element. A time step of 10 to 20 seconds was used in the thermal analysis. Taking composite column CC02 as an example, Figure 7.1 shows the discretisation of the composite column cross section, and Figure 7.2 shows the output of the thermal analysis at 240-minute. In the test, the composite column with an effective length of 3.54m was heated in the middle portion of 3m, with two ends of length 270mm each remained unheated outside the furnace at ambient temperature. As explained, this was because of the limited length of existing furnace. In SAFIR, similar profile along the column length was modelled. The midspan of 3m was heated under a similar temperature profile, and the two ends of length 270mm remained at ambient temperature throughout the test.

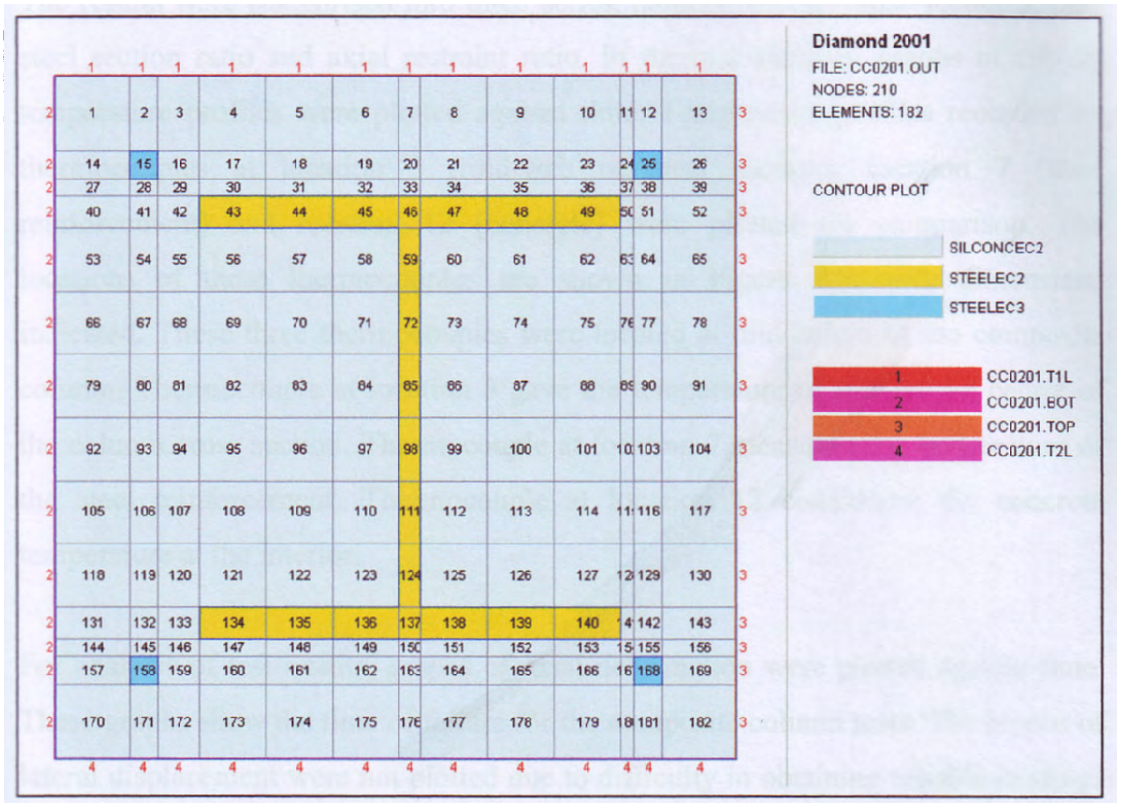

Figure 7.1 Discretisation of a composite column cross section in SAFIR

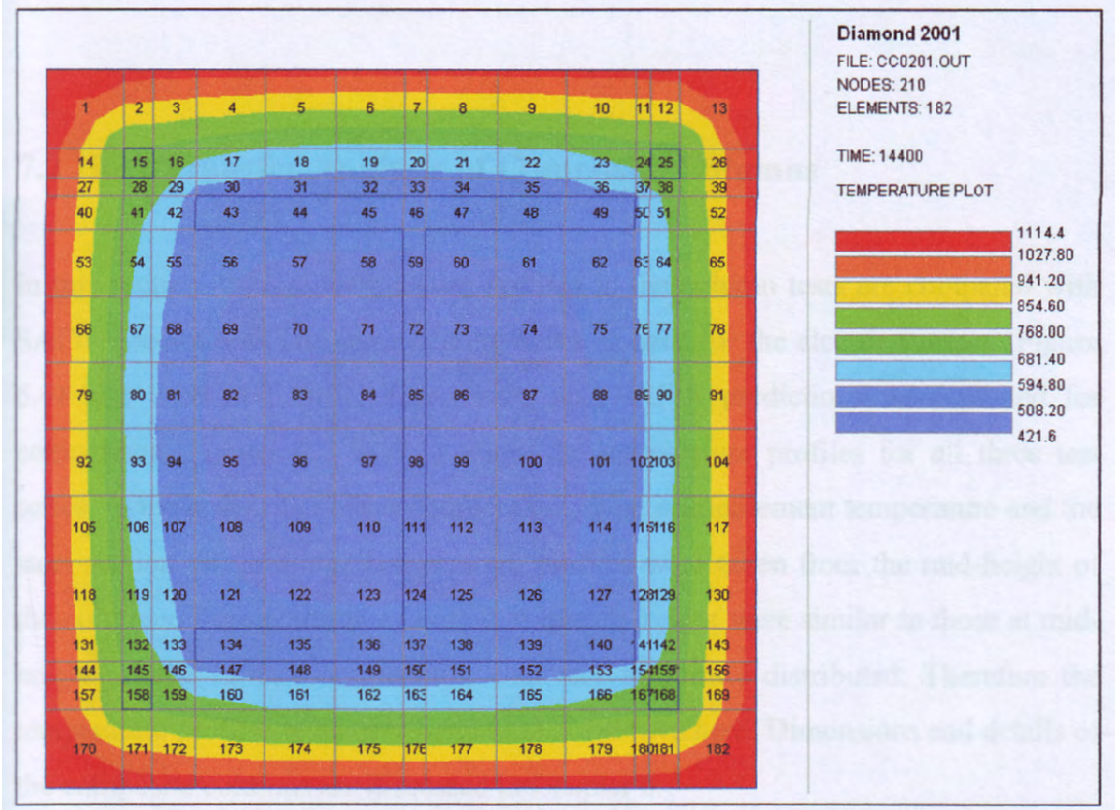

Figure 7.2 Output of SAFIR thermal analysis

The results were categorised into three series, namely, overall cross-sectional size, steel section ratio and axial restraint ratio. In thermal analysis, graphs of critical temperature profiles were plotted against time. Temperature profiles recorded by thermocouples at location 3 (mid-web of steel section), location 7 (steel reinforcement) and location 12 (concrete) were plotted for comparison. The locations of these thermocouples are shown in Figure 6.5, with dimensions indicated. These three thermocouples were located at mid-height of the composite column. Thermocouple at location 3 gave the temperature of steel at the centre of the column cross section. Thermocouple at location 7 measured the temperature of the steel reinforcement. Thermocouple at location 12 considered the concrete temperature at the interior.

For analysis of test results, graphs of axial deformation were plotted against time. These graphs show the time of failure for the composite column tests. The graphs of lateral displacement were not plotted due to difficulty in obtaining reliable readings during test, as occurrence of concrete cracking and spalling had caused disruption to the measurements.

7.2 Heat Transfer Analysis of Composite Columns

In this section, critical temperature profiles in the column tests are compared with SAFIR predictions. The same heating curve as used for the electric furnace (Figure 6.6) was used in SAFIR. Test results and SAFIR predictions were plotted for comparison. Figures 7.3 to 7.11 show the temperature profiles for all three test series, in the order of concrete temperature, steel reinforcement temperature and the steel section temperature. Temperature profiles were taken from the mid-height of the columns. Temperatures measured at quarter-height were similar to those at mid-height, as the furnace temperature was very uniformly distributed. Therefore the temperature profiles at quarter-height are not shown here. Dimensions and details of the composite columns are discussed in Chapter 6.

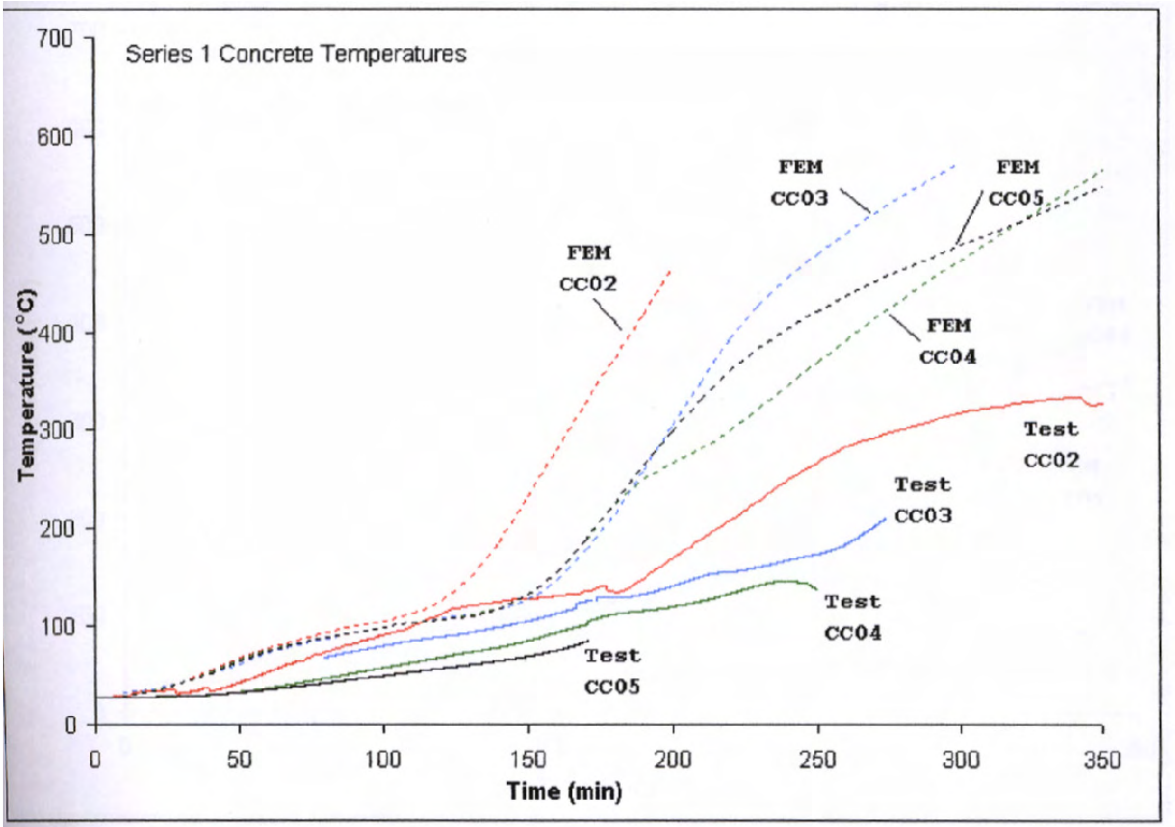

Figure 7.3 Experimental and FEM temperature profiles of concrete for Series 1 composite column tests

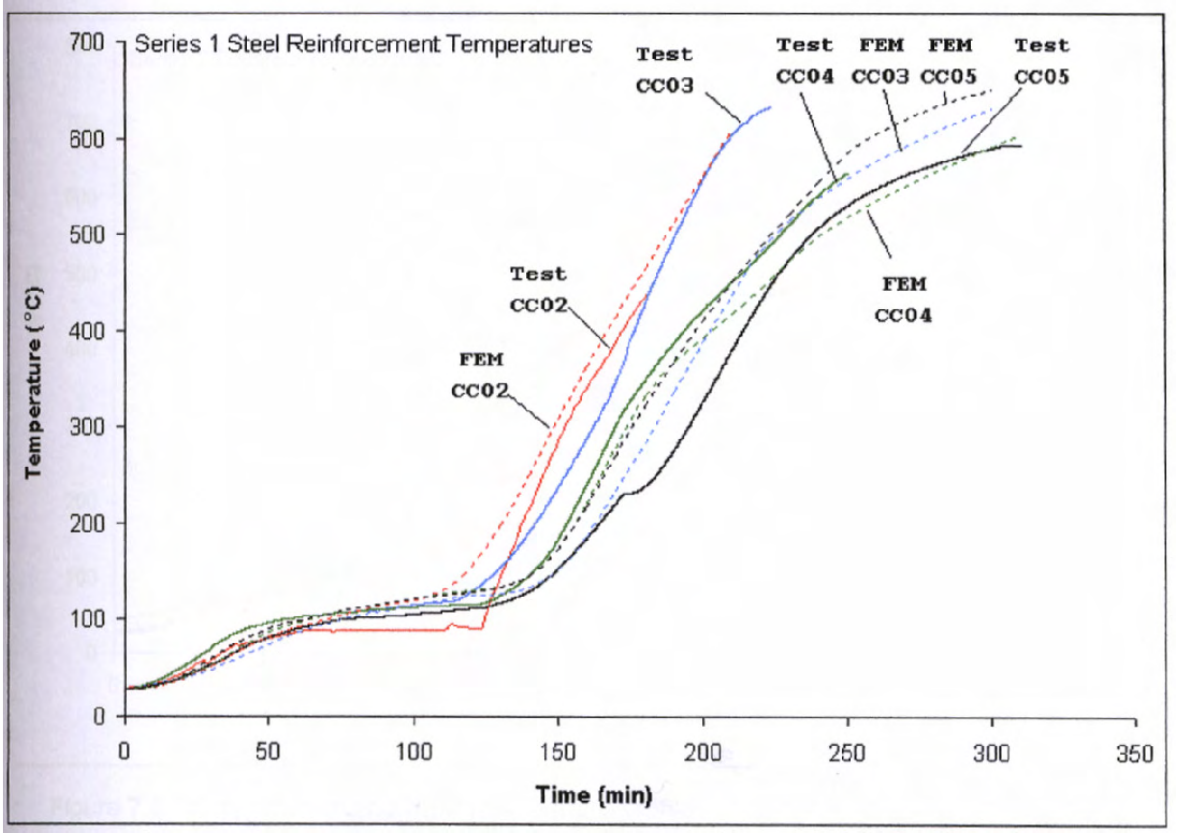

Figure 7.4 Experimental and FEM temperature profiles at steel reinforcement for Series 1 composite column tests

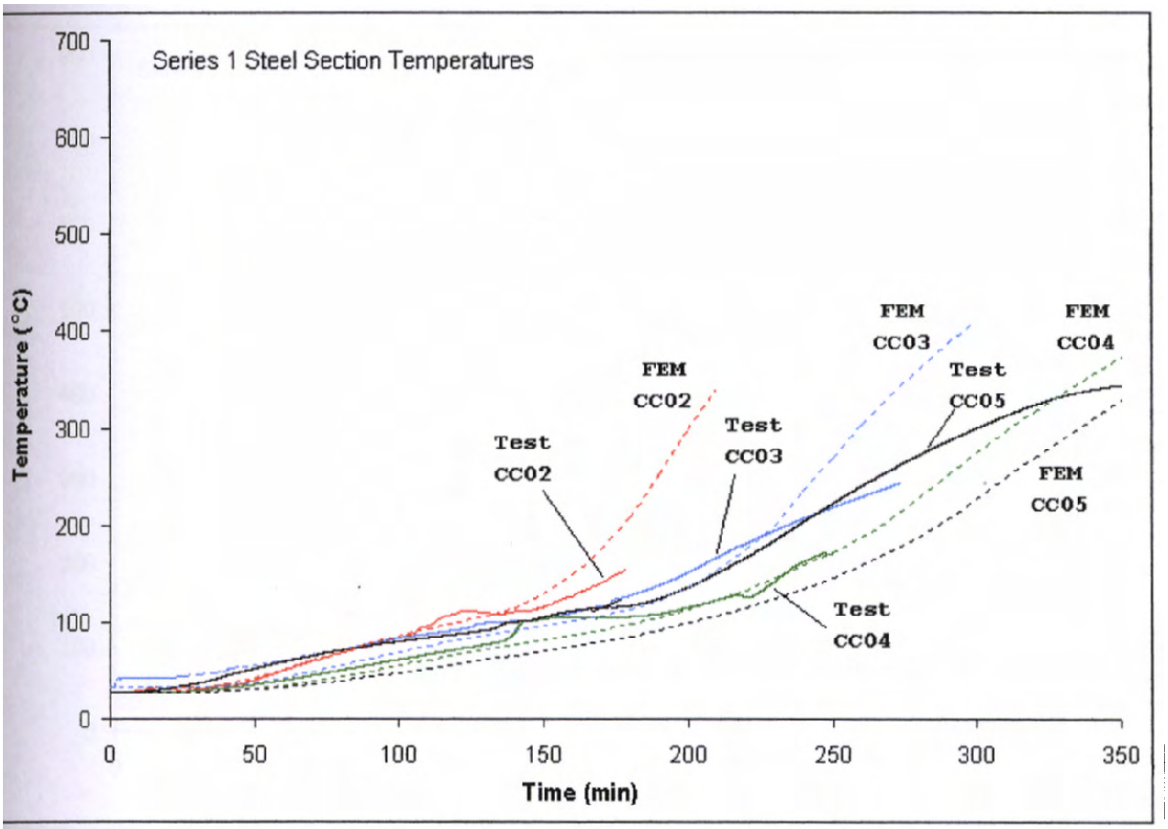

Figure 7.5 Experimental and FEM temperature profiles at mid-web of steel section for Series 1 composite column tests

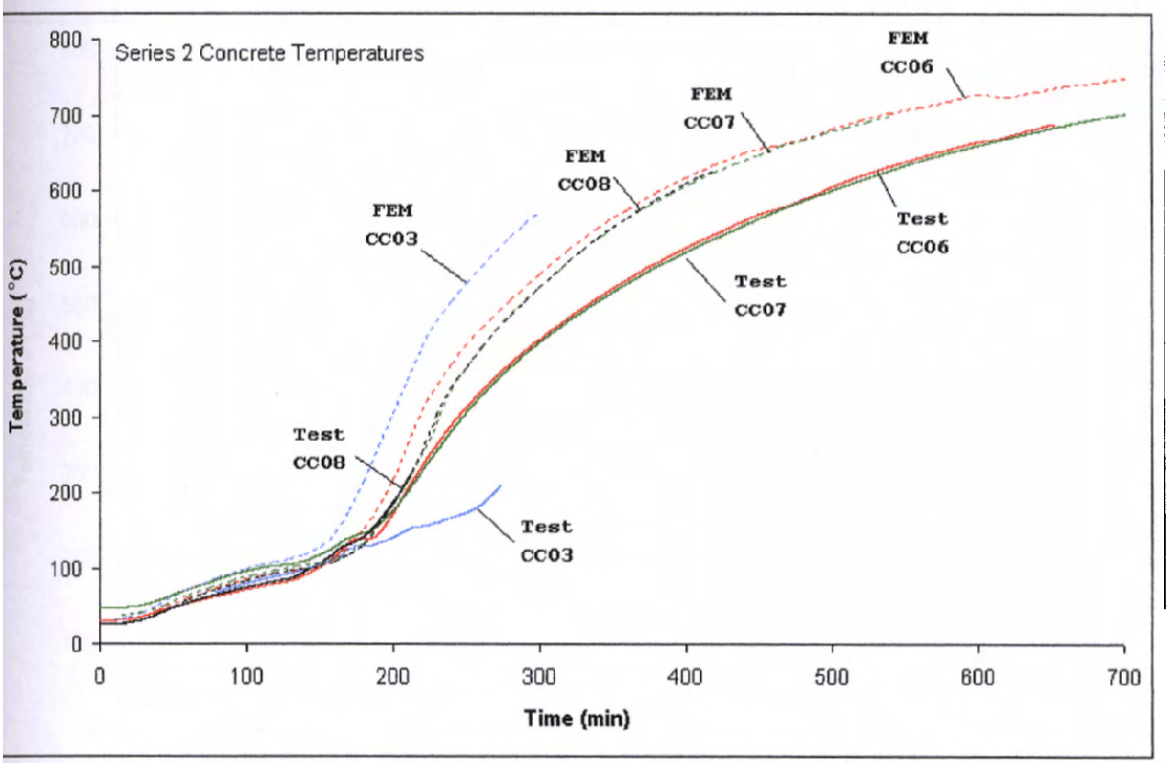

Figure 7.6 Experimental and FEM temperature profiles of concrete for Series 2 composite column tests

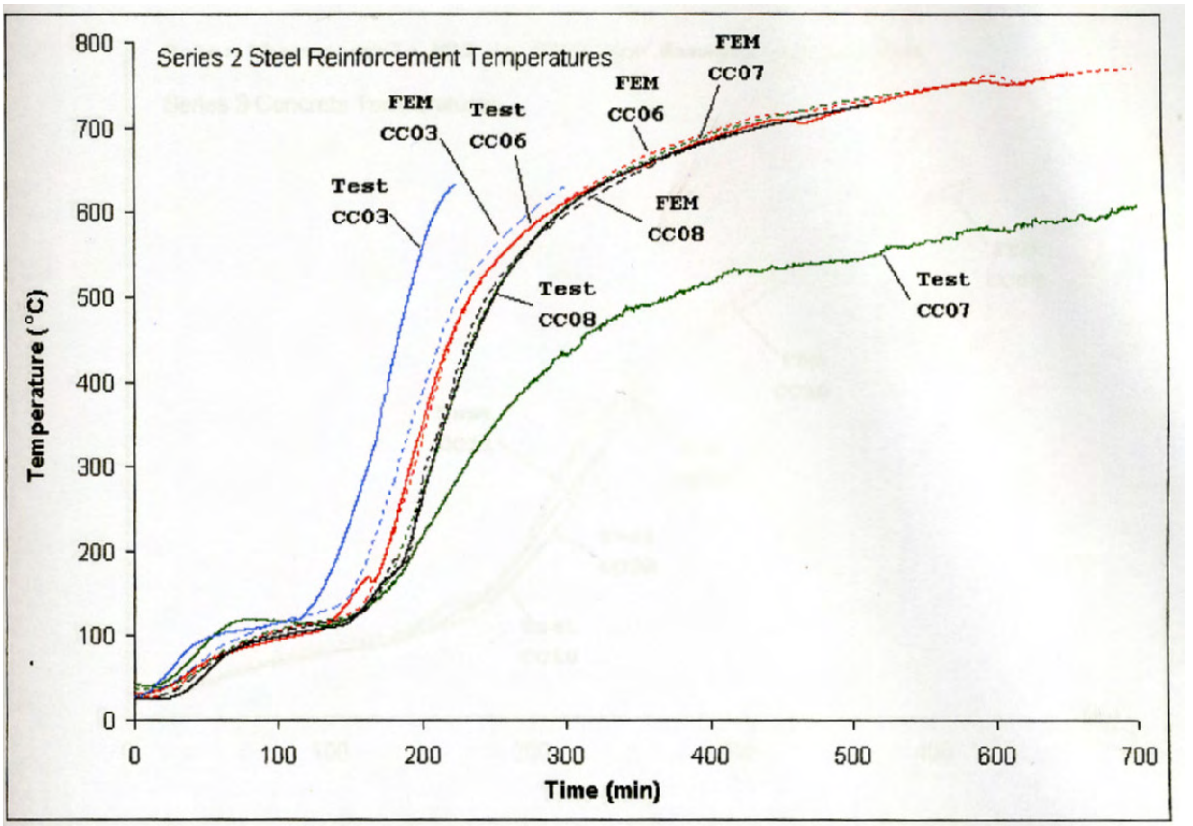

Figure 7.7 Experimental and FEM temperature profiles at steel reinforcement for Series 2 composite column tests

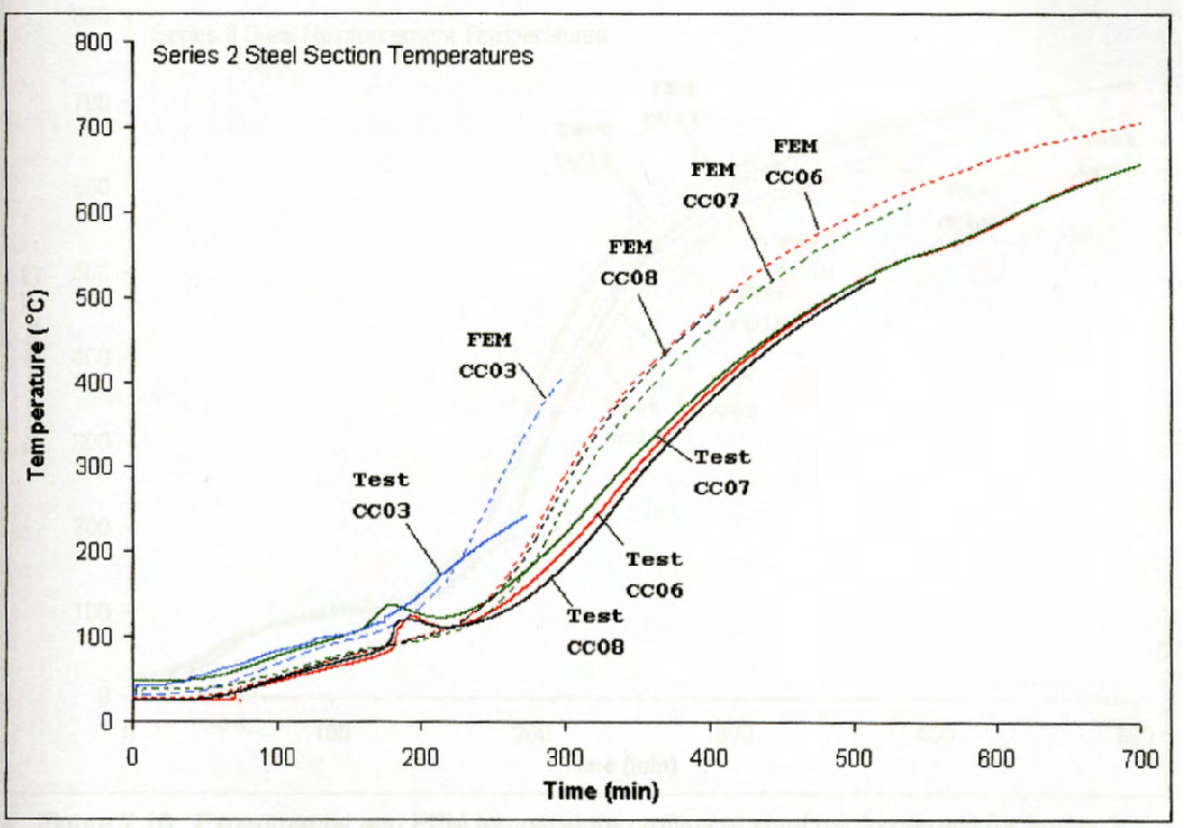

Figure 7.8 Experimental and FEM temperature profiles at mid-web of steel section for Series 2 composite column tests

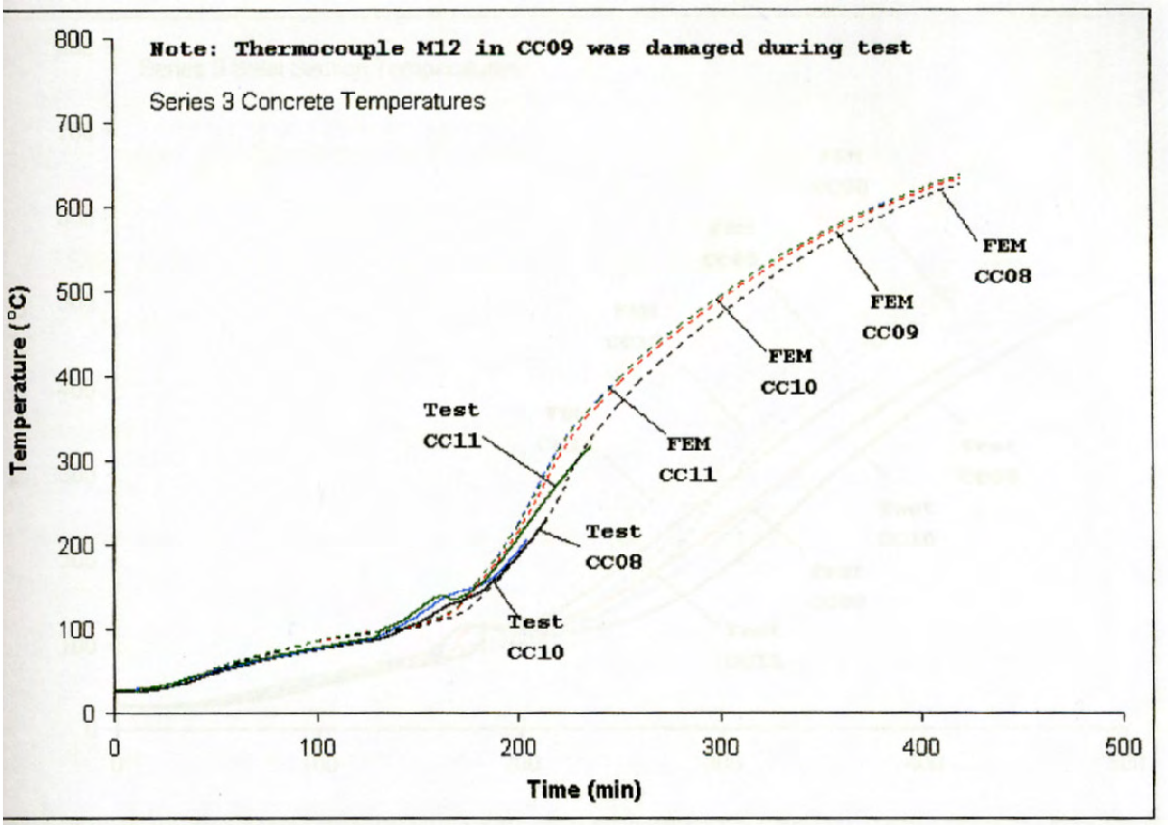

Figure 7.9 Experimental and FEM temperature profiles of concrete for Series 3 composite column tests

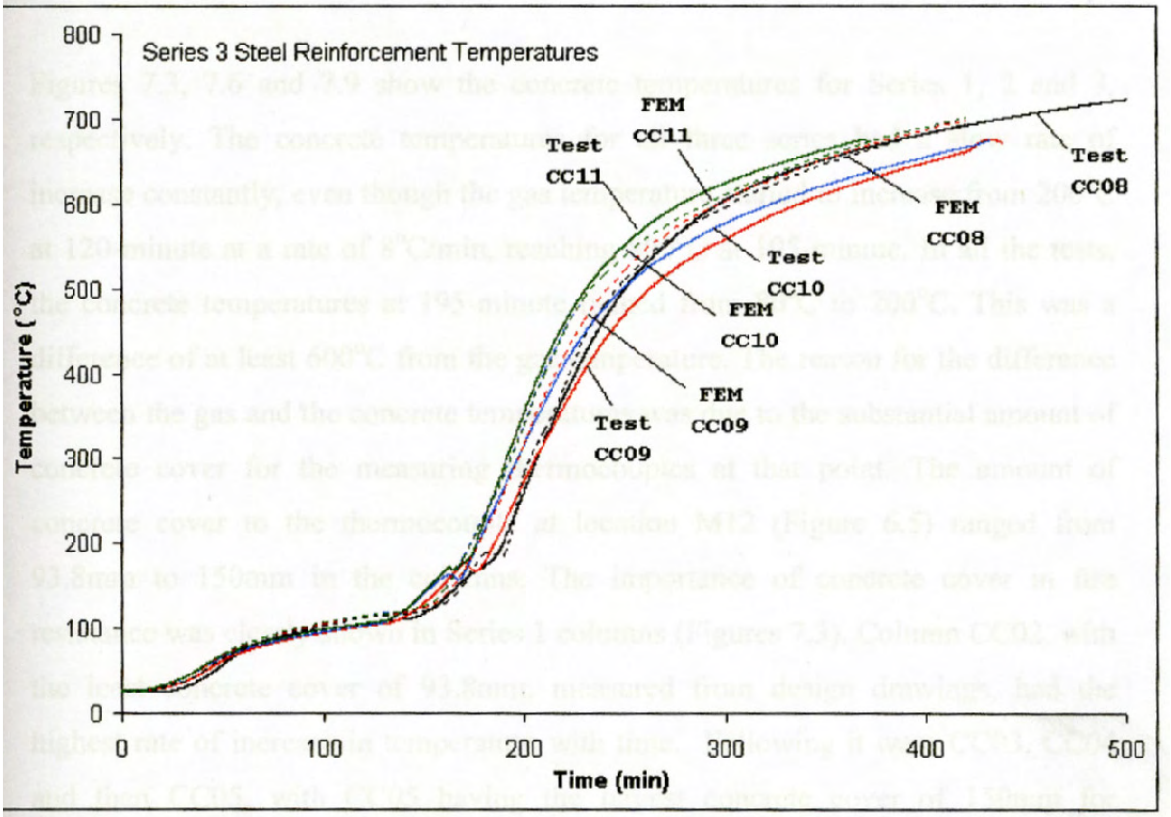

Figure 7.10 Experimental and FEM temperature profiles at steel reinforcement for Series 3 composite column tests

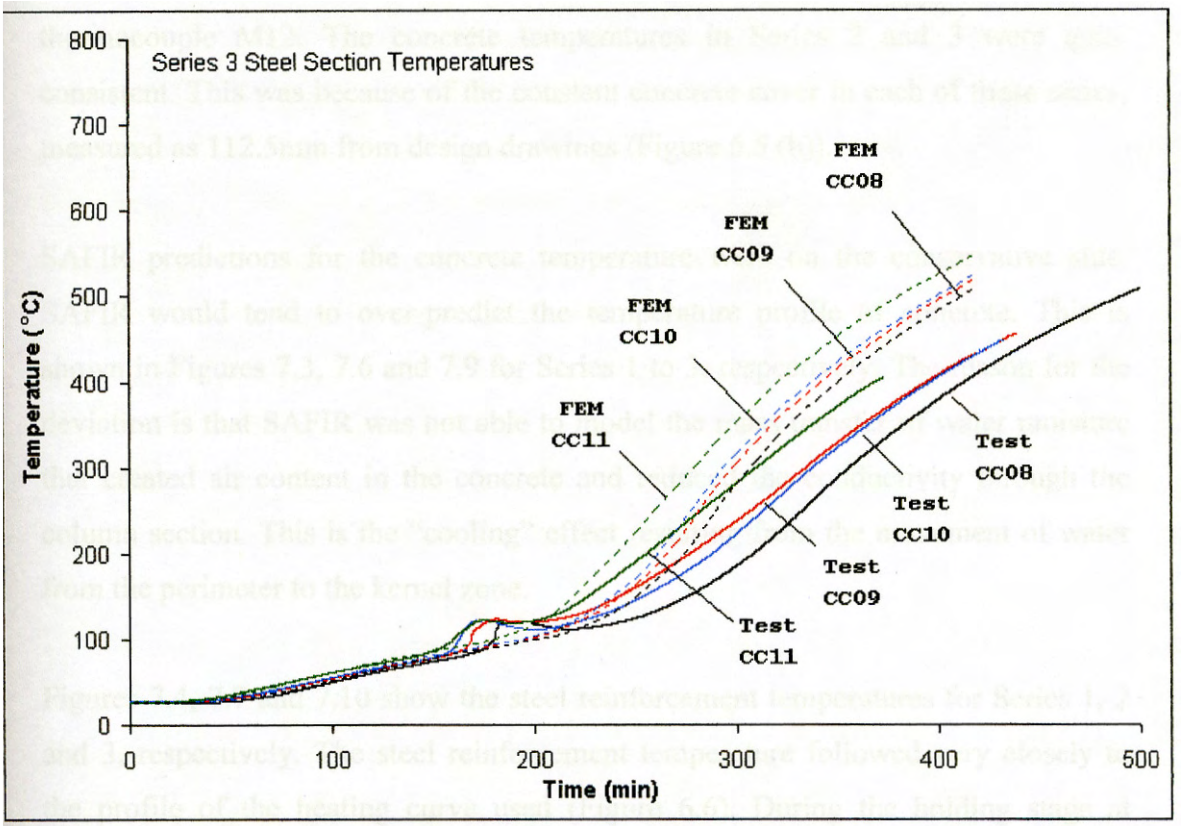

Figure 7.11 Experimental and FEM temperature profiles at mid-web of steel section for Series 3 composite column tests

Figures 7.3, 7.6 and 7.9 show the concrete temperatures for Series 1, 2 and 3, respectively. The concrete temperatures for all three series had a slow rate of increase constantly, even though the gas temperature started to increase from 200°C at 120-minute at a rate of 8°C/min, reaching 800°C at 195-minute. In all the tests, the concrete temperatures at 195-minute ranged from 80°C to 200°C. This was a difference of at least 600°C from the gas temperature. The reason for the difference between the gas and the concrete temperatures was due to the substantial amount of concrete cover for the measuring thermocouples at that point. The amount of concrete cover to the thermocouple at location M12 (Figure 6.5) ranged from 93.8mm to 150mm in the columns. The importance of concrete cover in fire resistance was clearly shown in Series 1 columns (Figures 7.3). Column CC02, with the least concrete cover of 93.8mm, measured from design drawings, had the highest rate of increase in temperature with time. Following it were CC03, CC04 and then CC05, with CC05 having the largest concrete cover of 150mm for

thermocouple M12. The concrete temperatures in Series 2 and 3 were quite consistent. This was because of the constant concrete cover in each of these series, measured as 112.5mm from design drawings (Figure 6.5 (b)).

SAFIR predictions for the concrete temperature were on the conservative side. SAFIR would tend to over-predict the temperature profile of concrete. This is shown in Figures 7.3, 7.6 and 7.9 for Series 1 to 3, respectively. The reason for the deviation is that SAFIR was not able to model the mass transfer of water moisture that created air content in the concrete and reduced the conductivity through the column section. This is the "cooling" effect resulting from the movement of water from the perimeter to the kernel zone.

Figures 7.4, 7.7 and 7.10 show the steel reinforcement temperatures for Series 1, 2 and 3, respectively. The steel reinforcement temperature followed very closely to the profile of the heating curve used (Figure 6.6). During the holding stage at 200°C, the temperatures of the steel reinforcement were around 100°C. When furnace temperature started to rise linearly to 800°C, the temperature of steel reinforcement started to increase too. The main factor that affected the temperature profile of steel reinforcement was the amount of concrete cover present. SAFIR predicted reasonably well for the steel reinforcement temperatures of CC06 and CC08 in Series 2 columns, but not so well for CC03 and CC07. From Figure 7.7, Column CC03 steel reinforcement experienced a much faster rate of increase in temperature than the FEM prediction. At 200-minute, FEM read 390°C while in the test, it was already 560°C for CC03 steel reinforcement. This rapid increase in temperature in the test might be due to some spalling of concrete in the earlier state, which could not be modelled in FEM. Figure 7.10 shows the temperature histories of the steel reinforcement in Series 3 specimens. SAFIR predictions for these were very close to test results. The four columns in this series of tests had very close temperature profiles in the test; this was because these four columns were of similar sizes and dimensions.

Figures 7.5, 7.8 and 7.11 show the steel section temperatures for Series 1, 2 and 3, respectively. The temperature at the innermost location of the composite column was located at mid-web of the steel section. This location had the maximum concrete cover from the exterior surface of the specimen. Generally, this point had a very slow rate of increase in temperature, owing to insulation from concrete, which had a low thermal conductivity compared to steel. In Series 1 composite columns design drawings, the concrete covers to the top flanges of the steel sections were found to be 44.1mm, 47.9mm, 47.7mm and 46.1mm, for Columns CC02 to CC05 respectively. The thinner concrete cover in CC02 contributed to the higher rate of increase in temperature to the steel section (Figure 7.5).

From Series 2 columns' cross-sectional dimensions, in order of ascending steel section ratios, the concrete covers to the top flanges of the steel sections were 72.2mm, 84.6mm, 68.2mm and 47.9mm, for Columns CC06, CC07, CC08 and CC03, respectively. The thinner concrete cover in CC03 resulted in a higher rate of increase of temperature in the steel section (Figures 7.7 and 7.8). All the other steel section temperature profiles were quite similar in the tests.

Figure 7.5 shows reasonable closeness between SAFIR steel section temperature predictions and tests for Series 1. However, from Figures 7.8 and 7.11, they show obvious differences between SAFIR and tests for the steel section temperatures in Series 2 and 3, where SAFIR predicted a higher rate of increase in temperature. This was because the mass transfer of water, from the perimeter of a cross-section (which was subjected to 4-face heating) to the centre of the section was not accounted for in SAFIR. Under such movement of water to the relatively cooler parts of a section, the temperature increase rate at the centre zone was noticeably reduced as shown in the figures. Beyond 300 minutes of heating, the difference between test data and numerical prediction maintained at around 100°C. This increased the overall specific heat of the specimen and delayed the heat transfer process to encased I-section.

On the whole, there were a few important factors that posed a great impact on the heat transfer across the composite column section. Firstly, spalling of concrete creates voids in the section and increases the rate of heat transfer from the exterior heated surface. SAFIR, which does not consider concrete spalling, tends to underestimate the temperature profile should this happen. Secondly, mass transfer of water moisture that creates air content in the concrete will reduce the conductivity through the column section. This "cooling" effect resulting from the movement of water from the perimeter zone to the kernel one will reduce the actual rate of temperature increase. SAFIR does not consider water moisture movement and tends to overestimate the temperature profile when water movement occurs. Thirdly, the thermal properties of concrete from EC3 (2000b) incorporated in SAFIR, such as thermal conductivity and specific heat may defer from the actual values. This will lead to either over or underestimation of heat transfer within the concrete section. Lastly, the electrical furnace might experience time lag where its heating was actually slower than the intended heating curve.

From Figures 7.3 to 7.5, SAFIR predictions for Series 1 heat transfer analysis were very close for CC03 and CC04 in their steel section temperatures, up to the time of column failure. CC02 steel section temperature was close to SAFIR prediction for the first 140 minutes, but was over-predicted for the next 47 minutes towards column failure. CC05 steel reinforcement temperature was overestimated but its steel section temperature was underestimated. It was difficult to obtain any improvement for CC02 and CC05 temperature predictions. SAFIR heat transfer analyses for Series 1 shown in Figures 7.3 to 7.5 were used as the heat transfer input files in FEMFAN-3D for structural analysis. SAFIR heat transfer analyses for Series 2 and 3 were found to overestimate the test results, as shown in Figures 7.6 to 7.11. It was especially so in the case of the steel section temperatures (Figure 7.8 (Series 2) and Figure 7.11 (Series 3)). Table 7.1 shows a comparison of the steel section temperatures between tests and SAFIR predictions, at the instant when individual columns failed in the actual test. It shows only the temperature at the time of each column failure. In Series 1, Column CC02 steel section temperature was overestimated at the time of actual column failure, but its earlier temperature

prediction was closer to test (Figure 7.5). Column CC05, as discussed earlier, was overestimated for steel reinforcement temperature but underestimated for steel section temperature. Steel section temperatures for Columns CC06 to CC11 in Series 2 and 3 were all overestimated in SAFIR. Steps were taken to achieve closer temperature profile predictions in SAFIR for use in FEMFAN-3D structural analysis. This is discussed in the following section.

Table 7.1 Experimental and SAFIR steel section temperatures at the end of actual test

Series	Column Marking	$t_{cr,test}$ (min)	$T_{cr,test}$ (°C)	$T_{cr,SAFIR}$ (°C)	$\frac{T_{cr,SAFIR}}{T_{cr,test}}$
Series 1	CC02	187	154	200	1.30
	CC03	229	193	194	1.01
	CC04	247	171	169	0.99
	CC05	290	286	195	0.68
Series 2	CC06	651	628	685	1.09
	CC07	554	555	615	1.11
	CC08	414	402	500	1.24
	CC03	229	193	194	1.01
Series 3	CC08	414	402	500	1.24
	CC09	417	430	510	1.19
	CC10	422	436	525	1.20
	CC11	366	396	469	1.18

7.3 Improved Heat Transfer Analysis in SAFIR

As discussed in Section 7.2, the electrical furnace might be slower than the intended heating curve in heating up the columns. A slightly amended heating curve was used in SAFIR to re-analyse the heat transfer process for Series 2 and 3 columns.

The new heating curve used in SAFIR is shown in Figure 7.12. The only change made to the new heating curve was the small gradient from 195-minute to the end, increasing the temperature from 700°C to 800°C. This new SAFIR input heating curve was close to the actual tests in Series 2 and 3, and would compensate for any delay in the heat transfer process.

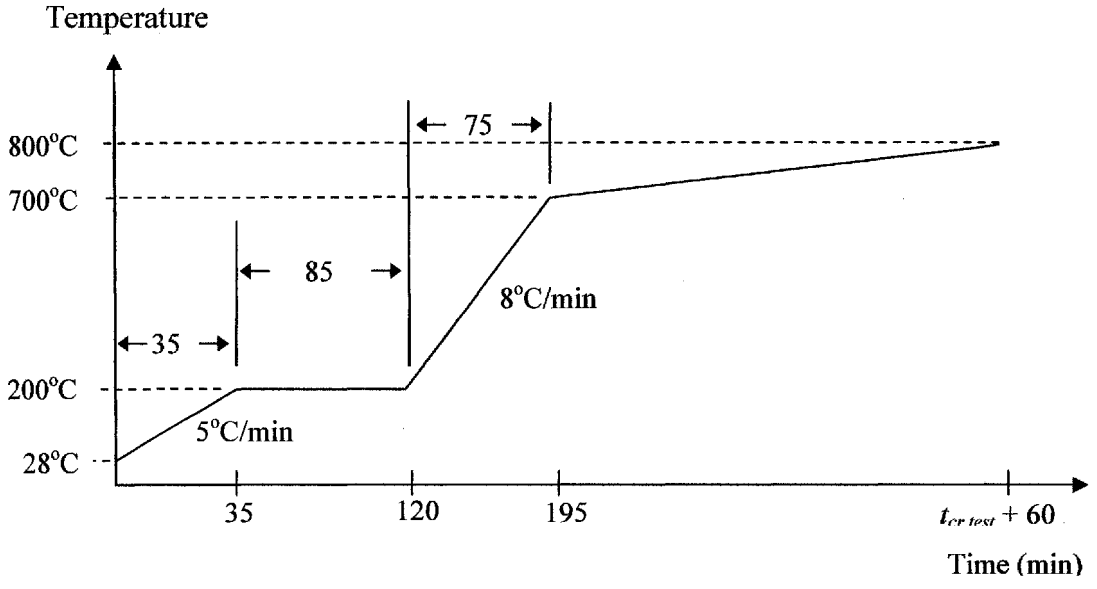

Figure 7.12 Modified heating curve applied in SAFIR

Figures 7.13 to 7.18 show the improved SAFIR predictions for the heat transfer analysis of Series 2 and 3 columns. The figures show the temperature profiles in the order of concrete temperature, steel reinforcement temperature and the steel section temperature. The use of the new heating curve (Figure 7.12) in SAFIR allowed a slower heat transfer across the column cross section after 195 minutes. The steel section and concrete temperatures were closer to test results than before. Table 7.2 shows the improvement in accuracy in the steel section temperature predictions for Series 2 and 3. These heat transfer profiles in Figures 7.13 to 7.18 were used in FEMFAN-3D to analyse the structural response of Series 2 and 3 composite columns.

Table 7.2 Experimental and SAFIR steel section temperatures at the end of actual test after rerunning SAFIR analysis for Series 2 and 3

Series	Column Marking	$t_{cr,test}$ (min)	$T_{cr,test}$ (°C)	$T_{cr,SAFIR}$ (°C)	$\frac{T_{cr,SAFIR}}{T_{cr,test}}$
Series 2	CC06	651	628	641	1.02
	CC07	554	555	580	1.05
	CC08	414	402	465	1.16
	CC03	229	193	194	1.01
Series 3	CC08	414	402	465	1.16
	CC09	417	430	472	1.10
	CC10	422	436	481	1.10
	CC11	366	396	405	1.02

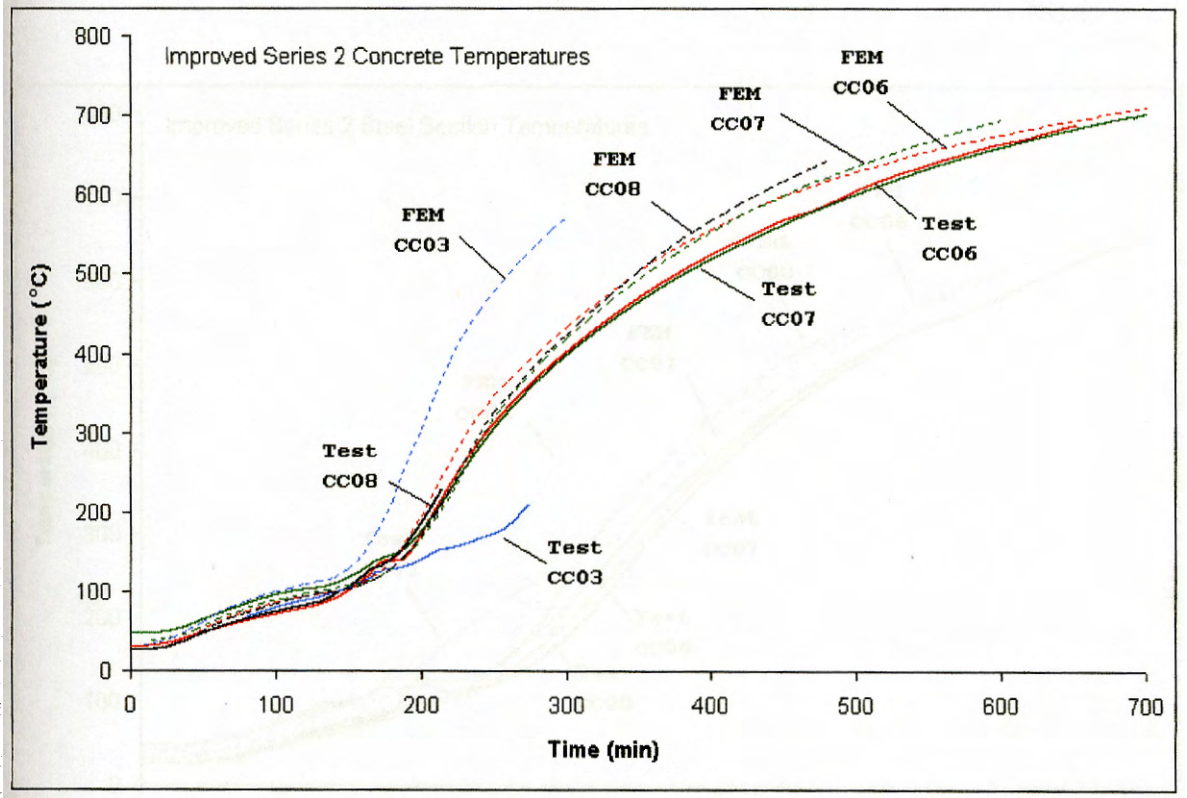

Figure 7.13 Experimental and improved FEM temperature profiles of concrete for Series 2 composite column tests

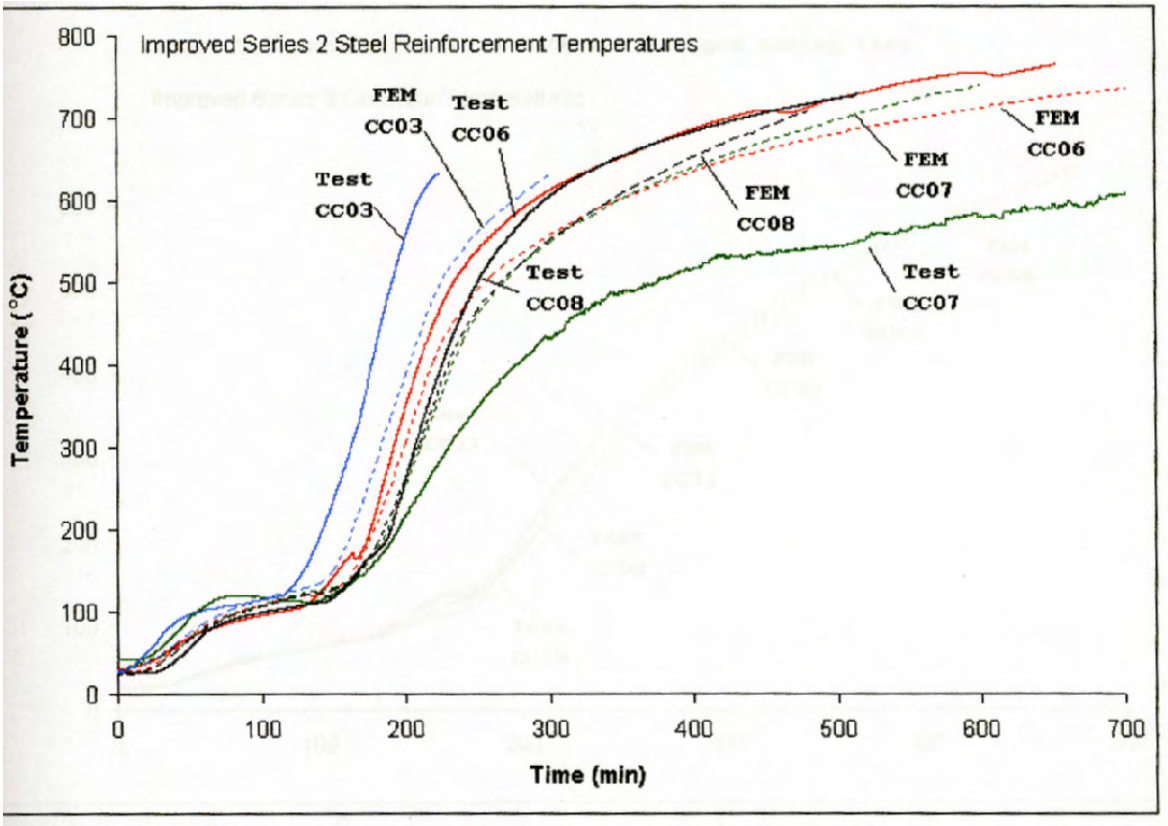

Figure 7.14 Experimental and improved FEM temperature profiles at steel reinforcement for Series 2 composite column tests

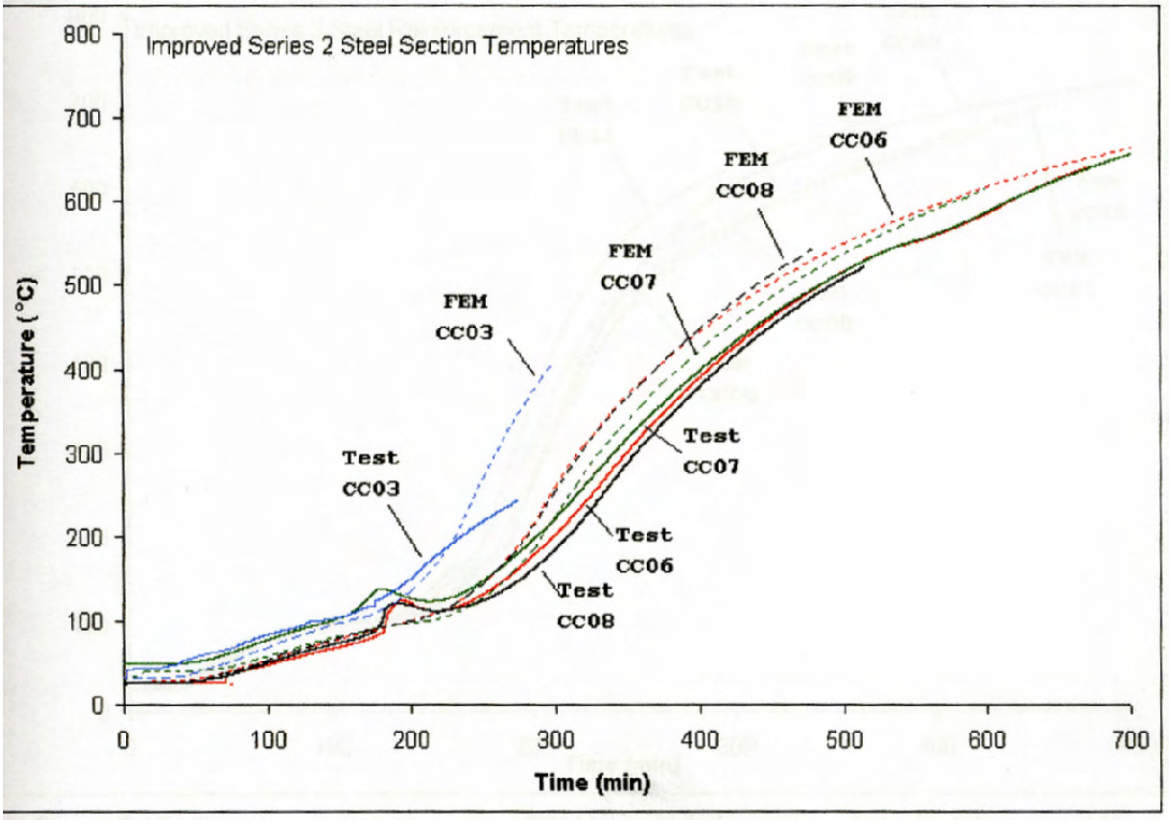

Figure 7.15 Experimental and improved FEM temperature profiles at mid-web of steel section for Series 2 composite column tests

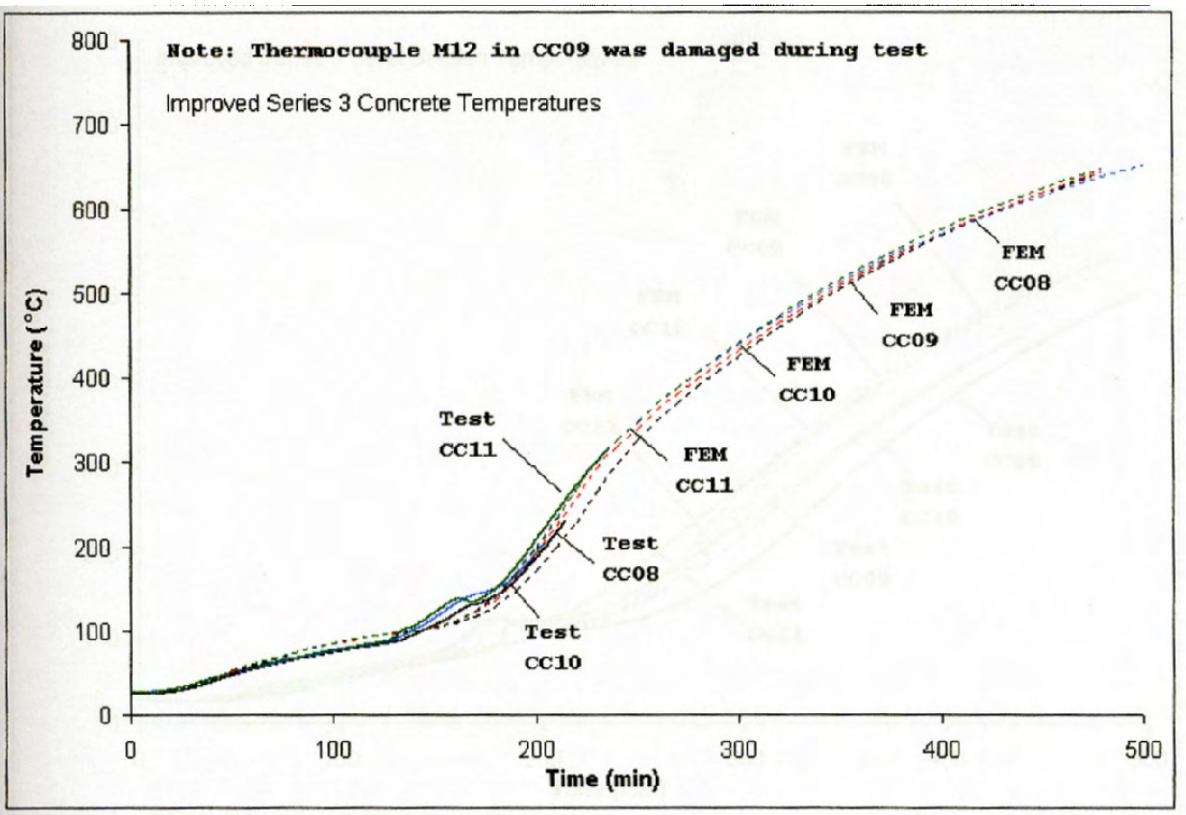

Figure 7.16 Experimental and improved FEM temperature profiles of concrete for Series 3 composite column tests

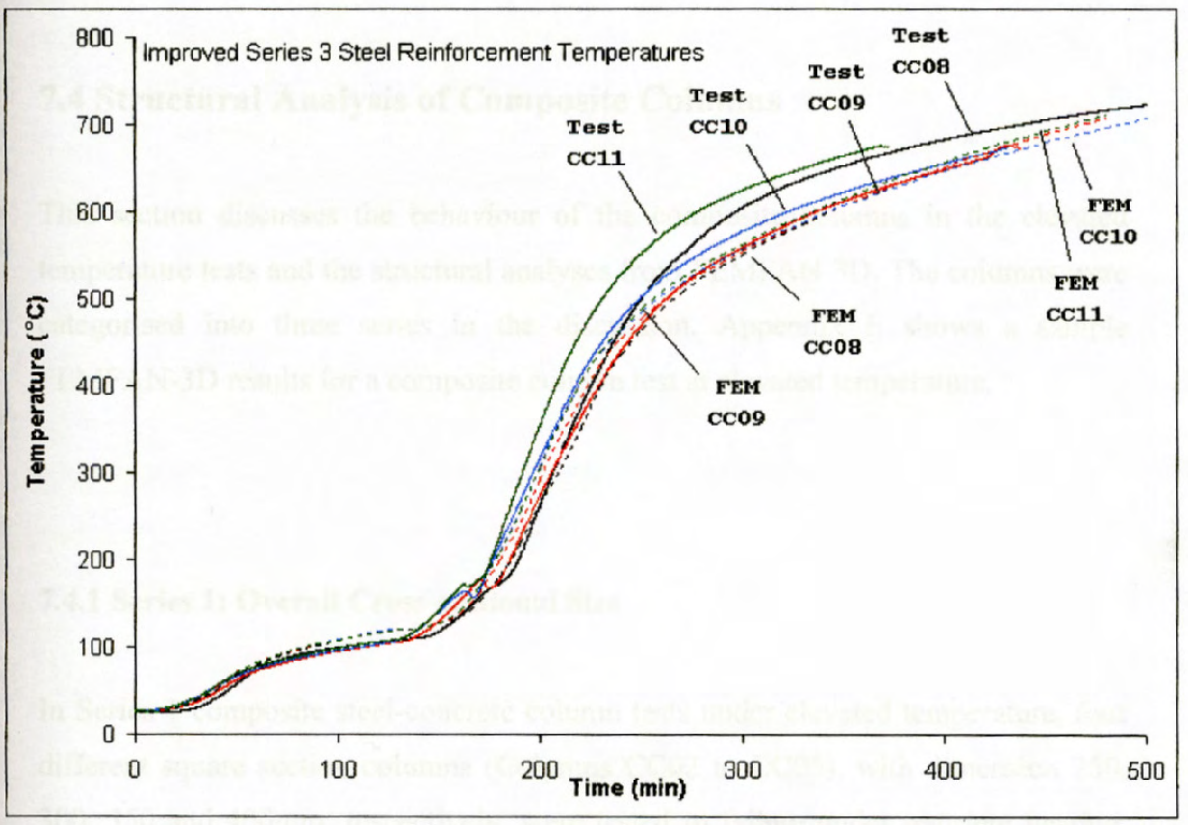

Figure 7.17 Experimental and improved FEM temperature profiles at steel reinforcement for Series 3 composite column tests

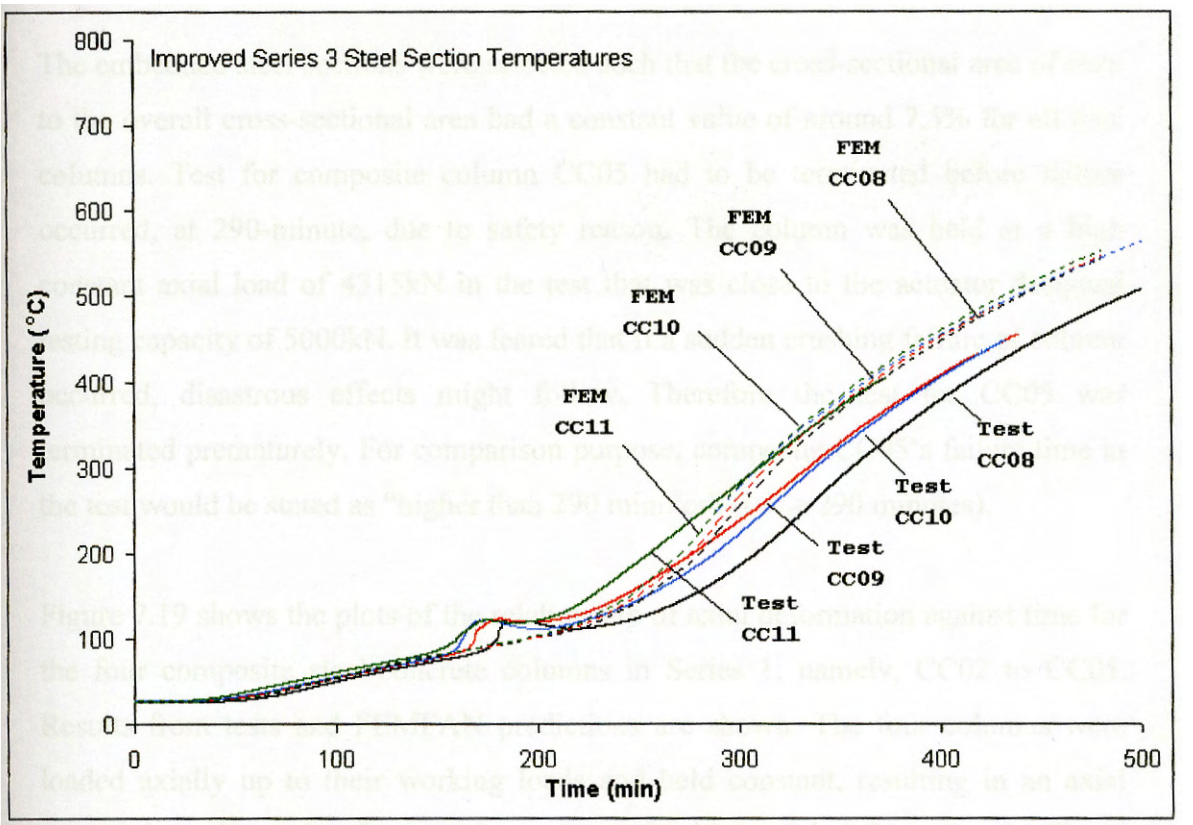

Figure 7.18 Experimental and improved FEM temperature profiles at mid-web of steel section for Series 3 composite column tests

7.4 Structural Analysis of Composite Columns

This section discusses the behaviour of the composite columns in the elevated temperature tests and the structural analyses from FEMFAN-3D. The columns were categorised into three series in the discussion. Appendix E shows a sample FEMFAN-3D results for a composite column test at elevated temperature.

7.4.1 Series 1: Overall Cross-sectional Size

In Series 1 composite steel-concrete column tests under elevated temperature, four different square section columns (Columns CC02 to CC05), with dimension 250, 300, 350 and 400mm, respectively, were tested to failure under transient heating.

The embedded steel sections were selected such that the cross-sectional area of steel to the overall cross-sectional area had a constant value of around 7.5% for all four columns. Test for composite column CC05 had to be terminated before failure occurred, at 290-minute, due to safety reason. The column was held at a high constant axial load of 4315kN in the test that was close to the actuator designed testing capacity of 5000kN. It was feared that if a sudden crushing failure of column occurred, disastrous effects might follow. Therefore the test for CC05 was terminated prematurely. For comparison purpose, composite CC05's failure time in the test would be stated as "higher than 290 minutes" (i.e. > 290 minutes).

Figure 7.19 shows the plots of the relationship of axial deformation against time for the four composite steel-concrete columns in Series 1; namely, CC02 to CC05. Results from tests and FEMFAN predictions are shown. The four columns were loaded axially up to their working loads and held constant, resulting in an axial contraction, shown by the negative values of initial axial deformation in Figure 7.19. When the working load was achieved, a period of 20 minutes was given for stabilisation of the applied axial load. With the commencement of heating from the furnace, axial deformation of the composite column was observed to take place towards the positive direction, due to thermal expansion. At high temperature, the rate of increase in the axial deformation was reduced due to deteriorating values of elastic modulus of concrete and steel, and the mechanical shortening became more important.

When approaching failure, mechanical shortening overtook free thermal expansion of the column. Column axial deformation changed direction and started to contract until it could not sustain the initial applied constant load. This shortening of the composite column coincided with the lateral deflection of column. After reaching the highest point of axial deformation, failure of the specimen occurred.

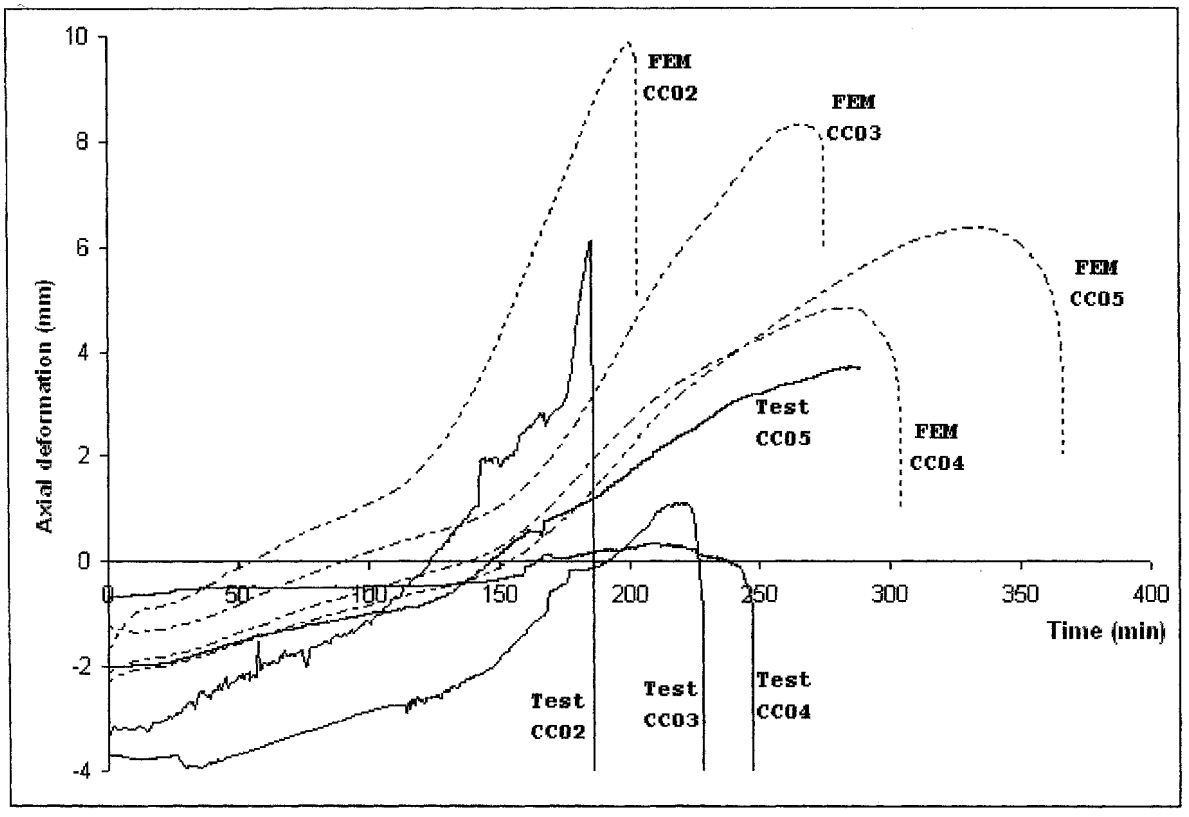

Figure 7.19 Series 1 experimental and FEMFAN results for axial deformation-time relationship

Table 7.3 Experimental and FEM failure times (Series 1)

Column Marking	Concrete Cover to Rebar / Steel Section (mm)	Cross-sectional Area (mm^2)	Po (kN)	$t_{cr,test}$	$t_{cr,FEMFAN}$	$\frac{t_{cr,FEMFAN}}{t_{cr,test}}$
CC02	31.3 / 44.1	62500	882.21	187	203	1.09
CC03	37.5 / 47.9	90000	1723.17	229	275	1.20
CC04	43.8 / 47.7	122500	2951.11	247	304	1.23
CC05	50.0 / 46.1	160000	4538.52	> 290	366	1.27
					Mean:	1.20
					Standard Deviation (SD):	0.08
					Coefficient of Variation (COV):	0.07

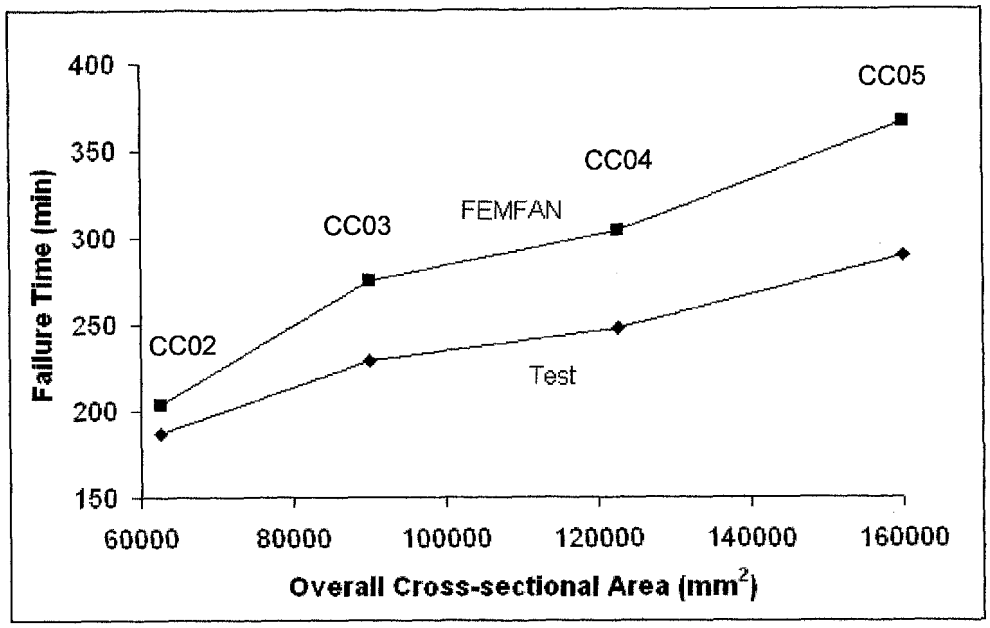

Figure 7.20 Series 1 trends of failure temperatures with overall cross-sectional area

It was noticed that the rate of increase in axial expansion of the column was the greatest for Column CC02, in both its experimental and FEMFAN results. This was due to a higher rate of increase of temperature in its cross section, as compared to the other three columns (Figures 7.3 to 7.5). Concrete covers to the top flanges of the steel sections were found to be 44.1mm, 47.9mm, 47.7mm and 46.1mm, for Columns CC02 to CC05 respectively (Table 7.3). The thinner concrete cover in CC02 contributed to the faster rate of increase in temperature to the steel section beyond the concrete casing, therefore resulting in a higher rate of increase in axial deformation. It is known that steel elongates faster than concrete at certain temperature. Differences in steel temperatures among the four composite columns, CC02 to CC05, gave different thermal elongations. A composite column with a larger cross-sectional area had a lower temperature in the inner section and therefore, smaller thermal elongation compared to smaller sized columns (Figure 7.19).

Concrete loses its strength at elevated temperature and its contribution to resist axial load diminishes. At the time of failure, with the furnace temperature at 800°C, concrete temperature was higher than 550°C at locations near to the column surface. The strength of dense concrete starts to reduce when its temperature reaches 350°C. EC3 (2000b) states that the ratio of strength at 550°C to strength at 20°C is less than 0.5.

Due to the differences in temperatures at different locations in a column at any one time, it is not realistic to use temperature for comparison of failure between columns. Time is used as a basis for failure comparison. The time begins at the point when heating is introduced. Table 7.3 shows a summary of the experimental and FEM failure times of the composite columns in Series 1 tests. Columns CC02 to CC05 were named in ascending order of their cross-sectional areas. It shows that failure time increases when there is an increase in cross-sectional area. Figure 7.20 plots out the results in Table 7.3 graphically. There is a linear relationship between the overall cross-sectional area and failure time. FEMFAN predictions for this series of tests are not conservative, with overestimates of 20% for CC03 and 23% for CC04 (Table 7.3). This is due to the fact that FEMFAN is unable to model spalling of concrete. Concrete spalling was observed to be significant in Series 1 columns. Figures 7.21 (a) to (d) show the pictures of Series 1 failed columns. Concrete spalling was seen in the columns. When concrete spalling occurs, fire resistance of a structural member is seriously reduced. Firstly, detachment of pieces of concrete reduces the cross-sectional area of a member. Secondly, removal of concrete cover to reinforcement exposes the steel reinforcement to the intense heat, rapidly raising the temperature of inner concrete and steel section. Beside these effects, holes and orifices created by spalling may cause hot gases to penetrate deeply into the cross section. Table 7.3 gives a mean value of 1.20 for $t_{cr,FEMFAN} / t_{cr,test}$, with a standard deviation SD = 0.08 and a coefficient of variation COV = 0.07. For this series, FEMFAN consistently overestimated the test failure times with an average deviation of 20%. Series 1 columns failed by concrete crushing and flexural bending in the steel sections (Figures 7.21 (a) to (d)).

(a) Composite Column CC02

(b) Composite Column CC03

(c) Composite Column CC04

(d) Composite Column CC05

Figure 7.21 Failure modes of Series 1 composite columns under elevated temperature tests

7.4.2 Series 2: Steel Section Ratio

In Series 2 composite column tests under elevated temperature, four columns; namely Columns CC06, CC07, CC08 and CC03, with steel section ratios of 3.25, 3.83, 5.23 and 7.41 respectively, were tested. All four columns had the same overall cross-sectional area of 300 × 300mm (Table 6.3).

Figure 7.22 shows plots of the relationship of axial deformation against time for the four composite steel-concrete columns in Series 2. Results from both tests and

FEMFAN predictions are included. Composite Column CC03 in Series 2 was the same column tested in Series 1. Its dimensions and specifications made it suitable to be used in both series. In ascending order of steel section ratios, the column markings would be as follows: CC06, CC07, CC08 and CC03.

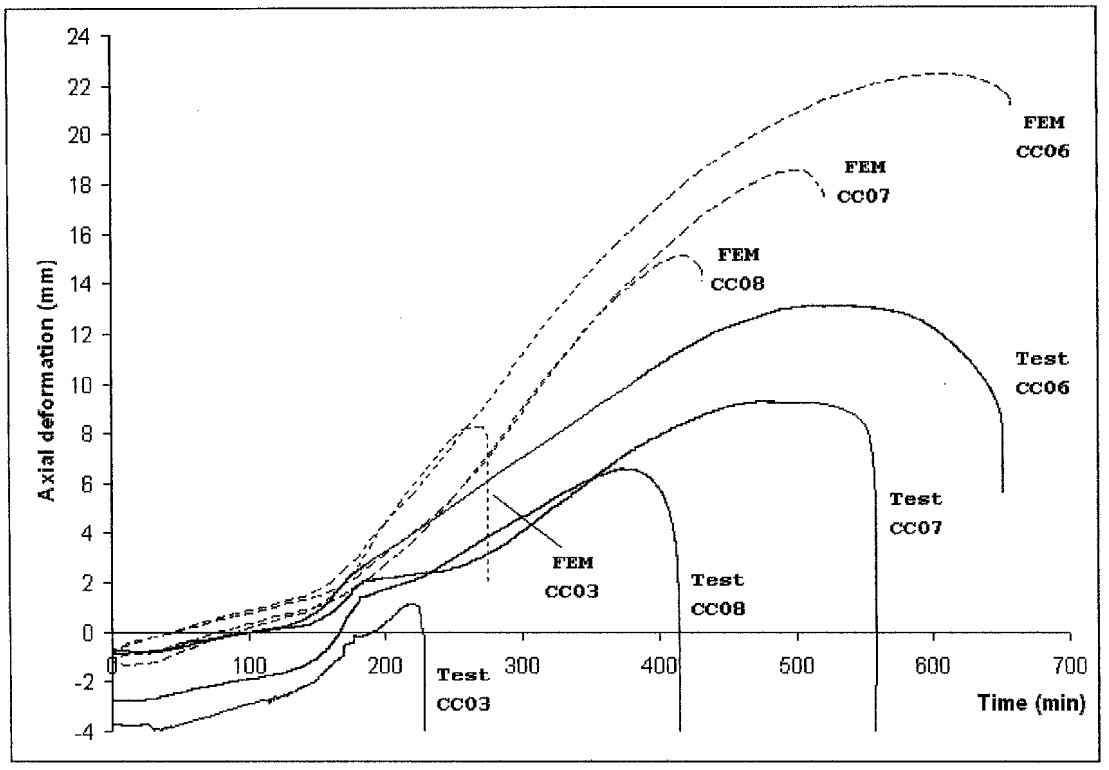

Figure 7.22 Series 2 experimental and FEMFAN results for axial deformation-time relationship

Table 7.4 Experimental and FEM failure times (Series 2)

Column Marking	Concrete Cover to Rebar / Steel Section (mm)	Steel Section Ratio (%)	*Po* (kN)	$t_{cr,test}$	$t_{cr,FEMFAN}$	$\frac{t_{cr,FEMFAN}}{t_{cr,test}}$
CC06	37.5 / 72.2	3.25	643.90	651	658	1.01
CC07	37.5 / 84.6	3.83	777.41	554	522	0.94
CC08	37.5 / 68.2	5.23	1105.90	414	431	1.04
CC03	37.5 / 47.9	7.41	1723.17	229	275	1.20
					Mean:	1.05
					Standard Deviation (SD):	0.11
					Coefficient of Variation (COV):	0.11

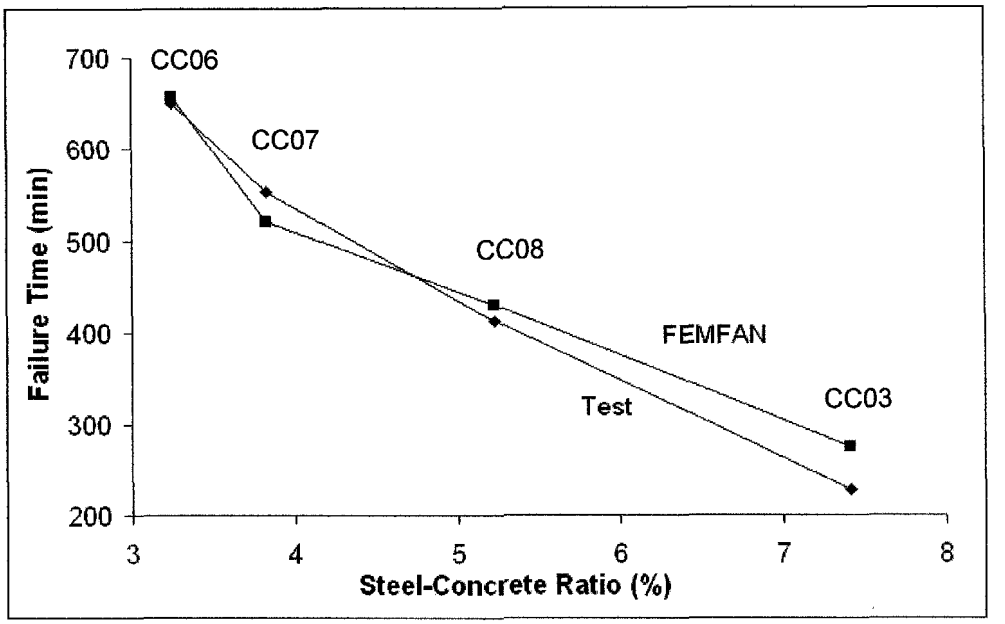

Figure 7.23 Series 2 trends of failure temperatures with steel section ratio

As expected, after loading up to the respective axial compressive loads and held constant, there were some negative axial deformations in all columns. With the introduction of heating from the furnace, the columns underwent thermal expansion in the positive direction. It was noted that all the columns in this series had more or less the same rate of thermal expansion. This could be observed from their similar rate of increase in axial deformation, represented by the gradients of the graphs (Figure 7.22). FEMFAN predictions show similar rate of expansion too. This was unlike Series 1, in which the composite columns did not show similar rate of thermal expansion, due to different column dimensions.

From the column cross-sectional dimensions, in order of ascending steel section ratios, their concrete covers to the top flanges of the steel sections were 72.2mm, 84.6mm, 68.2mm and 47.9mm, for Columns CC06, CC07, CC08 and CC03, respectively (Table 7.4). The thinner concrete cover in CC03 resulted in a higher rate of increase of temperature in the steel section as well as steel reinforcement (Figures 7.7 and 7.8). As discussed in Section 7.4.1, there was significant concrete

spalling in CC03, which resulted in a higher rate of increase in the column steel reinforcement and steel section temperatures.

Table 7.4 shows a summary of the experimental and FEM failure times of the composite columns in Series 2 tests. Columns CC06, CC07, CC08 and CC03 are arranged in the table in ascending order of their steel section ratios, from the smallest to the largest. It shows that failure time decreases when there is an increase in steel section ratio. Figure 7.23 plots out the results in Table 7.4 graphically. There is a linear relationship between the steel section ratio and failure time. Column CC03 had the largest steel section ratio among the four columns, and it had the shortest failure time. From Series 2 tests, it shows that under a typical load level, the greater the percentage of steel used in a composite column, while all other properties remained unchanged, the weaker will be the fire resistance of the column. This is because increasing the size of steel section will reduce the concrete percentage and concrete cover. Reduction in concrete cover, together with any occurrence of concrete spalling significantly increases the inner steel temperature and decreases its load bearing capacity.

FEMFAN predictions for this series of tests are very accurate for the first three columns; CC06, CC07 and CC08 (Table 7.4). For Column CC03, FEMFAN had overestimated the failure duration by 20%. This is because CC03 experienced a higher rate of increase steel reinforcement temperature in the test due to concrete spalling, which was not modelled in FEM. Table 7.4 shows a mean value of 1.05 for $t_{cr,FEMFAN}$ / $t_{cr,test}$, with a standard deviation SD = 0.11 and a coefficient of variation COV = 0.11.

Series 2 columns failed by concrete crushing and flexural bending in the steel sections (Figures 7.24 (a) to (d)).

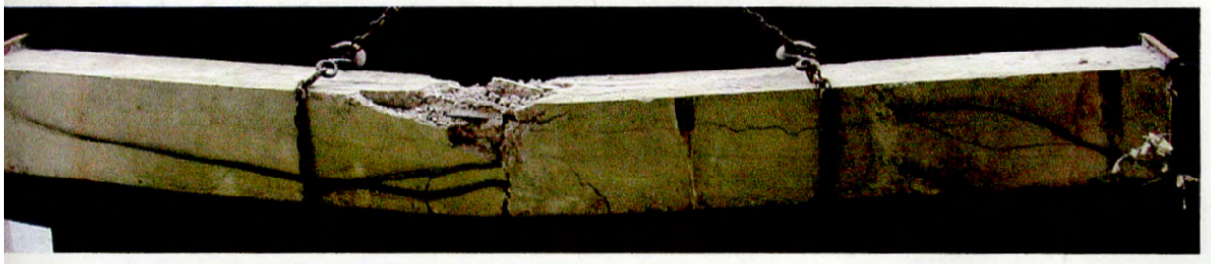

(a) Composite Column CC06

(b) Composite Column CC07

(c) Composite Column CC08

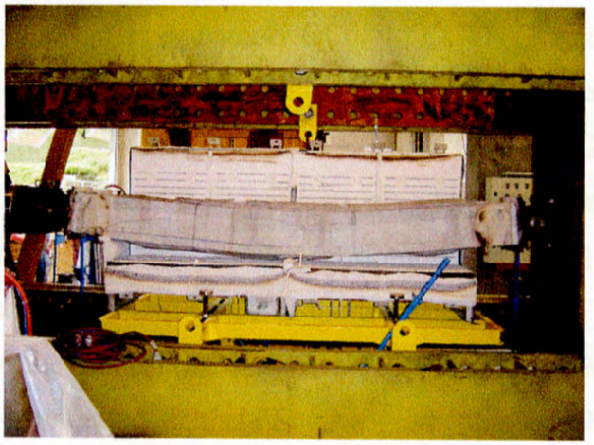

(d) Composite Column CC03

Figure 7.24 Failure modes of Series 2 composite columns under elevated temperature tests

7.4.3 Series 3: Axial Restraint Ratio

In Series 3 composite column tests under elevated temperature, four columns; namely Columns CC08 to CC11, were tested, subjected to different axial restraint ratios. All four columns had the same overall dimensions (Table 6.4). Composite Column CC08 in Series 3 was the same column tested in Series 2. Three restraint beams were used to provide axial restraint to Composite Columns CC09, CC10 and CC11 (Table 6.5). Column CC08 was without restraint in Series 3, this was the same column tested in Series 2. Its dimensions and specifications made it suitable to be used in these two series. Axial restraint ratios achieved experimentally were 10%, 9% and 17% for Columns CC09, CC10 and CC11, respectively. Column CC08 was tested without being subjected to any axial restraint. Actual axial restraint stiffness, $K_{s,test}$, was calculated in the same way as for the restrained steel column test, as discussed in Section 3.6. $K_{s,test}$ was the ratio of the imposed restrained force to the measured total deflection of the restraint beam. Imposed restraint force was plotted against the mid-span deflection of the restraint beam for each case (Figures 7.25 (a) to (c)). Values for actual axial restraint stiffness were calculated from the gradients of the linear graphs.

Figure 7.26 shows plots of the relationship of axial deformation against time for the four composite columns in Series 3; namely CC08 to CC11. Results from tests and FEMFAN predictions are included. In ascending order of axial restraint ratio, the column markings would be as follows: CC08, CC10, CC09 and CC11, with axial restraint ratios 0.00, 0.09, 0.10 and 0.17, respectively. All the four columns were of the same size and dimension, with similar working loads of 1105.90kN. Axial deformation for Composite Column CC09 in the test was observed to be increasing much more slowly than the other three, as shown by its lowest gradient in the graph. Transient strain is not modelled in the FEM program, this is why FEM always predict a higher rate of increase in axial deformation, compared to test results.

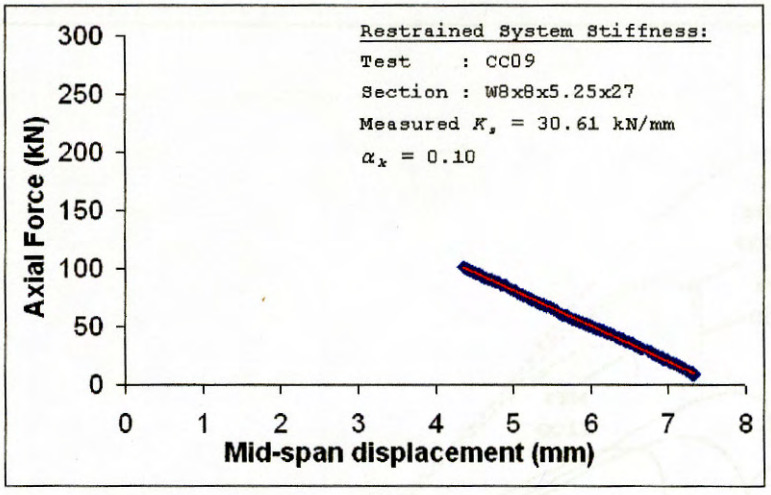

(a)

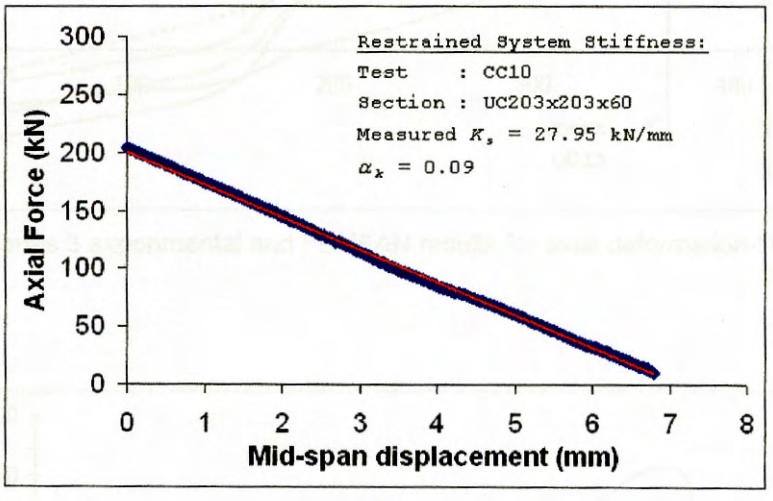

(b)

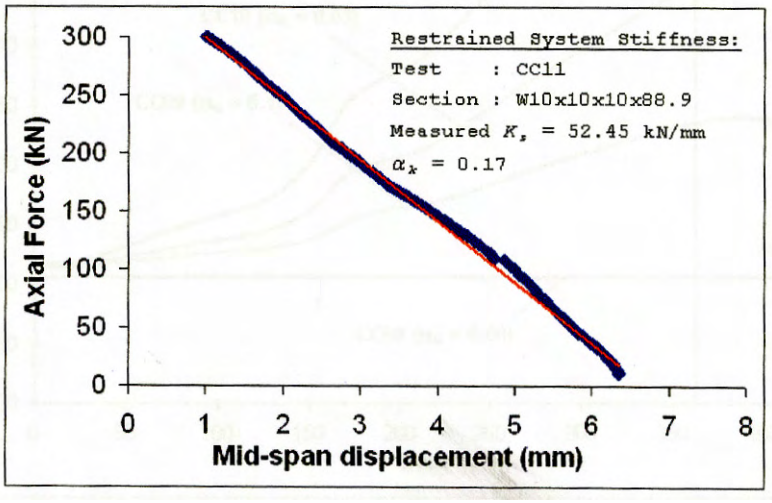

(c)

Figure 7.25 Force-displacement relationships of restraint beams

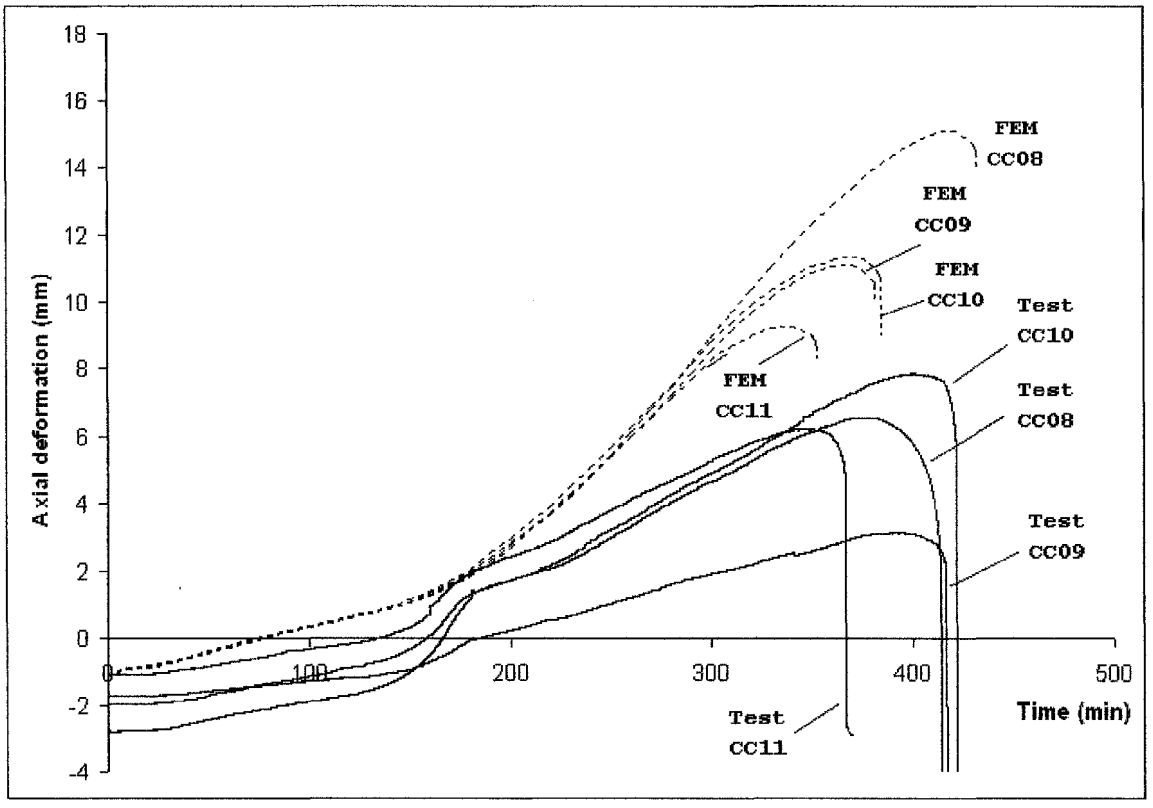

Figure 7.26 Series 3 experimental and FEMFAN results for axial deformation-time relationship

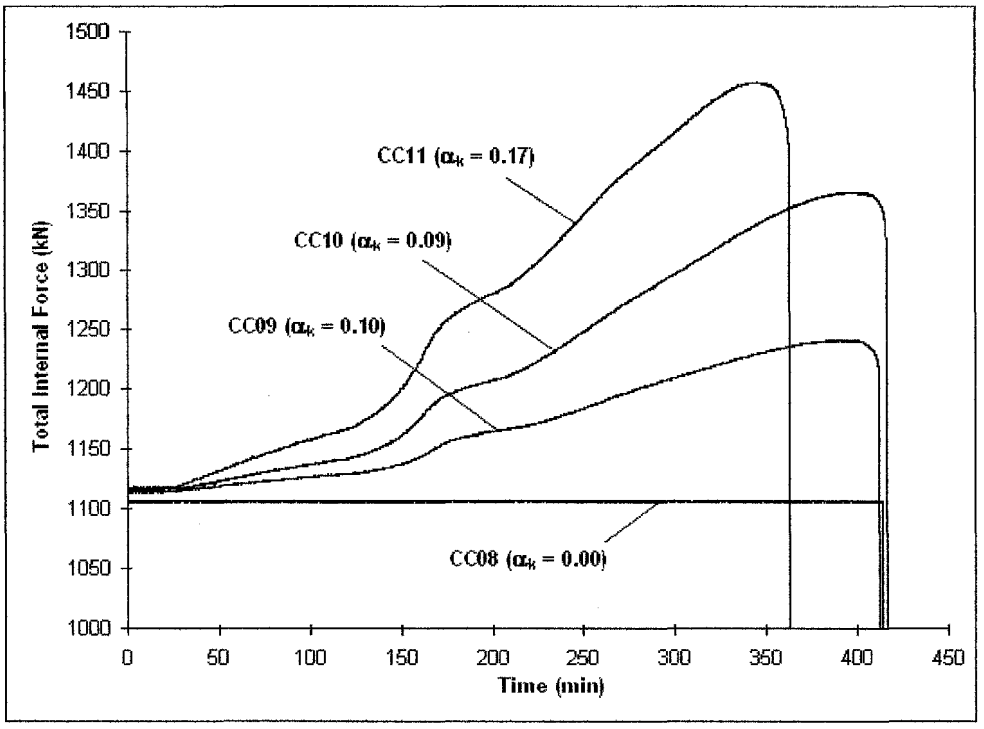

Figure 7.27 Series 3 experimental results for total internal force-time relationship

Table 7.5 Experimental and FEM failure times (Series 3)

Column Marking	Concrete Cover to Rebar / Steel Section (mm)	Axial Restraint Ratio (%)	*Po* (kN)	$t_{cr,test}$	$t_{cr,FEMFAN}$	$\frac{t_{cr,FEMFAN}}{t_{cr,test}}$
CC08	37.5 / 68.2	0.00	1105.90	414	431	1.04
CC09	37.5 / 68.2	0.10	1105.90	417	381	0.91
CC10	37.5 / 68.2	0.09	1105.90	422	384	0.91
CC11	37.5 / 68.2	0.17	1105.90	366	352	0.96
					Mean:	0.96
					Standard Deviation (SD):	0.06
					Coefficient of Variation (COV):	0.06

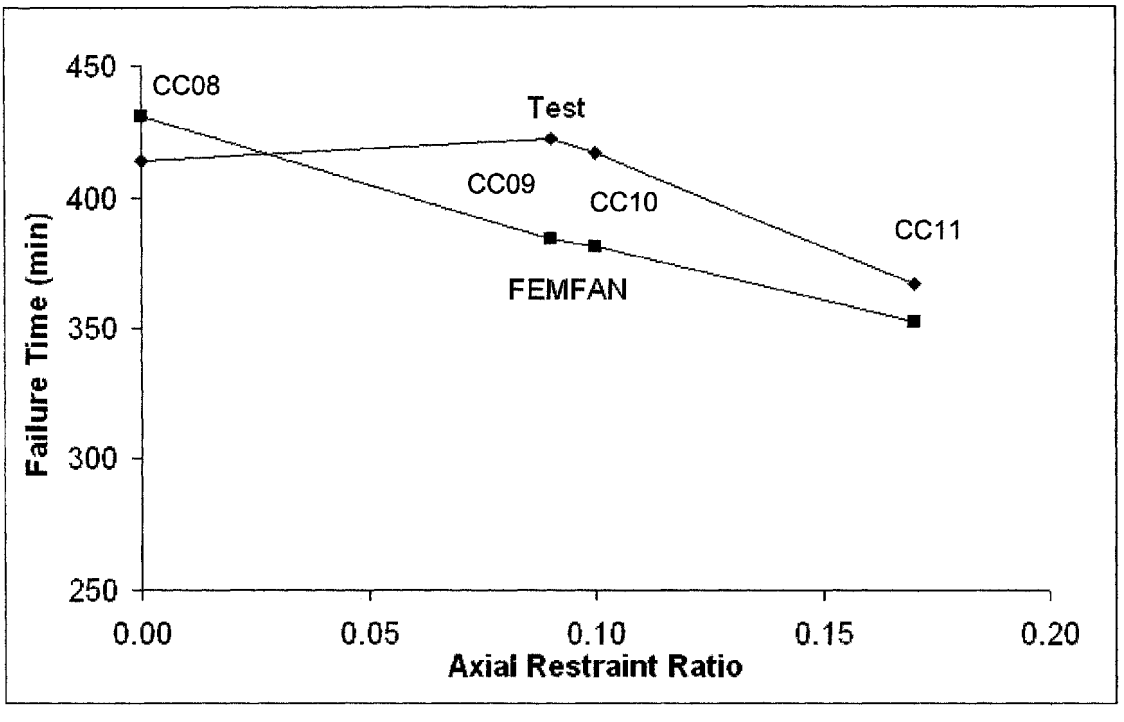

Figure 7.28 Series 3 trends of failure temperatures with axial restraint ratio

Axial restraint caused additional axial force to build up in the column, as there was thermal strain in the column due to elevated temperature. Figure 7.27 shows plots of total internal force against time for Series 3 columns. Additional axial force generated in the column was directly proportional to its axial expansion/deformation. Although Columns CC09 and CC10 were subjected to almost similar axial restraint ratios, which were 0.10 and 0.09 respectively, the additional axial forces generated were not the same. It was illustrated in Figure 7.26 that Column CC09 experienced a much smaller axial expansion in the test. Therefore it had a much smaller additional axial force generated too, compared to Column CC10 in the test (Figure 7.27). The rate of increase of total internal force for Column CC09 was lower than that of Column CC10 in the test. Their maximum total internal forces were also different; Column CC09 had a maximum total internal force of 1240kN, whereas CC10 had 1365kN. Column CC11, being subjected to the highest axial restraint ratio, had the highest rate of increase in total internal force, with a maximum internal axial force of 1456kN.

Table 7.5 shows a summary of the experimental and FEM failure times of the composite columns in Series 3 tests. Columns CC09 and CC10 had close failure times due to their axial restraint ratios being almost similar. Figure 7.28 plots out the results of Table 7.5 graphically. There is a linear relationship between the axial restraint ratio and failure time. Column CC11 had the highest axial restraint ratio among the four columns, and the shortest failure duration. From Series 3 tests, it shows that the greater the axial restraint subjected to a composite column, the weaker is the column fire resistance. This is because increasing the axial restraint will induce a faster rate of increase in total internal force when temperature rises. When the maximum capacity is reached, shortening of the composite column occurs. Material properties will degrade and load-bearing capacity of the column will reduce at this state.

FEMFAN predictions for Series 3 tests are very accurate. Table 7.5 shows a mean value of 0.96 for $t_{cr,FEMFAN}$ / $t_{cr,test}$, with a standard deviation SD = 0.06 and a

coefficient of variation COV = 0.06. This shows that FEMFAN had predicted quite consistently the test results, with a very low percentage of error.

Figures 7.29 (a) to (d) show the failure modes of Series 3 composite columns under the elevated temperature tests. The columns failed by concrete crushing and flexural bending in the steel sections.

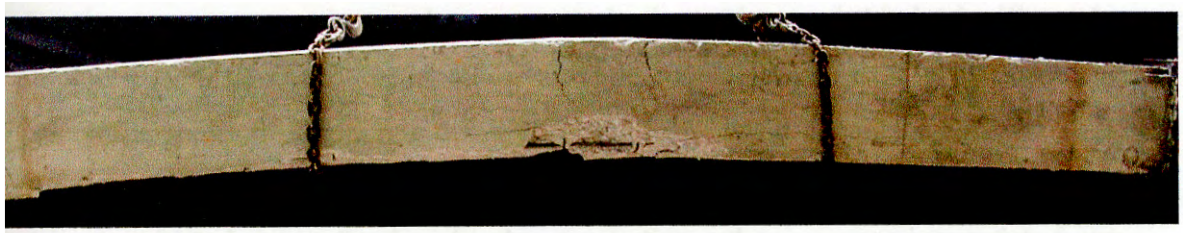

(a) Composite Column CC08

(b) Composite Column CC09

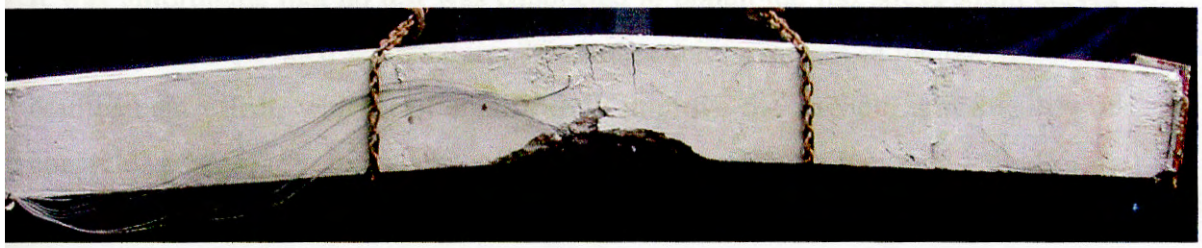

(c) Composite Column CC10

(d) Composite Column CC11

Figure 7.29 Failure modes of Series 3 composite columns under elevated temperature tests

7.5 Test and FEMFAN Observations

From the test results as well as finite element analyses, certain observations can be drawn:

In the axial deformation-time relationship, predictions by FEA were always greater than the respective experimental values. This was mainly due to three reasons. Firstly, there was transient and creep strain in the testing, and this is significant in concrete. Transient and creep strain are not considered in EC2 (1993) model. Secondly, spalling of concrete occurred in the tests, but it cannot be considered in the model. When concrete columns spalled, thermal expansion of these concretes was terminated immediately. At the same time, the compression axial force undertaken by these concretes moved to the kernel part of section including encasing steel and concrete confined by stirrups. With the congestion of axial force exerted on a smaller but hotter (due to direct exposure to heat at spalling spot) composite section, the whole heated column contracted more than one without spalling. Lastly, stress-strain model played a part. It should be noted that EC2 (1993) stress-strain model is conservative.

It was unfortunate that no test was conducted to obtain the full stress-strain curves for concrete at elevated temperature. Transverse reinforcement in the column has a confinement effect, which can significantly improve the strength and ductility of concrete, particularly for stocky columns. However, FEM does not include this effect. In the composite columns, there were nominal stirrups of size R6 placed 200mm centre to centre along its length. This effect of confinement in reinforced concrete columns is beneficial; with transverse reinforcement, strength and ductility of concrete are generally improved depending on the degree of confinement (Koji and Shamim (1989)). The stress-strain relationship of confined concrete is a function of many variables, such as characteristics of materials, characteristics of cross section, behaviour of reinforced concrete column and other mechanical characteristics and design constraints, such as detailing.

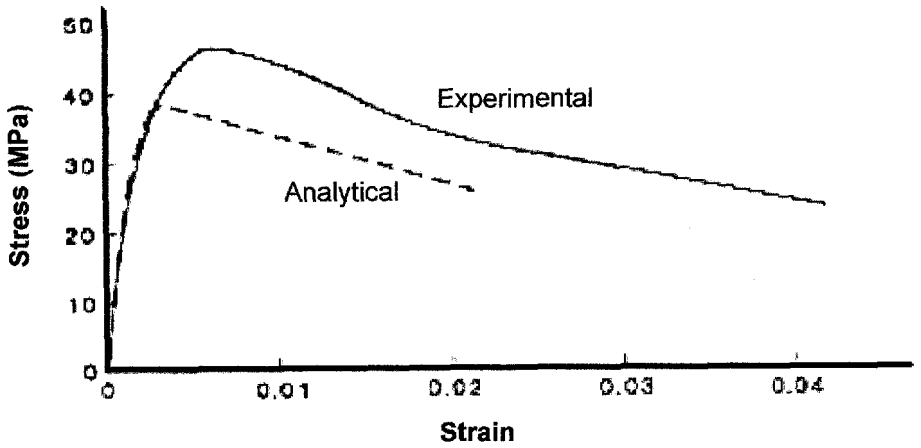

Figure 7.30 Comparison of experimental and analytical stress-strain curves of confined concrete

Koji and Shamim (1989) reported the stress-strain curve of confined concrete from test results as well as from the analytical model found by Scott *et al.* (1982). Figure 7.30 shows the difference between the two. In the model, the effect of concrete confinement was not included, yielding a very conservative prediction of actual behaviour. Similarly in EC2 (1993) and EC4 (1995), the effect of confinement in reinforced concrete column is not included, therefore the stress-strain curve from the codes is also quite conservative compared to test.

In Series 1 composite column tests, it shows that the fire resistance of concrete-encased steel composite column increases with an increase in overall cross–sectional size.

In Series 2 composite column tests, it shows that the fire resistance of composite column decreases with an increase in steel section ratio. To optimise the fire resistance of a concrete-encased steel composite column, it is better to minimise the steel section ratio, as this would increase the concrete cover to the steel. With a larger concrete cover, fire resistance is significantly increased.

In Series 3 composite column tests, it shows that the fire resistance of composite column decreases with an increase in axial restraint ratio. Axial restraint will induce an increase in total internal force when temperature rises, therefore shortening the duration of fire resistance of columns.

CHAPTER EIGHT

Conclusions and Suggestions for Future Research

8.1 Conclusions

The main objectives of this research are to study the behaviour of steel columns and concrete-encased steel section composite columns under elevated temperature conditions. A series of 20 bare steel column tests were conducted at elevated temperature. There were four different column slenderness ratios λ and section sizes, and varying levels of axial restraints α_k. Another series of 11 concrete-encased steel section composite column tests were conducted under elevated temperature conditions. The composite columns were categorised into three series with different variable parameters, namely overall cross-sectional size, steel section ratio and axial restraint ratio. Tensile coupon tests were carried out to determine the material properties of the test specimens at ambient temperature. Facility for testing material properties at elevated temperature was not available during the time of testing. Therefore, the true material properties at elevated temperature were not obtained. Results from finite element analyses were achieved from the program FEMFAN and were compared with experimental results for verification.

In the bare steel column tests, the test results show that axial expansion against restraint system generates additional compressive forces in the columns. Degradation of material properties, with shortening of columns and bending under an increased load counteracts thermal expansion, thereby decreasing the restraint force. Stocky columns are observed to experience gradual shortening prior to buckling, whereas slender columns will buckle quickly. Buckling temperature T_{cr} decreases as slenderness increases, under a fixed restraint ratio. Imposition of increased axial restraint to the columns has the effect of reducing the buckling temperatures, for columns with similar slenderness and applied working load, due to an increase in the rate of restraint force generation. An increase in axial restraint has

a more significant effect in reducing buckling temperature for slender columns, due to the more rapid degradation in elastic modulus compared to yield strength. Column lateral deflection develops more gently in a stocky column than in a slender column. Slender columns experiencing a more significant P-δ effect demonstrate runaway lateral deflections when approaching the buckling temperatures. The variations of two parameters, namely slenderness and axial restraint ratios, have significant effect on the column buckling temperatures. Interaction of these two parameters produces considerable variation in the column response.

From his work, Hoffend (1977, 1980 and 1983) concluded that slender columns had higher critical temperature than the more stocky ones. The author disagrees with that statement. In fact, it is found to be the opposite, with slender columns yielding lower critical temperature than stockier ones, based on the steel column tests. Faris *et al.* (2001) reported that an additional rotational restraint had a relatively minor effect on the values of generated restraint forces but failure temperatures were greatly increased. The author also observed this phenomenon in his experimental study and in addition, he pointed out that rotational restraint is beneficial as it will increase the column strength at ambient temperature and delay buckling at elevated temperature. Besides, rotational restraint is beneficial as it causes redistribution of moments, leading to a reduction in mid-span bending moment, thereby increasing the fire survival time.

In FEMFAN analysis, it is important to ensure that the material properties of steel are modelled as accurately as possible. Geometric imperfections such as initial load eccentricities and column crookedness also pose a great influence in FEM modelling. With accurate input, FEMFAN is able to yield close predictions to test results.

In the composite column tests, results show that the fire resistance of concrete-encased steel composite column increases with an increase in overall cross–sectional size. An increase in steel section ratio will lead to a decrease in the fire resistance of composite column. This is mainly due to a significant reduction in

concrete cover to the inner steel section when the cross sectional area of steel increases in a fixed area of concrete encasement. The fire resistance of composite column decreases when subjected to an increase in axial restraint ratio. Axial restraint induces a build-up of internal restraint force due to thermal elongation of member when temperature rises, thereby shortening the fire resistance time of composite columns.

Heat transfer analysis for the composite column test series was carried out using the program SAFIR, as the heat transfer program in FEMFAN-3D was still under development at the time of writing this report. SAFIR heat profiles which were close to tests were applied into FEMFAN-3D as a precursor to structural analysis. Structural predictions by FEMFAN-3D for the axial deformation-time relationship tend to be at a higher rate than the tests. This is mainly because finite element modelling does not consider concrete spalling, and the EC2 (1993) material model used in FEMFAN-3D does not incorporate transient and creep strain. Stress-strain model is also an important factor in FE modelling, both at ambient and elevated temperatures. In terms of column failure time, FEMFAN-3D yielded close predictions, especially for Series 2 and 3 tests.

8.2 Suggestions for Future Research

Before this research can be extended further, problems encountered in this study must be overcome. Recommendations for future research are listed as follows:

(1) Heating in this research was from an electric furnace, and it was unable to simulate a real fire. Similar tests should be conducted based on different fires, such as ISO 834 fire.

(2) Investigation on light-weight concrete as a composite material with steel could be carried out. The fire resistance of such composite column may be

stronger than normal-weight concrete, due to differences in thermal properties.

REFERENCES

Aasen, B. (1985), **An Experimental Study on Steel Columns Behaviour at Elevated Temperatures**, The Norwegian Institute of Technology, Trondhiem.

Beedle, L. S., Tall, L. (1960), **Basic Column Strength**, A.S.C.E. Journal of the Structural Division, No. 86, pp. 139-173.

Bijlarrd, F., Twilt, L., Witteveen, J. (1977), **Theoretical and Experimental Analysis of Steel Structures at Elevated Temperatures**, 10th Congress IABSE, Toyko, Final Report, Zurich.

British Standards Institution (BSI) (1985) British Standard BS8110, **Structural Use of Concrete**, British Standards Institution, London.

British Standards Institution (BSI) (1987a) British Standard 476, **Fire Tests on Building Materials and Structures, Part 20: Method for Determination of the Fire Resistance of Elements of Construction (General Principles)**, British Standards Institution, London.

British Standards Institution (BSI) (1990a) British Standard BS5950, **Structural Use of Steelwork in Buildings, Part 1: Code of Practice for Design in Simple and Continuous Construction: Hot Rolled Sections**, British Standards Institution, London.

British Standards Institution (BSI) (1990b) British Standard BS5950, **Structural Use of Steelwork in Buildings, Part 8: Code of Practice for Fire Resistant Design**, British Standards Institution, London.

Buchanan, A. H. (2001), **Structural Design for Fire Safety**, John Wiley & Sons Ltd, England.

Burgess, I. W., Olawale, A. O., Plank, R. J. (1992), **Failure of Steel Columns in Fire**, Fire Safety Journal, No. 18.

Burgess, I. W., Najjar, S. R. (1994), **A Simple Approach to the Behaviour of Steel Columns in Fire**, Journal of Constructional Steel Research, 31, pp. 115-134.

Cabrita Neves, I. (1995), **The Critical Temperature of Steel Columns with Restrained Thermal Elongation**, Fire Safety Journal, No. 24, pp. 211-227.

Cabrita Neves, I., Valente, J.C., Correia Rodrigues, J.P. (2002), **Thermal Restraint and Fire Resistance of Columns**, Fire Safety Journal, No. 37, pp. 753-771.

Chen, W .F., Soha, I. (1995), **Plastic Design and Second-Order Analysis of Steel Frames**, New York: Springer-Verlag.

Commission of European Communities (CEC). (1995), **Eurocode 3: Design of Steel Structures: Part 1.2. General Rules. Structural Fire Design**, EC3-1.2, Draft ENV 1993-1-2, Brussels.

Correia Rodrigues, J.P., Cabrita Neves, I., Valente, J.C. (2000), **Experimental Research on the Critical Temperature of Compressed Steel Elements with Restrained Thermal Elongation**, Fire Safety Journal, No. 35, pp. 77-98.

European Committee for Standardisation (CEN) (2000a) Draft prEN 1991-1-2, **Eurocode 1: Basis of Design and Actions on Structures, Part 1.2: Actions on Structures – Actions on Structures Exposed to Fire**, British Standards Institution, London.

European Committee for Standardisation (CEN) (1993) ENV 1992-1-2, **Eurocode 2: Design of Concrete Structures, General Rules, Structural Fire Design**, British Standards Institution, London.

European Committee for Standardisation (CEN) (2000b) Draft prEN 1993-1-2, **Eurocode 3: Design of Steel Structures, Part 1.2: General Rules, Structural Fire Design**, British Standards Institution, London.

European Committee for Standardisation (CEN) (1995) ENV 1994-1-1, **Eurocode 4: Design of Composite Steel and Concrete Structures, Part 1.1: General Rules and Rules for Building**, British Standards Institution, London.

European Committee for Standardisation (CEN) (1995) ENV 1994-1-2, **Eurocode 4: Design of Composite Steel and Concrete Structures, Part 1.2: General Rules, Structural Fire Design**, British Standards Institution, London.

European Convention for Constructional Steelwork (ECCS) (1983), **European Recommendations for the Fire Safety of steel Structures**, Elsevier Scientific Publishing Co., Amsterdam.

Faber, O (1956), **Savings to be Effected by the More Rational Design of Cased Stanchions as a Result of Recent Full Size Tests**, The Structural Engineer, March, pp. 88-109.

Faris Ali, David O'Connor (2001), **Structural Performance of Rotationally Restrained Steel Columns in Fire**, Fire Safety Journal, No. 36, pp. 679-691.

Frannsen, J-M, Dotreppe, J. C. (1992), **Fire Resistance of Columns in Steel Frames**, Fire Safety Journal, No. 19, pp. 159-175.

Han, L. H. (1999), **Fire Resistance of Concrete Filled Steel Tubes in China**, 2nd ICASS Proceedings, pp. 1039-1045, Hong Kong, China.

Han, L. H., Zhao, X. L., Yang, Y. F., Feng, J. B. (2003), **Experimental Study and Calculation of Fire Resistance of Concrete-Filled Hollow Steel Columns**, A.S.C.E. Journal of the Structural Engineering, 129(3), pp. 346-356.

Hoffend, F. (1977), **Das Brandverhalten von Stahlstützen – Versuche und Berechnung**, SFB 148, Arbeitsbericht 1975-1977, TU, Braunschweig.

Hoffend, F. (1980), **Brandverhalten von Stahlstützen bei ausmittiger Lasteinleitung, Dehnbe-hinderung oder teilweiser Bekleidung**, SFB 148, Arbeitsbericht 1978-1980, TU, Braunschweig.

Hoffend, F. (1980), **Brandversuche an Stahlrahmen. Versuchsergebnisse, deren Analyse und rechnerische Vergleiche**, SFB 148, Arbeitsbericht 1978-1980, TU, Braunschweig.

Hoffend, F. (1983), **Zum Brandverhalten von Stahlbauteilen. Versuchsergebnisse und rechnerische Untersuchungen**, SFB 148, Arbeitsbericht 1981-1983, TU, Braunschweig.

Huang, Z. F. (2002), **Users' Manual for FEMFAN Version 2.0 – A FEM Program for Fire Analysis of Plane Frames**, Nanyang Technological University, Singapore.

Huang, Z. F. (2001), **Progressive Collapse of Steel Frames in Fire**, Nanyang Technological University, Singapore.

Inwood, M. (1999), **Review of NZS 3101 for High Strength and Lightweight Concrete Exposed to Fire**, Fire Engineering Research Report 99/10, University of Canterbury, New Zealand.

Jacot, A., Rappaz, M., Reed, R. C. (1997), **Modelling of Phase Tranformations in Hypoeutectoid FE-C Steels during Heating**, Materials Week'97, The Minerals, Metals & Materials Society (TMS), Indianapolis, Indiana.

Janss, J., Minne, R. (1982), **Buckling of Steel Columns in Fire Conditions**, Fire Safety Journal, No. 4.

Jorgenson, J., Sorensen, A. (1980), **Mechanical Properties of Structural Steel at Elevated Temperatures**, Institute of Building Technology and Structural Engineering, Report No. 8010, July 1980.

Kato, B. (1996), **Column Curves of Steel-Concrete Composite Members**, Journal of Constructional Steel Research, 39, No 2, pp. 121-135.

Kerstma, J., Bijlarrd, F.S.K., Twilt, L. (1979), **Analyses of the Gap between the TNO-IBBC Buckling Curves and the Results of Full-scale Tests**, Nos. B1-79-74 and –75, TNO, Delft.

Khoury, G. A., Grainger, B.N., and Sullivan, P. J. E. (1985), **Strain of Concrete during First Heating to 600°C**, Magazine of Concrete Research, 37, pp. 195-215.

Knublauch, E., Rudolphi, R., Stanke, J. (1974), **Theoretische Ermittlung der Feuerwiderstandsdauer von Stahlstutzen und Vergleich mit Versuchen**, Bestimmung der Kritischen Stahltemperatur, Stahlbau, 8.

Koji, S., Shamim, A. S. (1989), **What Do We Know about Confinement in Reinforced Concrete Columns? (A Critical Review of Previous Work and Code Provisions)**, ACI Structural Journal, 86-S22, pp. 192-207.

Kordina, K. (1988), **Behaviour of Composite Columns and Girders in Fire**, Fire Safety Science, Proceedings of the 2nd International Symposium, Toyko, Japan, pp. 681-695.

Lie, T. T. (1980), **New Facility to Determine Fire Resistance of Columns**, Canadian Journal of Civil Engineering, Vol. 7.

Narayanan, R. (1988), **Steel-Concrete Composite Structures – Stability and Strength**, Wlsevier Applied Science.

Olawale, A. O. (1988), **Collapse Behaviour of Steel Columns in Fire**, PhD Thesis University of Sheffield.

Olawale, A. O., Plank, R.J. (1988), **The Collapse Analysis of Steel Columns in Fire Using a Finite Strip Method**, International Journal for Numerical Methods in Engineering, Vol. 26.

Plen, E. (1975), **Theoretical and Experimental Investigation of Point Set Structures**, Document D9, Swedish Council for Building Research.

Poh, K. W., Bennetts, I. D. (1995), **Behaviour of Steel Columns at Elevated Temperature**, A.S.C.E. Journal of Structural Engineering, 121(4), pp. 675-676.

Ramberg, W., Osgood, W. (1943), **Description of Stress Strain Curves by Three Parameters**, Technical Note No. 902, National Advisory Committee for Aeronautics, Washington, DC.

Randall, M. J. (1998), **The Effects of Axial Restraint on the Behaviour of Steel Columns in Fire**, PhD Thesis University of Ulster.

Robinson, J. T., Latham, D. J. (1986), **Fire Resistant Steel Design – the future challenge**, in R.D. Anchor, H.J. Malhotra & J.A. Purkiss (eds), Design of Structures Against Fire, pp. 225-236.

Roik, K., Bergmann, R. (1990), **Design Method for Composite Columns with Unsymmetrical Cross-sections**, Journal of Constructional Steel Research, 15, pp. 153-168.

Schleich, J. B., Dotreppe, J. C., Franssen, J. M. (1986), **Numerical Simulations of Fire Resistance Tests on Steel and Composite Structural Elements or Frames**, Fire Safety Science, Proceedings of the 1st International Symposium, California, pp 311-323.

Schneider, U. (1988), **Concrete at High Temperatures- a general view**, Fire Safety Journal, 13, pp. 55-68.

Scott, B. D., Park, R., Priestley, M. J. N (1982), **Stress-strain Behaviour of Concrete Confined by Overlapping Hoops at Low and High Strain Rates**, ACI Journal, Proceedings V.79, pp. 13-27.

Shakir-Khalil, H. (1991), **Composite Columns of Double-Skinned Shells**, Journal of Constructional Steel Research, 19, pp. 133-152.

Shanmugam, N. E., Lakshmi, B. (2001), **State of the Art Report on Steel-Concrete Composite Columns**, Journal of Constructional Steel Research, 57, pp.1041-1080.

Simms, W. I. (1997), **An Experimental Investigation of Axially Restrained Steel Columns in Fire**, PhD Thesis University of Ulster.

Skinner D. (1972), **Determination of High Temperature of Steel**, BHP Technical Bulletin, Vol. 16, No. 2, Nov. 1972.

Steel Construction Industry Forum (SCIF). (1991), **Investigation of Broadgate Phase 8 Fire**, Steel Construction Institute, Ascot, UK.

Tan, K. H., Yao, Y. (2001), **Fire Resistance of RC Columns**, The Eight Asia-Pacific Conference on Structural Engineering and Construction, No. 1138.

Tan, K. H., Yao, Y. (2003), **Fire Resistance of Four-Face Heated Reinforced Concrete Column**, Journal of the Structural Engineering, 129(9), pp. 1220-1229.

Tan, K. H., Tang, C. Y. (2004), **Interaction Model for Unprotected Concrete Filled Steel Columns under Standard Fire Conditions**, A.S.C.E. Journal of the Structural Engineering, 130(9), pp. 1405-1413.

Tan, K. H., Yao, Y. (2004), **Fire Resistance of Reinforced Concrete Columns Subjected to 1-, 2-, and 3-Face Heating**, A.S.C.E. Journal of the Structural Engineering, 130(11), pp. 1820-1828.

Toh, W. S. (2000), **Stability and Strength of Steel Structures under Thermal Effects**, Ph.D. Thesis, Nanyang Technological University, Singapore.

Trahair, N. S., Bradford, M. A., Nethercot, D. A. (2001), **The Behaviour and Design of Steel Structures to BS5950**, Spon Press, London and New York.

Vandamme, M., Janss, J. (1981), **Buckling of Axially Loaded Steel Columns in Fire Conditions**, IABSE Proceedings, pp. 43-81.

Wang, Y. C., Moore, D. B. (1994), **Effect of Thermal Restraint on Column Behaviour in a Fire**, Fire Safety Science 4th International Symposium, Ottowa.

Wang, Y. C. (1997), **Some Considerations in the Design of Unprotected Concrete-Filled Steel Tubular Columns under Fire Conditions,** Journal of Constructional Steel Research, Vol. 44, No. 3, pp. 203-223.

Wang, Y. C. (1998b), **Full Scale Testing of Multi-storey Buildings in the Large Building Test Facility, Cardington**, in D. Dubina, I. Vayas and I. Ungureanu (eds), New Technologies and Structures in Civil Engineering: Case Studies on Remarkable Constructions, Editura Orizonturi Universitare, Timisoara, pp. 219-235.

Wang, Y. C. (1999), **Tests on Slender Composite Columns**, Journal of Constructional Steel Research, 49, pp. 25-41.

Wang, Y. C. (1999b), **The Effects of Structural Continuity on the Fire Resistance of Concrete Filled Columns in Non-sway Frames**, Journal of Constructional Steel Research, 50, pp. 177-197.

Wang, Y. C. (2002), **Steel and Composite Structures - Behaviour and Design for Fire Safety**, Spon Press, London and New York.

Wang, Y. C., Davies, J. M. (2003), **An Experimental Study of the Fire Performance of Non-Sway Loaded Concrete-Filled Steel Tubular Column Assemblies with Extended End Plate Connections**, Journal of Constructional Steel Research, 59, pp. 819-838.

Wastney, C. (2002), **Performance of Unprotected Steel and Composite Steel Frames Exposed to Fire**, M.Eng (fire) Thesis University of Canterbury.

Witteveen, J., Twilt, L., Bijlarrd, F. (1977), **The Stability of Braced and Unbraced Frames at Elevated Temperatures, Stability of Steel Structures**, Liege, Preliminary Report.

APPENDIX A

Rotational Restraint Stiffness, K_R

The rotational restraint stiffness, K_R is given by:

$$K_R = \frac{0.2rP}{\theta}$$

where

the coefficient of friction between steel contact surfaces is taken as 0.2

K_R = rotational restraint stiffness (kNm/rad)

r = radius of cylinder block (m)

P = total internal force (kN)

θ = angle of rotation (rad)

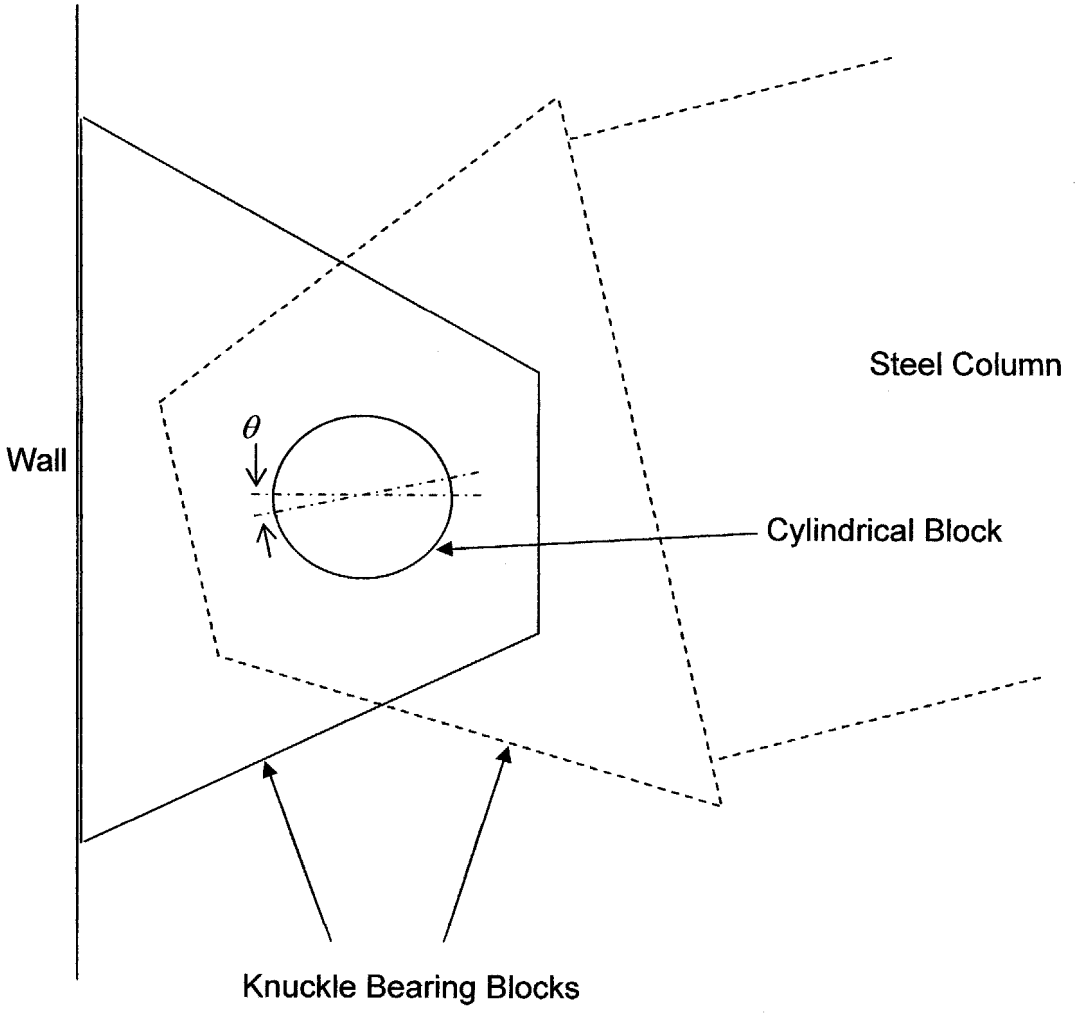

APPENDIX B

Composite Column Design Drawings

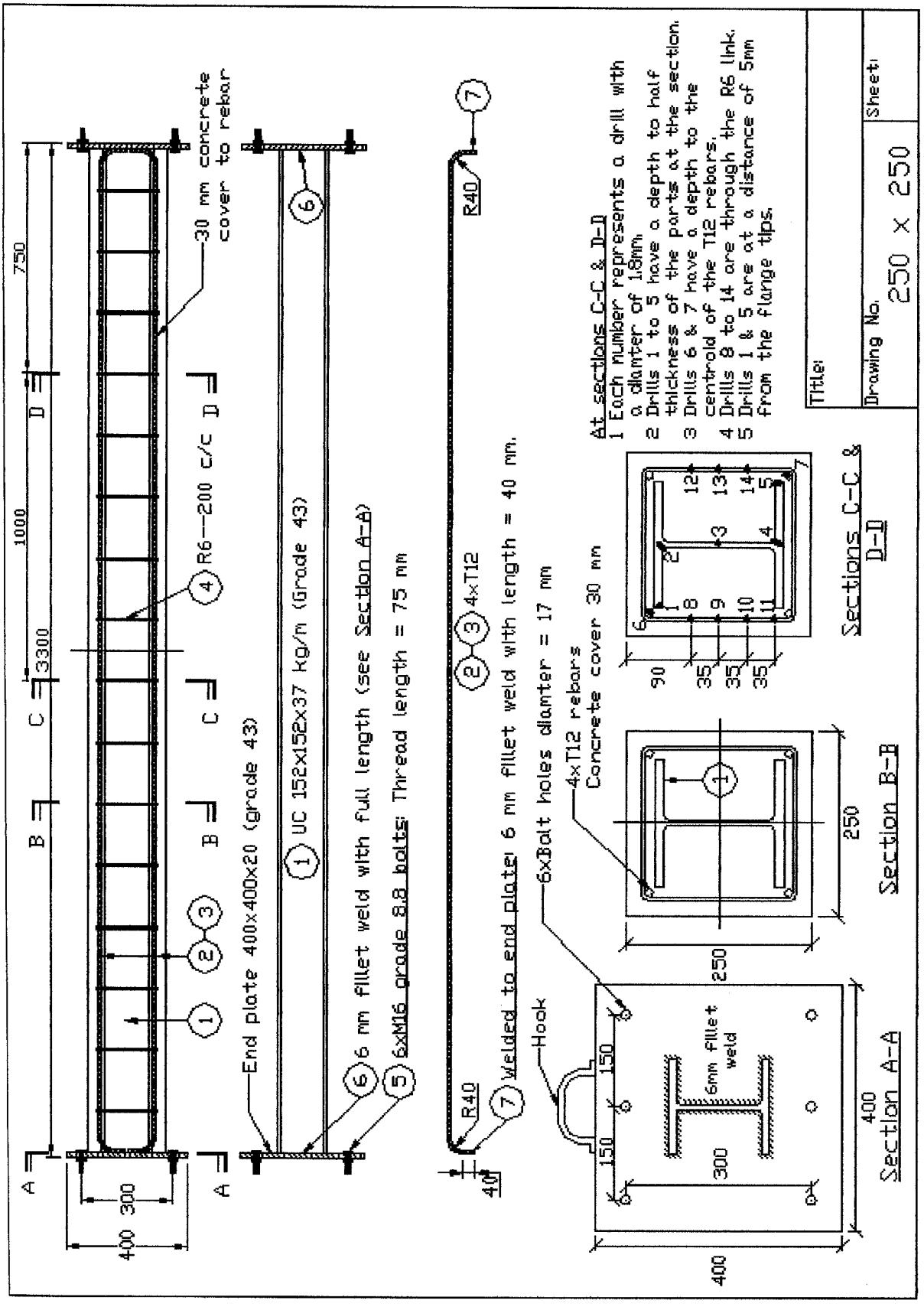

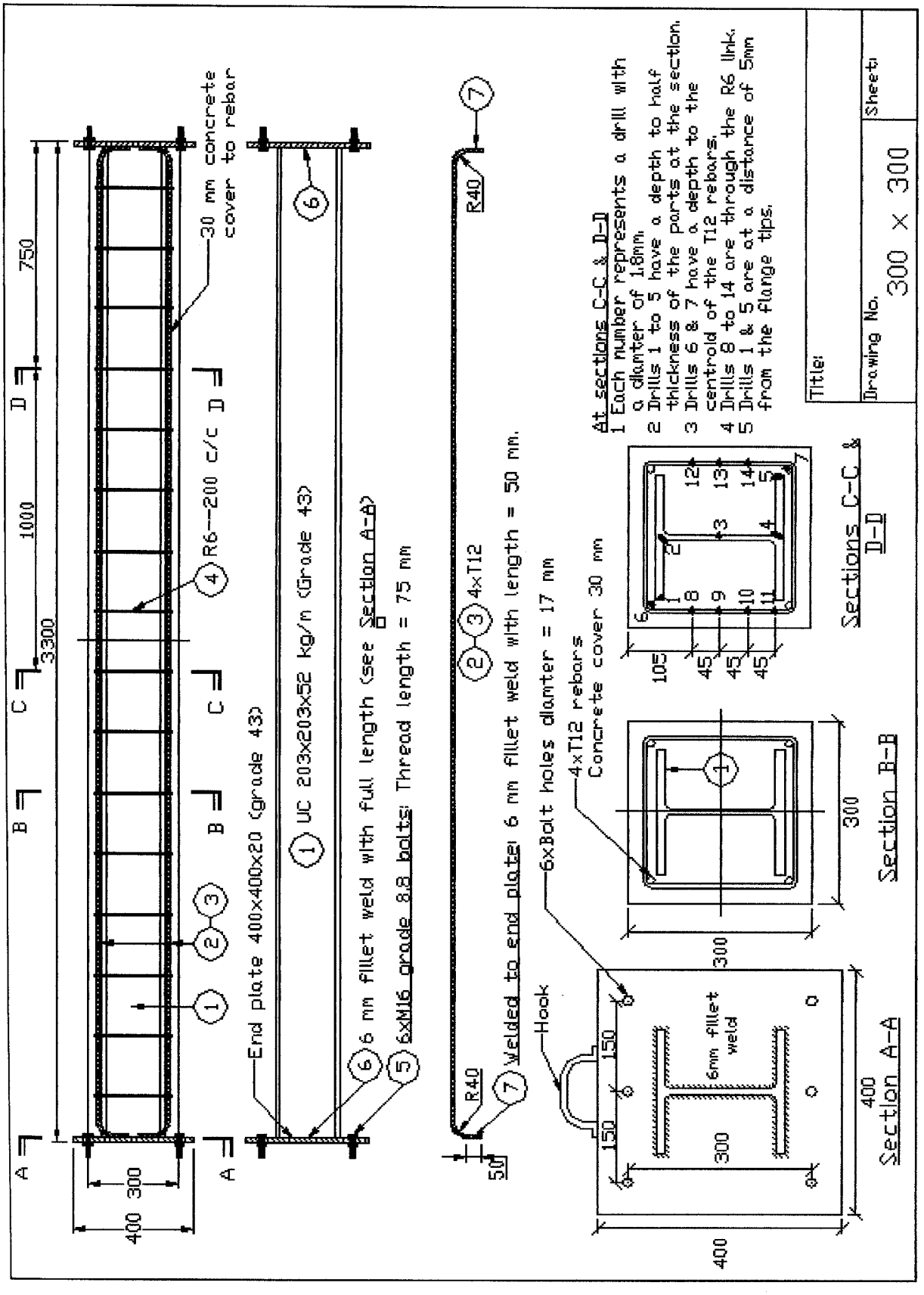

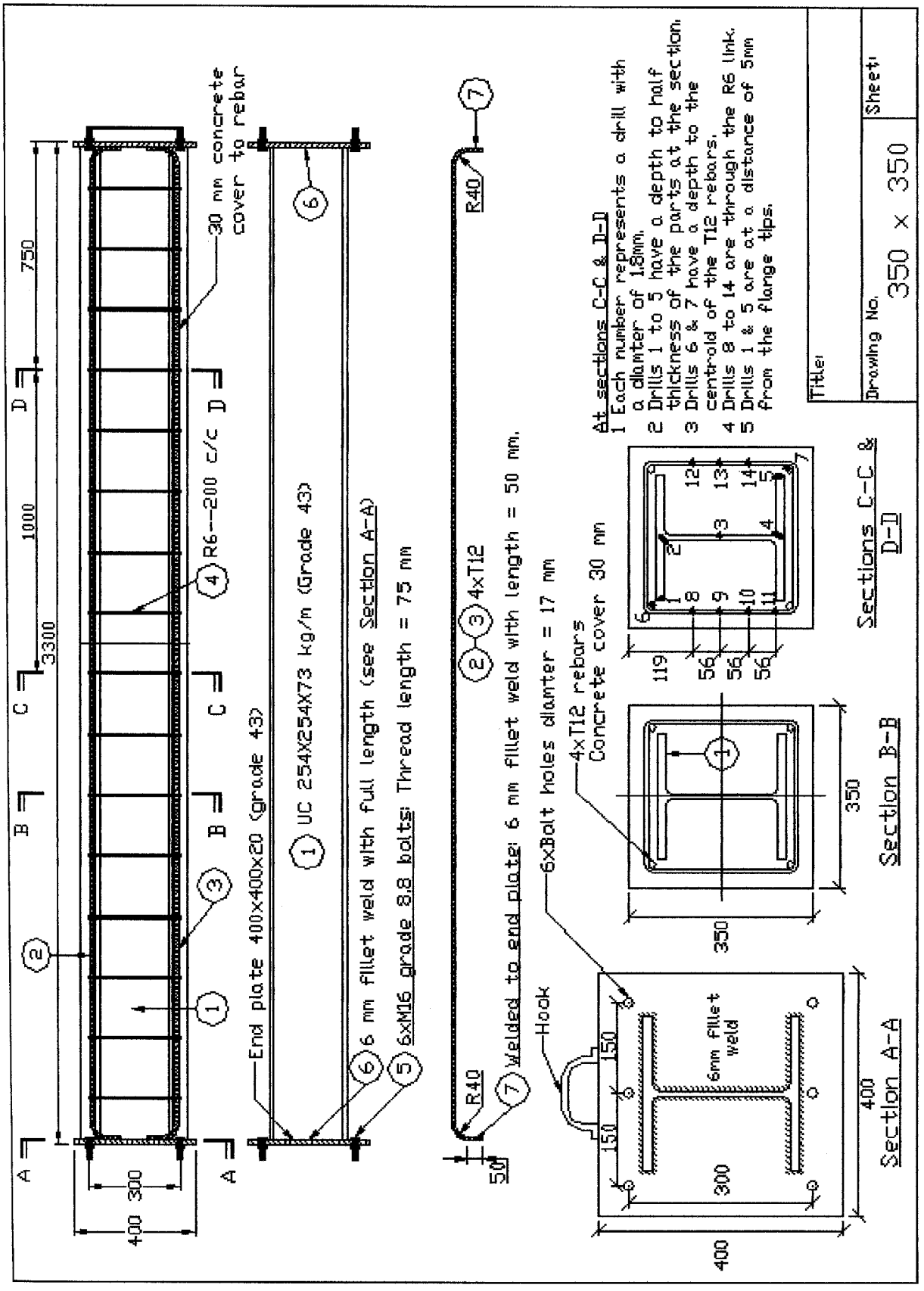

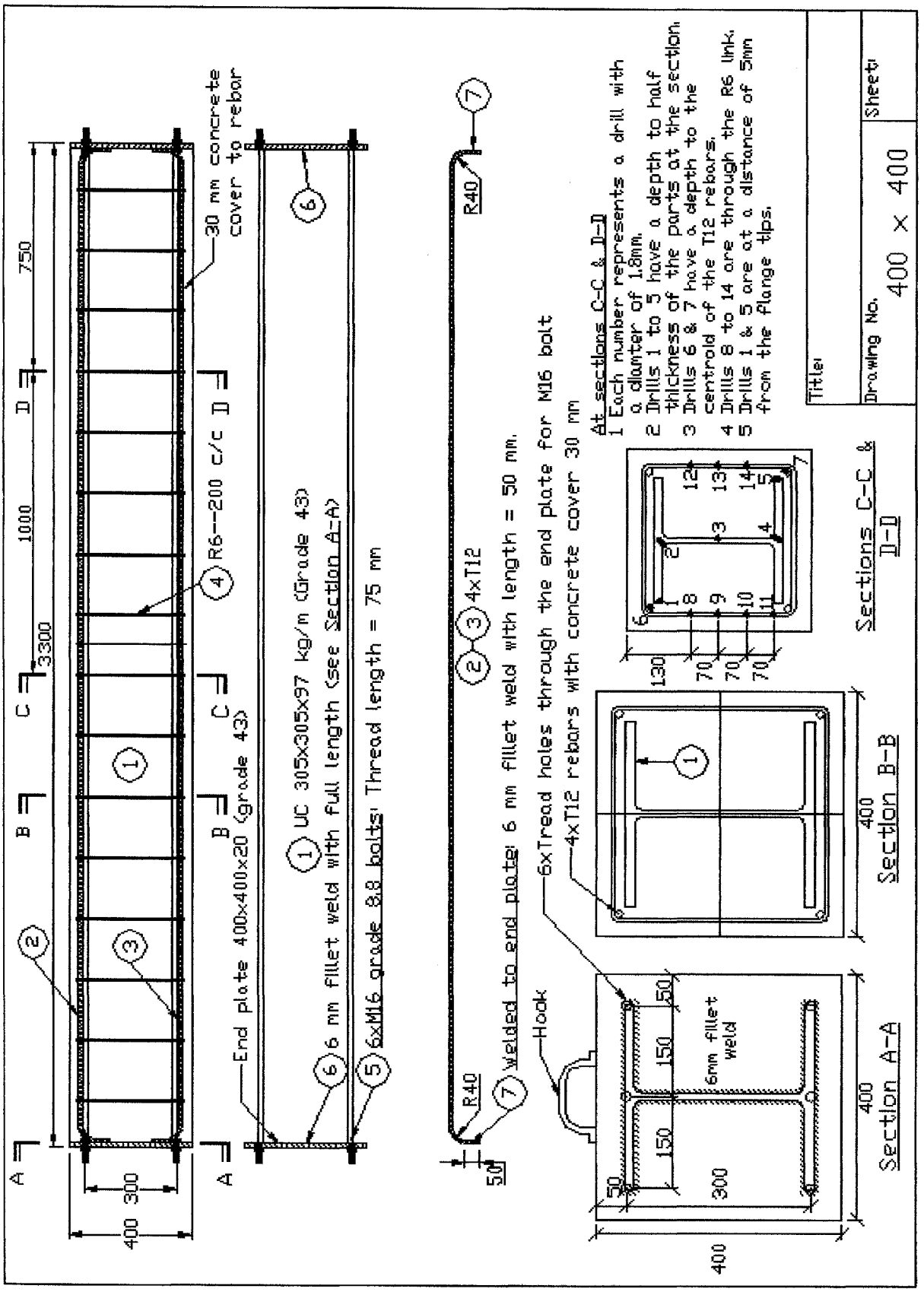

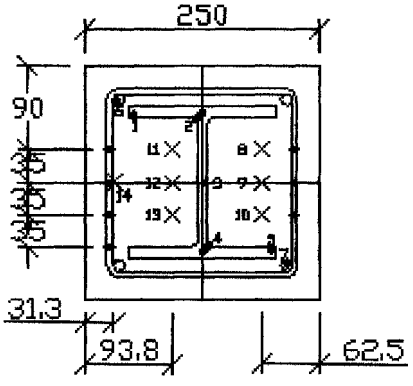

Column 250x250

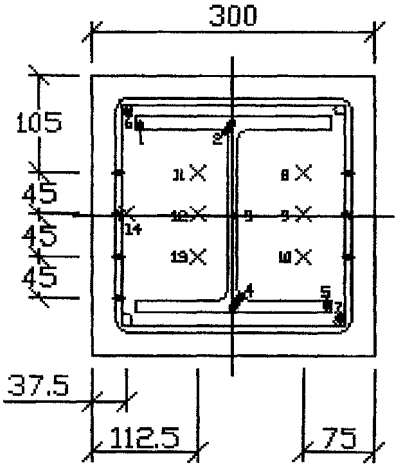

Column 300x300

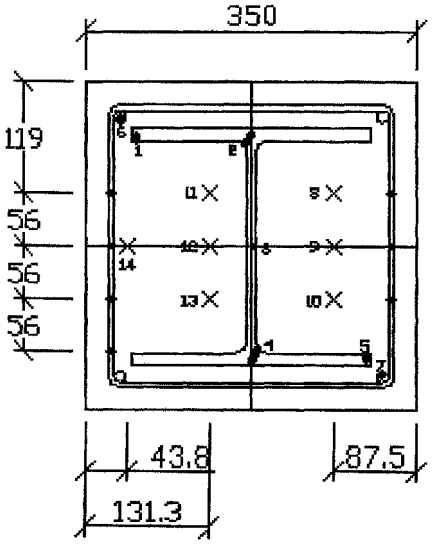

Column 350x350

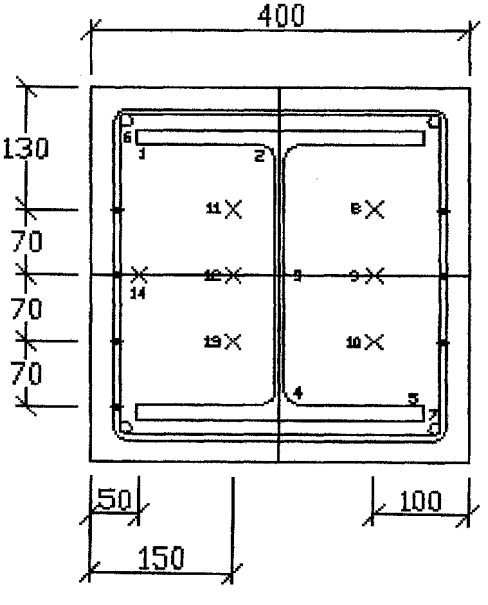

Column 400x400

APPENDIX C

Design Data for Composite Columns According to Eurocode 4

Test specimen - Bending about the minor-axis

No.	Overall size				Reinforcement								Ties		Steel section							
	b	h	Kl	Wgt	size	no.	area	A_s	I_s	f_{sk}	ρ_s	γ_s	size	spac. mm c/c	size	A_a	I_a	f_y	ρ	E	δ	γ_{Ma}
	mm	mm	mm	kg	T		mm^2	mm^2	mm^4	MPa	%					mm^2	mm^4	MPa	%	MPa	(-)	
1	250	250	3540	631	13	4	133	531	4.2E+06	460	0.85%	1	R6	200	UC152x152x37	4629	6.98E+06	332	7.41	205000	0.37	1
2	250	250	3540	630	13	4	133	531	4.2E+06	460	0.85%	1	R6	200	UC152x152x37	4590	6.97E+06	338	7.34	205000	0.37	1
3	300	300	3540	904	13	4	133	531	6.8E+06	460	0.59%	1	R6	200	UC203x203x52	6668	1.82E+07	317	7.41	205000	0.36	1
4	350	350	3540	1232	13	4	133	531	1.0E+07	460	0.43%	1	R6	200	UC254x254x73	9357	4.02E+07	320	7.64	205000	0.37	1
5	400	400	3540	1601	13	4	133	531	1.4E+07	460	0.33%	1	R6	200	UC305x305x97	11999	7.06E+07	400	7.50	205000	0.41	1
6	300	300	3540	831	13	4	133	531	6.8E+06	460	0.59%	1	R6	200	UC152x152x23	2925	4.00E+05	320	3.25	205000	0.19	1
7	300	300	3540	841	13	4	133	531	6.8E+06	460	0.59%	1	R6	200	Joist 114x114x27	3450	2.24E+06	320	3.83	205000	0.22	1
8	300	300	3540	866	13	4	133	531	6.8E+06	460	0.59%	1	R6	200	UC152x152x37	4711	7.06E+06	320	5.23	205000	0.28	1
9	300	300	3540	866	13	4	133	531	6.8E+06	460	0.59%	1	R6	200	UC152x152x37	4711	7.06E+06	320	5.23	205000	0.28	1
10	300	300	3540	866	13	4	133	531	6.8E+06	460	0.59%	1	R6	200	UC152x152x37	4711	7.06E+06	320	5.23	205000	0.28	1
11	300	300	3540	866	13	4	133	531	6.8E+06	460	0.59%	1	R6	200	UC152x152x37	4711	7.06E+06	320	5.23	205000	0.28	1

No.	Concrete					4.8.3.3 Squash	4.8.3.5		4.8.3.8 Strength	Applied P_0				Restraint beam	Test parameters
	A_c	I_c	f_{ck}	E_{cm}	E_c	$N_{pl.Rd}$	$(EI)_e$	N_{cr}	N_{Sd}	$0.7N_{Sd}$	$(EA)_e/L_e$	K_S	α_k		
	mm^2	mm^4	MPa	MPa	MPa	kN	Nmm^2	kN	kN	kN	kN/mm	N/mm			
1	57340	3.14E+08	40	34	25	3730.67	2.29E+12	1804.45	1251.76	876.24	299.23	-	-		Ambient
2	57379	3.14E+08	42	35	26	3844.21	2.29E+12	1803.37	1260.30	882.21	296.99	-	-		CSC
3	82801	6.50E+08	43	35	26	5384.25	5.15E+12	4055.54	2461.68	1723.17	417.47	-	-		CSC, SSR
4	112612	1.20E+09	44	35	26	7450.18	1.04E+13	8152.14	4215.88	2951.11	573.44	-	-		CSC
5	147471	2.05E+09	44	35	26	10559.05	1.74E+13	13728.87	6483.60	4538.52	726.66	-	-		CSC
6	86544	6.68E+08	45	35	26	4490.54	1.50E+12	1180.72	919.86	643.90	200.77	-	-		SSR
7	86019	6.66E+08	43	35	26	4492.22	1.88E+12	1477.64	1110.59	777.41	231.16	-	-		SSR
8	84758	6.61E+08	43	35	26	4849.65	2.86E+12	2256.17	1579.86	1105.90	304.17	0.00	0.000		SSR, ARR
9	84758	6.61E+08	43	35	26	4849.65	2.86E+12	2256.17	1579.86	1105.90	304.17	16.75	0.055	W8x8x5.27x27	ARR
10	84758	6.61E+08	43	35	26	4849.65	2.86E+12	2256.17	1579.86	1105.90	304.17	29.70	0.098	UC203x203x60	ARR
11	84758	6.61E+08	43	35	26	4849.65	2.86E+12	2256.17	1579.86	1105.90	304.17	49.19	0.162	W10x10x10x88.9	ARR

Note: CSC = Cross-Sectional Size; SSR = Steel Section Ratio; and ARR = Axial Restraint Ratio

APPENDIX D

Sample Results from FEMFAN

(Steel Column NRS15)

```
+-+-+-+-+-+-+-+-+-+-+-+-+-+-+-+-+-+-+-+-+-+-+-+-+-+-+-+-+-+-+-+-+-+-+-+-+-+-+-+-
NRS15 - UB152x89x16 Linear Spring kv = 0.14EA/L

Fire analysis

2nd-ORDER ANALYSIS & THERMAL LOADING.
+-+-+-+-+-+-+-+-+-+-+-+-+-+-+-+-+-+-+-+-+-+-+-+-+-+-+-+-+-+-+-+-+-+-+-+-+-+-+-+-
         I N P U T   D A T A   V E R I F I C A T I O N
■■■■■■■■■■■■■■■■■■■■■■■■■■■■■■■■■■■■■■■■■■■■■■■■■■■■■■■■■■■■■■■■■■■■■■■■■■■■■■

MAX NO. OF L-SEARCHES =  6

 LINE SEARCH PARAMS ARE
  TOLERANCE ON RATIO, PERMLS=      0.2000
  MAX. AMP. AT ANY STEP, AMPMX=     5.000
  MAX. TOTAL STEP-LENGTH, ETMXA=    25.00
  MIN. TOTAL STEP-LENGTH, ETMNA=   0.1000E-01
NONLINEAR SOLVING SCHEME(=1: N-R; =2: m.N-R) :  1
ANALYSIS TYPE:   1                MAX STEPS TO DISP-CONTROL:3000
MATRL. MODEL:    1
 NOTE 1: EC3;               2: EC3s;   3: FURUMURA;         4: G.ENGLAND
     5: RUBERTT;       6: ELASTIC;  7: BI-LINEAR E-P
     8: US GUIDE;   9: ECCSm;        10: CTICM
    11: HARMATHY TRI-LINEAR;    12: HARMATHY BI-LINEAR+ELLI.
          13: SKOWRONSKI BI-LINEAR;     14: EL-RAMAWI(Ramburg-Osgood)
CREEP STRAIN HARDENING LAW: STRAIN HARDENNING
DIR. EXCLUDED FROM DOF-QUEUING(1-X,2-Y,3-R):    0
REFER. DOF BY FORCE(0, NOT APPLIED):   19
CREEP EFFECT EXCLUDED
TOTAL ELEMENTS NUMBER:   12          TOTAL NODES NUMBER:  13
TOTAL SECTIONS TYPE:      2          HALF BAND_WIDTH:      5
TOTAL NUMBER OF NODES WITH SPRINGS (INCLUD. ELAS. & SEMI-
RIGID SPRINGS, '-' DENOTES GAP CONSIDERED): -1
MAX. ITERATIVE NUMBER:  100          ITER. TOL:  0.10000D-06
NUMBER OF TEMP PROFILE:   2
PIVOT[=0, NA; (0,10), PT; >=10, FL]:   7
TIME STEP FOR OUTPUT:     2

SECTION DATA
~~~~~~~~~~~~~~~~~~~~~~~~~~~~~~~~~~~~~~~~~~~~~~~~~~~~~~~~~~~~~~~~~~~~~~~~~~~~~~
No     Etop      Eweb      Ebot      Fytop     Fyweb      Fybot      B      Tf      H      Tw
r
 1 .2150D+09 .2150D+09 .2150D+09 .3050D+06 .3050D+06 .3050D+06  0.0899
0.0071  0.1541  0.0052  0.0076
 2 .2100D+09 .2100D+09 .2100D+09 .3000D+06 .3000D+06 .3000D+06  0.1500
0.0100  0.2460  0.1500  0.0000

SPRINGS-ON-NODE DATA
```

NODE Kx Ky Kr TIMELAG@X Y ROT GAP@X @Y ROT-GAP
13 0.00000D+00 0.61340D+05 0.00000D+00 0.0 11.0 0.0 0.000D+00 0.160D-02 0.000D+00

ELEMENT NO. OF INTERNAL FORCE OUTPUT

7

STRUCTURAL ELEMENT DATA

NO.	NAME	MATL	DELTA_X	DELTA_Y	I-NODE	J-NODE	BEND-AXIS
1	CO01	2	0.0000	0.1200	1	2	S
2	CO02	1	0.0032	0.2500	2	3	W
3	CO03	1	0.0013	0.1250	3	4	W
4	CO04	1	0.0010	0.1250	4	5	W
5	CO05	1	0.0006	0.1250	5	6	W
6	CO06	1	0.0002	0.1250	6	7	W
7	CO07	1	-0.0002	0.1250	7	8	W
8	CO08	1	-0.0006	0.1250	8	9	W
9	CO09	1	-0.0010	0.1250	9	10	W
10	CO10	1	-0.0013	0.1250	10	11	W
11	CO11	1	-0.0032	0.2500	11	12	W
12	CO12	2	0.0000	0.1200	12	13	S

DOF RESTRAINED DATA

THESE DOFs ARE RESTRAINED
1 2 37

LOADS DATA

NODE	Fx	Fy	M
1	0.0000	0.0000	-1.2620
13	0.0000	-199.00	1.2620

ELEMENT'S NO IN FIRES

THERE ARE 8 ELEMENTS IN FIRE PROFILE- 1
ELEMENT'S NO ARE: 3 4 5 6 7 8 9 10
THERE ARE 2 ELEMENTS IN FIRE PROFILE- 2
ELEMENT'S NO ARE: 2 11

NODES' NO WHOSE DISP. TO BE OUTPUT

NDISP= 2

NODE NO: 7 13

TEMP. PROFILE (Top -> Web -> Bottom)

NTS=10
NO. 1FIRE PROFILE, EIE. ENGAGED: 3 4 5 6 7 8 9 10
NO. 2FIRE PROFILE, EIE. ENGAGED: 2 11

	PROFILE - 1			PROFILE - 2			PROFILE - 3		
TIME	Tf	Tw	Tb	Tf	Tw	Tb	Tf	Tw	Tb
0.00	28.0	28.0	28.0	28.0	28.0	28.0	0.0	0.0	0.0
5.00	52.0	52.0	52.0	42.0	42.0	42.0	0.0	0.0	0.0
10.00	82.0	82.0	82.0	57.0	57.0	57.0	0.0	0.0	0.0
15.00	108.0	108.0	108.0	70.0	70.0	70.0	0.0	0.0	0.0
20.00	148.0	148.0	148.0	90.0	90.0	90.0	0.0	0.0	0.0
25.00	188.0	188.0	188.0	112.0	112.0	112.0	0.0	0.0	0.0
30.00	233.0	233.0	233.0	137.0	137.0	137.0	0.0	0.0	0.0
35.00	271.0	271.0	271.0	158.0	158.0	158.0	0.0	0.0	0.0
40.00	313.0	313.0	313.0	182.0	182.0	182.0	0.0	0.0	0.0
45.00	325.0	325.0	325.0	190.0	190.0	190.0	0.0	0.0	0.0

T INCR.	SPACING DIFFER @time	SPACING-1	SPACING-2
30.00	0.2000	0.0100	

ANALYSIS RESULTS

****

TB	ELE	Xj	Yj	Mj	NODE	U	V	THETA	NODE	U	V	THETA
28.0	7	0.00	-199.00	3.78	7	0.6678E-02	-0.3549E-03	0.5385E-16	13	0.0000E+00	-0.7098E-03	0.1229E-01
29.9	7	0.00	-199.00	3.78	7	0.6678E-02	-0.3397E-03	0.1215E-16	13	0.0000E+00	-0.6795E-03	0.1229E-01
31.8	7	0.00	-199.00	3.78	7	0.6678E-02	-0.3245E-03	-0.4163E-16	13	0.0000E+00	-0.6491E-03	0.1229E-01
33.8	7	0.00	-199.00	3.78	7	0.6679E-02	-0.3093E-03	0.4865E-16	13	0.0000E+00	-0.6186E-03	0.1229E-01
35.7	7	0.00	-199.00	3.78	7	0.6679E-02	-0.2941E-03	-0.2213E-16	13	0.0000E+00	-0.5882E-03	0.1229E-01
37.6	7	0.00	-199.00	3.78	7	0.6679E-02	-0.2789E-03	0.1426E-15	13	0.0000E+00	-0.5577E-03	0.1229E-01
39.5	7	0.00	-199.00	3.78	7	0.6680E-02	-0.2636E-03	0.2812E-16	13	0.0000E+00	-0.5272E-03	0.1229E-01
41.4	7	0.00	-199.00	3.78	7	0.6680E-02	-0.2483E-03	-0.9720E-16	13	0.0000E+00	-0.4966E-03	0.1229E-01

43.4 7 0.00 -199.00 3.78 7 0.6680E-02 -0.2330E-03 0.3820E-16 13
0.0000E+00 -0.4660E-03 0.1229E-01
45.3 7 0.00 -199.00 3.78 7 0.6680E-02 -0.2177E-03 0.6950E-16 13
0.0000E+00 -0.4354E-03 0.1229E-01
47.2 7 0.00 -199.00 3.78 7 0.6681E-02 -0.2024E-03 -0.6343E-16 13
0.0000E+00 -0.4048E-03 0.1229E-01
49.1 7 0.00 -199.00 3.78 7 0.6681E-02 -0.1870E-03 -0.4565E-16 13
0.0000E+00 -0.3741E-03 0.1229E-01
51.0 7 0.00 -199.00 3.78 7 0.6681E-02 -0.1717E-03 0.5939E-16 13
0.0000E+00 -0.3434E-03 0.1229E-01
53.2 7 0.00 -199.00 3.78 7 0.6682E-02 -0.1547E-03 0.2019E-16 13
0.0000E+00 -0.3094E-03 0.1229E-01
55.6 7 0.00 -199.00 3.78 7 0.6682E-02 -0.1361E-03 -0.4998E-16 13
0.0000E+00 -0.2721E-03 0.1229E-01
58.0 7 0.00 -199.00 3.78 7 0.6682E-02 -0.1174E-03 0.2040E-16 13
0.0000E+00 -0.2348E-03 0.1229E-01
60.4 7 0.00 -199.00 3.78 7 0.6683E-02 -0.9871E-04 0.2962E-16 13
0.0000E+00 -0.1974E-03 0.1229E-01
62.8 7 0.00 -199.00 3.78 7 0.6683E-02 -0.8000E-04 -0.9904E-16 13
0.0000E+00 -0.1600E-03 0.1229E-01
65.2 7 0.00 -199.00 3.78 7 0.6684E-02 -0.6127E-04 -0.5950E-16 13
0.0000E+00 -0.1225E-03 0.1229E-01
67.6 7 0.00 -199.00 3.78 7 0.6684E-02 -0.4251E-04 -0.6494E-16 13
0.0000E+00 -0.8502E-04 0.1229E-01
70.0 7 0.00 -199.00 3.78 7 0.6684E-02 -0.2373E-04 0.5335E-16 13
0.0000E+00 -0.4745E-04 0.1229E-01
72.4 7 0.00 -199.00 3.78 7 0.6685E-02 -0.4917E-05 -0.7331E-16 13
0.0000E+00 -0.9834E-05 0.1229E-01
74.8 7 0.00 -199.00 3.78 7 0.6685E-02 0.1392E-04 -0.3846E-16 13
0.0000E+00 0.2784E-04 0.1229E-01
77.2 7 0.00 -199.00 3.78 7 0.6685E-02 0.3278E-04 0.6521E-16 13
0.0000E+00 0.6556E-04 0.1229E-01
79.6 7 0.00 -199.00 3.78 7 0.6686E-02 0.5167E-04 -0.9150E-17 13
0.0000E+00 0.1033E-03 0.1229E-01
82.0 7 0.00 -199.00 3.78 7 0.6686E-02 0.7058E-04 0.1052E-15 13
0.0000E+00 0.1412E-03 0.1229E-01
84.1 7 0.00 -199.00 3.78 7 0.6686E-02 0.8699E-04 -0.1228E-16 13
0.0000E+00 0.1740E-03 0.1229E-01
86.2 7 0.00 -199.00 3.78 7 0.6687E-02 0.1034E-03 -0.1149E-15 13
0.0000E+00 0.2068E-03 0.1229E-01
88.2 7 0.00 -133.00 2.72 7 0.4926E-02 0.2620E-03 -0.4313E-16 13
0.0000E+00 0.5240E-03 0.9233E-02
90.3 7 0.00 -134.61 2.74 7 0.4964E-02 0.2752E-03 0.2534E-16 13
0.0000E+00 0.5503E-03 0.9297E-02
92.4 7 0.00 -136.22 2.76 7 0.5002E-02 0.2883E-03 0.1375E-16 13
0.0000E+00 0.5766E-03 0.9362E-02
94.5 7 0.00 -137.84 2.78 7 0.5039E-02 0.3015E-03 0.2608E-16 13
0.0000E+00 0.6029E-03 0.9427E-02

96.6 7 0.00 -139.45 2.81 7 0.5078E-02 0.3146E-03 -0.4123E-16 13
0.0000E+00 0.6292E-03 0.9493E-02
98.6 7 0.00 -141.07 2.83 7 0.5116E-02 0.3278E-03 -0.6881E-16 13
0.0000E+00 0.6556E-03 0.9560E-02
100.7 7 0.00 -142.67 2.85 7 0.5159E-02 0.3408E-03 0.1453E-16 13
0.0000E+00 0.6817E-03 0.9633E-02
102.8 7 0.00 -144.24 2.88 7 0.5209E-02 0.3536E-03 0.1026E-15 13
0.0000E+00 0.7072E-03 0.9718E-02
104.9 7 0.00 -145.80 2.90 7 0.5260E-02 0.3664E-03 -0.1216E-15 13
0.0000E+00 0.7328E-03 0.9805E-02
107.0 7 0.00 -147.37 2.93 7 0.5312E-02 0.3791E-03 -0.2262E-16 13
0.0000E+00 0.7583E-03 0.9893E-02
109.6 7 0.00 -149.36 2.96 7 0.5378E-02 0.3953E-03 0.6883E-16 13
0.0000E+00 0.7907E-03 0.1001E-01
112.8 7 0.00 -151.77 3.00 7 0.5460E-02 0.4150E-03 -0.1567E-16 13
0.0000E+00 0.8300E-03 0.1014E-01
116.0 7 0.00 -154.17 3.04 7 0.5544E-02 0.4346E-03 0.1007E-15 13
0.0000E+00 0.8692E-03 0.1029E-01
119.2 7 0.00 -156.58 3.08 7 0.5628E-02 0.4542E-03 0.6386E-16 13
0.0000E+00 0.9084E-03 0.1043E-01
122.4 7 0.00 -158.98 3.12 7 0.5715E-02 0.4738E-03 0.5335E-16 13
0.0000E+00 0.9476E-03 0.1058E-01
125.6 7 0.00 -161.39 3.16 7 0.5803E-02 0.4934E-03 -0.5698E-16 13
0.0000E+00 0.9868E-03 0.1073E-01
128.8 7 0.00 -163.79 3.21 7 0.5893E-02 0.5130E-03 0.4468E-16 13
0.0000E+00 0.1026E-02 0.1088E-01
132.0 7 0.00 -166.19 3.25 7 0.5985E-02 0.5325E-03 0.2891E-17 13
0.0000E+00 0.1065E-02 0.1104E-01
135.2 7 0.00 -168.59 3.29 7 0.6078E-02 0.5521E-03 0.7317E-16 13
0.0000E+00 0.1104E-02 0.1119E-01
138.4 7 0.00 -170.98 3.34 7 0.6173E-02 0.5716E-03 0.4845E-16 13
0.0000E+00 0.1143E-02 0.1136E-01
141.6 7 0.00 -173.38 3.38 7 0.6271E-02 0.5911E-03 0.8182E-16 13
0.0000E+00 0.1182E-02 0.1152E-01
144.8 7 0.00 -175.77 3.43 7 0.6370E-02 0.6106E-03 0.2455E-17 13
0.0000E+00 0.1221E-02 0.1169E-01
148.0 7 0.00 -178.16 3.48 7 0.6471E-02 0.6301E-03 0.1005E-15 13
0.0000E+00 0.1260E-02 0.1186E-01
151.2 7 0.00 -180.59 3.53 7 0.6575E-02 0.6499E-03 -0.3453E-16 13
0.0000E+00 0.1300E-02 0.1204E-01
154.4 7 0.00 -183.02 3.58 7 0.6682E-02 0.6697E-03 0.8442E-16 13
0.0000E+00 0.1339E-02 0.1222E-01
157.6 7 0.00 -185.45 3.63 7 0.6791E-02 0.6895E-03 -0.7606E-16 13
0.0000E+00 0.1379E-02 0.1240E-01

.....

320.0 7 0.00 -115.38 7.53 7 0.5007E-01 0.1184E-03 0.1191E-16 13
0.0000E+00 0.2368E-03 0.7552E-01
320.0 7 0.00 -115.37 7.53 7 0.5008E-01 0.1183E-03 0.8680E-16 13
0.0000E+00 0.2366E-03 0.7553E-01
320.1 7 0.00 -115.35 7.53 7 0.5009E-01 0.1181E-03 -0.3137E-16 13
0.0000E+00 0.2363E-03 0.7554E-01
320.1 7 0.00 -115.33 7.53 7 0.5010E-01 0.1180E-03 -0.1975E-17 13
0.0000E+00 0.2360E-03 0.7555E-01
320.2 7 0.00 -115.31 7.53 7 0.5010E-01 0.1179E-03 0.1862E-16 13
0.0000E+00 0.2357E-03 0.7557E-01
320.2 7 0.00 -115.30 7.53 7 0.5011E-01 0.1177E-03 -0.2922E-16 13
0.0000E+00 0.2354E-03 0.7558E-01
320.2 7 0.00 -115.28 7.53 7 0.5012E-01 0.1176E-03 -0.7695E-16 13
0.0000E+00 0.2351E-03 0.7559E-01
320.3 7 0.00 -115.26 7.53 7 0.5013E-01 0.1174E-03 0.5792E-16 13
0.0000E+00 0.2348E-03 0.7560E-01
320.3 7 0.00 -115.24 7.53 7 0.5014E-01 0.1173E-03 0.1275E-15 13
0.0000E+00 0.2346E-03 0.7562E-01
320.4 7 0.00 -115.23 7.53 7 0.5015E-01 0.1171E-03 -0.1531E-15 13
0.0000E+00 0.2343E-03 0.7563E-01
320.4 7 0.00 -115.21 7.53 7 0.5015E-01 0.1170E-03 -0.8364E-16 13
0.0000E+00 0.2340E-03 0.7564E-01
320.5 7 0.00 -115.19 7.53 7 0.5016E-01 0.1168E-03 0.1957E-15 13
0.0000E+00 0.2337E-03 0.7565E-01
320.5 7 0.00 -115.17 7.53 7 0.5017E-01 0.1167E-03 0.1683E-15 13
0.0000E+00 0.2334E-03 0.7567E-01
320.6 7 0.00 -115.16 7.53 7 0.5018E-01 0.1166E-03 0.2388E-16 13
0.0000E+00 0.2331E-03 0.7568E-01
320.6 7 0.00 -115.14 7.53 7 0.5019E-01 0.1164E-03 -0.4396E-16 13
0.0000E+00 0.2328E-03 0.7569E-01
320.7 7 0.00 -115.12 7.53 7 0.5020E-01 0.1163E-03 -0.1440E-16 13
0.0000E+00 0.2326E-03 0.7570E-01
320.7 7 0.00 -115.10 7.53 7 0.5020E-01 0.1161E-03 0.2745E-16 13
0.0000E+00 0.2323E-03 0.7572E-01
320.8 7 0.00 -115.09 7.53 7 0.5021E-01 0.1160E-03 0.1471E-16 13
0.0000E+00 0.2320E-03 0.7573E-01
320.8 7 0.00 -115.07 7.53 7 0.5022E-01 0.1159E-03 0.1601E-15 13
0.0000E+00 0.2317E-03 0.7574E-01
320.9 7 0.00 -115.05 7.53 7 0.5023E-01 0.1157E-03 0.4113E-16 13
0.0000E+00 0.2314E-03 0.7575E-01
320.9 7 0.00 -115.03 7.53 7 0.5024E-01 0.1156E-03 0.3093E-16 13
0.0000E+00 0.2311E-03 0.7577E-01
321.0 7 0.00 -115.02 7.53 7 0.5025E-01 0.1154E-03 0.9703E-16 13
0.0000E+00 0.2309E-03 0.7578E-01
321.0 7 0.00 -115.00 7.53 7 0.5025E-01 0.1153E-03 0.1590E-15 13
0.0000E+00 0.2306E-03 0.7579E-01
321.1 7 0.00 -114.98 7.53 7 0.5026E-01 0.1151E-03 -0.1782E-16 13
0.0000E+00 0.2303E-03 0.7580E-01

321.1 7 0.00 -114.96 7.53 7 0.5027E-01 0.1150E-03 0.2585E-15 13
0.0000E+00 0.2300E-03 0.7582E-01
321.2 7 0.00 -114.95 7.53 7 0.5028E-01 0.1149E-03 -0.4688E-16 13
0.0000E+00 0.2297E-03 0.7583E-01
321.2 7 0.00 -114.93 7.53 7 0.5029E-01 0.1147E-03 0.8366E-16 13
0.0000E+00 0.2294E-03 0.7584E-01
321.3 7 0.00 -114.91 7.53 7 0.5030E-01 0.1146E-03 0.8763E-16 13
0.0000E+00 0.2292E-03 0.7586E-01
321.3 7 0.00 -114.89 7.53 7 0.5030E-01 0.1144E-03 0.1401E-15 13
0.0000E+00 0.2289E-03 0.7587E-01
321.4 7 0.00 -114.88 7.53 7 0.5031E-01 0.1143E-03 0.1055E-15 13
0.0000E+00 0.2286E-03 0.7588E-01
321.4 7 0.00 -114.86 7.53 7 0.5032E-01 0.1142E-03 0.1136E-15 13
0.0000E+00 0.2283E-03 0.7589E-01
321.4 7 0.00 -114.84 7.53 7 0.5033E-01 0.1140E-03 0.1454E-15 13
0.0000E+00 0.2280E-03 0.7590E-01
321.5 7 0.00 -114.83 7.53 7 0.5034E-01 0.1139E-03 0.4068E-16 13
0.0000E+00 0.2277E-03 0.7592E-01
321.5 7 0.00 -114.81 7.53 7 0.5034E-01 0.1137E-03 0.3413E-16 13
0.0000E+00 0.2275E-03 0.7593E-01
321.6 7 0.00 -114.79 7.53 7 0.5035E-01 0.1136E-03 -0.2001E-17 13
0.0000E+00 0.2272E-03 0.7594E-01
321.6 7 0.00 -114.77 7.53 7 0.5036E-01 0.1134E-03 0.9648E-16 13
0.0000E+00 0.2269E-03 0.7595E-01
321.7 7 0.00 -114.76 7.53 7 0.5037E-01 0.1133E-03 0.3222E-16 13
0.0000E+00 0.2266E-03 0.7597E-01
321.7 7 0.00 -114.74 7.53 7 0.5038E-01 0.1132E-03 0.8430E-17 13
0.0000E+00 0.2263E-03 0.7598E-01
321.8 7 0.00 -114.72 7.53 7 0.5039E-01 0.1130E-03 0.6094E-16 13
0.0000E+00 0.2260E-03 0.7599E-01
321.8 7 0.00 -114.70 7.53 7 0.5039E-01 0.1129E-03 -0.2109E-16 13
0.0000E+00 0.2258E-03 0.7600E-01
321.9 7 0.00 -114.69 7.53 7 0.5040E-01 0.1127E-03 0.7220E-16 13
0.0000E+00 0.2255E-03 0.7602E-01
321.9 7 0.00 -114.67 7.53 7 0.5041E-01 0.1126E-03 0.9997E-17 13
0.0000E+00 0.2252E-03 0.7603E-01
322.0 7 0.00 -114.65 7.53 7 0.5042E-01 0.1125E-03 0.6211E-16 13
0.0000E+00 0.2249E-03 0.7604E-01
322.0 7 0.00 -114.64 7.53 7 0.5043E-01 0.1123E-03 0.1463E-15 13
0.0000E+00 0.2246E-03 0.7605E-01
322.1 7 0.00 -114.62 7.53 7 0.5044E-01 0.1122E-03 0.7338E-16 13
0.0000E+00 0.2244E-03 0.7607E-01
322.1 7 0.00 -114.60 7.53 7 0.5044E-01 0.1120E-03 -0.2530E-16 13
0.0000E+00 0.2241E-03 0.7608E-01
322.2 7 0.00 -114.58 7.53 7 0.5045E-01 0.1119E-03 0.9587E-17 13
0.0000E+00 0.2238E-03 0.7609E-01
322.2 7 0.00 -114.57 7.53 7 0.5046E-01 0.1118E-03 0.1613E-15 13
0.0000E+00 0.2235E-03 0.7610E-01

322.3 7 0.00 -114.55 7.53 7 0.5047E-01 0.1116E-03 0.6037E-16 13
0.0000E+00 0.2232E-03 0.7612E-01
322.3 7 0.00 -114.53 7.53 7 0.5048E-01 0.1115E-03 -0.3784E-18 13
0.0000E+00 0.2230E-03 0.7613E-01
322.4 7 0.00 -114.51 7.53 7 0.5048E-01 0.1113E-03 -0.1453E-15 13
0.0000E+00 0.2227E-03 0.7614E-01
322.4 7 0.00 -114.50 7.53 7 0.5049E-01 0.1112E-03 0.8812E-16 13
0.0000E+00 0.2224E-03 0.7615E-01
322.5 7 0.00 -114.48 7.53 7 0.5050E-01 0.1111E-03 0.1313E-16 13
0.0000E+00 0.2221E-03 0.7617E-01
322.5 7 0.00 -114.46 7.53 7 0.5051E-01 0.1109E-03 0.2512E-15 13
0.0000E+00 0.2218E-03 0.7618E-01
322.6 7 0.00 -114.45 7.53 7 0.5052E-01 0.1108E-03 0.8586E-16 13
0.0000E+00 0.2216E-03 0.7619E-01
322.6 7 0.00 -114.43 7.53 7 0.5053E-01 0.1106E-03 0.1482E-16 13
0.0000E+00 0.2213E-03 0.7620E-01
322.6 7 0.00 -114.41 7.53 7 0.5053E-01 0.1105E-03 0.1134E-15 13
0.0000E+00 0.2210E-03 0.7622E-01
322.7 7 0.00 -114.39 7.53 7 0.5054E-01 0.1104E-03 -0.1119E-15 13
0.0000E+00 0.2207E-03 0.7623E-01
322.7 7 0.00 -114.38 7.53 7 0.5055E-01 0.1102E-03 0.6508E-16 13
0.0000E+00 0.2204E-03 0.7624E-01
322.8 7 0.00 -114.36 7.53 7 0.5056E-01 0.1101E-03 0.1916E-16 13
0.0000E+00 0.2202E-03 0.7625E-01
322.8 7 0.00 -114.34 7.52 7 0.5057E-01 0.1099E-03 0.2706E-16 13
0.0000E+00 0.2199E-03 0.7627E-01
322.9 7 0.00 -114.33 7.52 7 0.5058E-01 0.1098E-03 -0.5925E-16 13
0.0000E+00 0.2196E-03 0.7628E-01
322.9 7 0.00 -114.31 7.52 7 0.5058E-01 0.1097E-03 0.1445E-15 13
0.0000E+00 0.2193E-03 0.7629E-01
323.0 7 0.00 -114.29 7.52 7 0.5059E-01 0.1095E-03 -0.4737E-17 13
0.0000E+00 0.2190E-03 0.7630E-01
323.0 7 0.00 -114.28 7.52 7 0.5060E-01 0.1094E-03 0.6476E-16 13
0.0000E+00 0.2188E-03 0.7632E-01
323.1 7 0.00 -114.26 7.52 7 0.5061E-01 0.1092E-03 -0.1256E-15 13
0.0000E+00 0.2185E-03 0.7633E-01
323.1 7 0.00 -114.24 7.52 7 0.5062E-01 0.1091E-03 0.7625E-16 13
0.0000E+00 0.2182E-03 0.7634E-01
323.2 7 0.00 -114.22 7.52 7 0.5062E-01 0.1090E-03 0.1188E-15 13
0.0000E+00 0.2179E-03 0.7635E-01
323.2 7 0.00 -114.21 7.52 7 0.5063E-01 0.1088E-03 0.1157E-15 13
0.0000E+00 0.2177E-03 0.7637E-01
323.3 7 0.00 -114.19 7.52 7 0.5064E-01 0.1087E-03 0.1646E-15 13
0.0000E+00 0.2174E-03 0.7638E-01
323.3 7 0.00 -114.17 7.52 7 0.5065E-01 0.1085E-03 -0.4290E-16 13
0.0000E+00 0.2171E-03 0.7639E-01
323.4 7 0.00 -114.16 7.52 7 0.5066E-01 0.1084E-03 0.1111E-16 13
0.0000E+00 0.2168E-03 0.7640E-01

323.4 7 0.00 -114.14 7.52 7 0.5067E-01 0.1083E-03 0.2643E-16 13
0.0000E+00 0.2165E-03 0.7642E-01
323.5 7 0.00 -114.12 7.52 7 0.5067E-01 0.1081E-03 -0.1648E-16 13
0.0000E+00 0.2163E-03 0.7643E-01
323.5 7 0.00 -114.10 7.52 7 0.5068E-01 0.1080E-03 0.5000E-16 13
0.0000E+00 0.2160E-03 0.7644E-01
323.6 7 0.00 -114.09 7.52 7 0.5069E-01 0.1079E-03 -0.3012E-16 13
0.0000E+00 0.2157E-03 0.7645E-01
323.6 7 0.00 -114.07 7.52 7 0.5070E-01 0.1077E-03 -0.7249E-16 13
0.0000E+00 0.2154E-03 0.7647E-01
323.7 7 0.00 -114.05 7.52 7 0.5071E-01 0.1076E-03 0.9354E-16 13
0.0000E+00 0.2152E-03 0.7648E-01
323.7 7 0.00 -114.04 7.52 7 0.5071E-01 0.1074E-03 0.1176E-15 13
0.0000E+00 0.2149E-03 0.7649E-01
323.8 7 0.00 -114.02 7.52 7 0.5072E-01 0.1073E-03 -0.7617E-17 13
0.0000E+00 0.2146E-03 0.7650E-01
323.8 7 0.00 -114.00 7.52 7 0.5073E-01 0.1072E-03 0.3236E-16 13
0.0000E+00 0.2143E-03 0.7651E-01
323.8 7 0.00 -113.99 7.52 7 0.5074E-01 0.1070E-03 0.2036E-16 13
0.0000E+00 0.2141E-03 0.7653E-01
323.9 7 0.00 -113.97 7.52 7 0.5075E-01 0.1069E-03 0.2195E-15 13
0.0000E+00 0.2138E-03 0.7654E-01
323.9 7 0.00 -113.95 7.52 7 0.5075E-01 0.1068E-03 0.9860E-16 13
0.0000E+00 0.2135E-03 0.7655E-01
324.0 7 0.00 -113.94 7.52 7 0.5076E-01 0.1066E-03 0.7973E-16 13
0.0000E+00 0.2132E-03 0.7656E-01
324.0 7 0.00 -113.92 7.52 7 0.5077E-01 0.1065E-03 0.2063E-15 13
0.0000E+00 0.2130E-03 0.7658E-01
324.1 7 0.00 -113.90 7.52 7 0.5078E-01 0.1063E-03 0.9282E-16 13
0.0000E+00 0.2127E-03 0.7659E-01
324.1 7 0.00 -113.88 7.52 7 0.5079E-01 0.1062E-03 0.1235E-15 13
0.0000E+00 0.2124E-03 0.7660E-01
324.2 7 0.00 -113.87 7.52 7 0.5080E-01 0.1061E-03 0.2433E-15 13
0.0000E+00 0.2121E-03 0.7661E-01
324.2 7 0.00 -113.85 7.52 7 0.5080E-01 0.1059E-03 -0.1312E-16 13
0.0000E+00 0.2119E-03 0.7663E-01
324.3 7 0.00 -113.83 7.52 7 0.5081E-01 0.1058E-03 0.7984E-16 13
0.0000E+00 0.2116E-03 0.7664E-01
324.3 7 0.00 -113.82 7.52 7 0.5082E-01 0.1057E-03 0.9519E-16 13
0.0000E+00 0.2113E-03 0.7665E-01
324.4 7 0.00 -113.80 7.52 7 0.5083E-01 0.1055E-03 0.1145E-15 13
0.0000E+00 0.2110E-03 0.7666E-01
324.4 7 0.00 -113.78 7.52 7 0.5084E-01 0.1054E-03 0.8526E-16 13
0.0000E+00 0.2108E-03 0.7668E-01
324.5 7 0.00 -113.77 7.52 7 0.5084E-01 0.1052E-03 0.2834E-16 13
0.0000E+00 0.2105E-03 0.7669E-01
324.5 7 0.00 -113.75 7.52 7 0.5085E-01 0.1051E-03 -0.8952E-16 13
0.0000E+00 0.2102E-03 0.7670E-01

```
 324.6   7    0.00 -113.73    7.52  7 0.5086E-01  0.1050E-03  0.1313E-15 13
0.0000E+00  0.2099E-03  0.7671E-01
 324.6   7    0.00 -113.72    7.52  7 0.5087E-01  0.1048E-03  0.1606E-15 13
0.0000E+00  0.2097E-03  0.7672E-01
 324.7   7    0.00 -113.70    7.52  7 0.5088E-01  0.1047E-03  0.6188E-16 13
0.0000E+00  0.2094E-03  0.7674E-01
 324.7   7    0.00 -113.68    7.52  7 0.5088E-01  0.1046E-03  0.4633E-16 13
0.0000E+00  0.2091E-03  0.7675E-01
 324.8   7    0.00 -113.67    7.52  7 0.5089E-01  0.1044E-03  0.4928E-16 13
0.0000E+00  0.2088E-03  0.7676E-01
 324.8   7    0.00 -113.65    7.52  7 0.5090E-01  0.1043E-03 -0.5359E-16 13
0.0000E+00  0.2086E-03  0.7677E-01
 324.9   7    0.00 -113.63    7.52  7 0.5091E-01  0.1041E-03  0.9273E-16 13
0.0000E+00  0.2083E-03  0.7679E-01
 324.9   7    0.00 -113.62    7.52  7 0.5092E-01  0.1040E-03  0.3399E-16 13
0.0000E+00  0.2080E-03  0.7680E-01
 325.0   7    0.00 -113.60    7.52  7 0.5093E-01  0.1039E-03  0.1853E-15 13
0.0000E+00  0.2077E-03  0.7681E-01
 325.0   7    0.00 -113.58    7.52  7 0.5093E-01  0.1037E-03  0.1554E-15 13
0.0000E+00  0.2075E-03  0.7682E-01

TIME HISTORY ENDS!

                    END
```

APPENDIX E

Sample Results from FEMFAN-3D

(Composite Column CC11)

```
+-+-+-+-+-+-+-+-+-+-+-+-+-+-+-+-+-+-+-+-+-+-+-+-+-+-+-+-+-+-+-+-+-+-+-+-+-+-+-
 NTU COMPOSITE COLUMN FIRE TEST: CC11
 (PIN-Rol, SQUARE 300X300 ENCASING UC152X152X37 STEEL, INITIAL
CROOK=L/300)
THIS IS A STEEL-RC COMPOSITE STRUCTURE
+-+-+-+-+-+-+-+-+-+-+-+-+-+-+-+-+-+-+-+-+-+-+-+-+-+-+-+-+-+-+-+-+-+-+-+-+-+-+-
         I N P U T   D A T A   V E R I F I C A T I O N
**********************************************************************
MAX NO. OF L-SEARCHES =  6


 LINE SEARCH PARAMS ARE
  TOLERANCE ON RATIO, PERMLS=    2.00000E-01
  MAX. AMP. AT ANY STEP, AMPMX=  5.00000E+00
  MAX. TOTAL STEP-LENGTH, ETMXA= 2.50000E+01
  MIN. TOTAL STEP-LENGTH, ETMNA= 1.00000E-02
NONLINEAR SOLVING SCHEME(=1: N-R) :  1
ANALYSIS TYPE:   1                MAX STEPS TO DISP-CONTROL:3000
MATERIAL MODELS: CONCRETE  21 STEEL   1 REBAR  15
 1: EC3;             2: EC3s;    3: FURUMURA;       4: G.ENGLAND
 5: RUBERTT;         6: ELASTIC;  7: ELASTO-PLASTIC
 8: US GUIDE;   9: ECCSm;   10: CTICM
 11: HARMATHY TRI-LINEAR;   12: HARMATHY BI-LINEAR+ELLI.
 13: SKOWRONSKI BI-LINEAR;    14: EL-RIMAWI RAMBERG-OSGOOD
 15: EC4 COLD-WORKED STEEL
 21:  EC2  NORMAL  WEIGHT  CONCRETE;  22:  EC4  LIGHT  WEIGHT
CONCRETE
 23: EC4 CALCAREOUS CONCRETE
CREEP STRAIN HARDENING LAW: STRAIN HARDENNING
DIR. EXCLUDED FROM DOF-QUEUING(1-X,2-Y,3-R):    0
REFER. DOF BY FORCE (IF =0, NOT APPLIED):    0
CREEP EFFECT EXCLUDED
WARPING NOT CONSIDERED
```

TOTAL ELEMENTS NUMBER: 14 TOTAL NODES NUMBER: 15

TOTAL SECTIONS TYPE: 3 HALF BAND_WIDTH: 25

MAX. ITERATIVE NUMBER: 100 ITER. TOL: 1.00000E-07

NUMBER OF STRUCTURAL T-t CURVES: 1

IN THIS ANALYSIS, MEMBER CROSS-SECTIONAL TEMP. IS TAKEN FROM SAFIR

THERMAL ANALYSIS RESULTS

PIVOT[=0, NA; (0,10), PT; >=10, FL]: 7

TIME STEP FOR OUTPUT: 2

MATERIAL DATA

No	Etop	Eweb	Ebot	Fytop	Fyweb	Fybot
1	3.3000E+07	0.0000E+00	0.0000E+00	4.3000E+04	0.0000E+00	0.0000E+00
2	2.0500E+08	2.0500E+08	2.0500E+08	3.2000E+05	3.2000E+05	3.2000E+05
3	2.0500E+08	0.0000E+00	0.0000E+00	4.6000E+05	0.0000E+00	0.0000E+00

SECTION DATA

No	TYPE	a1	a2	a3	a4	a5	a6	a7	a8	a9	a10	REBAR_x	_y
1	c1	0.3100	0.3100	0.1547	0.0113	0.1637	0.0080	0.0076	-0.0100	0.0000	0.0000	1	0
	DIAMETER	COORDINATE_x	_y (1st QUADRANT ONLY)										
	0.0120	0.1137	0.1137										
2	s1	0.4000	0.0500	0.4000	0.4000	0.0000	0.0000	0.0000	0.0000	0.0000	0.0000	0	0

ELEMENT NO. FOR INTERNAL FORCE OUTPUT

NFOR= 3

1 8 14

ELEMENT/NODE NO FOR DISP. OUTPUT

NDISP= -3(>0, ELE. <0, NODE)

1 8 15

STRUCTURAL ELEMENT DATA

NO.	NAME	MATC	MATS	MATR	SEC	DELTA_Z	DELTA_Y	DELTA_X	I	J
1	BEAR	0	2	0	2	0.000	0.020	0.000	1	2
2	CO01	1	2	3	1	0.003	0.250	0.003	2	3
3	CO02	1	2	3	1	0.002	0.200	0.002	3	4
4	CO03	1	2	3	1	0.003	0.300	0.003	4	5
5	CO04	1	2	3	1	0.002	0.300	0.002	5	6
6	CO05	1	2	3	1	0.001	0.300	0.001	6	7
7	CO06	1	2	3	1	0.000	0.300	0.000	7	8
8	CO07	1	2	3	1	0.000	0.300	0.000	8	9
9	CO08	1	2	3	1	-0.001	0.300	-0.001	9	10
10	CO09	1	2	3	1	-0.002	0.300	-0.002	10	11
11	CO10	1	2	3	1	-0.003	0.300	-0.003	11	12
12	CO11	1	2	3	1	-0.002	0.200	-0.002	12	13
13	CO12	1	2	3	1	-0.003	0.250	-0.003	13	14
14	BEAR	0	2	0	2	0.000	0.020	0.000	14	15

NO.	NAME	ORI_ROT	ALFA	BETA	GAMA(deg)
1	BEAR	0.000	0.000	90.000	0.000
2	CO01	0.000	-45.000	89.160	0.000
3	CO02	0.000	-45.000	89.199	0.000
4	CO03	0.000	-45.000	89.289	0.000
5	CO04	0.000	-45.000	89.446	0.000
6	CO05	0.000	-45.000	89.649	0.000
7	CO06	0.000	-45.000	89.880	0.000

8	CO07	0.000	135.000	89.880	0.000
9	CO08	0.000	135.000	89.649	0.000
10	CO09	0.000	135.000	89.446	0.000
11	CO10	0.000	135.000	89.289	0.000
12	CO11	0.000	135.000	89.199	0.000
13	CO12	0.000	135.000	89.160	0.000
14	BEAR	0.000	0.000	90.000	0.000

WARPING EFFECT: EXCLUDED

BEAM ELEMENT DOFS AT TWO ENDS

NO.	LEFT NODE (1ST ROW) & RIGHT NODE (2ND ROW)												
1	1	2	3	4	5	6	7	8	9	10	0	0	0
	11	12	13	14	15	16	17	18	19	20	0	0	0
2	11	12	13	14	15	16	17	18	19	20	0	0	0
	21	22	23	24	25	26	27	28	29	30	0	0	0
3	21	22	23	24	25	26	27	28	29	30	0	0	0
	31	32	33	34	35	36	37	38	39	40	0	0	0
4	31	32	33	34	35	36	37	38	39	40	0	0	0
	41	42	43	44	45	46	47	48	49	50	0	0	0
5	41	42	43	44	45	46	47	48	49	50	0	0	0
	51	52	53	54	55	56	57	58	59	60	0	0	0
6	51	52	53	54	55	56	57	58	59	60	0	0	0
	61	62	63	64	65	66	67	68	69	70	0	0	0
7	61	62	63	64	65	66	67	68	69	70	0	0	0
	71	72	73	74	75	76	77	78	79	80	0	0	0
8	71	72	73	74	75	76	77	78	79	80	0	0	0
	81	82	83	84	85	86	87	88	89	90	0	0	0
9	81	82	83	84	85	86	87	88	89	90	0	0	0
	91	92	93	94	95	96	97	98	99	100	0	0	0
10	91	92	93	94	95	96	97	98	99	100	0	0	0

```
    101  102  103  104  105  106  107  108  109  110   0   0   0
 11  101  102  103  104  105  106  107  108  109  110   0   0   0
    111  112  113  114  115  116  117  118  119  120   0   0   0
 12  111  112  113  114  115  116  117  118  119  120   0   0   0
    121  122  123  124  125  126  127  128  129  130   0   0   0
 13  121  122  123  124  125  126  127  128  129  130   0   0   0
    131  132  133  134  135  136  137  138  139  140   0   0   0
 14  131  132  133  134  135  136  137  138  139  140   0   0   0
    141  142  143  144  145  146  147  148  149  150   0   0   0

BEAM-TO-COLUMN CONNECTION's DATA
~~~~~~~~~~~~~~~~~~~~~~~~~~~~~~~~~~~~~~~~~~~~~~~~~~~~~~~~~~~~~~~~~~~~~~
 NO. @NODE  OF ELE  CONTYP    REDUCON    RUTMCON    @LOCAL
AXIS

BOUNDARY CONDITION DATA
~~~~~~~~~~~~~~~~~~~~~~~~~~~~~~~~~~~~~~~~~~~~~~~~~~~~~~~~~~~~~~~~~~~~~~
(a).ORIGINAL (FROM INPUT):
 NODE      U_Z   THETA-Z     V_Y   THETA-Y     W_X   THETA-X
WARPING
   1     1     0     1     0     1     0     0
  15     1     0     2     1     1     0     0

(b).PLUS THOSE IMPLICITLY RESTRAINED, ALL RESTRAINED DOFs ARE
AS FOLLOWS:
  1  2  4  7  8  10  12  18  20  22  28  30  32  38  40  42  48  50  52  58
 60  62  68  70  72  78  80  82  88  90  92  98 100 102 108 110 112 118 120 122
 128 130 132 138 140 141 142 146 147 148 150

BOUNDARY ATTACHED SPRINGS DATA
~~~~~~~~~~~~~~~~~~~~~~~~~~~~~~~~~~~~~~~~~~~~~~~~~~~~~~~~~~~~~~~~~~~~~~
 NODE     DOF    STIFFNESS
```

```
 15     144   0.4580E+05

LOADS DATA
~~~~~~~~~~~~~~~~~~~~~~~~~~~~~~~~~~~~~~~~~~~~~~~~~~~~~~~~~~~~~~~~~~~~~~~~~~~~~~~~

 NODE      N_X       N_Y       N_Z       M_X       M_Y       M_Z        B
  15    0.0000E+00  -1.1121E+03   0.0000E+00  -2.7800E+00    0.0000E+00
1.1120E+01  0.0000E+00
   1    0.0000E+00   0.0000E+00   0.0000E+00   2.7800E+00   0.0000E+00  -
1.1120E+01  0.0000E+00

SUMMATIONS OF EXTERNAL LOADS UNDER GLOBAL COORDINATES
LOADS(   3)= 1.11200E+01
LOADS(   9)=-2.78000E+00
LOADS( 143)=-1.11200E+01
LOADS( 144)=-1.11210E+03
LOADS( 149)= 2.78000E+00

t. INTERVAL  @  SAMPLING  MOMENTS,     INCRMENT  THRESHHOLD
SPACING-1   SPACING-2 (MIN)
              10.00          300.00    1.0000    0.2500

ELEMENT'S NO IN FIRES
~~~~~~~~~~~~~~~~~~~~~~~~~~~~~~~~~~~~~~~~~~~~~~~~~~~~~~~~~~~~~~~~~~~~~~~~~~~~~~~~

THERE ARE   10 ELEMENTS IN FIRE PROFILE- 1
 ELEMENT'S NO:  3   4   5   6   7   8   9  10  11  12

TEMP. PROFILE (Top -> Web -> Bottom)
~~~~~~~~~~~~~~~~~~~~~~~~~~~~~~~~~~~~~~~~~~~~~~~~~~~~~~~~~~~~~~~~~~~~~~~~~~~~~~~~


       T-t CURVE - 1  WITH  49 SAMPLING MOMENTS


 t( 1)=  0.00 MINUTES
```

20.00 20.00 20.00 20.00 20.00 20.00 20.00 20.00 20.00 20.00
20.00 20.00 20.00 20.00 20.00 20.00 20.00 20.00 20.00 20.00
20.00 20.00 20.00 20.00 20.00 20.00 20.00 20.00 20.00 20.00
20.00 20.00 20.00 20.00 20.00 20.00 20.00 20.00 20.00 20.00
20.00 20.00 20.00 20.00 20.00 20.00 20.00 20.00 20.00 20.00
20.00 20.00 20.00 20.00 20.00 20.00 20.00 20.00 20.00 20.00
20.00 20.00 20.00 20.00 20.00 20.00 20.00 20.00 20.00 20.00
20.00 20.00 20.00 20.00 20.00 20.00 20.00 20.00 20.00 20.00
20.00 20.00 20.00 20.00 20.00 20.00 20.00 20.00 20.00 20.00
20.00 20.00 20.00 20.00 20.00 20.00 20.00 20.00 20.00 20.00
20.00 20.00 20.00 20.00 20.00 20.00 20.00 20.00 20.00 20.00
20.00 20.00 20.00 20.00 20.00 20.00 20.00 20.00 20.00 20.00
20.00 20.00 20.00 20.00 20.00 20.00 20.00 20.00 20.00 20.00
20.00 20.00 20.00 20.00 20.00 20.00 20.00 20.00 20.00 20.00
20.00 20.00 20.00 20.00 20.00 20.00 20.00 20.00 20.00 20.00
20.00 20.00 20.00 20.00 20.00 20.00 20.00 20.00 20.00 20.00
20.00 20.00 20.00 20.00 20.00 20.00 20.00 20.00 20.00 20.00
20.00 20.00 20.00 20.00 20.00 20.00 20.00 20.00 20.00 20.00
20.00 20.00

t(2)= 10.00 MINUTES

34.60 30.50 30.60 30.70 30.70 30.70 30.70 30.70 30.70 30.60
30.50 30.50 34.50 30.70 26.20 26.30 26.30 26.40 26.40 26.40
26.40 26.40 26.30 26.20 26.20 30.60 30.70 26.20 26.30 26.40
26.40 26.40 26.40 26.40 26.40 26.30 26.30 26.20 30.60 30.80
26.30 26.30 26.50 26.50 26.50 26.50 26.50 26.40 26.40 26.30
26.30 30.70 30.90 26.30 26.40 26.50 26.50 26.50 26.50 26.50
26.50 26.40 26.40 26.30 30.70 30.90 26.40 26.40 26.50 26.50
26.50 26.50 26.50 26.50 26.50 26.40 26.40 30.70 30.90 26.40
26.40 26.50 26.50 26.50 26.50 26.50 26.50 26.50 26.40 26.40
30.70 30.90 26.40 26.40 26.50 26.50 26.50 26.50 26.50 26.50
26.50 26.40 26.40 30.70 30.90 26.40 26.40 26.50 26.50 26.50

26.50 26.50 26.50 26.50 26.40 26.40 30.70 30.90 26.30 26.40
26.50 26.50 26.50 26.50 26.50 26.50 26.40 26.40 26.30 30.70
30.80 26.30 26.30 26.50 26.50 26.50 26.50 26.50 26.40 26.40
26.30 26.30 30.70 30.70 26.20 26.30 26.40 26.40 26.40 26.40
26.40 26.40 26.30 26.20 26.20 30.60 30.70 26.20 26.30 26.30
26.40 26.40 26.40 26.40 26.40 26.30 26.20 26.20 30.60 34.70
30.70 30.70 30.80 30.80 30.80 30.80 30.80 30.80 30.80 30.70
30.70 34.60

t(3)= 20.00 MINUTES

52.20 41.80 40.80 40.30 40.30 40.30 40.30 40.30 40.30 40.40
41.00 41.80 51.90 42.40 30.90 29.70 28.70 28.80 28.80 28.80
28.80 28.80 28.90 30.00 31.00 42.10 41.50 29.90 28.20 27.10
27.20 27.20 27.20 27.20 27.30 27.30 28.40 29.90 41.20 41.00
28.90 27.20 26.50 26.50 26.50 26.50 26.50 26.50 26.60 27.30
28.90 40.70 41.00 28.80 27.10 26.40 26.50 26.50 26.50 26.50
26.50 26.60 27.30 28.90 40.60 41.00 28.80 27.10 26.40 26.40
26.50 26.50 26.50 26.50 26.60 27.40 28.90 40.60 41.00 28.80
27.10 26.40 26.50 26.50 26.50 26.50 26.50 26.60 27.40 28.90
40.60 41.00 28.80 27.10 26.40 26.50 26.50 26.50 26.50 26.50
26.60 27.40 28.90 40.60 41.00 28.80 27.10 26.40 26.40 26.50
26.50 26.50 26.50 26.60 27.40 28.90 40.60 41.00 28.80 27.10
26.40 26.50 26.50 26.50 26.50 26.50 26.60 27.30 28.90 40.60
41.00 28.90 27.20 26.50 26.50 26.50 26.50 26.50 26.50 26.60
27.30 28.90 40.70 41.60 29.90 28.20 27.10 27.20 27.30 27.30
27.30 27.30 27.40 28.40 30.00 41.20 42.50 31.00 29.80 28.80
28.90 28.90 28.90 28.90 28.90 29.00 30.10 31.10 42.10 52.70
42.30 41.30 40.80 40.90 40.90 40.90 40.90 40.90 41.00 41.50
42.40 52.40

t(4)= 30.00 MINUTES

75.90 58.80 56.00 54.00 53.90 53.90 53.90 53.90 54.10 54.70

56.60 58.80 75.20 59.90 40.90 37.40 34.20 34.10 34.10 34.10
34.10 34.30 35.20 38.40 41.00 59.20 57.60 38.20 33.40 29.80
29.80 29.70 29.80 29.80 30.00 30.70 34.00 38.10 56.90 56.00
35.30 30.30 27.50 27.40 27.30 27.30 27.50 27.70 28.10 30.60
35.10 55.20 55.50 34.70 29.90 27.10 27.00 27.00 27.10 27.10
27.30 27.90 30.50 34.60 54.80 55.30 34.40 29.50 26.60 26.50
26.70 26.80 26.70 26.80 27.60 30.40 34.40 54.50 55.20 34.30
29.50 26.60 26.50 26.60 26.70 26.60 26.70 27.60 30.30 34.40
54.50 55.20 34.30 29.50 26.60 26.50 26.60 26.70 26.60 26.70
27.60 30.30 34.40 54.50 55.30 34.40 29.50 26.60 26.50 26.70
26.80 26.70 26.80 27.60 30.40 34.40 54.50 55.50 34.70 29.90
27.10 27.00 27.10 27.10 27.10 27.30 27.90 30.50 34.60 54.80
56.00 35.30 30.40 27.50 27.40 27.40 27.40 27.50 27.80 28.10
30.70 35.20 55.20 57.70 38.30 33.50 29.90 29.90 29.90 29.90
30.00 30.20 30.80 34.20 38.30 57.00 60.10 41.20 37.70 34.50
34.40 34.40 34.40 34.40 34.60 35.50 38.70 41.30 59.50 76.90
59.90 57.10 55.20 55.00 55.10 55.10 55.10 55.20 55.90 57.70
59.90 76.30

t(5)= 40.00 MINUTES

98.40 78.80 74.00 70.00 69.40 69.30 69.30 69.40 69.90 71.60
75.10 78.70 97.80 80.10 55.80 49.40 42.90 42.40 42.30 42.30
42.40 43.00 45.20 51.10 55.70 79.30 76.60 51.00 41.90 34.70
34.40 34.20 34.20 34.40 35.10 36.60 43.00 50.50 75.40 73.60
45.70 36.10 30.00 29.70 29.60 29.50 29.80 30.50 31.40 36.50
45.00 72.30 72.40 44.10 34.90 29.10 28.60 28.70 28.90 29.00
29.40 30.80 36.00 43.70 71.20 71.70 43.20 34.00 27.90 27.30
27.70 28.10 27.80 28.00 30.10 35.70 43.00 70.50 71.50 43.00
33.70 27.50 26.90 27.30 27.70 27.50 27.70 29.90 35.50 42.90
70.40 71.50 43.00 33.70 27.50 26.90 27.30 27.70 27.50 27.70
29.90 35.50 42.90 70.40 71.70 43.20 34.00 27.90 27.30 27.70
28.20 27.90 28.00 30.10 35.70 43.00 70.50 72.50 44.20 35.00

29.10 28.70 28.80 29.00 29.00 29.40 30.90 36.10 43.70 71.20
73.70 45.80 36.20 30.20 29.80 29.60 29.60 29.90 30.60 31.50
36.60 45.10 72.40 76.80 51.40 42.20 35.00 34.70 34.50 34.50
34.70 35.40 36.90 43.40 50.90 75.70 80.40 56.40 50.00 43.60
43.00 42.90 42.90 43.10 43.60 45.80 51.70 56.30 79.60 99.40
80.20 75.80 71.90 71.30 71.20 71.20 71.30 71.80 73.50 76.90
80.10 98.80

t(6)= 50.00 MINUTES

111.10 92.00 86.90 82.00 80.50 80.20 80.20 80.50 81.50 84.20
88.20 91.70 110.30 93.00 71.10 62.70 53.40 52.00 51.60 51.70
52.00 53.10 56.80 64.90 70.70 92.10 89.40 65.10 52.50 41.80
40.80 40.40 40.40 40.90 42.10 44.70 53.90 64.00 88.30 86.30
58.10 44.30 34.60 34.00 33.50 33.40 34.00 35.30 36.80 44.70
56.50 85.00 84.70 55.30 42.20 32.90 31.90 32.00 32.30 32.40
33.20 35.80 43.70 54.30 83.20 83.30 53.60 40.50 30.60 29.10
29.90 30.80 30.30 30.60 34.40 43.00 53.00 81.90 82.80 53.00
39.80 29.80 28.30 29.10 30.00 29.50 29.90 33.90 42.60 52.60
81.60 82.80 53.00 39.80 29.80 28.30 29.10 30.00 29.50 29.90
33.90 42.60 52.60 81.60 83.30 53.60 40.50 30.60 29.20 30.00
30.90 30.30 30.60 34.50 43.00 53.00 82.00 84.70 55.50 42.40
33.00 32.00 32.10 32.50 32.60 33.40 35.90 43.80 54.40 83.30
86.50 58.30 44.50 34.80 34.20 33.80 33.60 34.20 35.50 37.00
44.90 56.70 85.20 89.60 65.60 53.00 42.30 41.30 41.00 40.90
41.40 42.60 45.20 54.40 64.50 88.60 93.50 71.80 63.50 54.50
53.00 52.70 52.70 53.00 54.20 57.70 65.70 71.30 92.60 112.50
93.40 88.60 84.20 82.80 82.50 82.50 82.70 83.80 86.10 89.70
93.10 111.70

.....

t(45)=440.00 MINUTES

753.30 728.20 714.80 698.50 691.80 689.50 689.20 690.50 694.80 703.90
715.90 723.60 750.70 728.30 685.90 656.80 621.00 610.20 606.40 606.00
608.30 615.20 631.70 660.00 677.70 723.60 720.10 667.80 619.50 573.00
565.50 561.90 561.20 563.90 570.60 582.80 618.90 655.60 714.10 710.60
644.40 587.00 540.30 535.80 532.30 531.00 534.30 540.90 548.00 582.60
629.40 703.60 703.20 630.60 576.90 531.40 523.50 523.00 524.60 525.40
530.60 544.30 578.90 619.50 697.50 696.80 619.40 566.50 517.90 505.70
509.40 515.10 512.80 516.30 537.90 575.90 612.90 693.10 694.00 614.60
560.90 511.10 498.30 503.20 510.20 507.20 510.80 533.80 573.00 610.50
691.50 694.00 614.70 560.90 511.10 498.40 503.30 510.20 507.30 510.90
533.80 573.10 610.60 691.60 696.80 619.50 566.60 518.00 505.80 509.50
515.20 512.90 516.40 538.00 576.00 613.00 693.10 703.30 630.80 577.10
531.60 523.60 523.10 524.70 525.60 530.80 544.50 579.00 619.60 697.50
710.70 644.60 587.20 540.50 536.10 532.50 531.20 534.50 541.10 548.20
582.80 629.60 703.70 720.30 668.00 619.80 573.30 565.70 562.20 561.50
564.20 570.80 583.10 619.20 655.80 714.20 728.50 686.20 657.10 621.30
610.60 606.80 606.40 608.60 615.60 632.00 660.30 678.00 723.80 753.50
728.50 715.20 698.80 692.20 689.90 689.60 690.90 695.10 704.30 716.20
723.90 750.90

t(46)=450.00 MINUTES

758.00 733.60 720.70 704.90 698.40 696.20 695.90 697.20 701.30 710.20
721.80 729.20 755.50 733.80 692.40 664.20 629.50 619.00 615.30 614.90
617.10 623.90 639.90 667.30 684.60 729.20 725.90 674.90 627.90 582.70
575.30 571.90 571.20 573.80 580.30 592.20 627.40 663.10 720.00 716.60
652.30 596.30 550.80 546.40 543.00 541.70 544.90 551.40 558.30 592.00
637.60 709.80 709.50 638.90 586.60 542.20 534.40 533.90 535.40 536.20
541.30 554.70 588.40 628.00 703.90 703.30 628.00 576.50 529.00 517.00
520.60 526.20 523.90 527.40 548.50 585.50 621.70 699.70 700.60 623.40
571.00 522.40 509.90 514.60 521.40 518.50 522.10 544.50 582.80 619.40
698.20 700.60 623.40 571.00 522.50 510.00 514.70 521.40 518.60 522.10

544.60 582.80 619.40 698.20 703.30 628.10 576.60 529.20 517.20 520.70
526.30 524.00 527.50 548.60 585.60 621.70 699.70 709.60 639.00 586.70
542.40 534.50 534.00 535.60 536.40 541.50 554.90 588.60 628.20 704.00
716.70 652.50 596.50 551.00 546.60 543.20 541.90 545.10 551.50 558.50
592.20 637.80 709.90 726.00 675.10 628.20 583.00 575.60 572.20 571.40
574.10 580.50 592.50 627.60 663.30 720.10 733.90 692.70 664.50 629.80
619.30 615.70 615.20 617.40 624.20 640.20 667.60 684.80 729.30 758.10
733.90 721.00 705.20 698.80 696.50 696.20 697.50 701.60 710.50 722.00
729.40 755.70

t(47)=460.00 MINUTES

762.60 738.90 726.50 711.10 704.90 702.70 702.50 703.70 707.70 716.30
727.50 734.60 760.30 739.10 698.80 671.40 637.70 627.50 623.90 623.50
625.60 632.20 647.80 674.40 691.20 734.70 731.40 681.80 636.10 592.00
584.90 581.50 580.80 583.40 589.70 601.30 635.50 670.30 725.80 722.50
659.90 605.30 560.80 556.60 553.30 552.00 555.10 561.40 568.20 601.10
645.60 715.90 715.60 646.90 595.80 552.50 544.90 544.30 545.90 546.70
551.60 564.70 597.60 636.30 710.20 709.60 636.30 586.00 539.70 528.00
531.40 536.90 534.60 538.10 558.70 594.90 630.10 706.10 707.00 631.90
580.70 533.30 521.00 525.60 532.10 529.40 532.90 554.90 592.20 627.90
704.70 707.10 631.90 580.80 533.30 521.10 525.60 532.20 529.40 532.90
554.90 592.30 627.90 704.70 709.70 636.40 586.10 539.80 528.10 531.50
536.90 534.70 538.20 558.80 595.00 630.20 706.10 715.70 647.00 596.00
552.70 545.00 544.50 546.00 546.80 551.80 564.90 597.80 636.40 710.20
722.60 660.00 605.50 561.00 556.80 553.40 552.20 555.30 561.60 568.40
601.30 645.70 716.00 731.50 682.00 636.30 592.30 585.10 581.70 581.00
583.60 589.90 601.50 635.80 670.50 725.90 739.20 699.00 671.70 638.00
627.80 624.20 623.80 625.90 632.50 648.10 674.70 691.40 734.80 762.80
739.20 726.70 711.40 705.20 703.00 702.70 703.90 707.90 716.50 727.70
734.80 760.40

t(48)=470.00 MINUTES

767.20 744.20 732.10 717.20 711.20 709.10 708.80 710.00 713.90 722.20
733.10 740.00 764.90 744.20 705.00 678.40 645.60 635.70 632.20 631.80
633.90 640.30 655.40 681.30 697.60 740.00 736.90 688.50 643.90 601.00
594.00 590.80 590.10 592.60 598.70 610.00 643.40 677.30 731.40 728.20
667.20 614.00 570.50 566.40 563.10 561.90 564.90 571.10 577.70 609.90
653.30 721.80 721.60 654.60 604.80 562.40 555.00 554.40 555.90 556.70
561.60 574.40 606.50 644.20 716.30 715.80 644.40 595.20 550.00 538.50
541.80 547.10 545.00 548.40 568.60 603.90 638.30 712.30 713.30 640.00
590.10 543.70 531.70 536.10 542.50 539.90 543.30 564.80 601.30 636.10
711.00 713.30 640.00 590.10 543.80 531.80 536.20 542.50 539.90 543.40
564.90 601.40 636.20 711.00 715.80 644.40 595.30 550.10 538.60 541.90
547.20 545.10 548.50 568.70 604.00 638.30 712.40 721.70 654.70 604.90
562.60 555.10 554.60 556.00 556.80 561.70 574.50 606.70 644.40 716.40
728.30 667.40 614.10 570.70 566.60 563.30 562.10 565.10 571.20 577.90
610.00 653.40 721.90 737.00 688.70 644.10 601.20 594.20 591.00 590.30
592.80 598.90 610.20 643.60 677.50 731.50 744.40 705.20 678.60 645.80
635.90 632.50 632.10 634.10 640.50 655.70 681.50 697.80 740.10 767.30
744.30 732.30 717.40 711.40 709.30 709.00 710.20 714.10 722.40 733.20
740.10 765.00

t(49)=480.00 MINUTES

771.70 749.20 737.60 723.20 717.30 715.30 715.00 716.20 719.90 728.00
738.50 745.20 769.50 749.30 711.00 685.10 653.30 643.60 640.20 639.80
641.90 648.10 662.80 688.00 703.80 745.20 742.20 695.00 651.50 609.70
602.90 599.70 599.00 601.40 607.40 618.50 651.00 684.10 736.90 733.80
674.30 622.30 579.90 575.90 572.60 571.40 574.40 580.40 586.90 618.30
660.70 727.60 727.40 662.10 613.40 572.00 564.70 564.10 565.60 566.40
571.20 583.70 615.10 652.00 722.30 721.80 652.10 604.10 559.90 548.70
551.80 557.00 554.90 558.30 578.10 612.60 646.20 718.40 719.40 647.90
599.20 553.80 542.10 546.30 552.50 549.90 553.40 574.40 610.10 644.10
717.10 719.40 647.90 599.20 553.90 542.10 546.30 552.50 550.00 553.40
574.40 610.10 644.10 717.10 721.80 652.20 604.20 560.00 548.70 551.90

557.10 555.00 558.40 578.10 612.60 646.20 718.40 727.50 662.20 613.50
572.20 564.80 564.30 565.70 566.50 571.30 583.80 615.20 652.10 722.30
733.90 674.50 622.50 580.10 576.00 572.80 571.60 574.60 580.60 587.00
618.50 660.90 727.70 742.30 695.10 651.70 609.90 603.10 599.90 599.20
601.60 607.60 618.60 651.20 684.20 737.00 749.40 711.10 685.30 653.50
643.80 640.50 640.10 642.10 648.30 663.00 688.20 704.00 745.30 771.80
749.40 737.70 723.30 717.50 715.40 715.20 716.30 720.10 728.10 738.60
745.30 769.60

ANALYSIS RESULTS

****

TIME= 0.000 NO OF TEMPERATURE INCREMENT: 0.0

==========

==========

ELEMENT END FORCES

NO.	P_X	P_Y	P_Z	M_X	M_Y	M_Z	B
1	-8.4953E-06	1.0633E+03	1.8843E-05	2.7800E+00	4.2763E-12	1.1120E+01	0.0000E+00
	8.4953E-06	-1.0633E+03	-1.8843E-05	-2.8002E+00	-4.2763E-12	-1.1167E+01	0.0000E+00
8	-8.4966E-06	1.0633E+03	1.8842E-05	1.5215E+01	5.2424E-03	2.4154E+01	0.0000E+00
	8.4966E-06	-1.0633E+03	-1.8842E-05	-1.4731E+01	-5.3268E-03	-2.3613E+01	0.0000E+00
14	-8.4990E-06	1.0633E+03	1.8841E-05	2.8047E+00	9.6851E-03	1.1162E+01	0.0000E+00
	8.4990E-06	-1.0633E+03	-1.8841E-05	-2.7800E+00	-9.6851E-03	-1.1120E+01	0.0000E+00

DISPLACEMENTS AT NODES

NO.	W_X	V_Y	U_Z	THETA_X	THETA_Y	THETA_Z	TWIST_Z'
1	0.0000E+00	0.0000E+00	0.0000E+00	6.1096E-04	-3.3396E-06	-1.4087E-03	0.0000E+00
8	1.2543E-03	-5.3420E-04	6.9127E-04	7.0977E-05	5.0496E-06	7.1063E-05	0.0000E+00
15	0.0000E+00	-1.0661E-03	0.0000E+00	-7.4770E-04	0.0000E+00	1.2718E-03	0.0000E+00

SPRINGS' REACTIONS

NO.	@DOF	FORCE
15	144	4.8831E+01

TIME= 2.000 NO OF TEMPERATURE INCREMENT: 2.0

==========

ELEMENT END FORCES

NO.	P_X	P_Y	P_Z	M_X	M_Y	M_Z	B
1	-8.5168E-06	1.0649E+03	1.8995E-05	2.7800E+00	-5.1565E-15	1.1120E+01	0.0000E+00
	8.5168E-06	-1.0649E+03	-1.8995E-05	-2.8004E+00	5.1536E-15	-1.1167E+01	0.0000E+00
8	-8.5169E-06	1.0649E+03	1.8995E-05	1.5241E+01	5.3067E-03	2.4187E+01	0.0000E+00
	8.5169E-06	-1.0649E+03	-1.8995E-05	-1.4757E+01	-5.3924E-03	-2.3645E+01	0.0000E+00
14	-8.5166E-06	1.0649E+03	1.8994E-05	2.8049E+00	9.7988E-03	1.1162E+01	0.0000E+00

8.5166E-06 -1.0649E+03 -1.8994E-05 -2.7800E+00 -9.7988E-03 -1.1120E+01 0.0000E+00

DISPLACEMENTS AT NODES

NO.	W_X	V_Y	U_Z	THETA_X	THETA_Y	THETA_Z	TWIST_Z'
1	0.0000E+00	0.0000E+00	0.0000E+00	6.1626E-04	-3.3865E-06	-1.4216E-03	0.0000E+00
8	1.2666E-03	-5.1631E-04	6.9790E-04	7.2017E-05	5.0626E-06	7.2420E-05	0.0000E+00
15	0.0000E+00	-1.0303E-03	0.0000E+00	-7.5457E-04	0.0000E+00	1.2827E-03	0.0000E+00

SPRINGS' REACTIONS

NO.	@DOF	FORCE
15	144	4.7190E+01

TIME= 4.000 NO OF TEMPERATURE INCREMENT: 4.0

ELEMENT END FORCES

NO.	P_X	P_Y	P_Z	M_X	M_Y	M_Z	B
1	-8.5419E-06	1.0665E+03	1.9157E-05	2.7800E+00	7.1285E-16	1.1120E+01	0.0000E+00
	8.5419E-06	-1.0665E+03	-1.9157E-05	-2.8005E+00	-7.1574E-16	-1.1167E+01	0.0000E+00
8	-8.5421E-06	1.0665E+03	1.9157E-05	1.5267E+01	5.3714E-03	2.4220E+01	0.0000E+00
	8.5421E-06	-1.0665E+03	-1.9157E-05	-1.4782E+01	-5.4585E-03	-2.3676E+01	0.0000E+00

14 -8.5420E-06 1.0665E+03 1.9156E-05 2.8051E+00 9.9125E-03 1.1163E+01 0.0000E+00

8.5420E-06 -1.0665E+03 -1.9156E-05 -2.7800E+00 -9.9125E-03 -1.1120E+01 0.0000E+00

DISPLACEMENTS AT NODES

NO. W_X V_Y U_Z THETA_X THETA_Y THETA_Z TWIST_Z'

1 0.0000E+00 0.0000E+00 0.0000E+00 6.2150E-04 -3.4355E-06 -1.4346E-03 0.0000E+00

8 1.2789E-03 -4.9859E-04 7.0452E-04 7.3110E-05 5.0745E-06 7.3827E-05 0.0000E+00

15 0.0000E+00 -9.9482E-04 0.0000E+00 -7.6146E-04 0.0000E+00 1.2936E-03 0.0000E+00

SPRINGS' REACTIONS

NO. @DOF FORCE

15 144 4.5565E+01

TIME= 6.000 NO OF TEMPERATURE INCREMENT: 6.0

==========

ELEMENT END FORCES

NO. P_X P_Y P_Z M_X M_Y M_Z B

1 -8.5645E-06 1.0682E+03 1.9320E-05 2.7800E+00 9.7888E-15 1.1120E+01 0.0000E+00

8.5645E-06 -1.0682E+03 -1.9320E-05 -2.8007E+00 -9.7917E-15 -1.1168E+01 0.0000E+00

8 -8.5647E-06 1.0682E+03 1.9320E-05 1.5293E+01 5.4363E-03 2.4253E+01 0.0000E+00

8.5647E-06 -1.0682E+03 -1.9320E-05 -1.4807E+01 -5.5248E-03 -2.3707E+01 0.0000E+00

14 -8.5645E-06 1.0682E+03 1.9320E-05 2.8053E+00 1.0027E-02 1.1163E+01 0.0000E+00

8.5645E-06 -1.0682E+03 -1.9320E-05 -2.7800E+00 -1.0027E-02 -1.1120E+01 0.0000E+00

DISPLACEMENTS AT NODES

NO. W_X V_Y U_Z THETA_X THETA_Y THETA_Z TWIST_Z'

1 0.0000E+00 0.0000E+00 0.0000E+00 6.2671E-04 -3.4853E-06 -1.4475E-03 0.0000E+00

8 1.2912E-03 -4.8087E-04 7.1112E-04 7.4224E-05 5.0859E-06 7.5249E-05 0.0000E+00

15 0.0000E+00 -9.5935E-04 0.0000E+00 -7.6836E-04 0.0000E+00 1.3044E-03 0.0000E+00

SPRINGS' REACTIONS

NO. @DOF FORCE

15 144 4.3940E+01

TIME= 8.000 NO OF TEMPERATURE INCREMENT: 8.0

==========

ELEMENT END FORCES

NO. P_X P_Y P_Z M_X M_Y M_Z B

1 -8.5839E-06 1.0698E+03 1.9485E-05 2.7800E+00 -2.3383E-15 1.1120E+01 0.0000E+00

8.5839E-06 -1.0698E+03 -1.9485E-05 -2.8008E+00 2.3354E-15 -1.1168E+01 0.0000E+00

8 -8.5846E-06 1.0698E+03 1.9485E-05 1.5319E+01 5.5015E-03 2.4286E+01 0.0000E+00

8.5846E-06 -1.0698E+03 -1.9485E-05 -1.4833E+01 -5.5915E-03 -2.3739E+01 0.0000E+00

14 -8.5841E-06 1.0698E+03 1.9485E-05 2.8055E+00 1.0141E-02 1.1163E+01 0.0000E+00

8.5841E-06 -1.0698E+03 -1.9485E-05 -2.7800E+00 -1.0141E-02 -1.1120E+01 0.0000E+00

DISPLACEMENTS AT NODES

NO. W_X V_Y U_Z THETA_X THETA_Y THETA_Z TWIST_Z'

1 0.0000E+00 0.0000E+00 0.0000E+00 6.3190E-04 -3.5360E-06 -1.4604E-03 0.0000E+00

8 1.3035E-03 -4.6315E-04 7.1772E-04 7.5358E-05 5.0970E-06 7.6688E-05 0.0000E+00

15 0.0000E+00 -9.2388E-04 0.0000E+00 -7.7526E-04 0.0000E+00 1.3151E-03 0.0000E+00

SPRINGS' REACTIONS

NO. @DOF FORCE

15 144 4.2315E+01

TIME= 10.000 NO OF TEMPERATURE INCREMENT: 10.0

==========

ELEMENT END FORCES

NO. P_X P_Y P_Z M_X M_Y M_Z B

1 -8.6015E-06 1.0714E+03 1.9651E-05 2.7800E+00 -1.1316E-14 1.1120E+01 0.0000E+00

8.6015E-06 -1.0714E+03 -1.9651E-05 -2.8010E+00 1.1313E-14 -1.1168E+01 0.0000E+00

8 -8.6016E-06 1.0714E+03 1.9651E-05 1.5345E+01 5.5670E-03 2.4319E+01 0.0000E+00

8.6016E-06 -1.0714E+03 -1.9651E-05 -1.4858E+01 -5.6585E-03 -2.3770E+01 0.0000E+00

14 -8.6013E-06 1.0714E+03 1.9650E-05 2.8057E+00 1.0256E-02 1.1163E+01 0.0000E+00

8.6013E-06 -1.0714E+03 -1.9650E-05 -2.7800E+00 -1.0256E-02 -1.1120E+01 0.0000E+00

DISPLACEMENTS AT NODES

NO. W_X V_Y U_Z THETA_X THETA_Y THETA_Z TWIST_Z'

1 0.0000E+00 0.0000E+00 0.0000E+00 6.3706E-04 -3.5874E-06 -1.4734E-03 0.0000E+00

8 1.3158E-03 -4.4543E-04 7.2431E-04 7.6513E-05 5.1076E-06 7.8143E-05 0.0000E+00

15 0.0000E+00 -8.8841E-04 0.0000E+00 -7.8218E-04 0.0000E+00 1.3259E-03 0.0000E+00

SPRINGS' REACTIONS

NO. @DOF FORCE

15 144 4.0691E+01

TIME= 12.000 NO OF TEMPERATURE INCREMENT: 12.0

==========

==========

ELEMENT END FORCES

NO. P_X P_Y P_Z M_X M_Y M_Z B

1 -8.4411E-06 1.0721E+03 1.9386E-05 2.7800E+00 1.7301E-14 1.1120E+01 0.0000E+00

8.4411E-06 -1.0721E+03 -1.9386E-05 -2.8011E+00 -1.7304E-14 -1.1169E+01 0.0000E+00

8 -8.4409E-06 1.0721E+03 1.9385E-05 1.5358E+01 5.6088E-03 2.4338E+01 0.0000E+00

8.4409E-06 -1.0721E+03 -1.9385E-05 -1.4870E+01 -5.6999E-03 -2.3789E+01 0.0000E+00

14 -8.4412E-06 1.0721E+03 1.9386E-05 2.8058E+00 1.0347E-02 1.1164E+01 0.0000E+00

8.4412E-06 -1.0721E+03 -1.9386E-05 -2.7800E+00 -1.0347E-02 -1.1120E+01 0.0000E+00

DISPLACEMENTS AT NODES

NO. W_X V_Y U_Z THETA_X THETA_Y THETA_Z TWIST_Z'

1 0.0000E+00 0.0000E+00 0.0000E+00 6.4302E-04 -3.5520E-06 -1.4833E-03 0.0000E+00

8 1.3261E-03 -4.3819E-04 7.2968E-04 7.5108E-05 5.1565E-06 7.7989E-05 0.0000E+00

15 0.0000E+00 -8.7390E-04 0.0000E+00 -7.8613E-04 0.0000E+00 1.3360E-03 0.0000E+00

SPRINGS' REACTIONS

NO. @DOF FORCE

15 144 4.0026E+01

.....

TIME=350.000 NO OF TEMPERATURE INCREMENT: 500.0

ELEMENT END FORCES

NO.	P_X	P_Y	P_Z	M_X	M_Y	M_Z	B
1	3.7209E-03	1.5235E+03	1.7535E-03	2.7800E+00	-1.0789E-12	1.1120E+01	0.0000E+00
	-3.7209E-03	-1.5235E+03	-1.7535E-03	-2.9893E+00	1.0788E-12	-1.2482E+01	0.0000E+00
8	3.7209E-03	1.5235E+03	1.7535E-03	3.0781E+01	3.4374E-01	8.0446E+01	0.0000E+00
	-3.7209E-03	-1.5235E+03	-1.7535E-03	-3.0347E+01	-3.4826E-01	-7.6970E+01	0.0000E+00
14	3.7209E-03	1.5235E+03	1.7535E-03	3.1086E+00	6.5683E-01	1.2355E+01	0.0000E+00
	-3.7209E-03	-1.5235E+03	-1.7535E-03	-2.7800E+00	-6.5683E-01	-1.1120E+01	0.0000E+00

DISPLACEMENTS AT NODES

NO.	W_X	V_Y	U_Z	THETA_X	THETA_Y	THETA_Z	TWIST_Z'
1	0.0000E+00	0.0000E+00	0.0000E+00	5.1715E-03	-5.9565E-05	-3.3635E-02	0.0000E+00
8	3.4615E-02	4.3726E-03	7.4359E-03	1.8956E-03	1.1192E-04	1.8056E-03	0.0000E+00
15	0.0000E+00	8.9816E-03	0.0000E+00	-8.1810E-03	0.0000E+00	3.0746E-02	0.0000E+00

SPRINGS' REACTIONS

NO.	@DOF	FORCE
15	144	-4.1138E+02

TIME=350.500 NO OF TEMPERATURE INCREMENT: 502.0

==========

==========

ELEMENT END FORCES

NO.	P_X	P_Y	P_Z	M_X	M_Y	M_Z	B
1	3.8449E-03	1.5218E+03	1.8405E-03	2.7800E+00	-1.1419E-12	1.1120E+01	0.0000E+00
	-3.8449E-03	-1.5218E+03	-1.8405E-03	-2.9854E+00	1.1419E-12	-1.2505E+01	0.0000E+00
8	3.8449E-03	1.5218E+03	1.8405E-03	3.0614E+01	3.5263E-01	8.1398E+01	0.0000E+00
	-3.8449E-03	-1.5218E+03	-1.8405E-03	-3.0191E+01	-3.5725E-01	-7.7869E+01	0.0000E+00
14	3.8449E-03	1.5218E+03	1.8405E-03	3.1052E+00	6.7437E-01	1.2378E+01	0.0000E+00
	-3.8449E-03	-1.5218E+03	-1.8405E-03	-2.7800E+00	-6.7437E-01	-1.1120E+01	0.0000E+00

DISPLACEMENTS AT NODES

NO.	W_X	V_Y	U_Z	THETA_X	THETA_Y	THETA_Z	TWIST_Z'
1	0.0000E+00	0.0000E+00	0.0000E+00	5.0796E-03	-5.9490E-05	-3.4239E-02	0.0000E+00
8	3.5291E-02	4.3509E-03	7.3463E-03	1.9105E-03	1.1528E-04	1.8380E-03	0.0000E+00
15	0.0000E+00	8.9453E-03	0.0000E+00	-8.1036E-03	0.0000E+00	3.1329E-02	0.0000E+00

SPRINGS' REACTIONS

NO. @DOF FORCE

15 144 -4.0971E+02

TIME=351.000 NO OF TEMPERATURE INCREMENT: 504.0

==========

ELEMENT END FORCES

NO. P_X P_Y P_Z M_X M_Y M_Z B

1 3.9921E-03 1.5198E+03 1.9377E-03 2.7800E+00 -1.5852E-12 1.1120E+01 0.0000E+00

-3.9921E-03 -1.5198E+03 -1.9377E-03 -2.9801E+00 1.5851E-12 -1.2531E+01 0.0000E+00

8 3.9921E-03 1.5198E+03 1.9377E-03 3.0384E+01 3.6299E-01 8.2475E+01 0.0000E+00

-3.9921E-03 -1.5198E+03 -1.9377E-03 -2.9975E+01 -3.6772E-01 -7.8884E+01 0.0000E+00

14 3.9921E-03 1.5198E+03 1.9377E-03 3.1003E+00 6.9482E-01 1.2402E+01 0.0000E+00

-3.9921E-03 -1.5198E+03 -1.9377E-03 -2.7800E+00 -6.9482E-01 -1.1120E+01 0.0000E+00

DISPLACEMENTS AT NODES

NO. W_X V_Y U_Z THETA_X THETA_Y THETA_Z TWIST_Z'

1 0.0000E+00 0.0000E+00 0.0000E+00 4.9531E-03 -5.9298E-05 -3.4922E-02 0.0000E+00

8 3.6060E-02 4.3253E-03 7.2186E-03 1.9271E-03 1.1920E-04 1.8757E-03 0.0000E+00

15 0.0000E+00 8.9023E-03 0.0000E+00 -7.9922E-03 0.0000E+00 3.1989E-02 0.0000E+00

SPRINGS' REACTIONS

NO.	@DOF	FORCE
15	144	-4.0774E+02

TIME=351.500 NO OF TEMPERATURE INCREMENT: 506.0

ELEMENT END FORCES

NO.	P_X	P_Y	P_Z	M_X	M_Y	M_Z	B
1	4.1817E-03	1.5174E+03	2.0539E-03	2.7800E+00	1.4890E-12	1.1120E+01	0.0000E+00
	-4.1817E-03	-1.5174E+03	-2.0539E-03	-2.9720E+00	-1.4891E-12	-1.2562E+01	0.0000E+00
8	4.1817E-03	1.5174E+03	2.0540E-03	3.0039E+01	3.7585E-01	8.3749E+01	0.0000E+00
	-4.1817E-03	-1.5174E+03	-2.0540E-03	-2.9651E+01	-3.8072E-01	-8.0082E+01	0.0000E+00
14	4.1817E-03	1.5174E+03	2.0539E-03	3.0929E+00	7.2015E-01	1.2432E+01	0.0000E+00
	-4.1817E-03	-1.5174E+03	-2.0539E-03	-2.7800E+00	-7.2015E-01	-1.1120E+01	0.0000E+00

DISPLACEMENTS AT NODES

NO.	W_X	V_Y	U_Z	THETA_X	THETA_Y	THETA_Z	TWIST_Z'
1	0.0000E+00	0.0000E+00	0.0000E+00	4.7609E-03	-5.9016E-05	-3.5734E-02	0.0000E+00
8	3.6977E-02	4.2933E-03	7.0198E-03	1.9499E-03	1.2405E-04	1.9268E-03	0.0000E+00

15 0.0000E+00 8.8490E-03 0.0000E+00 -7.8187E-03 0.0000E+00 3.2769E-02 0.0000E+00

SPRINGS' REACTIONS

NO. @DOF FORCE

15 144 -4.0530E+02

TIME=352.000 NO OF TEMPERATURE INCREMENT: 508.0

==========

ELEMENT END FORCES

NO. P_X P_Y P_Z M_X M_Y M_Z B

1 4.4499E-03 1.5141E+03 2.2084E-03 2.7800E+00 -7.1783E-13 1.1120E+01 0.0000E+00

-4.4499E-03 -1.5141E+03 -2.2084E-03 -2.9594E+00 7.1773E-13 -1.2601E+01 0.0000E+00

8 4.4499E-03 1.5141E+03 2.2084E-03 2.9495E+01 3.9298E-01 8.5365E+01 0.0000E+00

-4.4499E-03 -1.5141E+03 -2.2084E-03 -2.9138E+01 -3.9804E-01 -8.1599E+01 0.0000E+00

14 4.4500E-03 1.5141E+03 2.2084E-03 3.0810E+00 7.5387E-01 1.2468E+01 0.0000E+00

-4.4500E-03 -1.5141E+03 -2.2084E-03 -2.7800E+00 -7.5387E-01 -1.1120E+01 0.0000E+00

DISPLACEMENTS AT NODES

NO. W_X V_Y U_Z THETA_X THETA_Y THETA_Z TWIST_Z'

1 0.0000E+00 0.0000E+00 0.0000E+00 4.4559E-03 -5.8726E-05 -3.6768E-02 0.0000E+00

8 3.8150E-02 4.2494E-03 6.6991E-03 1.9814E-03 1.3045E-04 1.9971E-03 0.0000E+00

15 0.0000E+00 8.7768E-03 0.0000E+00 -7.5393E-03 0.0000E+00 3.3758E-02 0.0000E+00

SPRINGS' REACTIONS

NO.	@DOF	FORCE
15	144	-4.0200E+02

TIME=352.500 NO OF TEMPERATURE INCREMENT: 510.0

ELEMENT END FORCES

NO.	P_X	P_Y	P_Z	M_X	M_Y	M_Z	B
1	4.8452E-03	1.5093E+03	2.4221E-03	2.7800E+00	-6.7648E-13	1.1120E+01	0.0000E+00
	-4.8452E-03	-1.5093E+03	-2.4221E-03	-2.9398E+00	6.7638E-13	-1.2653E+01	0.0000E+00
8	4.8452E-03	1.5093E+03	2.4221E-03	2.8651E+01	4.1693E-01	8.7543E+01	0.0000E+00
	-4.8452E-03	-1.5093E+03	-2.4221E-03	-2.8343E+01	-4.2228E-01	-8.3638E+01	0.0000E+00
14	4.8453E-03	1.5093E+03	2.4221E-03	3.0625E+00	8.0099E-01	1.2517E+01	0.0000E+00
	-4.8453E-03	-1.5093E+03	-2.4221E-03	-2.7800E+00	-8.0099E-01	-1.1120E+01	0.0000E+00

DISPLACEMENTS AT NODES

NO.	W_X	V_Y	U_Z	THETA_X	THETA_Y	THETA_Z	TWIST_Z'

1 0.0000E+00 0.0000E+00 0.0000E+00 3.9834E-03 -5.8381E-05 -3.8173E-02 0.0000E+00

8 3.9752E-02 4.1852E-03 6.1955E-03 2.0251E-03 1.3924E-04 2.1048E-03 0.0000E+00

15 0.0000E+00 8.6712E-03 0.0000E+00 -7.1007E-03 0.0000E+00 3.5096E-02 0.0000E+00

SPRINGS' REACTIONS

NO.	@DOF	FORCE
15	144	-3.9716E+02

THE END